Interface Studies of Metal/2D Material Contacts

A Dissertation

Presented to

the faculty of the School of Engineering and Applied Science

University of Virginia

in partial fulfillment
of the requirements for the degree

Doctor of Philosophy

by

Keren M Freedy

APPROVAL SHEET

This Dissertation
is submitted in partial fulfillment of the requirements
for the degree of
Doctor of Philosophy

Author Signature: Kevin Healy

This Dissertation has been read and approved by the examining committee:

Advisor: Stephen J. McDonnell

Committee Member: Jerrold A. Floro

Committee Member: Petra Reinke

Committee Member: Patrick E. Hopkins

Committee Member: Avik Ghosh

Committee Member:

Accepted for the School of Engineering and Applied Science:

Craig H. Benson, School of Engineering and Applied Science

May 2019

Abstract

The imminent end of Moore's Law motivated the exploration of alternative materials for electronic device applications. One category of materials that has attracted interest for nanoelectronics is two dimensional (2D) materials, which are characterized by vertically stacked layers of covalently bonded material held together by weak van der Waals forces in the out-of-plane direction. The isolation of single layer graphene by exfoliation and the subsequent rise of graphene in the 2000s led to renewed interest in other types of layered materials such as transition metal dichalcogenides (TMDs). The unique electronic, optical, and thermal properties of 2D materials make them promising for a variety of applications including low power electronics and photodetectors, as well as solar and thermoelectric energy conversion.

A fundamental component of any type of device is the contact that connects the device to external circuitry and controls the flow of current and heat into and out of the device. Numerous experimental and theoretical studies have concluded that the contact interface is the dominant performance limiting factor for 2D transistors particularly at short channel lengths. Due to processing challenges that are unique to 2D materials, the chemical composition and transport properties of the contact interface become more difficult to control. Furthermore, as electrical energy is converted to heat in resistive electrical contacts, thermal contact resistance becomes extremely important since excessive heat generation can severely compromise device operation, reliability, and lifetime. Like electrical resistance, the thermal resistance in the cross-plane direction of metal/2D systems is limited by the interface and has been found to be highly dependent on the nature of chemical interaction between the metal and the 2D material.

There currently exists a gap in understanding the relationship between contact processing conditions, interface chemistry, and electrical and thermal transport properties. Central to the work

presented here is the study of chemical reactions at the metal/2D interface using X-ray photoelectron spectroscopy. Interface studies in this work utilize chemical vapor deposition (CVD) grown graphene, geological and CVD MoS_2, as well as molecular beam epitaxy-grown WSe_2. In combination with photoelectron spectroscopy and metal depositions in high and ultra-high vacuum, ex-situ electrical and thermal interface characterization methods are employed. Different aspects of contact processing are addressed, including contact deposition conditions, post-deposition heat treatments, and polymer-aided processes. The results obtained have profound implications for both fundamental materials science and 2D device design and fabrication processes.

Acknowledgements

I would first like to thank my advisor, Professor Stephen McDonnell. Thank you for taking me on as your student and thank you for being a patient, enthusiastic, and supportive advisor. Thank you for your consistent guidance and helpful feedback, for encouraging my independence as a researcher, for challenging me to achieve new milestones, and for imparting tremendous technical knowledge as well as skills that extend beyond research.

I would also like to thank my committee members, Professor Jerry Floro, Professor Patrick Hopkins, Professor Petra Reinke, and Professor Avik Ghosh who have been excellent teachers and mentors throughout my time in UVA. Thank you for supporting me in this journey and for guiding me through my research, coursework, and career plans.

The work presented here would have not have been possible without the contributions of many collaborators and co-authors here at UVA. Huge thanks to Professor Hopkins, Dr. Ash Giri, Dr. Brian Foley, and Hans Olson for your contributions to all thermal transport characterization in this work and for the many helpful discussions and productive collaborations. Thank you to our first undergraduate students Matt Barone and Genevieve Glista who helped me get started with graphene, to William Blades and Dr. Chris Duska for help with AFM, to Professor Jerry Floro for letting us use your AFM and UV-O_3, to Professor Petra Reinke for helpful discussions, to Richard White and Joe Thompson for help with Raman, and to Professor Mona Zebarjadi and Tianhui Zhu for your recent contributions.

I owe many thanks to our collaborators elsewhere who have provided us with materials to work with, performed characterization, and offered their insights: Professor Rodney Ruoff and Dr. Ming Huang for sharing their high quality CVD graphene, Dr. Thomas Beechem for expert

analysis of Raman data, Dr. Sergiy Krylyuk for providing synthetic MoS_2, Dr. Huairuo Zhang for TEM analysis, Dr. Albert Davydov for collaborating on both MoS_2 thermal stability and residue cleaning projects, and Dr. Pranab Mohapatra and Dr. Ariel Ismach for providing CVD MoS_2, and Professor Costel Constantin for access to AFM.

I am extremely grateful for having the best labmates possible, Peter and Meg, who have not only been instrumental contributors to a number of my projects, but have also made it fun to be in the lab everyday even during the most stressful and challenging times. Thank you for always being so eager to help with any task and for always offering your intelligent insights, motivational words, emotional support, and sense of humor. You have both been not only colleagues but also close friends who I will really miss.

I am eternally grateful for the other incredible friendships I have formed here at UVA. Veronica and Sarah, you have been family to me since the very beginning of this journey and I can't imagine what my time here would have been like without you. Thank you also to Rachel for always being there for the past 14 years and to all my other wonderful friends who have been there for me and brought me joy.

I've been fortunate to have my brother and his family close by here in Virginia - thank you for being my home away from home. Thank you to my sister for always being there for me even from so far away. The greatest thanks are for my parents - Thank you for everything you've done for me. Thank you for encouraging me to pursue this path, for keeping me motivated, and offering your wise advice whenever needed. I wouldn't have achieved this without your constant support.

Table of Contents

List of Figures

Publications

The following publications have resulted / will result from the work presented in this dissertation:

1. Freedy, K. M.; Litwin, P. M.; McDonnell, S. J., (Invited) In-Vacuo Studies of Transition Metal Dichalcogenide Synthesis and Layered Material Integration. *ECS Transactions* **2017**, *77* (8), 11-25
2. Freedy, K. M.; Giri, A.; Foley, B. M.; Barone, M. R.; Hopkins, P. E.; McDonnell, S., Titanium contacts to graphene: process-induced variability in electronic and thermal transport. *Nanotechnology* **2018**, *29* (14), 145201.
3. Freedy, K. M.; Beechem, T. E.; Litwin, P. M.; Sales, M. G.; Huang, M.; Ruoff, R. S.; McDonnell, S. J., Unraveling Chemical Interactions between Titanium and Graphene for Electrical Contact Applications. *ACS Applied Nano Materials* **2018,** *1* (9), 4828-4835.
4. Freedy, K. M.; Sales, M. G.; Litwin, P. M.; Krylyuk, S.; Mohapatra, P.; Ismach, A.; Davydov, A. V.; McDonnell, S. J., MoS_2 cleaning by acetone and UV-ozone: Geological and synthetic material. *Applied Surface Science* **2019**, *478*, 183-188.
5. Freedy, K. M., Olson, D. H., Hopkins, P. E., McDonnell, S. J., Titanium Contacts to MoS_2 with Interfacial Oxide: Interface Chemistry and Thermal Transport. *Submitted.*
6. Freedy, K. M., Zhang, H., Davydov, A., McDonnell, S. J., Thermal Stability of the Ti Contacts to MoS_2. *In preparation.*
7. Freedy, K. M., Olson, D. H., Hopkins, P. E., McDonnell, S. J., Interface Chemistry and Thermal Transport of Titanium Contacts to WSe_2. *In preparation.*
8. Freedy, K. M., McDonnell, S. J. (Invited Review) Contacts for 2D Materials: Interface Chemistry and Thermal Stability. *Materials. In preparation.*

1 INTRODUCTION

1.1 2D Materials

A single material – silicon – has dominated the semiconductor industry for the past 50 years. Si-based metal oxide semiconductor field effect transistors (MOSFETs) have formed the building blocks of complementary metal oxide semiconductor (CMOS) integrated circuits, the basis of digital computing.[2] With developments in fabrication processes, MOSFETs have been reduced in size to increasingly enhance computing performance as a function of time at a roughly constant cost. This trend , often referred to as Moore's Law, has governed the tremendous progress in the semiconductor industry to date.[3] However, as channel lengths are reduced to the nanometer scale, the performance and reliability of devices will be hindered due to quantum tunneling effects and excessive heat generation. This imminent end of Moore's Law motivated the exploration of alternative materials, device geometries, and computing paradigms.[2]

One category of materials that has attracted interest for "beyond Moore" electronics is two dimensional (2D) materials. This family of materials is characterized by vertically stacked layers of material held together by weak van der Waals forces as shown in Figure 1.1.1. Owing to the lack of dangling bonds in the out-of-plane direction, it possible to isolate or synthesize a stable 2D sheet of material. For transistor scaling, the ability to achieve atomically thin channels is particularly appealing as it provides superior electrostatic control of the channel region.[4] Achieving electrostatic control of the channel charge by the gate is a major challenge in scaling silicon and III-V MOSFETs to overcome short channel effects.[5]

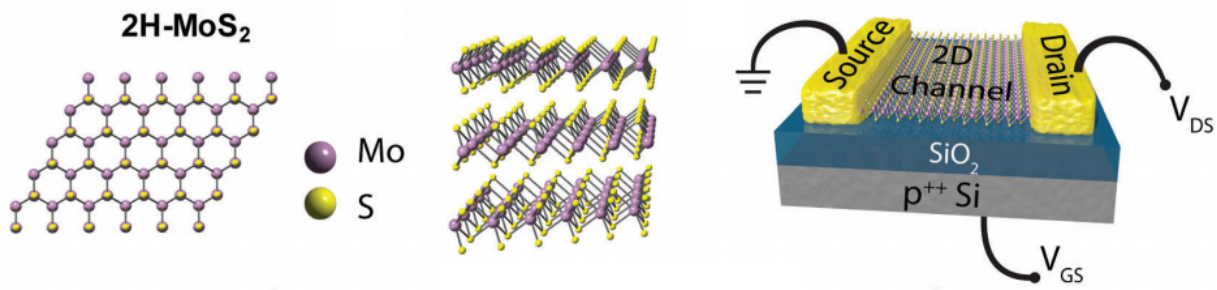

Figure 1.1.1. Example of electronics using 2D materials showing crystal structure of MoS_2 (top and side views), and back-gated field effect transistor. Adapted from Ref. 1.

The growing interest in electronics based on 2D materials was catalyzed by graphene, for which the 2010 Nobel Prize in Physics was awarded to Andre Geim and Konstantin Novoselov. [6] In 2004, the team at Manchester University demonstrated the isolation of a sheet of carbon atoms and the fabrication of a field-effect transistor (FET) with remarkable electronic properties such as exceptionally high electron mobility and ambipolar conduction.[7-9] Subsequently, graphene became the focus of an immense volume of research, with the number of scientific publications growing exponentially with time as shown in Figure 1.1.2 on the left.[10] Its unique properties make it a versatile material for numerous applications in the field of electronics, including analog devices[11-12], spintronics[13-15], transparent conductive electrodes[16-17], optoelectronics[17-19], and heat management in electronics packaging[20-21].

The success of graphene and the fascinating physics of quantum-confinement in atomically thin layers of material led to the exploration of other 2D materials to drive the development of new transistor technologies.[4, 22-30] In 2011, the first report of a FET based on a single layer of MoS_2, sparked a renewed interest in a class of 2D materials known as transition metal dichalcogenides (TMDs). TMDs have been studied since the early 1900s[31-35] primarily for applications in tribology[36-39], catalysis[40-41], and photocatalysis[42-43]. The first use of MoS_2 as a component in an electrical circuit was reported in 1908.[32-33] TMDs have the chemical structure MX_2 where M is the

transition metal (such as Mo, W, Sn, Hf, Zr) and X is the chalcogen (S, Se, and Te).[23] TMDs exhibit a layered structure that is very similar to that of graphite, where layers of covalently bonded atoms are weakly bonded to each other through van der Waals forces. Like graphite, TMDs are also naturally occurring minerals with MoS_2 being the most abundant. In fact, the "scotch tape" method which Geim and Novoselov used to isolate graphene from bulk graphite was previously reported for the exfoliation of few-layer MoS_2 from a bulk geological crystal in 1966.[44] Since the FET report in 2011, research on TMDs for electronic applications has followed a trend similar to that of graphene as shown in Figure 1.1.2. on the right.

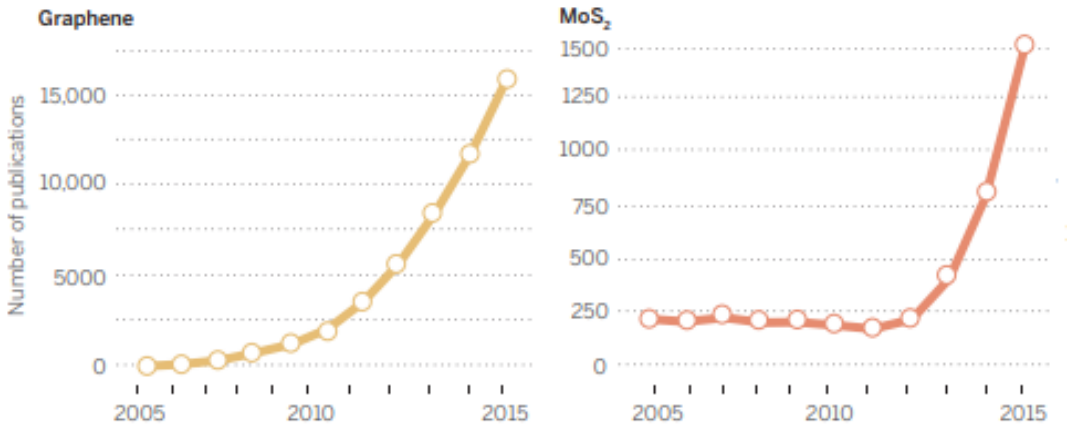

Figure 1.1.2. Growth rate of research on graphene and MoS_2 between 2005 and 2015. Adapted from Ref. 10.

Unlike graphene, many TMDs, including MoS_2 and WSe_2, have a band gap close to that of conventional semiconductors (~1.1-1.9 eV) which makes them better suited for transistor and optoelectronic applications. [45-46] A unique advantage presented by TMDs is the ability tune to the band structure by varying the number of layers.[46] TMDs have a heavy carrier effective mass. On the one hand, this may make them less susceptible than Si to source-drain tunneling on the sub-5 nm scale, but on the other hand, their low carrier mobility values ultimately make them unsuitable

for high performance logic applications.[22] While the search for Si CMOS alternatives is what sparked current research efforts in 2D materials, graphene and TMDs are unlikely to be direct successors to Si in large scale, commercial digital computing: whereas graphene is limited primarily by its lack of a band gap which inhibits switching, TMDs are limited by low carrier mobility. Nevertheless, like graphene, TMDs have demonstrated significant potential as materials for low power electronics[47-48] and photodetectors[25, 49], as well as solar and thermoelectric energy conversion[50-52]. As a result, research in these fields continues to grow in volume and expand into new domains.

1.2 Metal/2D Interfaces

A fundamental hindrance to the commercialization of 2D technology is the large contact resistance at the metal/2D interface. The contact is an essential component of any device as its properties determine the flow of electrical current and heat between the device and external circuitry. Numerous experimental and theoretical studies have concluded that contact interface is the dominant performance limiting factor for 2D transistors particularly at short channel lengths.[53-57] In the 2D limit, contact resistance dominates the overall device resistance. Due to processing challenges that are unique to 2D materials, including polymer-aided transfer processes and the inability to implement standard doping techniques, the chemical composition and transport properties of the contact interface become more difficult to control. Furthermore, as electrical energy is converted to heat in resistive electrical contacts, thermal contact resistance is an extremely important quantity since excessive heat generation can severely compromise device operation and lifetime.[58] Like electrical resistance, the thermal resistance in the cross-plane

direction of metal/2D systems is dominated by the interface[59] and has been found to be highly dependent on the nature of chemical interaction between the metal and the 2D material.[60-61]

Currently, a substantial volume of work is focused on the synthesis and characterization of 2D materials and on the fabrication and characterization of devices using 2D materials. Some studies have focused on optimizing transport properties of 2D/contact interface[1, 53, 60, 62-71] while a very small number have specifically examined the chemistry of the interface.[72-75] There exists a gap between these two topics of research, resulting in a lack of understanding of the relationship between contact processing, interface chemistry, and electrical and thermal transport properties. Central to the work presented here is the study of interface chemistry using X-ray photoelectron spectroscopy. Different aspects of contact processing are addressed, including contact deposition conditions, post-deposition heat treatments, polymer-aided processes. In combination with photoelectron spectroscopy and metal depositions in high and ultra-high vacuum, ex-situ electrical and thermal interface characterization methods are employed. The results obtained have profound implications for both fundamental materials science and 2D device design and fabrication processes.

1.3 Dissertation Overview

This dissertation is organized into six chapters of experimental work presented following Materials and Methods (Part 2). Each experimental chapter investigates the interface chemistry or transport properties resulting from a particular process related to the contact interface. The chapters are grouped into a section on graphene (Part 3) and another on TMDs (Part 4). An introduction to relevant aspects of the properties, applications and processing of graphene and metal contacts to

graphene will be presented in the introduction of Part 3 followed by two separate experimental studies on titanium/graphene interface chemistry and effects of processing conditions. A review of literature on metal interfaces with a focus on MoS_2 and WSe_2 is provided in the introduction to Part 4. Four chapters investigating topics such as reactivity of metal/MoS_2 interfaces, property engineering in titanium contacts to MoS_2 and WSe_2, and effects of polymer removal procedures on geological and synthetic MoS_2 surface chemistry. Potential directions for future study are discussed at the end of chapter, and the far-reaching implications of the work presented are summarized in Part 5.

1.4 References

1. Schulman, D. S.; Arnold, A. J.; Das, S., Contact engineering for 2D materials and devices. *Chemical Society Reviews* **2018,** *47* (9), 3037-3058.
2. Shalf, J. M.; Leland, R., Computing beyond Moore's Law. *Computer* **2015,** *48* (12), 14-23.
3. Waldrop, M. M., The chips are down for Moore's law. *Nature News* **2016,** *530* (7589), 144.
4. Fiori, G.; Bonaccorso, F.; Iannaccone, G.; Palacios, T.; Neumaier, D.; Seabaugh, A.; Banerjee, S. K.; Colombo, L., Electronics based on two-dimensional materials. *Nature Nanotechnology* **2014,** *9*, 768.
5. del Alamo, J. A., Nanometre-scale electronics with III–V compound semiconductors. *Nature* **2011,** *479*, 317.
6. Gerstner, E., Nobel Prize 2010: Andre Geim & Konstantin Novoselov. *Nature Physics* **2010,** *6*, 836.
7. Novoselov, K. S.; Geim, A. K.; Morozov, S. V.; Jiang, D.; Zhang, Y.; Dubonos, S. V.; Grigorieva, I. V.; Firsov, A. A., Electric Field Effect in Atomically Thin Carbon Films. *Science* **2004,** *306* (5696), 666.
8. Novoselov, K. S.; Geim, A. K.; Morozov, S. V.; Jiang, D.; Katsnelson, M. I.; Grigorieva, I. V.; Dubonos, S. V.; Firsov, A. A., Two-dimensional gas of massless Dirac fermions in graphene. *Nature* **2005,** *438*, 197.
9. Castro Neto, A. H.; Guinea, F.; Peres, N. M. R.; Novoselov, K. S.; Geim, A. K., The electronic properties of graphene. *Reviews of Modern Physics* **2009,** *81* (1), 109-162.
10. Service, R. F., Beyond graphene. *Science* **2015,** *348* (6234), 490.
11. Schwierz, F., Graphene transistors. *Nature Nanotechnology* **2010,** *5*, 487.
12. Liao, L.; Duan, X., Graphene for radio frequency electronics. *Materials Today* **2012,** *15* (7), 328-338.
13. Semenov, Y.; Kim, K.; Zavada, J., Spin field effect transistor with a graphene channel. *Applied Physics Letters* **2007,** *91* (15), 153105.
14. Han, W.; Kawakami, R. K.; Gmitra, M.; Fabian, J., Graphene spintronics. *Nature nanotechnology* **2014,** *9* (10), 794.
15. Banerjee, S. K.; Register, L. F.; Tutuc, E.; Reddy, D.; MacDonald, A. H., Bilayer PseudoSpin Field-Effect Transistor (BiSFET): A Proposed New Logic Device. *IEEE Electron Device Letters* **2009,** *30* (2), 158-160.
16. Li, X.; Zhu, Y.; Cai, W.; Borysiak, M.; Han, B.; Chen, D.; Piner, R. D.; Colombo, L.; Ruoff, R. S., Transfer of Large-Area Graphene Films for High-Performance Transparent Conductive Electrodes. *Nano Letters* **2009,** *9* (12), 4359-4363.
17. Avouris, P., Graphene: Electronic and Photonic Properties and Devices. *Nano Letters* **2010,** *10* (11), 4285-4294.
18. Mueller, T.; Xia, F.; Avouris, P., Graphene photodetectors for high-speed optical communications. *Nature Photonics* **2010,** *4*, 297.
19. Xia, F.; Mueller, T.; Lin, Y.-m.; Valdes-Garcia, A.; Avouris, P., Ultrafast graphene photodetector. *Nature Nanotechnology* **2009,** *4*, 839.
20. Shahil, K. M. F.; Balandin, A. A., Thermal properties of graphene and multilayer graphene: Applications in thermal interface materials. *Solid State Communications* **2012,** *152* (15), 1331-1340.

21. Pop, E.; Varshney, V.; Roy, A. K., Thermal properties of graphene: Fundamentals and applications. *MRS Bulletin* **2012,** *37* (12), 1273-1281.
22. Schwierz, F.; Pezoldt, J.; Granzner, R., Two-dimensional materials and their prospects in transistor electronics. *Nanoscale* **2015,** *7* (18), 8261-8283.
23. McDonnell, S. J.; Wallace, R. M., Atomically-thin layered films for device applications based upon 2D TMDC materials. *Thin Solid Films* **2016,** *616*, 482-501.
24. Butler, S. Z.; Hollen, S. M.; Cao, L.; Cui, Y.; Gupta, J. A.; Gutiérrez, H. R.; Heinz, T. F.; Hong, S. S.; Huang, J.; Ismach, A. F., Progress, challenges, and opportunities in two-dimensional materials beyond graphene. *ACS nano* **2013,** *7* (4), 2898-2926.
25. Wang, Q. H.; Kalantar-Zadeh, K.; Kis, A.; Coleman, J. N.; Strano, M. S., Electronics and optoelectronics of two-dimensional transition metal dichalcogenides. *Nature Nanotechnology* **2012,** *7*, 699.
26. Novoselov, K. S.; Jiang, D.; Schedin, F.; Booth, T. J.; Khotkevich, V. V.; Morozov, S. V.; Geim, A. K., Two-dimensional atomic crystals. *Proceedings of the National Academy of Sciences of the United States of America* **2005,** *102* (30), 10451-10453.
27. Radisavljevic, B.; Radenovic, A.; Brivio, J.; Giacometti, V.; Kis, A., Single-layer MoS2 transistors. *Nat Nano* **2011,** *6* (3), 147-150.
28. Lemme, M. C.; Li, L.-J.; Palacios, T.; Schwierz, F., Two-dimensional materials for electronic applications. *MRS Bulletin* **2014,** *39* (8), 711-718.
29. Ayari, A.; Cobas, E.; Ogundadegbe, O.; Fuhrer, M. S., Realization and electrical characterization of ultrathin crystals of layered transition-metal dichalcogenides. *Journal of Applied Physics* **2007,** *101* (1), 014507.
30. Chhowalla, M.; Jena, D.; Zhang, H., Two-dimensional semiconductors for transistors. *Nature Reviews Materials* **2016,** *1*, 16052.
31. Dickinson, R. G.; Pauling, L., The crystal structure of molybdenite. *Journal of the American Chemical Society* **1923,** *45* (6), 1466-1471.
32. Pierce, G. W., A Simple Method of Measuring the Intensity of Sound. *Proceedings of the American Academy of Arts and Sciences* **1908,** *43* (13), 377-395.
33. Pierce, G. W., Crystal Rectifiers for Electric Currents and Electric Oscillations. II. Carborundum, Molybdenite, Anatase, Brookite. *Proceedings of the American Academy of Arts and Sciences* **1909,** *44* (12), 317-349.
34. Waterman, A. T., The Electrical Conductivity of Molybdenite. *Physical Review* **1923,** *21* (5), 540-549.
35. Wells, R. C.; Butler, B. S., Tungstenite, a new mineral. *Journal of the Washington Academy of Sciences* **1917,** *7* (20), 596-599.
36. Lavik, M. T.; Daniel, T. B.; Abbott, A. N., Friction of molybdenum diselenide. *Journal of Applied Physics* **1961,** *32* (9), 1795-1795.
37. Salomon, G.; Begelinger, A.; Van Bloois, F.; De Gee, A., Characterization and Tribological Properties of MoS2 Powders and of Related Chalcogenides. *ASLE TRANSACTIONS* **1970,** *13* (2), 134-147.
38. Winer, W. O., Molybdenum disulfide as a lubricant: A review of the fundamental knowledge. *Wear* **1967,** *10* (6), 422-452.
39. Cooper, H. S.; Damerell, V. R., Lubricant. Google Patents: 1939.
40. De Beer, V.; Dahlmans, J.; Smeets, J., Hydrodesulfurization and hydrogenation properties of promoted MoS2 and WS2 catalysts under medium pressure conditions. *J. Catal* **1976,** *42*, 467.
41. Gwynn, M. H., Catalysts for hydrogenation. *Oil & Soap* **1939,** *16* (2), 25-28.

42. Tributsch, H.; Bennett, J. C., Electrochemistry and photochemistry of MoS2 layer crystals. I. *Journal of Electroanalytical Chemistry and Interfacial Electrochemistry* **1977,** *81* (1), 97-111.
43. Ahmed, S. M.; Gerischer, H., Influence of crystal surface orientation on redox reactions at semiconducting MoS2. *Electrochimica Acta* **1979,** *24* (6), 705-711.
44. Frindt, R., Single crystals of MoS2 several molecular layers thick. *Journal of Applied Physics* **1966,** *37* (4), 1928-1929.
45. Splendiani, A.; Sun, L.; Zhang, Y.; Li, T.; Kim, J.; Chim, C.-Y.; Galli, G.; Wang, F., Emerging Photoluminescence in Monolayer MoS2. *Nano Letters* **2010,** *10* (4), 1271-1275.
46. Mak, K. F.; Lee, C.; Hone, J.; Shan, J.; Heinz, T. F., Atomically Thin ${\mathrm{MoS}}_{2}$: A New Direct-Gap Semiconductor. *Physical Review Letters* **2010,** *105* (13), 136805.
47. Jena, D., Tunneling Transistors Based on Graphene and 2-D Crystals. *Proceedings of the IEEE* **2013,** *101* (7), 1585-1602.
48. Das, S.; Prakash, A.; Salazar, R.; Appenzeller, J., Toward Low-Power Electronics: Tunneling Phenomena in Transition Metal Dichalcogenides. *ACS Nano* **2014,** *8* (2), 1681-1689.
49. Tsai, D.-S.; Liu, K.-K.; Lien, D.-H.; Tsai, M.-L.; Kang, C.-F.; Lin, C.-A.; Li, L.-J.; He, J.-H., Few-Layer MoS2 with High Broadband Photogain and Fast Optical Switching for Use in Harsh Environments. *ACS Nano* **2013,** *7* (5), 3905-3911.
50. Akama, T.; Okita, W.; Nagai, R.; Li, C.; Kaneko, T.; Kato, T., Schottky solar cell using few-layered transition metal dichalcogenides toward large-scale fabrication of semitransparent and flexible power generator. *Scientific Reports* **2017,** *7* (1), 11967.
51. Tsai, M.-L.; Su, S.-H.; Chang, J.-K.; Tsai, D.-S.; Chen, C.-H.; Wu, C.-I.; Li, L.-J.; Chen, L.-J.; He, J.-H., Monolayer MoS2 Heterojunction Solar Cells. *ACS Nano* **2014,** *8* (8), 8317-8322.
52. Wang, X.; Zebarjadi, M.; Esfarjani, K., First principles calculations of solid-state thermionic transport in layered van der Waals heterostructures. *Nanoscale* **2016,** *8* (31), 14695-14704.
53. Allain, A.; Kang, J.; Banerjee, K.; Kis, A., Electrical contacts to two-dimensional semiconductors. *Nat Mater* **2015,** *14* (12), 1195-1205.
54. Nagashio, K.; Nishimura, T.; Kita, K.; Toriumi, A. In *Metal/graphene contact as a performance Killer of ultra-high mobility graphene analysis of intrinsic mobility and contact resistance*, IEEE Int. Electron Devices Meet., 7-9 Dec. 2009; 2009; pp 1-4.
55. Seul Ki, H.; Sang Chul, J.; Wan Sik, H.; Byung Jin, C., Resistance analysis and device design guideline for graphene RF transistors. *2D Materials* **2015,** *2* (3), 034011.
56. Liu, H.; Neal, A. T.; Ye, P. D., Channel Length Scaling of MoS2 MOSFETs. *ACS Nano* **2012,** *6* (10), 8563-8569.
57. Giannazzo, F.; Fisichella, G.; Piazza, A.; Di Franco, S.; Greco, G.; Agnello, S.; Roccaforte, F., Impact of contact resistance on the electrical properties of MoS(2) transistors at practical operating temperatures. *Beilstein Journal of Nanotechnology* **2017,** *8*, 254-263.
58. Pop, E., Energy dissipation and transport in nanoscale devices. *Nano Research* **2010,** *3* (3), 147-169.
59. Goni, M.; Yang, J.; Schmidt, A. J., Enhanced thermal transport across monolayer MoS2. *Nano Research* **2018,** *11* (4), 2173-2180.
60. Hopkins, P. E.; Baraket, M.; Barnat, E. V.; Beechem, T. E.; Kearney, S. P.; Duda, J. C.; Robinson, J. T.; Walton, S. G., Manipulating Thermal Conductance at Metal–Graphene Contacts via Chemical Functionalization. *Nano Letters* **2012,** *12* (2), 590-595.

61. Yan, Z.; Chen, L.; Yoon, M.; Kumar, S., The Role of Interfacial Electronic Properties on Phonon Transport in Two-Dimensional MoS2 on Metal Substrates. *ACS Applied Materials & Interfaces* **2016,** *8* (48), 33299-33306.
62. English, C. D.; Shine, G.; Dorgan, V. E.; Saraswat, K. C.; Pop, E., Improved Contacts to MoS2 Transistors by Ultra-High Vacuum Metal Deposition. *Nano Letters* **2016,** *16* (6), 3824-3830.
63. Robinson, J. A.; LaBella, M.; Zhu, M.; Hollander, M.; Kasarda, R.; Hughes, Z.; Trumbull, K.; Cavalero, R.; Snyder, D., Contacting graphene. *Applied Physics Letters* **2011,** *98* (5), 053103.
64. Cusati, T.; Fiori, G.; Gahoi, A.; Passi, V.; Lemme, M. C.; Fortunelli, A.; Iannaccone, G., Electrical properties of graphene-metal contacts. *Scientific Reports* **2017,** *7* (1), 5109.
65. Nagashio, K.; Nishimura, T.; Kita, K.; Toriumi, A., Contact resistivity and current flow path at metal/graphene contact. *Applied Physics Letters* **2010,** *97* (14), 143514.
66. Gahoi, A.; Passi, V.; Kataria, S.; Wagner, S.; Bablich, A.; Lemme, M. C. In *Systematic comparison of metal contacts on CVD graphene*, 2015 45th European Solid State Device Research Conference (ESSDERC), 14-18 Sept. 2015; 2015; pp 184-187.
67. Gahoi, A.; Wagner, S.; Bablich, A.; Kataria, S.; Passi, V.; Lemme, M. C., Contact resistance study of various metal electrodes with CVD graphene. *Solid-State Electronics* **2016,** *125*, 234-239.
68. Russo, S.; Craciun, M. F.; Yamamoto, M.; Morpurgo, A. F.; Tarucha, S., Contact resistance in graphene-based devices. *Physica E: Low-dimensional Systems and Nanostructures* **2010,** *42* (4), 677-679.
69. Venugopal, A.; Colombo, L.; Vogel, E. M., Contact resistance in few and multilayer graphene devices. *Applied Physics Letters* **2010,** *96* (1), 013512.
70. Foley, B. M.; Hernández, S. C.; Duda, J. C.; Robinson, J. T.; Walton, S. G.; Hopkins, P. E., Modifying Surface Energy of Graphene via Plasma-Based Chemical Functionalization to Tune Thermal and Electrical Transport at Metal Interfaces. *Nano Letters* **2015,** *15* (8), 4876-4882.
71. Das, S.; Chen, H.-Y.; Penumatcha, A. V.; Appenzeller, J., High Performance Multilayer MoS2 Transistors with Scandium Contacts. *Nano Letters* **2013,** *13* (1), 100-105.
72. McDonnell, S.; Smyth, C.; Hinkle, C. L.; Wallace, R. M., MoS2–Titanium Contact Interface Reactions. *ACS Applied Materials & Interfaces* **2016,** *8* (12), 8289-8294.
73. Smyth, C. M.; Addou, R.; McDonnell, S.; Hinkle, C. L.; Wallace, R. M., WSe2-contact metal interface chemistry and band alignment under high vacuum and ultra high vacuum deposition conditions. *2D Materials* **2017,** *4* (2), 025084.
74. Smyth, C. M.; Addou, R.; McDonnell, S.; Hinkle, C. L.; Wallace, R. M., Contact Metal–MoS2 Interfacial Reactions and Potential Implications on MoS2-Based Device Performance. *The Journal of Physical Chemistry C* **2016,** *120* (27), 14719-14729.
75. Smyth, C. M.; Walsh, L. A.; Bolshakov, P.; Catalano, M.; Addou, R.; Wang, L.; Kim, J.; Kim, M. J.; Young, C. D.; Hinkle, C. L.; Wallace, R. M., Engineering the Palladium–WSe2 Interface Chemistry for Field Effect Transistors with High-Performance Hole Contacts. *ACS Applied Nano Materials* **2019,** *2* (1), 75-88.

2 MATERIALS AND METHODS

2.1 Overview

The experiments reported in this dissertation were performed using both geological and synthetic 2D materials as well as *in-vacuo* and *ex-situ* characterization methods. Synthetic materials include both chemical-vapor deposited (CVD) materials as well as those deposited in the McDonnell lab UHV system via molecular beam epitaxy (MBE). The primary characterization method used in this work is X-ray photoelectron spectroscopy (XPS) for analysis of interface chemistry. XPS results are supplemented by ex-situ materials characterization techniques including Raman spectroscopy, atomic force microscopy (AFM), and transmission electron microscopy (TEM). Electrical and thermal transport properties are measured using probe station and time domain thermoreflectance (TDTR). This chapter provides an overview of the capabilities of our laboratory and our collaborators, as well as an explanation of the physical principles governing the materials and methods which were used in this work.

2.2 Materials and Synthesis

2.2.1 Geological Materials

Geological MoS_2 (0001) crystals are used in this work in Part 4. Due to their natural earth-abundance, they are commonly used in laboratory settings for the fabrication of MoS_2 devices[1-4] as well as fundamental studies[5-10]. Crystals are mined from different geographic locations including Canada and Australia, and can be purchased at a low cost from a number of different vendors.[8] A typical crystal used in this work is shown in Figure 2.2.1(a). Geological material can be mechanically exfoliated using scotch tape to isolate thin flakes of material down to one

monolayer.[1] A single geological crystal can therefore yield countless samples depending on the application. Mechanical exfoliation using adhesive tape is the same procedure that has been applied to highly-ordered pyrolytic graphite (HOPG) crystals in order to isolate graphene.[11] This method is possible due to the weak van der Waals forces between layers which are easily overcome by adhesion to scotch tape. Other techniques for processing geological material include exfoliation in the liquid phase using solvents or ion intercalation.[12-14] While the experiments in this dissertation utilize bulk crystals rather than thin flakes, exfoliation via scotch tape is implemented as a method of cleaning the sample prior to experiments as shown in Figure 2.2.1(b). Upon exfoliation, the surface layers are removed, exposing a clean surface free of oxides and adventitious carbon species.

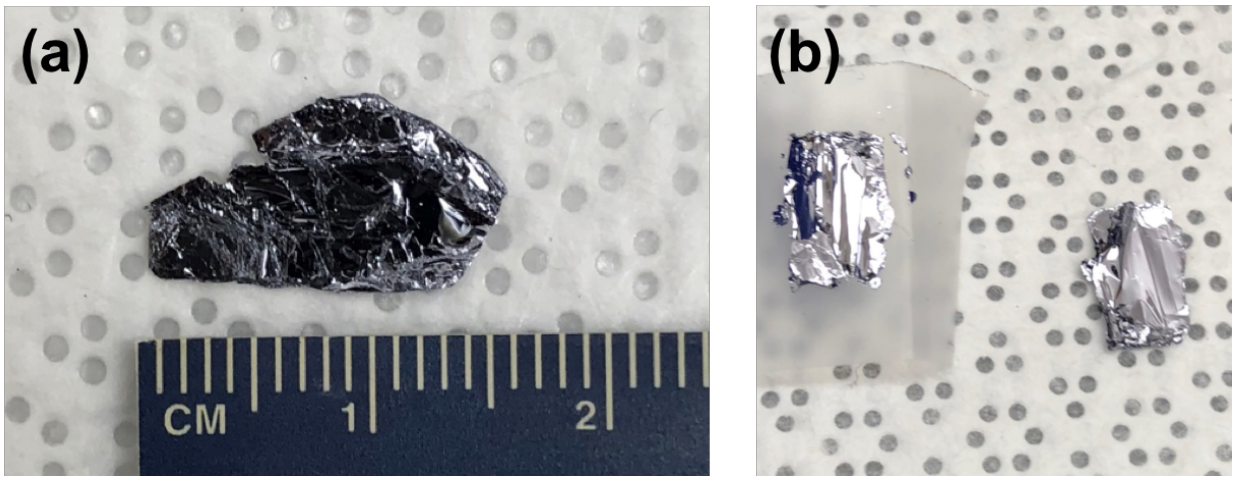

Figure 2.2.1. (a) As-received geological MoS2 (0001) used in this work. The crystals are purchased from SPI.[15] Smaller sample sizes can be obtained by slicing the crystal with a razor blade. (b) The surface is cleaned via scotch tape exfoliation immediately prior to an experiment.

Geological material, as well as most synthetic material, occurs in the semiconducting 2H polymorph. The 2H polymorph is the most stable among the four polytypes which include the metallic 1T type, distorted 1T (1T') and semiconducting 3R.[8, 16] The number in the polymorph name represents the number of layers per unit cell and the letter designates the type of symmetry

(trigonal, hexagonal, or rhombohedral) as shown in Figure 2.2.2. Geological material exhibits different types of intrinsic defects including S vacancies, Mo-rich metallic clusters[6], and impurities such as Fe (~1000 ppm), W (~4000 ppm), and Re (~5000 ppm)[8]. McDonnell *et al*.[6] have identified variations in MoS_X stoichiometry from X=1.8 to 2.3 on the surface of a single crystal. The work function has been found to vary from 4.4 to 5.3 eV resulting in both n- and p-type conductivities.[6, 8] Macroscopically, the material is rough and exhibits regions of bunched step edges and flakes that are partially delaminated, however flakes on the order of microns are atomically flat exhibiting extremely low surface roughness.[17]

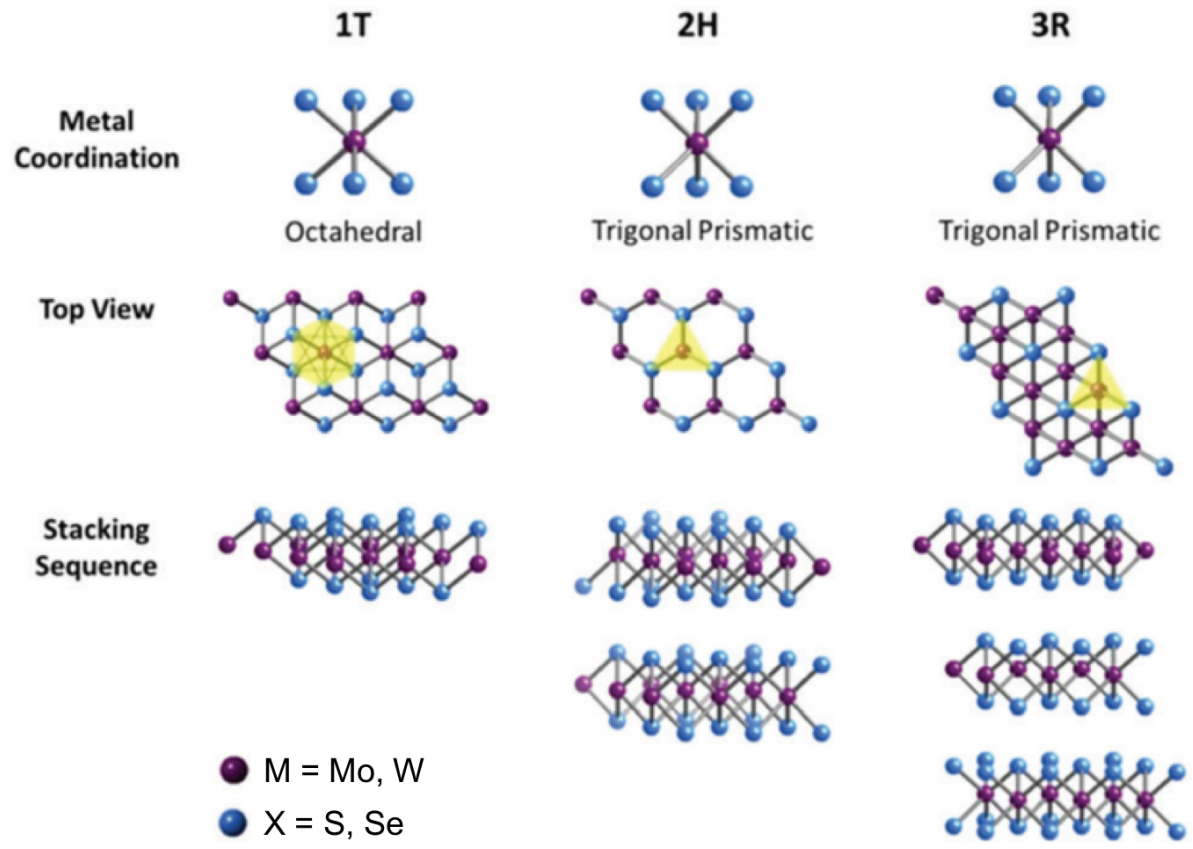

Figure 2.2.2. Metal coordination and stacking sequences of TMD structural unit cells. The geological crystals used in this work exhibit the 2H structure. Adapted from Ref. 18.

2.2.2 Chemical Vapor Deposition

Exfoliation of graphene from HOPG or thin flakes of MoS_2 from a bulk geological crystals yields a low volume of samples with poor control over thickness and area.[19] Chemical vapor deposition (CVD) is a low-cost route to high throughput synthesis of wafer-scale thin films. It has been used in the semiconductor industry to synthesize a wide range of materials including III-V semiconductors and SiGe[20-21] and has been widely applied to the fabrication of 2D materials. In general, the CVD process is defined as the reaction of precursor materials in the vapor phase resulting in the formation of a thin film on a heated substrate.[22] The graphene used in Chapters 3.2-3.3 and the MoS_2 used in Chapter 4.5 were synthesized using this method. The CVD samples used in this work were purchased from commercial vendors or acquired from collaborating institutions.

In CVD synthesis of graphene, gaseous reactants, typically CH_4:H_2, form a stable solid over a catalytic substrate at temperatures around 1000 ºC.[23] The dissociation of the C-H bonds in CH_4, or dehydrogenation, is a highly endothermic process requiring energy of approximately 4-5 eV. The dissociation energy is largely reduced on metal surfaces making metal foils a suitable substrate material as it also acts as a catalyst. The CVD process involves initial annealing of the substrate in a controlled atmosphere to clean its surface, introducing the precursor gases over the substrate to achieve film growth, and cooling in an inert atmosphere to prevent oxidation. The CVD process for graphene growth was initially developed on Ni substrates but failed to yield uniform, monolayer graphene due to the high C solubility in Ni.[24] During growth, carbon atoms diffuse into the bulk of the Ni substrate. Graphene growth on Ni occurs via precipitation of carbon out of Ni during cooling step after growth. Cu substrates have been found to result in substantially improved control over number of layers due to the relatively low C solubility in Cu, resulting in

surface-mediated, self-limiting process.[23] A comparison of the growth mechanism on the two substrates is shown in Figure 2.2.3. The material used in this work was grown on Cu.

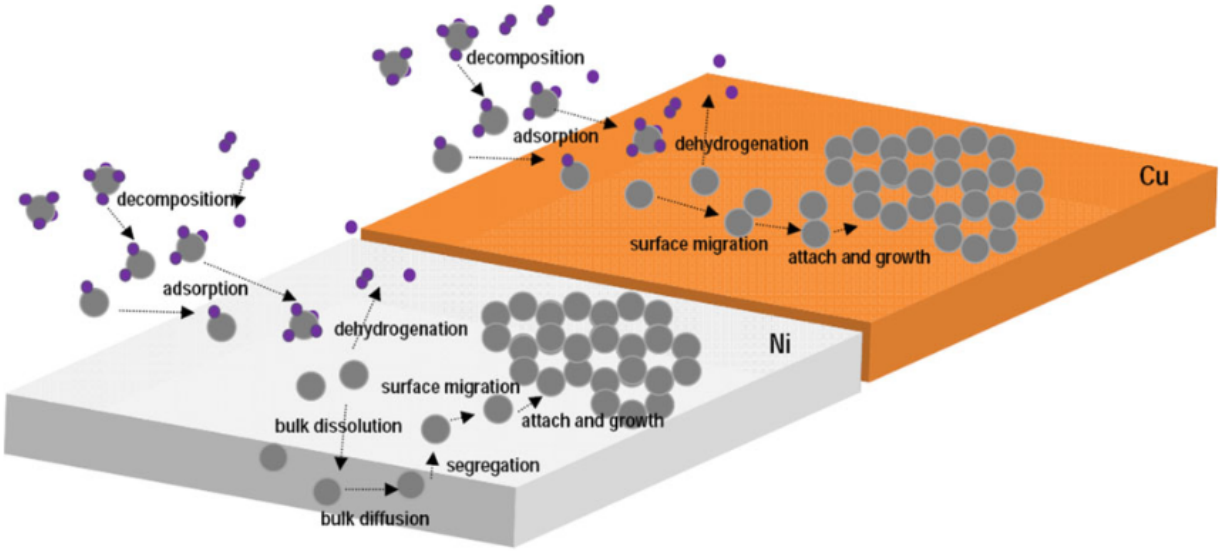

Figure 2.2.3. Growth mechanisms in CVD-graphene on Ni and Cu substrates with CH_4 precursors. Adapted from Ref. 23.

There are a number of different approaches to CVD synthesis of MoS_2.[25-26] The first is the sulfurization of Mo metal or oxide thin films which were pre-deposited on the substrate by electron beam evaporation.[19, 27-30] The second approach involves the reaction of Mo and S species in the gas phase, which can be achieved by evaporation of sulfur and MoO_3 powders in an inert atmosphere[31-34], or utilizing metalorganic gas phase precursors such as $Mo(CO)_6$ and $(C_2H_5)_2S$.[35] Lastly, direct evaporation and recrystallization of TMD powders has also been reported via a vapor-solid process.[36] In each of the methods mentioned, a number of parameters are tunable including substrate material, substrate temperature, background pressure, and precursor quantity, and flow rate. As a result, the literature exhibits a large variability in reported chemical, morphological, and electronic properties of MoS_2

A set of samples used in this work in Chapter 4.5 was created by our collaborators at the National Institute of Standards and Technology (NIST) via sulfurization of an electron-beam deposited Mo metal film on SiO_2/Si Sulfurization was achieved by flowing H_2S diluted with Ar carrier gas. This method produces multilayer MoS_2 where the thickness of the MoS_2 film depends on the thickness of the Mo metal precursor initially deposited. This process is typically performed at growth temperatures of 700-1000 °C[19] at which the migration of Mo metal atoms is suppressed given the high melting point of Mo (2610 °C). The result is typically a highly polycrystalline film.[26] MoO_3, which evaporates at 700 °C, can be deposited as an alternative precursor to Mo metal to achieve higher quality material at sulfurization temperature around 500 °C.[30] We note that even when Mo metal is deposited, some oxide is present due to a partial pressure of oxygen in the electron-beam evaporator or due to subsequent air exposure.

A second set of samples used in Chapter 4.5, created by our collaborators at Tel Aviv University, were grown in the vapor phase on sapphire substrates by the evaporation of MoO_3 and S powders at a temperature of 750 °C with 20 sccm of Ar flow at atmospheric pressure. This type of CVD process has been found to be highly sensitive to the substrate treatment prior to growth.[25, 31, 34] The sapphire substrate was cleaned prior to growth by sonication in acetone and isopropanol for 15 minutes each followed by piranha solution (H_2SO_4:H_2O_2, 3:1) for 1 hour at 90 °C. Following growth the films were transferred from sapphire onto SiO_2 substrates using a polystyrene mediated transfer process.[37] Polymer mediated transfer processes are commonly used to fabricate devices on SiO_2 from CVD material grown on different substrates.[38-39] CVD synthesis in the vapor phase exhibits inherently different growth kinetics than the sulfurization of solid precursors, yielding samples that are morphologically different. An example comparison form the literature is shown in Figure 2.2.4. Micrographs of the material used in our work is shown in Chapter 4.5.

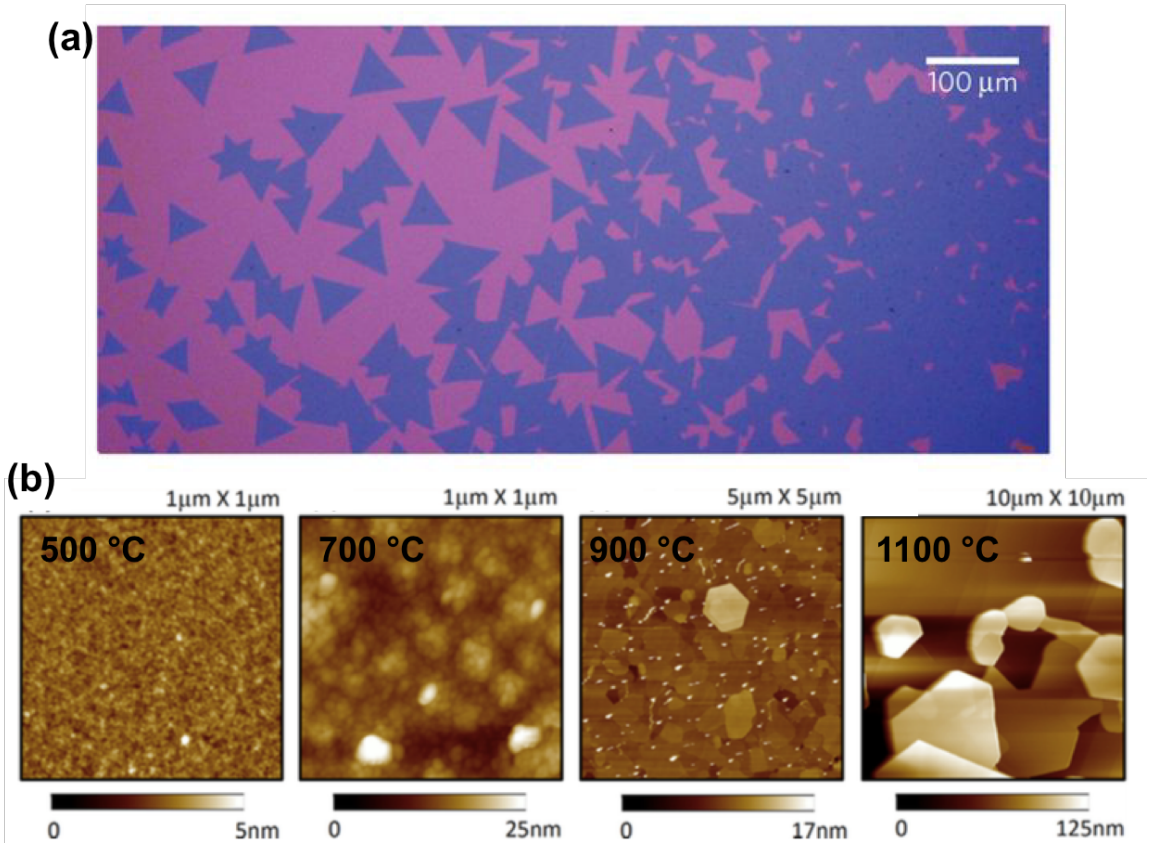

Figure 2.2.4. Comparison of CVD MoS_2 by (a) reactions in the vapor phase (from Ref. 34) and (b) sulfurization of Mo films at different temperatures (Ref. 19).

2.2.3 Molecular Beam Epitaxy

Like CVD, molecular beam epitaxy (MBE) has also been widely used for traditional semiconductors such as Si, SiGe, and III-V materials[40-42], and reports of MBE growth of TMDs were first published in the 1980s.[43-46] During MBE growth, evaporated material impinges on a substrate that is held at a high enough temperature to enable the adatoms to arrive at lattice sites to slowly form a crystal. The pressure for MBE is low enough such that the mean-free path between molecular collisions is longer than the source-substrate distance, making the reactant transport a molecular beam.[42, 47] The major advantage of MBE over CVD is the minimal contamination and

high purity achieved in UHV, in addition to precise electronic control over fluxes of the reactants which provides a superior ability to tune stoichiometry, morphology, and thickness. What distinguishes MBE growth of TMDs growth from the growth of 3D-bonded materials is the ability to grow on arbitrary substrates due to the absence of dangling bonds on the TMD surface, a consequence of its layered structure.[43-46, 48] This means that high quality heterostructures can be synthesized regardless of the lattice mismatch between the substrate and the film.

MBE was applied in this work to produce WSe_2 films in Chapter 4.4 The MBE module in our lab, shown in Figure 2.2.5 on the right, is maintained at a base pressure of $< 8 \times 10^{-11}$ mbar achieved with a combination of turbo molecular, titanium sublimation, and ion getter pumps. The chamber is also equipped with a liquid nitrogen-cooling shroud to minimize oxidizing species during growth. A built-in manipulator heater allows for sample heating to ~1000 °C. The chamber is fitted with two EFM-4 2 kV electron-beam evaporators capable of co-evaporating refractory metals. Electron-beam (sometimes abbreviated as e-beam) evaporation will be discussed in a later section. The reported deposition rate capabilities are 0.1 monolayer/minute to 1000 monolayers/second; however, in our work deposition rates as low as 0.1 monolayers/hour have been achieved. The films grown for this work were deposited at approximately 0.5 monolayers/hour. Two NTEZ 40-10-KS effusion cells allow for the controlled co-deposition of chalcogens. The chamber is also fitted with an SRS 200 amu residual gas analyzer for the monitoring partial pressures during source outgassing and growth. The MBE is isolated from the analysis module with a single gate valve, allowing for *in-vacuo* transfer of samples between the two chambers for post-growth characterization.

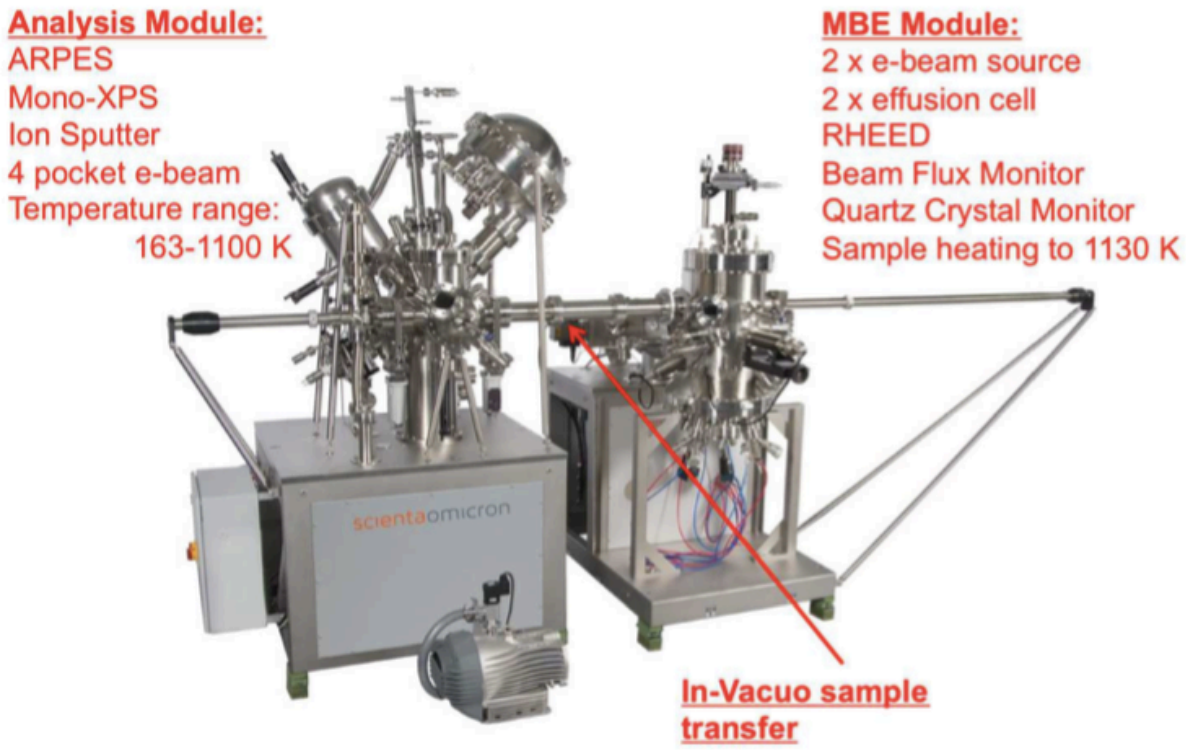

Figure 2.2.5. ARPES-MBE ultra-high vacuum system from ScientaOmircon

WSe_2 samples for this work were grown on grade 1 high ordered pyrolytic graphite (HOPG) purchased from SPI[15]. Prior to loading into UHV, HOPG is cleaved using tape and mounted onto a Mo sample plate with Ta foil. HOPG substrates are typically outgassed overnight at 200 °C and then for 10 minutes prior to growth at 600 °C to remove physisorbed contaminants. The substrates are then set to the growth temperature of 550 °C, and Se (99.999%, Kurt J. Lesker) and W (99.9+%, Goodfellow) are simultaneously evaporated onto the substrate after the appropriate beam equivalent pressures (BEPs) are achieved as indicated by the beam flux monitor. A typical BEP for W is 0.4×10^{-9} mbar and for Se is 2.8×10^{-6} mbar. The first stage of growth is performed with an "interrupted growth method" to create a ripening layer.[49-51] During this process

the W shutter is cyclically open for 30 seconds and closed for 90 seconds for a total of 38 minutes. After this process, the deposited material is left to cool in a Se flux to a temperature of 250 °C and is then re-heated to the growth temperature. The remainder of the film growth is conducted with the W shutter open continuously. After growth is complete, the sample is held at the growth temperature for 2 min then allowed to naturally cool to room temperature in a Se flux to avoid evaporation of Se from the film. The Se shutter is closed when the samples reach 250 °C to avoid Se condensation.

The thickness of an MBE-grown film is monitored during growth by in-situ reflection high-energy electron diffraction (RHEED), which is commonly used for surface structural analysis on MBE-grown films. Due to the grazing angle of the electron beam, only the top few planes of material are probed.[52] The diffraction pattern of the scattered electrons appears on a phosphor screen. Before growth, the substrate pattern is visible and as the film reaches one monolayer thickness, the pattern corresponding to the 2D film begins to appear and eventually bury that of the substrate. The evolution of the RHEED pattern and corresponding line profiles acquired during the growth of WSe_2 on an HOPG substrate is shown in Figure 2.2.6. The time for the disappearance of the substrate RHEED pattern is measured to determine the deposition rate for approximately one monolayer. This deposition rate is then used to estimate the time necessary to achieve the desired thickness. The spacing between the diffraction lines obtained from the change in intensity (dI/dx) can be used to determine the lattice parameter.

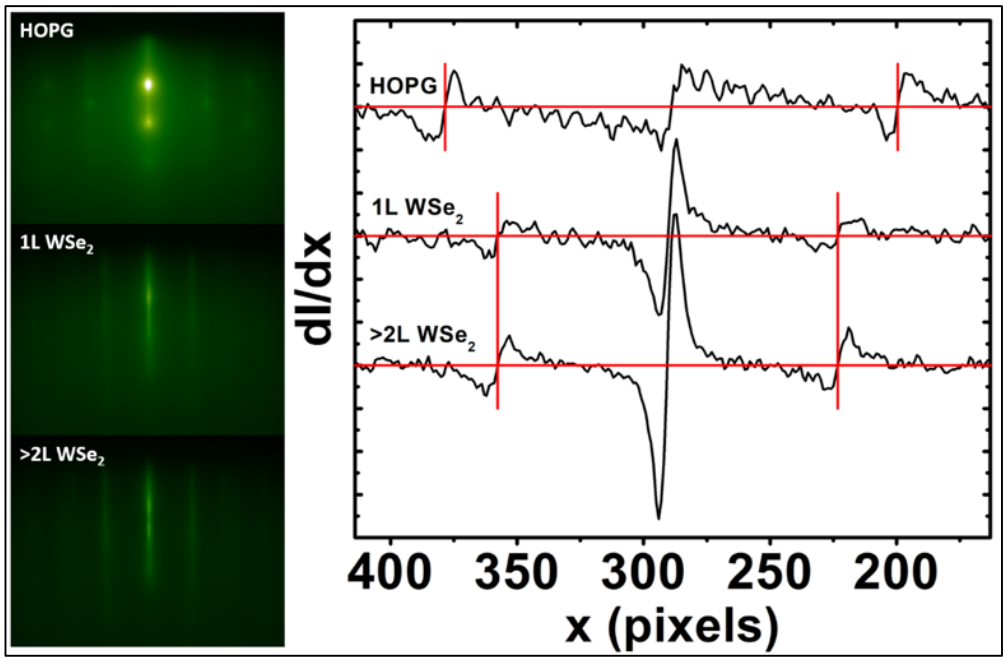

Figure 2.2.6. RHEED patterns acquired during the growth of WSe_2 on HOPG. Line profiles of the intensity were taken horizontally across each captured photo yielding intensity (I) vs. position (x). The locations where dI/dx is equal to zero represents inflection points. Courtesy of Peter Litwin.

2.2.4 Electron Beam Evaporation

Electron beam evaporation[53-55] is an effective method of depositing high purity thin films. High power densities can be achieved (10^4-10^9 W/cm^2) making it possible to evaporate materials with high melting temperatures at controllable deposition rates with a minimal consumption of energy. Metals, metal oxides, and other compounds including organic materials can be evaporated using this method. Electron beam evaporation is a common method for depositing metal contacts in device fabrication and is used in this work to deposit metals onto 2D materials for interface studies.

Electron beam evaporation requires pressures at least as low as HV (~10^{-6} mbar). Electrons bombard the source material at a high kinetic energy which is converted to heat, causing the source

material to melt or sublime. Different types of electron beam sources exist, but thermionic emission guns, also known as e-type guns, are most commonly used.[54] In this type of electron beam source, a high current is passed through a wire filament of W, a low work function metal, to emit electrons via thermionic emission.[53-54] The electrons emitted from the filament are accelerated to an anode held at a high voltage and focused on the source materials. Depending on the type of evaporation system and the melting temperature of the source material, some source materials are evaporated as pellets in a crucible and some are evaporated as rods. In some systems, the thickness of the deposited film is monitored by a quartz crystal monitor.

The work in this dissertation utilizes two separate electron beam evaporation systems for the deposition of metal films on 2D materials. The analysis module of our Scienta Omicron UHV chamber is equipped with a Mantis QUAD EV-C electron beam evaporator holding four separate evaporation sources. This evaporator was used for depositing metals for in-situ interface characterization. Evaporation in UHV results in cleaner interfaces, and yields oxide free films of metals which are highly susceptible to oxidation under HV conditions. Ni and Ti are evaporated as rods whereas Au pellets are evaporated in a BN-lined Mo crucible. Deposition rates are on the order of 1 Å/min and are adjusted by manual control of the power supply. The thickness of the deposited film is calculated using attenuation analysis with XPS which will be discussed in Chapter 2.3.

The UVA Microfabrication Laboratory (UVML) houses a six crucible CHA electron beam evaporator that operates at 10^{-6} Torr (1 Torr = 1.33 mbar) or 10^{-7} Torr when pumped down overnight. This system similar to those used in typical device fabrication processes. This evaporator was used in Chapter 3.3 for Ti contact deposition and for the deposition of thick Au capping layers for all electrical and thermal transport measurements in this work. All materials are

evaporated from pellets in crucibles. Thickness is measured by a quartz crystal monitor, and the desired thickness is specified by the user prior to the deposition. In addition to thickness, deposition rates can also be programmed in the range of 0.1-5 Å/s.

2.3 Characterization Methods

2.3.1 Photoelectron Spectroscopy

Photoelectron spectroscopy[56-58] is heavily used in this work to characterize interface chemistry at metal/2D material contacts. In this surface-sensitive method, a monochromatic photon source is focused on the sample resulting in photoionization and emission of electrons from the atoms in the sample as shown in Figure 2.3.1.

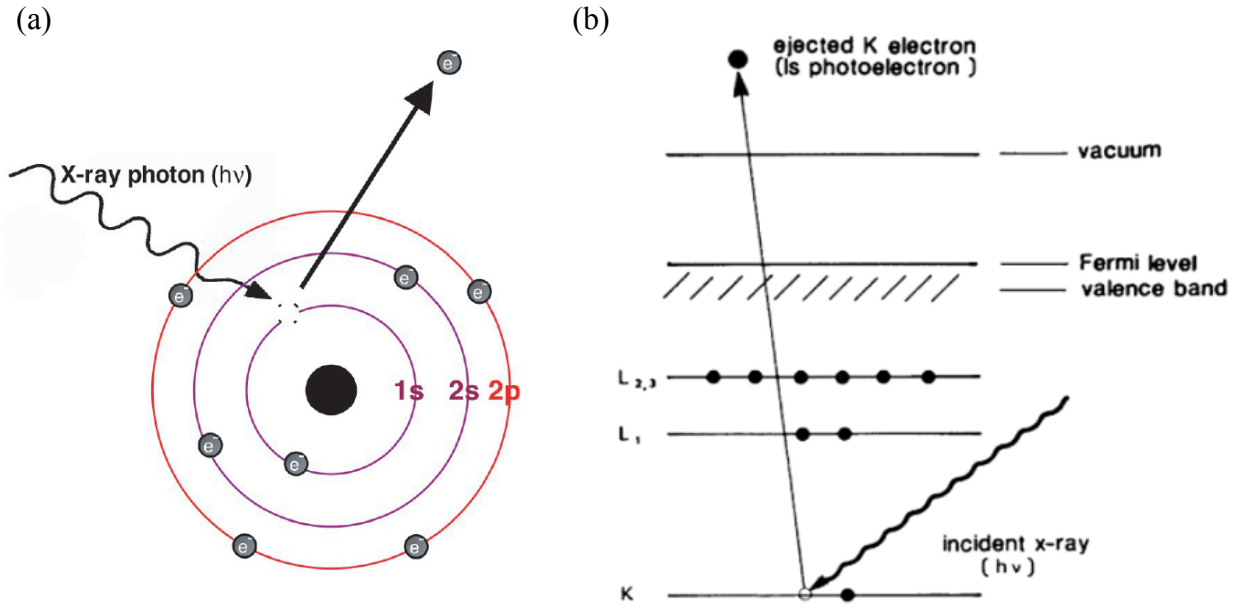

Figure 2.3.1. Schematic of the photoemission process showing an incident X-ray ejecting a core-level electron into vacuum, leaving behind a core-hole (a) in the atomic view (adapted from Ref. 59 and (b) in an energy band diagram (adapted from Ref. 58).

The kinetic energies of the photoemitted electrons are detected by a hemispherical electron analyzer. The kinetic energy of the photoelectron E_k^1 is related to the binding energy E_b as follows:

$$hv = E_b + E_k^1 + \phi_s \qquad \text{Equation 2.1}$$

The actual kinetic energy of the photoelectron E_k^1 is related to the kinetic energy that is measured by the analyzer E_k according to[56]

$$E_k = E_k^1 - (\phi_{sp} - \phi_s) \qquad \text{Equation 2.2}$$

where ϕ_{sp} is the work function of the spectrometer and ϕ_s is the work function of the sample. This work function difference and its effect on kinetic energy is illustrated in Figure 2.3.2. The work function is defined as the minimum energy needed by an electron to overcome the attractive forces that bind it to the material and escape from the material's surface into vacuum.[60] The binding energy of the sample photoelectron is effectively the difference between the initial ground state of the neutral atom and the final excited state of the ionized atom, of an electron depends on the number of protons in the nucleus, the density of electrons around the respective atom, and electron-electron interactions.[57] As a result, the measured value of binding energy is highly sensitive to the environment of the electron making this technique an effective method of compositional and chemical analysis of materials at or near the surface.

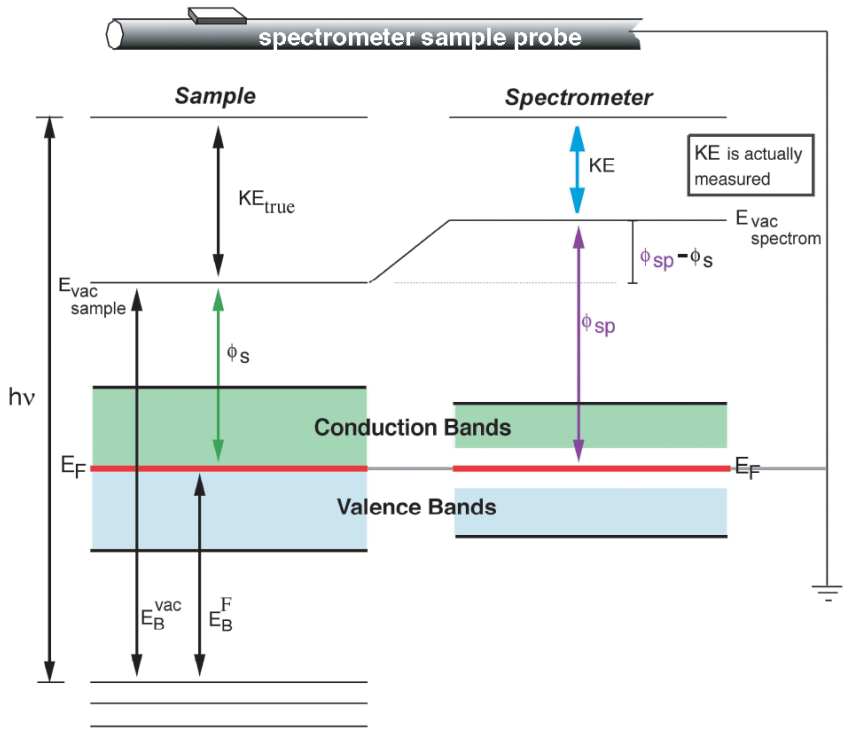

Figure 2.3.2. Energy band diagram showing the sample in electrical contact with the spectrometer. Adapted from Ref. 59 The diagram illustrates that the difference in work function between the spectrometer and the sample must be accounted for in order to determine the true kinetic energy of the photoemitted electron.

2.3.1.1 Analysis System Features

Our analysis module, shown in Figure 2.2.5 on the left, is comprised of a monochromated Al kα X-ray source, a He UV photon source, the R3000 analyzer and a four-pocket electron beam evaporator. The manipulator which holds the sample in the analysis module allows for both polar and azimuthal motorized rotation and as well as control over the sample temperature from 100-1103 K using liquid nitrogen cooling and a built-in heater. The R3000 ScientaOmicron analyzer is optimized for high-resolution photoemission spectroscopy. The hemispherical analyzer is 135 mm in diameter and is equipped with three curved and three straight slits for balancing intensity and energy resolution. The 2D low noise digital CCD-MCP detector has a noise level of <0.01

cps/channel. The energy resolution at 2 eV pass energy and 20 eV kinetic energy is <3 meV. In transmission mode, the analyzer has an acceptance angle of ±15° and angle lens modes allow for the collection of up to ±10° data. Chemical analysis can be carried out using x-ray photoelectron spectroscopy. Al Kα (1486.7 eV) X-rays are generated using a XM1200 monochromated X-ray source with a 500 mm Rowland circle diameter and a spot size of ~ 1mm. For ultra-violet photoelectron spectroscopy and angle resolved photoelectron spectroscopy, the photon source is a HIS 13 high intensity VUV source offering a flux of 6×10^{12} photons/s using He I and II. The use of a three-stage differential pump allows for data acquisition while maintaining a chamber pressure of $< 2 \times 10^{-9}$ mbar.

2.3.1.2 Core Level Shifts

Quantum mechanics dictates that electrons bound to an atom or ion can exist only in specific energy states referred to as stationary states[57] or bulk Bloch eigenstates[61]. States that are spatially close to the atomic nucleus are called core levels. Each core level is designated by the principal quantum number and the angular momentum quantum number that is associated with the atomic orbitals *s*, *p*, *d*, and *f*. These orbitals represent the spatial distribution of the electrons around the atomic nucleus. All *p*, *d*, and *f* orbitals exhibit spin orbit splitting, meaning that a single state will have two energetically distinct sub-states related to the magnetic quantum number. This results in doublet peaks with distinct binding energies. An example survey spectrum from X-ray photoelectron spectroscopy (XPS) is shown in Figure 2.3.4. The spectrum was acquired following the deposition of Au on MoS_2. Each peak or doublet represents a different atomic core level as labeled in the figure.

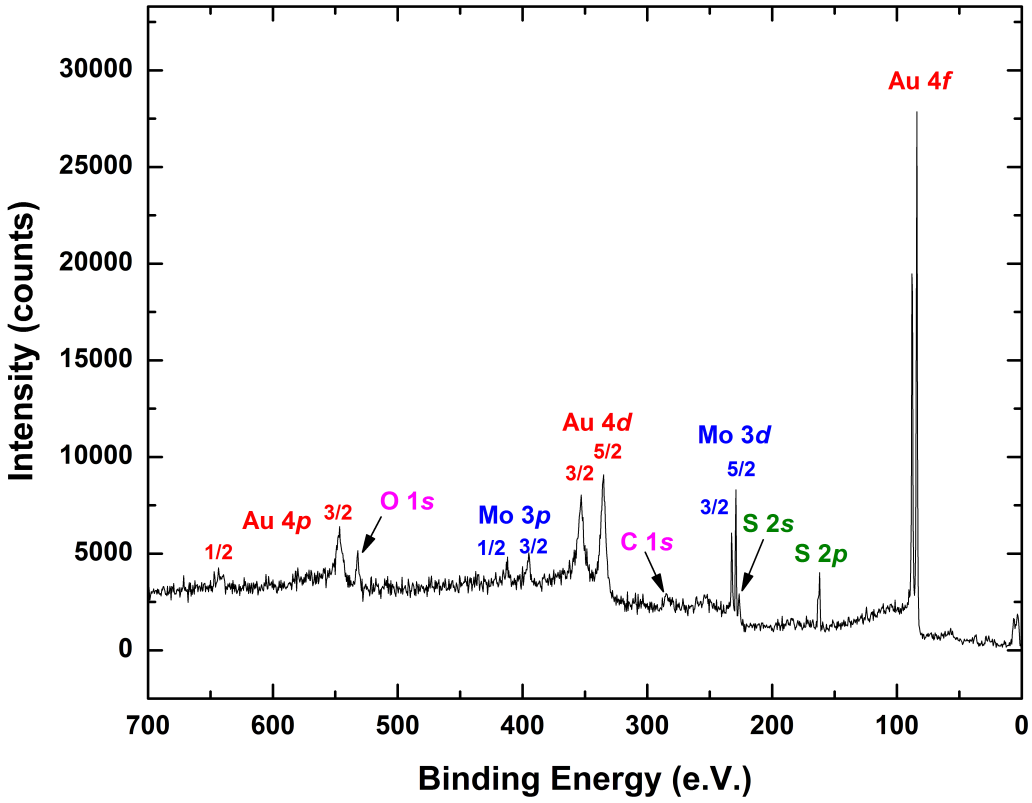

Figure 2.3.3. Survey spectrum of Au/MoS_2

A particular core level in a particular atom has a unique binding energy that is dictated by the Coulombic interaction between its neighboring electrons and protons. When an atom exists in a chemical state other than its elemental solid form and is bonded to a different atom, its core level electrons are in a different environment and exhibit different Coulombic interactions. This results in a change in binding energy to a value that is different than the elemental solid form. An example is shown in Figure 2.3.4. Here we see a comparison of metallic Ti (Ti^0) with Ti that is partially oxidized to form TiO_2. The oxidation of Ti results in a shift of the Ti $2p_{3/2}$ core-level from 454.1 eV to 458.8 eV.[62] A change in the spin orbit splitting between the $2p_{3/2}$ and $2p_{1/2}$ components also occurs from 6.17 eV for the metal to 5.54 eV for the oxide. The relative compositions of metal and oxide can be easily calculated using the integrated intensities of the two chemical states. In this

case of core level shift due to bonding, both types of atoms involved in the bond will exhibit a chemical state corresponding to the bond in all of its core levels. This type of core level shift is called a chemical shift.

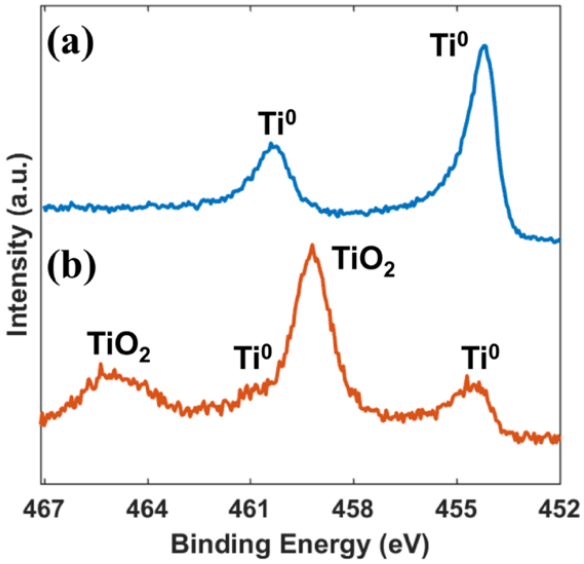

Figure 2.3.4. XPS spectrum of the Ti 2*p* region showing (a) Ti metal and (b) partially oxidized Ti to illustrate core-level shifts due to chemical reactions.

A different type of core level shift which does not correspond to chemical bonds can also be observed. This is an electrostatic shift, which occurs due to a change in doping which causes a change in the position of the Fermi level.[63-64] In this type of core level shift, all core levels and the valence band of the material shifts by the same magnitude in the same direction. This is often observed after the deposition of a metal overlayer on a sample which can result in charge-transfer doping or after annealing a sample which causes the removal of surface adsorbates that contribute to doping. As the Fermi level of the material aligns with that of the adlayer, the valence and conduction bands bend at the interface as shown in Figure 2.3.5. Due to the surface sensitivity of XPS, given that the metal is sufficiently thin as to not completely attenuate the substrate signal,

the area probed is within the depletion width even for a bulk semiconductor such as a geological MoS_2 crystal allowing us to probe electronic interactions at the interface.[65]

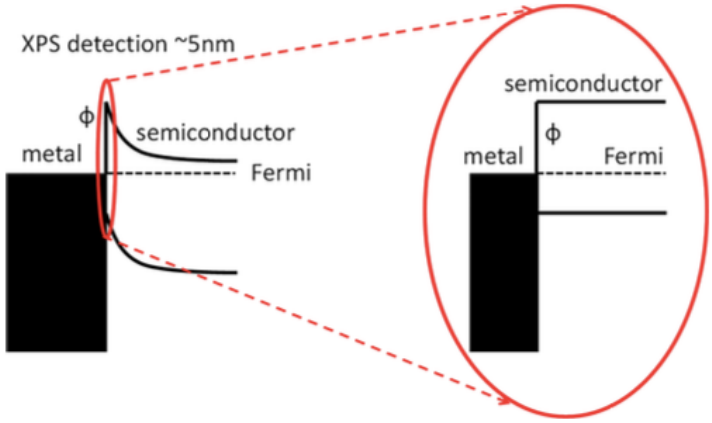

Figure 2.3.5. Illustration of how XPS probes band bending at metal/semiconductor interfaces from Ref. 65.

2.3.1.3 Spectral Deconvolution

To determine both peak positions and intensities for any type of quantitative analysis of XPS data, spectral deconvolution of the experimental data in this work is implemented using a specialized software package, kolXPD.[66] In kolXPD it is possible to subtract the background and construct fits to the data using appropriate line-shapes for each spectral feature. Background subtraction removes the contribution of inelastically scattered electrons.[67] Most metal peaks, such as the Ti 2*p* peak shown in Figure 2.3.3(a), are fit with an asymmetric Doniach-Sunjic line shape[68] convoluted with a Gaussian to account for instrumental broadening.[67] The asymmetry on the high-binding energy side arises from a potential created between the core-hole remaining from photoemission and the valence electrons of the metal.[67-69] Non-metallic core-level states are typically fit with a symmetric Voigt function, which is a convolution of a Lorentzian and Gaussian profile.[70-71] The Lorentzian component is the natural line shape of the photoemission peak as it

originates from the finite lifetime for the core-hole state, and the Gaussian contribution stems from instrumental broadening as well as crystal disorder. During the peak fitting process, initial values of asymmetry, Lorentzian and Gaussian widths, amplitude, and binding energy are iteratively adjusted to achieve the best possible fit to the data. When reference spectra are available for a given material, values of widths and asymmetry are fixed accordingly. In spectra with spin-orbit splitting, the ratio of the two spin-orbit split components is fixed to the ratio of photoionization cross sections reported by Scofield.[72] The spin orbit splitting value of binding energy can be fixed based on the XPS Handbook[62] or values reported in the literature for the specific material being measured. An example of spectral deconvolution is shown in Figure 2.3.6. The goodness of fit is assessed by a plot of the residuals which represents the difference between experimental data and the fit envelope. The residuals shown indicate a good fit to the data as the overall shape of the curve is flat and deviations from 0 correspond only to noise in the data. If the fit were in poor agreement with the experimental data, this would be reflected in the residuals as peak or a dip.

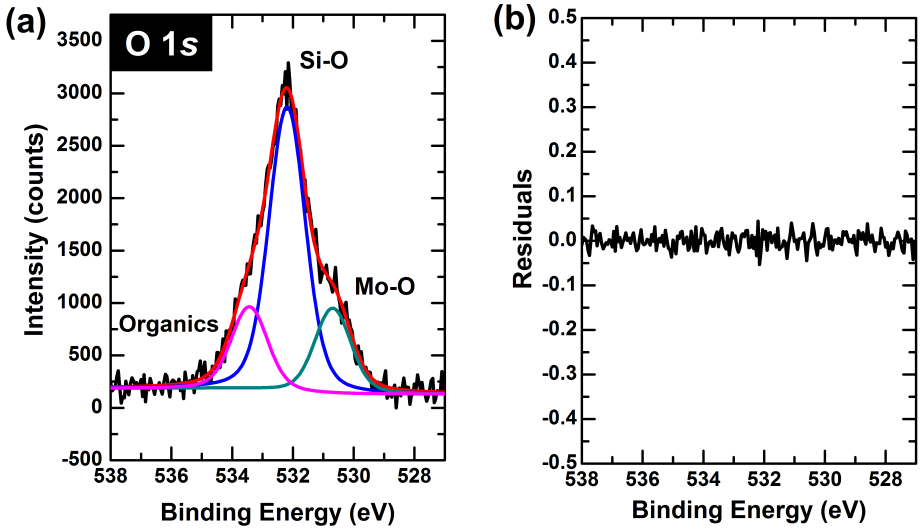

Figure 2.3.6. O 1*s* spectrum of UV-O_3 exposed CVD MoS_2 on a SiO_2 substrate with three O 1*s* components corresponding to the substrate, physisorbed organic species, and Mo oxide. Residuals are shown in (b).

2.3.1.4 Quantitative Compositional Analysis

While the binding energy provides information about the chemical state of the atom, the relative intensities of different chemical states and different atomic core levels provide quantitative compositional information. XPS was first implemented as a quantitative analytical tool in 1951 by Stienhardt and Serfass[73] and was later developed further by Nordling *et al.*[74] earning them the Nobel Prize in 1981.[75] The measured intensity of a core-level peak from an infinitely thick sample is given by[76]

$$I = nf\sigma\phi yAT\lambda \qquad \text{Equation 2.3}$$

where n is the number of atoms per cm^3 of the given element that is present in the measured material, f is the flux of X-ray photons impinging on the sample, σ is the photoelectric cross-section, ϕ is the angle between the photon path and the path of the photoemitted electrons, y the photoelectric ground state efficiency factor, A is the area of the sample from photoelectrons are emitted, T is the efficiency of detection of photoelectrons by the analyzer, and λ is the mean-free path of the photoelectrons. To calculate atomic composition of a specific element based on a particular core-level intensity, the measured intensity is divided by the product $\sigma\phi yAT\lambda$ which is known as the relative sensitivity factor (RSF). The RSF can be determined for each core level using the physical constants specific to each core-level, like the Hartee-Slater subshell photoionization cross section energies[72], and analyzer-specific values such as the transmission function[77]. The RSF-normalized intensity of a given core-level, or n, can then be compared with that of other core-levels to determine composition as an atomic percentage. We note that due to the nonlinearity of transmission function of the R3000 analyzer, there are errors in our calculated RSF values, resulting in errors in our calculated values of composition and stoichiometry.

2.3.1.5 Layered Structures and Angular-Resolved Measurements

XPS data can also be used to quantitatively determine the thickness of a thin film on a substrate. An electron from the substrate will travel a finite distance before being scattered in the overlayer leading to an attenuation of the signal from the substrate that reaches the detector. The probability of scattering, and therefore the degree of attenuation, depends on the thickness of the overlayer. The thickness of a film can then be measured by calculating the attenuation of the signal from a core level in the substrate *S* according to the following equation[78-80]:

$$I_S = I_S^{\infty} \exp\left(\frac{-d}{\lambda_{S,A} * \cos\theta}\right) \qquad \text{Equation 2.4}$$

and the corresponding intensity of overlayer *A* is

$$I_A = I_A^{\infty}(1 - \exp\left(\left(\frac{-d}{\lambda_{A,A} * \cos\theta}\right)\right) \qquad \text{Equation 2.5}$$

I_S and I_A are the integrated intensities of the core-level peak of the substrate and overlayer, respectively, I_S^{∞} and I_A^{∞} are the intensities of an infinitely thick substrate or film without any overlayer, *d* is the overlayer thickness, θ is the photoelectron take-off angle relative to the surface normal (45° under typical measurement conditions), and $\lambda_{S,A}$is the effective attenuation length (EAL), or mean free path, of an electron from the substrate that is being attenuated in the overlayer. Similarly $\lambda_{A,A}$ is the EAL of a core level electron from the overlayer in the overlayer. The theoretical mean free path as a function of the kinetic energy of the electron is shown in Figure 2.3.7. The EAL of an electron from a particular atomic core level in a particular elemental or compound overlayer can be calculated more accurately using the NIST EAL database which accounts for the atomic number and density of the overlayer.[81] We note that when a ratio of I_A / I_S is calculated using equations 2.4 and 2.5, the RSF can be used instead of an experimentally determined $I_A^{\infty} / I_S^{\infty}$, however the latter is more accurate due to the error in RSFs.

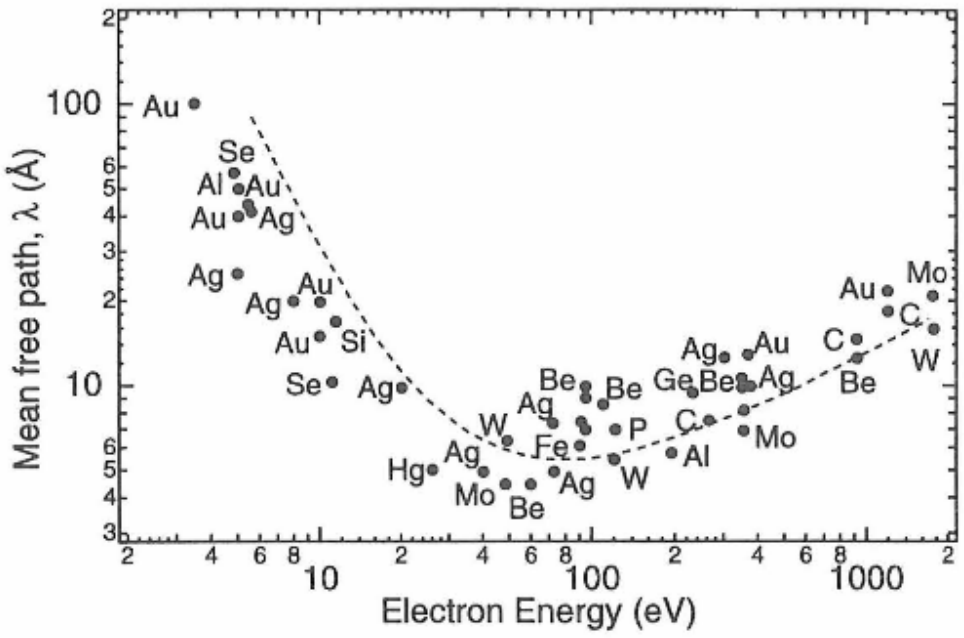

Figure 2.3.7. The universal curve for electron mean free path as a function of kinetic energy, adapted from Ref. 82.

Attenuation analysis can be implemented in the case of *n* layers on a substrate S. The intensity ratio between any layer *i* and the substrate where 1 is the topmost layer and N is the layer directly on top of the substrate is given as[79]

$$\frac{I_i}{I_S} = \frac{I_i^\infty}{I_S^\infty}\left[1 - \exp\left(\frac{-d_i}{\lambda_{i,i}*\cos\theta}\right)\right]\exp\left(\frac{1}{\cos\theta}\left(\sum_{j=1}^{j=n}\frac{d_j}{\lambda_{S,j}} - \sum_{j=1}^{j=i-1}\frac{d_j}{\lambda_{i,j}}\right)\right) \qquad \text{Equation 2.6}$$

where $\lambda_{S,j}$ is the EAL of the substrate in layer *j* and $\lambda_{i,j}$ is the EAL of layer *i* in layer *j*. The equations can be fit to experimental data acquired at different angles to determine the thickness of any given overlayer.

The angular dependence on the volume of material probed by XPS is useful for depth profiling, as the surface sensitivity of the measurement can be varied by changing the angle between the sample surface and the detector as illustrated in Figure 2.3.8. In the case of unknown

overlayer composition or thickness, the equations presented above can be used to generate theoretical intensity ratios at each angle, which can then be compared with experimental data acquired at each angle to estimate thickness and/or composition. This is implemented in Chapter 4.2 to determine the spatial distribution of reaction products resulting from the deposition of Ti on MoS_2.

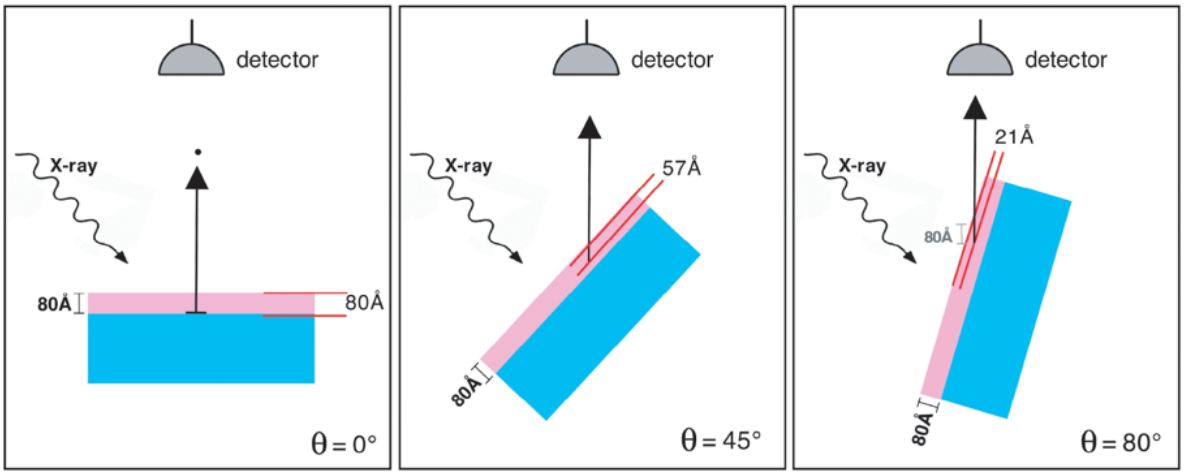

Figure 2.3.8. Schematic illustration of angular resolved XPS with θ defined relative to the normal of the surface

In the case where an overlayer is comprised of two different materials A and B which are spatially located at the same vertical depth on the sample, we assume a total thickness of d that is a sum of contributions from materials A and B such that $d = d_A + d_B$.[80] Alternatively $d_A = x * d$ where x is the fractional composition of material A and $d_B = (1 - x) * d$. The intensity ratio I_A/I_S is therefore

$$\frac{I_A}{I_S} = \frac{I_A^\infty}{I_S^\infty}\left[\frac{1-\exp\left(-\frac{-d*x}{\lambda_{A,A}\cos\theta}\right)}{\exp\left(\frac{-d*x}{\lambda_{S,A}\cos\theta}+\frac{-d(x-1)}{\lambda_{S,B}\cos\theta}\right)}\right] \qquad \text{Equation 2.7}$$

and I_B/I_S is similarly

$$\frac{I_B}{I_S} = \frac{I_B^\infty}{I_S^\infty}\left[\frac{1-\exp\left(-\frac{-d*(1-x)}{\lambda_{B,B}\cos\theta}\right)}{\exp\left(\frac{-d*x}{\lambda_{S,A}\cos\theta}+\frac{-d(1-x)}{\lambda_{S,B}\cos\theta}\right)}\right] \qquad \text{Equation 2.8}$$

where $0 < x < 1$. In the case where the total thickness d and the compositional fraction x are unknown, the two variables can be simultaneously optimized numerically. This will be demonstrated in Chapter 4.2.

Finally, when a substrate is only partially covered by an overlayer A, the ratio I_A/I_S is dependent on the fraction of the surface covered by the overlayer. The ratio is given by[83]

$$\frac{I_A}{I_S} = \frac{x*I_A^\infty*\left[1-\exp\left(\frac{-d}{\lambda_{A,A}\cos\theta}\right)\right]}{(1-x)*I_S^\infty+x*I_S^\infty*\exp\left(\frac{-d}{\lambda_{S,A}\cos\theta}\right)} \qquad \text{Equation 2.9}$$

where x corresponds to the fraction of the substrate surface covered by the overlayer and $0 < x < 1$. Equation 2.9 is useful for determining the quantity of material present on the surface with incomplete surface coverage when Equations 2.4 and 2.5 are inapplicable. It can also be used to model intensities of overlayers that exhibit agglomeration. This method is implemented in Chapter 3.2 to calculate the percent surface coverage of Ti islands on graphene.

We note that all equations described above yield semiquantitative results. The first reason for this is that the thickness *d* in the above equations is assumed to correspond to a layer of uniform thickness. In many cases this assumption is not realistic due to a number of factors. The equations also assume that the angle measured corresponds to the angle that was set in the manipulator. For example, the surface of a geological MoS2 crystal is very rough

2.3.1.6 Ultra-Violet Photoelectron Spectroscopy

Ultra-violet photoelectron spectroscopy (UPS) is employed in this work to determine the work function. This is achieved by measuring the difference between the Fermi level and the inelastic secondary electron energy cutoff.[84] At the low binding energy region of the spectrum, the

valence band features are visible. The signal between the valence band features and the secondary electron energy cutoff is due to electrons which were emitted from the valence band states and then inelastically scattered. An example spectrum, acquired on UHV-deposited infinitely thick Ti metal, is shown in Figure 2.3.9. The cutoff, which occurs at about 17.03 eV corresponds to electrons that had the minimum energy necessary to escape from the surface of the material into vacuum. By simply subtracting the secondary electron cutoff energy from the photon energy, which was 21.2 eV, the work function is determined to be 4.17 eV. A bias (~9 V) is typically applied to the sample by connecting a battery to shift the spectrum away from features associated with the spectrometer.[84] UPS is also useful for angular resolved photoelectron spectroscopy (ARPES) for probing the band structure of a material. This is possible due to the angular resolution of an R3000 analyzer. ARPES is implemented in Chapter 3.2 to image the band structure of CVD graphene.

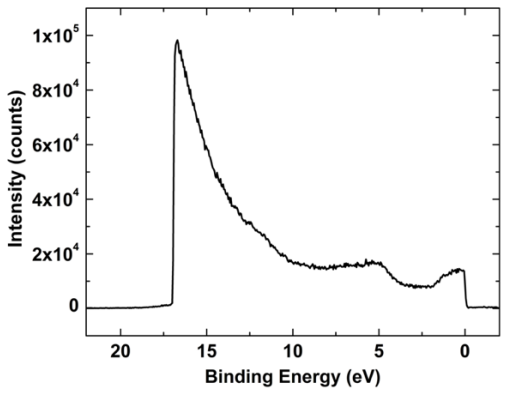

Figure 2.3.9. UPS spectrum of UHV-deposited infinitely thick Ti metal showing the low energy cutoff (at ~17 eV) used to determine work function.

2.3.2 Raman Spectroscopy

Raman spectroscopy[85-86] optically probes the vibration modes in a material. During a Raman measurement, a laser beam is focused on the sample causing phonons in the material to

scatter the incident photons by both elastic and inelastic processes. Raman spectroscopy is based on the inelastic process in which the incident photons (with energy $h\nu_0$) exchange energy with the atomic vibrations (with an energy of $h\nu_s$). This interaction results in a shift in the energy of the scattered photons, given by $h\nu_0$- $h\nu_s$. In Raman measurements, a spectrometer records these energy shifts which corresponds to a particular vibrational mode in the material. Different laser wavelengths can be used to excite different vibrational modes. The Raman spectrometer at the UVA's Nano Materials Characterization Facility is the inVia system by Renishaw. The system is equipped with 405 nm and 514 nm lasers. The presence of particular phonon modes, and their relative intensities and Raman shifts provide valuable chemical and structural information about layered 2D materials including thickness, strain, doping, and defect levels.[5, 87-92] An example Raman spectrum of CVD graphene transferred to SiO_2 is shown in Figure 2.3.10. The ratio of the D peak intensity to that of the G peak in the graphene Raman spectrum is related to the concentration of defects.[89] The ratio of the intensity peak 2D peak to that of the G peak can provide information doping.[93] Thorough Raman analysis of the Ti/graphene interface is implemented in Chapter 3.2 on graphene, and Raman has been routinely to assess the quality and thickness of materials used in our lab.

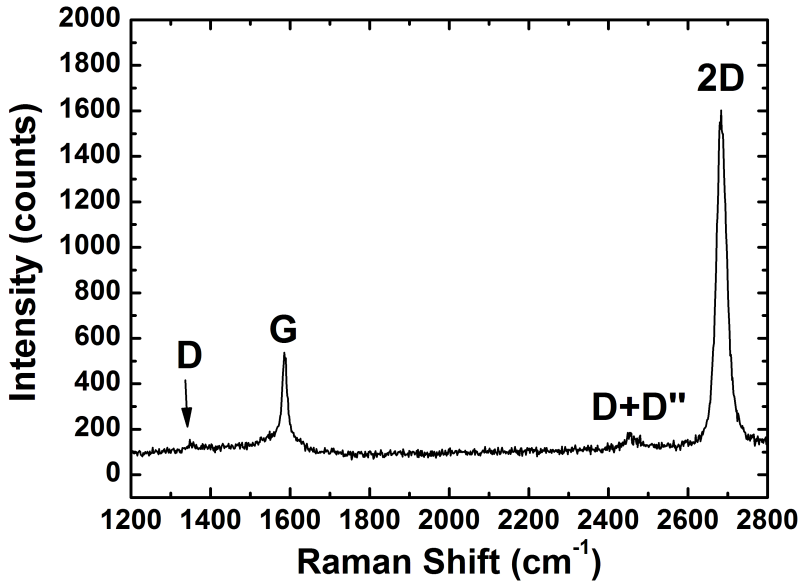

Figure 2.3.10. Raman spectra of CVD graphene after transfer to SiO_2 acquired with 514 nm laser. The D, G, and 2D positions and intensity ratios provide quantitative information about thickness, strain, doping, and defects.

2.3.3 Atomic Force Microscopy

Atomic force microscopy (AFM)[94-95] is used to image the surface topography of various samples in this work. The AFM is comprised of a micro-machined cantilever probe with a sharp tip is mounted onto a piezoelectric actuator. The tip interacts with the surface of the sample via two types of atomic forces. The first type is a short-range repulsive force resulting from the overlap of charges which dominates at short tip-to-sample distances. The second is a long range attractive force resulting from dipole or van der Waals interactions.[96] A laser beam is deflected from the cantilever onto a position-sensitive photodetector as the tip scans over the sample surface. The mode of operation used in this work is semi-contact mode, or tapping mode, where the tip lightly taps the surface at a set frequency. In this mode of contact, the attractive van der Waals forces are dominant in causing the bending of the cantilever. The oscillation amplitude of the cantilever is sensitive to surface topography. A feedback loop uses the signal from the photodetector to keep

the tip oscillations at a constant amplitude by adjusting the piezoelectric actuator to change the tip to sample distance. The changes in height are recorded as a function of the lateral position of the tip to generate images of surface topography. Two AFM systems were used in this work. The first is a system from NT-MDT Spectrum Instruments located in Prof. Floro's lab at UVA. The second is Bruker Dimension Icon located at James Madison University.

2.3.4 Transmission Electron Microscopy

Transmission electron microscopy[97] (TEM) was performed by our collaborators at NIST to image metal/TMD cross sections in Chapter 4.2. TEM provides images of a cross section of material with atomic resolution. Prior to TEM measurement the sample is cross sectioned and thinned using a focused ion beam (FIB). The sample must be no thicker than 100 nm in order to be transparent to electrons. Electrons are emitted from a cathode and accelerated at a high voltage to form a high-energy beam near 200 keV. Electromagnetic lenses, a solenoid with two poles, focus and deflect the electron beam onto the sample. The magnification power of the lens is adjusted via the current in the solenoid. An objective aperture is used to select the non-diffracted or diffracted electron beams. Contrast in TEM images is relies on there being a difference in the number of electrons being scattered away from the transmitted beam. This can be achieved by differences in density or diffraction in crystalline materials.

An FEI Nova NanoLab 600 dual-beam (SEM/FIB) scanning electron microscopy and focused ion beam system was employed to prepare cross-sectional scanning transmission electron microscopy (STEM) samples of Ti/MoS_2 and Ni/MoS_2 in Chapter 4.2. Using electron beam deposition, 10 nm carbon and subsequently 100 nm Pt was initially deposited on top of the sample to protect the sample surface. Next, 2 μm Pt was deposited by ion-beam induced deposition. To reduce Ga-ions damage in the final step of FIB preparation, the STEM samples were thinned with

2 kV Ga-ions using a low beam current of 29 pA and a small incident angle of 3 degrees. An FEI Titan 80-300 STEM/TEM equipped with a monochromator and a probe spherical-aberration corrector was employed to acquire atomic-resolution STEM images, X-ray energy dispersive spectroscopy (EDS) and electron energy loss spectroscopy (EELS) spectrum-images. Atomic-resolution annular dark field (ADF) STEM images were acquired with an operating voltage of 300 kV, probe convergence angle of 14 mrad and collection angle of 34-195 mrad.

2.3.5 Transfer Length Measurements

Electrical transport is characterized by transfer length measurements (TLM) which is a commonly used method for measuring contact resistance of metal/2D interfaces.[98-99] In this method, the resistance is measured at a probe station as a function of separation distance between two identically shaped contacts. This TLM structure is achieved by electron-beam evaporation of the contact metal onto the substrate through a patterned shadow mask. The contact resistance of the interface is determined by plotting contact resistance vs. separation distance and extrapolating the y- intercept from a linear fit to the data. In the limit of zero spacing between contacts, the device resistance is that of the contacts. The measured resistance at each spacing is given by[100]:

$$R = R_{sh}\frac{l}{W} + 2R_c \qquad \text{Equation 2.10}$$

where R_{sh} is the sheet resistance, l is the channel length, W is the length of the contact, and R_c is the contact resistance. The measurements in Chapter 3.3 were performed in Prof. Hopkins' lab using 19 micron tips from CascadeMicrotech in the probe station (JmicroTechnology, LMS-2709) connected to a SourceMeter unit (SMU, Keithley Instruments 2612A). The source current applied is 1 mA.

2.3.6 Time-Domain Thermoreflecance

Time-domain thermoreflectance (TDTR) [98, 101-106], performed by members of Prof. Hopkins' group, is a technique used to determine the thermal boundary conductance across metal/2D interfaces. The thermal boundary conductance h_K relates the heat flux across an interface q_{int} to the temperature drop ΔT such that $h_K = \frac{q_{int}}{\Delta T}$.[106] It is inversely related to the thermal boundary resistance. The TDTR method involves a two-step, pump-probe process. In the first step, a pump signal from a laser impinges on the sample generating a heating event. Prior to measurement, samples for TDTR are coated in a reflective metal film (70-80 nm Au in this work) that converts the incident photons from the pump signal into thermal energy. The energy is transported to the underlying layers through phonon-phonon interactions for semiconducting or insulating layers and through electron-electron interactions for metallic layers.[105] The heating event causes a temperature change in the sample that affects the reflectivity of the top metal layer.[101, 106] The second step of the measurement involves the probe pulse, that is time-delayed with respect to the pump pulses, which measures the changes in the reflectivity of the sample that occur due to the heating event from the pump signal. The reflected probe signal is measured by a photodiode. The laser used in this work is a 80 MHz Ti:Sapphire laser that is split into the pump and probe paths with a beam splitter as shown in Figure 2.3.11. The pump and probe $1/e^2$ radii are ~8 and ~4.5 mm, respectively, after being focused through a 10 x objective. The pump signal wavelength is 400 nm after passing through a bismuth triborate (BiBO) crystal and red filter.

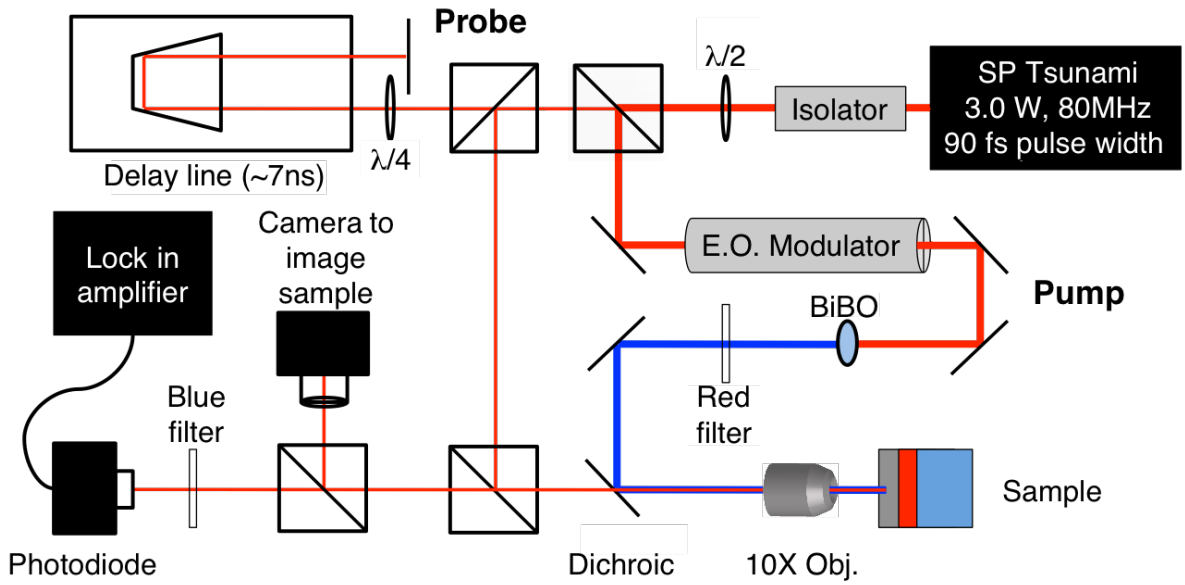

Figure 2.3.11. Schematic representation of the TDTR experimental setup from Ref. 106.

The repetition rate of the pulse signal, on the order of 12.5 ns for a 80 MHz laser, does not allow sufficient time for the material to return to equilibrium between laser pulses.[104-105] This means that the measured signal is the accumulation of the heating events initiated by multiple pulses. These include the response to a single impulse as well as the response to a modulated thermal wave. The pump signal is modulated electro-optically at a frequency ω_0 and a lock-in amplifier measures the in-phase and out-of-phase components of the probe signal at the modulation frequency, returning an amplitude and phase that are functions of the time delay between the pump and probe pulses as well as the physical properties of the material.[105] The in-phase component represents the temperature rise due to the impulse and the out-of-phase component represents the temperature rise from the modulated thermal wave.[106] The thermal response of the sample is modeled by the one-dimensional thermal diffusion equation. The equation can be adapted to account for radial conduction due to the non-negligible size of the Gaussian laser spot compared to the length scale of the thermal response.[101, 104] The equations are solved numerically for various

pump probe delay times to extract the interfacial conductance. An in-depth mathematical description can be found in the reports by Cahil in Ref. 101 and Schmidt *et al*. in Refs. 104-105.

2.3.7 Measurement of Cross-Plane Seebeck Coefficient

The Seebeck coefficient is defined as $S = V/\Delta T$ where V is the voltage generated due to a temperature gradient ΔT across the material.[107] Therefore, the Seebeck coefficient is measured by applying a temperature gradient and measuring the resulting voltage, and performing a linear fit to V vs. ΔT. To collect this data, the sample is placed on a thermoelectric module which provides a temperature gradient in the cross-plane direction. The temperature gradient is measured using two K type thermocouples at the top and bottom contacts. The temperature signals from the thermocouples are converted by the NI 9211 temperature input module. The voltage is measured with probes at the top and bottom contacts using a Keithley 2400 source meter. A schematic of the measurement is for a metal/WSe_2/HOPG sample is shown in Figure 2.3.12. Measurements of the Seebeck coefficient are performed in collaboration with Prof. Zebarjadi.

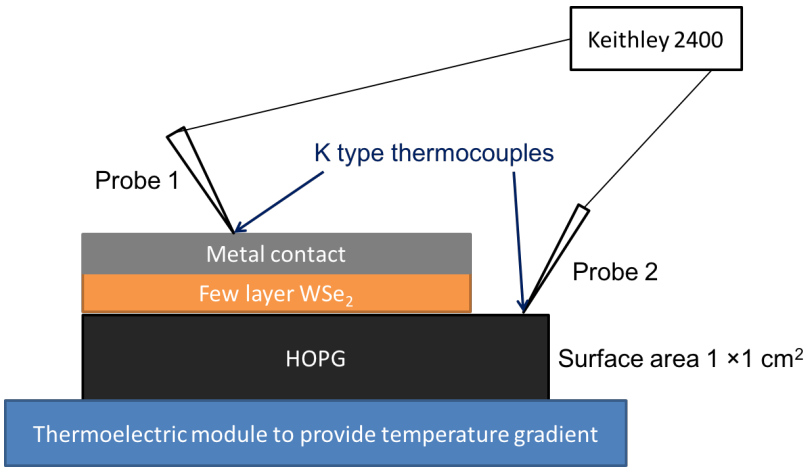

Figure 2.3.12. Illustration of the Seebeck measurement implemented in Chapter 4.4.

2.3.8 Measurement of Cross-Plane Electrical Resistance

A standard four-wire sensing method is used to measure cross-plane electrical resistance in Chapter 4.4. This four point probe method eliminates the parasitic contact resistance at the probe/contact interface.[108] Like in the Seebeck measurement, two probes are placed on the top contact and two are placed on the bottom. On the top and bottom, one of the probes injects a current through the sample while the other measures the voltage drop across. The current and voltage were supplied and measured by a Keithley 2400 source meter. The resistance is derived from the slope of a linear fit of the current vs. voltage curves. These measurements are performed in collaboration with Prof. Zebarjadi.

2.4 References

1. Radisavljevic, B.; Radenovic, A.; Brivio, J.; Giacometti, V.; Kis, A., Single-layer MoS2 transistors. *Nat Nano* **2011,** *6* (3), 147-150.
2. Das, S.; Chen, H.-Y.; Penumatcha, A. V.; Appenzeller, J., High Performance Multilayer MoS2 Transistors with Scandium Contacts. *Nano Letters* **2013,** *13* (1), 100-105.
3. Chuang, S.; Battaglia, C.; Azcatl, A.; McDonnell, S.; Kang, J. S.; Yin, X.; Tosun, M.; Kapadia, R.; Fang, H.; Wallace, R. M.; Javey, A., MoS2 P-type Transistors and Diodes Enabled by High Work Function MoOx Contacts. *Nano Letters* **2014,** *14* (3), 1337-1342.
4. Zhang, Y.; Ye, J.; Matsuhashi, Y.; Iwasa, Y., Ambipolar MoS2 Thin Flake Transistors. *Nano Letters* **2012,** *12* (3), 1136-1140.
5. Li, H.; Zhang, Q.; Yap, C. C. R.; Tay, B. K.; Edwin, T. H. T.; Olivier, A.; Baillargeat, D., From Bulk to Monolayer MoS2: Evolution of Raman Scattering. *Advanced Functional Materials* **2012,** *22* (7), 1385-1390.
6. McDonnell, S.; Addou, R.; Buie, C.; Wallace, R. M.; Hinkle, C. L., Defect-dominated doping and contact resistance in MoS2. *ACS nano* **2014,** *8* (3), 2880-2888.
7. McDonnell, S.; Smyth, C.; Hinkle, C. L.; Wallace, R. M., MoS2–Titanium Contact Interface Reactions. *ACS Applied Materials & Interfaces* **2016,** *8* (12), 8289-8294.
8. Addou, R.; McDonnell, S.; Barrera, D.; Guo, Z.; Azcatl, A.; Wang, J.; Zhu, H.; Hinkle, C. L.; Quevedo-Lopez, M.; Alshareef, H. N.; Colombo, L.; Hsu, J. W. P.; Wallace, R. M., Impurities and Electronic Property Variations of Natural MoS2 Crystal Surfaces. *ACS Nano* **2015,** *9* (9), 9124-9133.
9. Amani, M.; Lien, D.-H.; Kiriya, D.; Xiao, J.; Azcatl, A.; Noh, J.; Madhvapathy, S. R.; Addou, R.; KC, S.; Dubey, M.; Cho, K.; Wallace, R. M.; Lee, S.-C.; He, J.-H.; Ager, J. W.; Zhang, X.; Yablonovitch, E.; Javey, A., Near-unity photoluminescence quantum yield in MoS2. *Science* **2015,** *350* (6264), 1065-1068.
10. Eda, G.; Yamaguchi, H.; Voiry, D.; Fujita, T.; Chen, M.; Chhowalla, M., Photoluminescence from Chemically Exfoliated MoS2. *Nano Letters* **2011,** *11* (12), 5111-5116.
11. Novoselov, K. S.; Geim, A. K.; Morozov, S. V.; Jiang, D.; Zhang, Y.; Dubonos, S. V.; Grigorieva, I. V.; Firsov, A. A., Electric Field Effect in Atomically Thin Carbon Films. *Science* **2004,** *306* (5696), 666.
12. Jawaid, A.; Nepal, D.; Park, K.; Jespersen, M.; Qualley, A.; Mirau, P.; Drummy, L. F.; Vaia, R. A., Mechanism for Liquid Phase Exfoliation of MoS2. *Chemistry of Materials* **2016,** *28* (1), 337-348.
13. Nicolosi, V.; Chhowalla, M.; Kanatzidis, M. G.; Strano, M. S.; Coleman, J. N., Liquid Exfoliation of Layered Materials. *Science* **2013,** *340* (6139), 1226419.
14. Coleman, J. N.; Lotya, M.; O'Neill, A.; Bergin, S. D.; King, P. J.; Khan, U.; Young, K.; Gaucher, A.; De, S.; Smith, R. J.; Shvets, I. V.; Arora, S. K.; Stanton, G.; Kim, H.-Y.; Lee, K.; Kim, G. T.; Duesberg, G. S.; Hallam, T.; Boland, J. J.; Wang, J. J.; Donegan, J. F.; Grunlan, J. C.; Moriarty, G.; Shmeliov, A.; Nicholls, R. J.; Perkins, J. M.; Grieveson, E. M.; Theuwissen, K.; McComb, D. W.; Nellist, P. D.; Nicolosi, V., Two-Dimensional Nanosheets Produced by Liquid Exfoliation of Layered Materials. *Science* **2011,** *331* (6017), 568.
15. SPI, https://www.2spi.com/.
16. Yu, Y.; Nam, G.-H.; He, Q.; Wu, X.-J.; Zhang, K.; Yang, Z.; Chen, J.; Ma, Q.; Zhao, M.; Liu, Z.; Ran, F.-R.; Wang, X.; Li, H.; Huang, X.; Li, B.; Xiong, Q.; Zhang, Q.; Liu, Z.; Gu, L.;

Du, Y.; Huang, W.; Zhang, H., High phase-purity 1T′-MoS2- and 1T′-MoSe2-layered crystals. *Nature Chemistry* **2018,** *10* (6), 638-643.
17. Quereda, J.; Castellanos-Gomez, A.; Agraït, N.; Rubio-Bollinger, G., Single-layer MoS2 roughness and sliding friction quenching by interaction with atomically flat substrates. *Applied Physics Letters* **2014,** *105* (5), 053111.
18. Toh, R. J.; Sofer, Z.; Luxa, J.; Sedmidubský, D.; Pumera, M., 3R phase of MoS2 and WS2 outperforms the corresponding 2H phase for hydrogen evolution. *Chemical Communications* **2017,** *53* (21), 3054-3057.
19. Laskar, M. R.; Ma, L.; Kannappan, S.; Sung Park, P.; Krishnamoorthy, S.; Nath, D. N.; Lu, W.; Wu, Y.; Rajan, S., Large area single crystal (0001) oriented MoS2. *Applied Physics Letters* **2013,** *102* (25), 252108.
20. Ludowise, M. J., Metalorganic chemical vapor deposition of III-V semiconductors. *Journal of Applied Physics* **1985,** *58* (8), R31-R55.
21. de Boer, W. B.; Meyer, D. J., Low-temperature chemical vapor deposition of epitaxial Si and SiGe layers at atmospheric pressure. *Applied Physics Letters* **1991,** *58* (12), 1286-1288.
22. Carlsson, J.-O.; Martin, P. M., Chapter 7 - Chemical Vapor Deposition. In *Handbook of Deposition Technologies for Films and Coatings (Third Edition)*, Martin, P. M., Ed. William Andrew Publishing: Boston, 2010; pp 314-363.
23. Muñoz, R.; Gómez-Aleixandre, C., Review of CVD Synthesis of Graphene. *Chemical Vapor Deposition* **2013,** *19* (10-11-12), 297-322.
24. Chae, S. J.; Güneş, F.; Kim, K. K.; Kim, E. S.; Han, G. H.; Kim, S. M.; Shin, H.-J.; Yoon, S.-M.; Choi, J.-Y.; Park, M. H.; Yang, C. W.; Pribat, D.; Lee, Y. H., Synthesis of Large-Area Graphene Layers on Poly-Nickel Substrate by Chemical Vapor Deposition: Wrinkle Formation. *Advanced Materials* **2009,** *21* (22), 2328-2333.
25. Shi, Y.; Li, H.; Li, L.-J., Recent advances in controlled synthesis of two-dimensional transition metal dichalcogenides via vapour deposition techniques. *Chemical Society Reviews* **2015,** *44* (9), 2744-2756.
26. Ji, Q.; Zhang, Y.; Zhang, Y.; Liu, Z., Chemical vapour deposition of group-VIB metal dichalcogenide monolayers: engineered substrates from amorphous to single crystalline. *Chemical Society Reviews* **2015,** *44* (9), 2587-2602.
27. Zhan, Y.; Liu, Z.; Najmaei, S.; Ajayan, P. M.; Lou, J., Large-Area Vapor-Phase Growth and Characterization of MoS2 Atomic Layers on a SiO2 Substrate. *Small* **2012,** *8* (7), 966-971.
28. Wang, X.; Feng, H.; Wu, Y.; Jiao, L., Controlled Synthesis of Highly Crystalline MoS2 Flakes by Chemical Vapor Deposition. *Journal of the American Chemical Society* **2013,** *135* (14), 5304-5307.
29. Tarasov, A.; Campbell, P. M.; Tsai, M. Y.; Hesabi, Z. R.; Feirer, J.; Graham, S.; Ready, W. J.; Vogel, E. M., Highly Uniform Trilayer Molybdenum Disulfide for Wafer-Scale Device Fabrication. *Advanced Functional Materials* **2014,** *24* (40), 6389-6400.
30. Lin, Y.-C.; Zhang, W.; Huang, J.-K.; Liu, K.-K.; Lee, Y.-H.; Liang, C.-T.; Chu, C.-W.; Li, L.-J., Wafer-scale MoS 2 thin layers prepared by MoO 3 sulfurization. *Nanoscale* **2012,** *4* (20), 6637-6641.
31. Lee, Y.-H.; Zhang, X.-Q.; Zhang, W.; Chang, M.-T.; Lin, C.-T.; Chang, K.-D.; Yu, Y.-C.; Wang, J. T.-W.; Chang, C.-S.; Li, L.-J.; Lin, T.-W., Synthesis of Large-Area MoS2 Atomic Layers with Chemical Vapor Deposition. *Advanced Materials* **2012,** *24* (17), 2320-2325.

32. Najmaei, S.; Liu, Z.; Zhou, W.; Zou, X.; Shi, G.; Lei, S.; Yakobson, B. I.; Idrobo, J.-C.; Ajayan, P. M.; Lou, J., Vapour phase growth and grain boundary structure of molybdenum disulphide atomic layers. *Nature Materials* **2013,** *12*, 754.
33. Xia, J.; Huang, X.; Liu, L.-Z.; Wang, M.; Wang, L.; Huang, B.; Zhu, D.-D.; Li, J.-J.; Gu, C.-Z.; Meng, X.-M., CVD synthesis of large-area, highly crystalline MoSe2 atomic layers on diverse substrates and application to photodetectors. *Nanoscale* **2014,** *6* (15), 8949-8955.
34. van der Zande, A. M.; Huang, P. Y.; Chenet, D. A.; Berkelbach, T. C.; You, Y.; Lee, G.-H.; Heinz, T. F.; Reichman, D. R.; Muller, D. A.; Hone, J. C., Grains and grain boundaries in highly crystalline monolayer molybdenum disulphide. *Nature Materials* **2013,** *12*, 554.
35. Kang, K.; Xie, S.; Huang, L.; Han, Y.; Huang, P. Y.; Mak, K. F.; Kim, C.-J.; Muller, D.; Park, J., High-mobility three-atom-thick semiconducting films with wafer-scale homogeneity. *Nature* **2015,** *520*, 656.
36. Wu, S.; Huang, C.; Aivazian, G.; Ross, J. S.; Cobden, D. H.; Xu, X., Vapor–Solid Growth of High Optical Quality MoS2 Monolayers with Near-Unity Valley Polarization. *ACS Nano* **2013,** *7* (3), 2768-2772.
37. Gurarslan, A.; Yu, Y.; Su, L.; Yu, Y.; Suarez, F.; Yao, S.; Zhu, Y.; Ozturk, M.; Zhang, Y.; Cao, L., Surface-energy-assisted perfect transfer of centimeter-scale monolayer and few-layer MoS2 films onto arbitrary substrates. *ACS nano* **2014,** *8* (11), 11522-11528.
38. Tsai, M.-L.; Su, S.-H.; Chang, J.-K.; Tsai, D.-S.; Chen, C.-H.; Wu, C.-I.; Li, L.-J.; Chen, L.-J.; He, J.-H., Monolayer MoS2 Heterojunction Solar Cells. *ACS Nano* **2014,** *8* (8), 8317-8322.
39. Fang, H.; Chuang, S.; Chang, T. C.; Takei, K.; Takahashi, T.; Javey, A., High-Performance Single Layered WSe2 p-FETs with Chemically Doped Contacts. *Nano Letters* **2012,** *12* (7), 3788-3792.
40. Shiraki, Y., Silicon molecular beam epitaxy. *Progress in Crystal Growth and Characterization* **1986,** *12* (1), 45-66.
41. Amatya, J. M.; Heinrich, H.; Tersoff, J.; Floro, J. A., Growth of SiGe epitaxial quantum dots on patterned Si (001) surfaces by in situ annealing of initially conformal layers. *Journal of Applied Physics* **2018,** *124* (20), 204302.
42. Tsang, W. T., From chemical vapor epitaxy to chemical beam epitaxy. *Journal of Crystal Growth* **1989,** *95* (1), 121-131.
43. Koma, A., Van der Waals epitaxy for highly lattice-mismatched systems. *Journal of Crystal Growth* **1999,** *201–202*, 236-241.
44. Koma, A.; Ueno, K.; Saiki, K., Heteroepitaxial growth by Van der Waals interaction in one-, two- and three-dimensional materials. *Journal of Crystal Growth* **1991,** *111* (1–4), 1029-1032.
45. Saiki, K.; Ueno, K.; Shimada, T.; Koma, A., Application of Van der Waals epitaxy to highly heterogeneous systems. *Journal of Crystal Growth* **1989,** *95* (1), 603-606.
46. Ueno, K.; Shimada, T.; Saiki, K.; Koma, A., Heteroepitaxial growth of layered transition metal dichalcogenides on sulfur-terminated GaAs{111} surfaces. *Applied Physics Letters* **1990,** *56* (4), 327.
47. Herman, M. A.; Sitter, H., *Molecular Beam Epitaxy: Fundamentals and Current Status*. Springer Berlin Heidelberg: 2013.
48. Koma, A., Papers presented at the International Workshop on Science and Technology of Thin Films for the 21st Century, Evanston,IL, USA, July 28-August 2, 1991 Van der Waals epitaxy—a new epitaxial growth method for a highly lattice-mismatched system. *Thin Solid Films* **1992,** *216* (1), 72-76.

49. Walsh, L. A.; Yue, R.; Wang, Q.; Barton, A. T.; Addou, R.; Smyth, C. M.; Zhu, H.; Kim, J.; Colombo, L.; Kim, M. J.; Wallace, R. M.; Hinkle, C. L., W Te2thin films grown by beam-interrupted molecular beam epitaxy. *2D Materials* **2017,** *4* (2), 025044.
50. Nakano, M.; Wang, Y.; Kashiwabara, Y.; Matsuoka, H.; Iwasa, Y., Layer-by-layer epitaxial growth of scalable WSe2 on sapphire by molecular beam epitaxy. *Nano letters* **2017,** *17* (9), 5595-5599.
51. Zhang, X.; Choudhury, T. H.; Chubarov, M.; Xiang, Y.; Jariwala, B.; Zhang, F.; Alem, N.; Wang, G.-C.; Robinson, J. A.; Redwing, J. M., Diffusion-controlled epitaxy of large area coalesced WSe2 monolayers on sapphire. *Nano letters* **2018,** *18* (2), 1049-1056.
52. Ichimiya, A.; Cohen, P. I.; Cohen, P. I.; Cambridge University, P., *Reflection High-Energy Electron Diffraction*. Cambridge University Press: 2004.
53. Kern, W., *Thin film processes II*. Elsevier: 2012; Vol. 2.
54. Wang, Z.; Zhang, Z., Electron beam evaporation deposition. *Advanced Nano Deposition Methods* **2016**.
55. Sree Harsha, K. S., Chapter 5 - Thermal Evaporation Sources. In *Principles of Vapor Deposition of Thin Films*, Sree Harsha, K. S., Ed. Elsevier: Oxford, 2006; pp 367-452.
56. Chusuei, C. C.; Goodman, D. W., X-Ray Photoelectron Spectroscopy. *Encyclopedia of Physical Science and Technology* **2002,** *17*, 921-937.
57. van der Heide, P., *X-ray Photoelectron Spectroscopy*. Wiley: 2011.
58. Watts, J. F., X-ray photoelectron spectroscopy. *Vacuum* **1994,** *45* (6–7), 653-671.
59. Vickerman, J. C.; Gilmore, I. S., *Surface analysis: the principal techniques*. John Wiley & Sons: 2011.
60. Eisberg, R. M.; Resnick, R., *Quantum physics of atoms, molecules, solids, nuclei, and particles*. Wiley: 1985.
61. Andrea, D., Probing the Electronic Structure of Complex Systems by ARPES. *Physica Scripta* **2004,** *2004* (T109), 61.
62. Briggs, D., Handbook of X-ray Photoelectron Spectroscopy. *Surface and Interface Analysis* **1981,** *3* (4), 72-73.
63. Smyth, C. M.; Addou, R.; McDonnell, S.; Hinkle, C. L.; Wallace, R. M., WSe2-contact metal interface chemistry and band alignment under high vacuum and ultra high vacuum deposition conditions. *2D Materials* **2017,** *4* (2), 025084.
64. Meyer, J.; Kidambi, P. R.; Bayer, B. C.; Weijtens, C.; Kuhn, A.; Centeno, A.; Pesquera, A.; Zurutuza, A.; Robertson, J.; Hofmann, S., Metal Oxide Induced Charge Transfer Doping and Band Alignment of Graphene Electrodes for Efficient Organic Light Emitting Diodes. *Scientific Reports* **2014,** *4*, 5380.
65. Dong, H.; Gong, C.; Addou, R.; McDonnell, S.; Azcatl, A.; Qin, X.; Wang, W.; Wang, W.; Hinkle, C. L.; Wallace, R. M., Schottky Barrier Height of Pd/MoS2 Contact by Large Area Photoemission Spectroscopy. *ACS Applied Materials & Interfaces* **2017,** *9* (44), 38977-38983.
66. http://kolxpd.kolibrik.net/.
67. Aronniemi, M.; Sainio, J.; Lahtinen, J., Chemical state quantification of iron and chromium oxides using XPS: the effect of the background subtraction method. *Surface Science* **2005,** *578* (1), 108-123.
68. Doniach, S.; Sunjic, M., Many-electron singularity in X-ray photoemission and X-ray line spectra from metals. *Journal of Physics C: Solid State Physics* **1970,** *3* (2), 285.

69. Sacher, E., Asymmetries in Transition Metal XPS Spectra: Metal Nanoparticle Structure, and Interaction with the Graphene-Structured Substrate Surface. *Langmuir* **2010,** *26* (6), 3807-3814.
70. Hesse, R.; Chassé, T.; Szargan, R., Peak shape analysis of core level photoelectron spectra using UNIFIT for WINDOWS. *Fresenius' Journal of Analytical Chemistry* **1999,** *365* (1), 48-54.
71. Jain, V.; Biesinger, M. C.; Linford, M. R., The Gaussian-Lorentzian Sum, Product, and Convolution (Voigt) functions in the context of peak fitting X-ray photoelectron spectroscopy (XPS) narrow scans. *Applied Surface Science* **2018,** *447*, 548-553.
72. Scofield, J. H., Hartree-Slater subshell photoionization cross-sections at 1254 and 1487 eV. *Journal of Electron Spectroscopy and Related Phenomena* **1976,** *8* (2), 129-137.
73. Steinhardt, R.; Serfass, E., X-ray photoelectron spectrometer for chemical analysis. *Analytical Chemistry* **1951,** *23* (11), 1585-1590.
74. Nordling, C.; Sokolowski, E.; Siegbahn, K., Precision Method for Obtaining Absolute Values of Atomic Binding Energies. *Physical Review* **1957,** *105* (5), 1676-1677.
75. Siegbahn, K., Electron Spectroscopy for Atoms, Molecules, and Condensed Matter. *Science* **1982,** *217* (4555), 111.
76. Wagner, C. D.; Davis, L. E.; Zeller, M. V.; Taylor, J. A.; Raymond, R. H.; Gale, L. H., Empirical atomic sensitivity factors for quantitative analysis by electron spectroscopy for chemical analysis. *Surface and Interface Analysis* **1981,** *3* (5), 211-225.
77. Drera, G.; Salvinelli, G.; Åhlund, J.; Karlsson, P. G.; Wannberg, B.; Magnano, E.; Nappini, S.; Sangaletti, L., Transmission function calibration of an angular resolved analyzer for X-ray photoemission spectroscopy: Theory vs experiment. *Journal of Electron Spectroscopy and Related Phenomena* **2014,** *195*, 109-116.
78. Himpsel, F. J.; McFeely, F. R.; Taleb-Ibrahimi, A.; Yarmoff, J. A.; Hollinger, G., Microscopic structure of the SiO_2/Si interface. *Physical Review B* **1988,** *38* (9), 6084-6096.
79. Vitchev, R. G.; Pireaux, J. J.; Conard, T.; Bender, H.; Wolstenholme, J.; Defranoux, C., X-ray photoelectron spectroscopy characterisation of high-k dielectric Al2O3 and HfO2 layers deposited on SiO2/Si surface. *Applied Surface Science* **2004,** *235* (1), 21-25.
80. McDonnell, S. Spectroscopic characterisation of high dielectric constant materials on semiconducting surfaces. Dublin City University, 2009.
81. NIST X-ray Photoelectron Spectroscopy Database, Version 4.1 (National Institute of Standards and Technology, Gaithersburg. https://srdata.nist.gov/xps/ **2012**.
82. Magnuson, M., Electronic Structure Studies Using Resonant X-ray and Photemission Spectroscopy. **1999**.
83. McDonnell, S.; Longo, R. C.; Seitz, O.; Ballard, J. B.; Mordi, G.; Dick, D.; Owen, J. H.; Randall, J. N.; Kim, J.; Chabal, Y. J.; Cho, K.; Wallace, R. M., Controlling the atomic layer deposition of titanium dioxide on silicon: dependence on surface termination. *The Journal of Physical Chemistry C* **2013,** *117* (39), 20250-20259.
84. Y. Park, V. C., Y. Gao, Work function of indium tin oxide transparent conductor measured by photoelectron spectroscopy. *Applied Physics Letters* **1996,** *68* (19), 2699-2701.
85. McCreery, R. L., *Raman Spectroscopy for Chemical Analysis*. Wiley: 2005.
86. Schrader, B., *Infrared and Raman Spectroscopy: Methods and Applications*. Wiley: 2008.
87. Terrones, H.; Corro, E. D.; Feng, S.; Poumirol, J. M.; Rhodes, D.; Smirnov, D.; Pradhan, N. R.; Lin, Z.; Nguyen, M. A. T.; Elías, A. L.; Mallouk, T. E.; Balicas, L.; Pimenta, M. A.; Terrones, M., New First Order Raman-active Modes in Few Layered Transition Metal Dichalcogenides. *Scientific Reports* **2014,** *4*, 4215.

88. Tonndorf, P.; Schmidt, R.; Böttger, P.; Zhang, X.; Börner, J.; Liebig, A.; Albrecht, M.; Kloc, C.; Gordan, O.; Zahn, D. R. T.; Michaelis de Vasconcellos, S.; Bratschitsch, R., Photoluminescence emission and Raman response of monolayer MoS2, MoSe2, and WSe2. *Opt. Express* **2013,** *21* (4), 4908-4916.
89. Ferrari, A. C.; Meyer, J. C.; Scardaci, V.; Casiraghi, C.; Lazzeri, M.; Mauri, F.; Piscanec, S.; Jiang, D.; Novoselov, K. S.; Roth, S.; Geim, A. K., Raman Spectrum of Graphene and Graphene Layers. *Physical Review Letters* **2006,** *97* (18), 187401.
90. Ferrari, A. C., Raman spectroscopy of graphene and graphite: Disorder, electron–phonon coupling, doping and nonadiabatic effects. *Solid State Communications* **2007,** *143* (1–2), 47-57.
91. DasA; PisanaS; ChakrabortyB; PiscanecS; Saha, S. K.; Waghmare, U. V.; Novoselov, K. S.; Krishnamurthy, H. R.; Geim, A. K.; Ferrari, A. C.; Sood, A. K., Monitoring dopants by Raman scattering in an electrochemically top-gated graphene transistor. *Nat Nano* **2008,** *3* (4), 210-215.
92. Schmidt, D. A.; Ohta, T.; Beechem, T. E., Strain and charge carrier coupling in epitaxial graphene. *Physical Review B* **2011,** *84* (23), 235422.
93. Das, A.; Pisana, S.; Chakraborty, B.; Piscanec, S.; Saha, S.; Waghmare, U.; Novoselov, K.; Krishnamurthy, H.; Geim, A.; Ferrari, A., Monitoring Dopants by Raman scattering in an Electrochemically Top-Gated Graphene Transistor. *Nature Nanotechnology* **2008,** *3* (4), 210-215.
94. Jalili, N.; Laxminarayana, K., A review of atomic force microscopy imaging systems: application to molecular metrology and biological sciences. *Mechatronics* **2004,** *14* (8), 907-945.
95. Giessibl, F. J., Advances in atomic force microscopy. *Reviews of Modern Physics* **2003,** *75* (3), 949-983.
96. Goodman, F. O.; Garcia, N., Roles of the attractive and repulsive forces in atomic-force microscopy. *Physical Review B* **1991,** *43* (6), 4728.
97. Leng, Y., *Materials Characterization: Introduction to Microscopic and Spectroscopic Methods*. Wiley: 2009.
98. Foley, B. M.; Hernández, S. C.; Duda, J. C.; Robinson, J. T.; Walton, S. G.; Hopkins, P. E., Modifying Surface Energy of Graphene via Plasma-Based Chemical Functionalization to Tune Thermal and Electrical Transport at Metal Interfaces. *Nano Letters* **2015,** *15* (8), 4876-4882.
99. Venugopal, A.; Colombo, L.; Vogel, E. M., Contact resistance in few and multilayer graphene devices. *Applied Physics Letters* **2010,** *96* (1), 013512.
100. Cohen, S. S., Contact resistance and methods for its determination. *Thin Solid Films* **1983,** *104* (3), 361-379.
101. Cahill, D. G., Analysis of heat flow in layered structures for time-domain thermoreflectance. *Review of Scientific Instruments* **2004,** *75* (12), 5119-5122.
102. Hopkins, P. E.; Serrano, J. R.; Phinney, L. M.; Kearney, S. P.; Grasser, T. W.; Harris, C. T., Criteria for Cross-Plane Dominated Thermal Transport in Multilayer Thin Film Systems During Modulated Laser Heating. *Journal of Heat Transfer* **2010,** *132* (8), 081302-081302.
103. Giri, A.; Gaskins, J. T.; Donovan, B. F.; Szwejkowski, C.; Warzoha, R. J.; Rodriguez, M. A.; Ihlefeld, J.; Hopkins, P. E., Mechanisms of nonequilibrium electron-phonon coupling and thermal conductance at interfaces. *Journal of Applied Physics* **2015,** *117* (10), 105105.
104. Schmidt, A. J.; Chen, X.; Chen, G., Pulse accumulation, radial heat conduction, and anisotropic thermal conductivity in pump-probe transient thermoreflectance. *Review of Scientific Instruments* **2008,** *79* (11), 114902.
105. Schmidt, A. J. Optical characterization of thermal transport from the nanoscale to the macroscale. Massachusetts Institute of Technology, 2008.

106. Hopkins, P. E., Thermal transport across solid interfaces with nanoscale imperfections: effects of roughness, disorder, dislocations, and bonding on thermal boundary conductance. *ISRN Mechanical Engineering* **2013,** *2013*.
107. Zhang, G.; Zhang, Y.-W., Thermoelectric properties of two-dimensional transition metal dichalcogenides. *Journal of Materials Chemistry C* **2017,** *5* (31), 7684-7698.
108. Miccoli, I.; Edler, F.; Pfnür, H.; Tegenkamp, C., The 100th anniversary of the four-point probe technique: the role of probe geometries in isotropic and anisotropic systems. *Journal of Physics: Condensed Matter* **2015,** *27* (22), 223201.

3 GRAPHENE

3.1 Introduction

3.1.1 Properties, Applications, and Processing

Graphene is a single atomic layer of sp^2 bonded carbon atoms arranged in a honeycomb structure and can be described as a triangular lattice with two atoms per unit cell, with a lattice parameter of 2.46 Å and a bond length of 1.42 Å.[1] Each atom forms three covalent σ bonds by hybridization of the 2s, $2p_x$, and $2p_y$ orbitals. One electron per atom forms the out-of-plane π bond that is delocalized and therefore responsible for the energy bands near the Fermi level. Graphene can be characterized as a zero band gap semiconductor or a zero-overlap semimetal[2] as demonstrated by its unique band structure shown in Figure 3.1.1(c). Unlike most materials, the valence and conduction bands are linear rather than parabolic, and they meet in the K and K' points of the Brillouin zone. The point of intersection is known as the Dirac point and the band structure at the Dirac point is described as a Dirac cone. The linear dispersion relation of graphene describes massless Dirac fermions[3], resulting in an extremely high carrier mobility ($\mu > 10^5$ cm^2 V^{-1} s^{-1} for exfoliated material) which is two orders of magnitude higher than Si and one order of magnitude higher than III-V semiconductors.[4] The Fermi level (E_F) lies exactly at the Dirac point in intrinsic graphene and can be shifted into the valence or conduction band by electrostatic or chemical doping. The density of states in graphene vanishes near E_F.

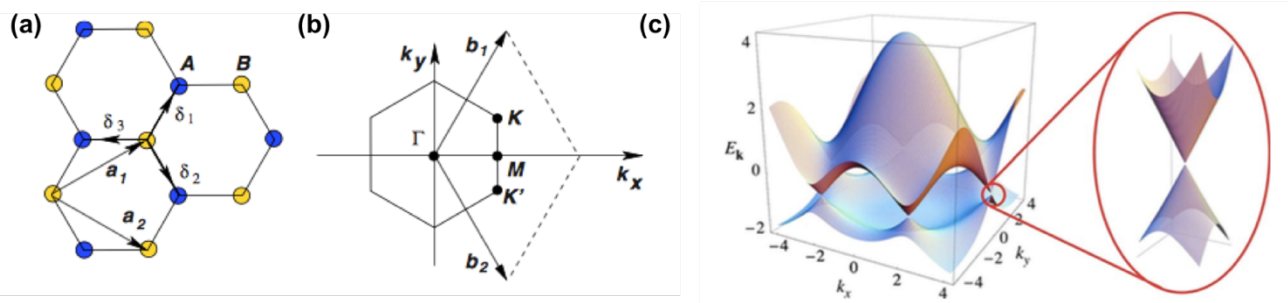

Figure 3.1.1. (a) Lattice structure of graphene where a1,2 are the lattice vectors and δ1,2,3 are nearest neighbor vectors; (b) Brillouin zone of graphene; (c) Electronic dispersion showing the Dirac cone at the K and K' points. Adapted from Ref. 1.

The unique electronic properties of graphene present both advantages and challenges in terms of device design. High mobility is the most frequently stated advantage of graphene for use in transistors, but the absence of a band gap in graphene is problematic for digital logic FET applications as it inhibits switching between ON and OFF states.[5] Conventional Si CMOS devices exhibit I_{ON}/I_{OFF} ratios on the order of 10^4-10^7 whereas this value is typically ≤ 10 in graphene devices.[6] A band gap can be introduced by applying strain or by constraining the graphene film in one direction to form nanoribbons, but significant limitations are associated with these approaches including edge roughness, reproducibility, and scalability.[5-7] An ideal application for zero band gap graphene is in radio frequency (RF) analog devices such as small-signal amplifiers which are typically operated in the ON mode.[5, 8] The combination of high conductivity and high light transmittance (~98%) of graphene makes it a suitable as a conductive electrode in applications such as solar cells and light emitting diodes.[6] Applications in photodetection have been demonstrated by using an external field or metal-induced internal field to separate charges in the absence of a band gap.[9-10] The thermal properties of graphene also make it an excellent candidate for applications in nanoelectronics as well as thermal interface materials.[11-12] Graphene has an in-

plane thermal conductivity of 2000-4000 $Wm^{-1}K^{-1}$, one of the highest reported values for any material.[12]

The first graphene devices were created from flakes which were mechanically exfoliated from bulk highly ordered pyrolytic graphite (HOPG) crystals.[13] While this method is commonly used to produce high quality micron-sized flakes in research settings, it is not amenable to large scale device fabrication and commercialization of graphene technology. The rapidly growing interest in graphene led to the development of large area synthesis via chemical vapor deposition (CVD).[14-16] In this process, gaseous reactants, typically CH_4:H_2, form a stable solid over a catalytic substrate which aids in the decomposition of CH_4 at temperatures around 1000 ºC. The CVD process for graphene growth was initially developed on Ni substrates but failed to yield uniform, monolayer graphene due to the high C solubility in Ni. Cu substrates have been found to result in substantially improved control over number of layers due to the relatively low C solubility in Cu.[16] Another route to the synthesis of high quality graphene is the sublimation of Si from SiC at 1200 -1600 °C under vacuum.[17-18] This method produces epitaxial graphene on a semi-insulating substrate, presenting the possibility of device fabrication directly on the growth substrate.[19]

While growth of graphene on insulating substrates has also been demonstrated[20], the CVD method is the most suitable for large scale processing. For device fabrication using CVD-grown graphene, graphene must be transferred onto an insulating substrate such SiO_2. To achieve this, CVD-grown graphene is coated with a polymer film, typically polymethyl methacrylate (PMMA), to mechanically support the fragile graphene film as the Cu growth foil is dissolved.[21] After transfer onto SiO_2, the PMMA film is dissolved in acetone. Removal of PMMA residues by annealing in UHV or an ambient gas is typically employed as residues have been found to affect

doping and carrier mobility.[22-24] After transfer onto the target substrate, graphene is patterned, etched, and metallized via conventional photolithography and electron beam evaporation methods.

3.1.2 Metal/Graphene Contacts

Efficient electrical and thermal transport across the metal/graphene interface is an essential requirement for the realization of graphene devices, however the crystal and electronic structure of graphene present fundamental obstacles to the formation of low resistance contacts. The absence of dangling bonds on the surface inhibits chemical bonding at the interface and limits the degree of interaction between graphene and the metal, and the small density of states near the Fermi level (E_F) of graphene is thought to suppress charge injection from the metal.[7, 25] A large volume of theoretical and experimental studies in the literature are aimed at understanding the nature of the metal/graphene interface. Relevant findings are summarized in this section to provide a context for the work completed in this dissertation.

3.1.2.1 Types of Metal/Graphene Interfaces

Theoretical studies by Giovanetti *et al.*[26], Gong *et al.*[27], and Khomyakov *et al.*[28] classify metal/graphene contacts as either physisorption or chemisorption interfaces depending on the *d*-orbital configuration of the metal. Density functional theory (DFT) calculations conclude that metals such as Ag, Al, Cu, Cd, Ir, Pt, and Au are physisorbed when deposited on graphene. A metal that is physisorbed forms an interface that exhibits no chemical interactions. The only change that occurs in graphene due to the presence of a physisorbed metal overlayer is a change in doping due to charge transfer across the interface and the intrinsic band structure remains unperturbed.[27] This means that the linear Dirac cone structure is preserved, but E_F shifts away from the Dirac point to align with that of the metal. Physisorbed metals with a work function less than 5.4 eV are expected to result in n-type doping while those with a higher work function are likely to be p-type

dopants.[7] Physisorption interfaces have an equilibrium interfacial distance > 3.0 Å and metals are easily detached from the graphene surface due to weak adhesion.[27]

A chemisorption interface – formed by metals such a Ni, Co, Ru, Pd, and Ti – causes strong perturbation of graphene's intrinsic band structure via orbital hybridization between the p_z states in graphene (which form the π band) and the *d*-orbitals of the metal.[27-28] DFT calculations reveal that a combination of orbital hybridization and a small contribution from Pauli exclusion interactions result in the opening of a band gap with a high density of randomly distributed "gap states" within the hybridization region. This changes graphene from a "semimetal" to a metallic material under the contact. The equilibrium interfacial distance for these interfaces is < 2.5 Å, and chemisorbed metals have been experimentally found to adhere well to the graphene surface following deposition.

3.1.2.2 Transport Properties

The two quantities of interest in this dissertation in the discussion of transport across metal/graphene interfaces are R_C, the electrical contact resistance, and h_K, the thermal boundary conductance. Both are highly relevant parameters in the realization of nanoelectronic devices. R_C is considered to be the major limiting factor in the ON state current of a graphene FET[29] and in device scaling of RF transistors[30]. h_K is of equal importance as inefficient thermal transport can lead to localized heating at the contact, hindering device performance and reliability. Measurement techniques for these properties are discussed in Sections 2.3.5 and 2.3.6.

Reported values of R_C for graphene/metal contacts are summarized in a review by Giubileo *et al*.[7] The most commonly used metals are Au, Pd, Ti, and Ni. Values of R_C for all of these metals, and for a single given metal, vary over a wide range. Furthermore, no single metal consistently outperforms the rest. For example, reported R_C of Au contacts ranges from 50–2000 Ω μm, and

values spanning 23–7500 Ω μm are reported for Ti. While one might expect chemisorbed interfaces to yield better electronic transport properties, this is not necessarily the case. The larger interfacial gap in physisorbed interfaces is a tunneling barrier with a considerably high probability of transmission.[27] The variability in reported values of R_C for a given metal, and the difficulty in identifying the "ideal contact", can be explained by differences in contact geometry, measurement technique, graphene type (exfoliated, CVD, or sublimated SiC), as well as processing conditions which will be addressed in the next section. Several experimental reports demonstrate that R_C is independent of the gate voltage and the number of graphene layers, indicating that it is dominated by the properties of the metal/graphene interface.[29, 31-32]

Measurements of h_K across bulk graphite/metal interfaces, used as an approximation for graphene/metal interfaces, have shown that chemisorption interfaces exhibit higher h_K than those which are physisorbed.[33] For example, values of h_K of 7–20 MW m^{-2} K^{-1} are reported for Au/graphite[34] whereas values as a high as 120 MW m^{-2} K^{-1} have been reported for Ti/graphite.[33] Thermal transport across graphene/metal interfaces, which is dominated by acoustic phonons, has been found to be highly dependent on the degree of bonding at the interface as it affects the phonon flux and energy mismatch between the phonon modes in graphene and the metal overlayer.[33, 35-36] Work by Koh *et al.*[35] and Guzman *et al.*[37] suggests that metals with higher Debeye temperatures result in higher values of h_K. Functionalization of graphene with interface adsorbates by Hopkins *et al.*[36] and Foley *et al.*[38] provides evidence of the link between bonding at the interface and h_K. Huang *et al.*[39] reveal that the transfer process of CVD graphene compromises h_K due to the presence of voids at the interface.

3.1.2.3 Effects of Processing

The key processing steps which are addressed in this dissertation are surface cleaning procedures and contact deposition conditions. Surface cleaning is essential for the removal of adventitious carbon or PMMA residues in the case of transferred CVD graphene. Different methods of surface cleaning are employed in the literature, including annealing in UHV or background gases, and exposure to UV-O_3.[22, 24, 40-41] Hydrocarbon contaminants and oxygen species present on the surface of graphene, or those impinging on the surface during contact deposition, can react with the metal contact or otherwise interfere with adhesion and electronic interactions at the interface. For example, Joiner *et al.*[42] have shown that Ti reacts with PMMA residues, and McDonnell *et al.*[43] have shown that Ti deposited under in high-vacuum results in Ti oxide. Therefore, both surface cleaning and contact deposition undoubtedly affect interface chemistry and transport properties. Improvements in R_C have been attributed to enhanced removal of PMMA residues[40-41] or the employment of PMMA-free transfer methods.[44] Russo *et al.*[31] have suggested that deposition base pressure may have an effect on measured R_C in graphene devices contacted with Ti/Au. They experimentally measured a R_C value of 800 ± 200 Ωμm when Ti was deposited at a base pressure of 8×10^{-7} Torr, whereas lower values of < 400 Ωμm and < 250 Ωμm were achieved in the literature when the deposition was performed at lower base pressures of 2.5×10^{-8} and 8×10^{-9} Torr, respectively. This provides strong evidence for R_C dependence on base pressure, yet deposition parameters are scarcely reported in device papers.

3.1.3 Motivation for Titanium/Graphene Contact Studies

A wealth of literature is focused on graphene-based devices. Despite the widespread interest in improving contact properties, characterization of interface chemistry – which is required in order to truly understand chemical and electronic interactions at the interface – is largely lacking.

Due to its prevalent use in devices and generally favorable electrical and thermal transport properties, Ti has been selected to be the focus of this work. The Ti/graphene interface is repeatedly classified as one that is chemisorbed, yet the extent of interaction between the two materials, and the effect of processing conditions, is unknown. The first set of experiments described in Chapter 3.2 aim to closely examine interface chemistry, effects of surface cleanliness, and the thermal stability of the Ti/graphene contact interface under "clean" conditions – in UHV and without any polymer-aided transfer. Given the well-documented susceptibility of Ti to oxidation, the effect of more realistic device processing conditions including HV deposition with PMMA transfer are examined in Chapter 3.3. The two chapters presented here address the gap in the literature from two angles, each providing insight into the relationship between interface chemistry, processing conditions, and transport properties.

3.1.4 References

1. Castro Neto, A. H.; Guinea, F.; Peres, N. M. R.; Novoselov, K. S.; Geim, A. K., The electronic properties of graphene. *Reviews of Modern Physics* **2009,** *81* (1), 109-162.
2. Geim, A. K.; Novoselov, K. S., The rise of graphene. *Nat Mater* **2007,** *6* (3), 183-191.
3. Novoselov, K. S.; Geim, A. K.; Morozov, S. V.; Jiang, D.; Katsnelson, M. I.; Grigorieva, I. V.; Dubonos, S. V.; Firsov, A. A., Two-dimensional gas of massless Dirac fermions in graphene. *Nature* **2005,** *438*, 197.
4. del Alamo, J. A., Nanometre-scale electronics with III–V compound semiconductors. *Nature* **2011,** *479*, 317.
5. Schwierz, F., Graphene transistors. *Nature Nanotechnology* **2010,** *5*, 487.
6. Avouris, P., Graphene: Electronic and Photonic Properties and Devices. *Nano Letters* **2010,** *10* (11), 4285-4294.
7. Giubileo, F.; Di Bartolomeo, A., The role of contact resistance in graphene field-effect devices. *Progress in Surface Science* **2017,** *92* (3), 143-175.
8. Palacios, T.; Hsu, A.; Wang, H., Applications of graphene devices in RF communications. *IEEE Communications Magazine* **2010,** *48* (6), 122-128.
9. Mueller, T.; Xia, F.; Avouris, P., Graphene photodetectors for high-speed optical communications. *Nature Photonics* **2010,** *4*, 297.
10. Xia, F.; Mueller, T.; Lin, Y.-m.; Valdes-Garcia, A.; Avouris, P., Ultrafast graphene photodetector. *Nature Nanotechnology* **2009,** *4*, 839.
11. Shahil, K. M. F.; Balandin, A. A., Thermal properties of graphene and multilayer graphene: Applications in thermal interface materials. *Solid State Communications* **2012,** *152* (15), 1331-1340.
12. Pop, E.; Varshney, V.; Roy, A. K., Thermal properties of graphene: Fundamentals and applications. *MRS Bulletin* **2012,** *37* (12), 1273-1281.
13. Novoselov, K. S.; Geim, A. K.; Morozov, S. V.; Jiang, D.; Zhang, Y.; Dubonos, S. V.; Grigorieva, I. V.; Firsov, A. A., Electric Field Effect in Atomically Thin Carbon Films. *Science* **2004,** *306* (5696), 666.
14. Mattevi, C.; Kim, H.; Chhowalla, M., A review of chemical vapour deposition of graphene on copper. *Journal of Materials Chemistry* **2011,** *21* (10), 3324-3334.
15. Obraztsov, A. N., Making graphene on a large scale. *Nature Nanotechnology* **2009,** *4*, 212.
16. Muñoz, R.; Gómez-Aleixandre, C., Review of CVD Synthesis of Graphene. *Chemical Vapor Deposition* **2013,** *19* (10-11-12), 297-322.
17. Shivaraman, S.; Barton, R. A.; Yu, X.; Alden, J.; Herman, L.; Chandrashekhar, M. V. S.; Park, J.; McEuen, P. L.; Parpia, J. M.; Craighead, H. G.; Spencer, M. G., Free-Standing Epitaxial Graphene. *Nano Letters* **2009,** *9* (9), 3100-3105.
18. Berger, C.; Song, Z.; Li, X.; Wu, X.; Brown, N.; Naud, C.; Mayou, D.; Li, T.; Hass, J.; Marchenkov, A. N.; Conrad, E. H.; First, P. N.; de Heer, W. A., Electronic Confinement and Coherence in Patterned Epitaxial Graphene. *Science* **2006,** *312* (5777), 1191.
19. Lin, Y.-M.; Dimitrakopoulos, C.; Jenkins, K. A.; Farmer, D. B.; Chiu, H.-Y.; Grill, A.; Avouris, P., 100-GHz transistors from wafer-scale epitaxial graphene. *Science* **2010,** *327* (5966), 662-662.
20. Murakami, K.; Tanaka, S.; Hirukawa, A.; Hiyama, T.; Kuwajima, T.; Kano, E.; Takeguchi, M.; Fujita, J.-i., Direct synthesis of large area graphene on insulating substrate by gallium vapor-assisted chemical vapor deposition. *Applied Physics Letters* **2015,** *106* (9), 093112.

21. Li, X.; Zhu, Y.; Cai, W.; Borysiak, M.; Han, B.; Chen, D.; Piner, R. D.; Colombo, L.; Ruoff, R. S., Transfer of Large-Area Graphene Films for High-Performance Transparent Conductive Electrodes. *Nano Letters* **2009,** *9* (12), 4359-4363.
22. Lin, Y. C.; Lu, C. C.; Yeh, C. H.; Jin, C.; Suenaga, K.; Chiu, P. W., Graphene annealing: how clean can it be? *Nano Lett* **2012,** *12* (1), 414-9.
23. Pirkle, A.; Chan, J.; Venugopal, A.; Hinojos, D.; Magnuson, C. W.; McDonnell, S.; Colombo, L.; Vogel, E. M.; Ruoff, R. S.; Wallace, R. M., The effect of chemical residues on the physical and electrical properties of chemical vapor deposited graphene transferred to SiO2. *Applied Physics Letters* **2011,** *99* (12), 122108.
24. Gong, C.; Floresca, H. C.; Hinojos, D.; McDonnell, S.; Qin, X.; Hao, Y.; Jandhyala, S.; Mordi, G.; Kim, J.; Colombo, L.; Ruoff, R. S.; Kim, M. J.; Cho, K.; Wallace, R. M.; Chabal, Y. J., Rapid Selective Etching of PMMA Residues from Transferred Graphene by Carbon Dioxide. *The Journal of Physical Chemistry C* **2013,** *117* (44), 23000-23008.
25. Kosuke, N.; Akira, T., Density-of-States Limited Contact Resistance in Graphene Field-Effect Transistors. *Japanese Journal of Applied Physics* **2011,** *50* (7R), 070108.
26. Giovannetti, G.; Khomyakov, P. A.; Brocks, G.; Karpan, V. M.; van den Brink, J.; Kelly, P. J., Doping Graphene with Metal Contacts. *Physical Review Letters* **2008,** *101* (2), 026803.
27. Gong, C.; Lee, G.; Shan, B.; Vogel, E. M.; Wallace, R. M.; Cho, K., First-principles study of metal–graphene interfaces. *Journal of Applied Physics* **2010,** *108* (12), 123711.
28. Khomyakov, P. A.; Giovannetti, G.; Rusu, P. C.; Brocks, G.; van den Brink, J.; Kelly, P. J., First-principles study of the interaction and charge transfer between graphene and metals. *Physical Review B* **2009,** *79* (19), 195425.
29. Venugopal, A.; Colombo, L.; Vogel, E. M., Contact resistance in few and multilayer graphene devices. *Applied Physics Letters* **2010,** *96* (1), 013512.
30. Seul Ki, H.; Sang Chul, J.; Wan Sik, H.; Byung Jin, C., Resistance analysis and device design guideline for graphene RF transistors. *2D Materials* **2015,** *2* (3), 034011.
31. Russo, S.; Craciun, M. F.; Yamamoto, M.; Morpurgo, A. F.; Tarucha, S., Contact resistance in graphene-based devices. *Physica E: Low-dimensional Systems and Nanostructures* **2010,** *42* (4), 677-679.
32. Nagashio, K.; Nishimura, T.; Kita, K.; Toriumi, A., Contact resistivity and current flow path at metal/graphene contact. *Applied Physics Letters* **2010,** *97* (14), 143514.
33. Chen, L.; Huang, Z.; Kumar, S., Impact of bonding at multi-layer graphene/metal interfaces on thermal boundary conductance. *Rsc Advances* **2014,** *4* (68), 35852-35861.
34. Norris, P. M.; Smoyer, J. L.; Duda, J. C.; Hopkins, P. E., Prediction and Measurement of Thermal Transport Across Interfaces Between Isotropic Solids and Graphitic Materials. *Journal of Heat Transfer* **2011,** *134* (2), 020910-020910-7.
35. Koh, Y. K.; Bae, M.-H.; Cahill, D. G.; Pop, E., Heat Conduction across Monolayer and Few-Layer Graphenes. *Nano Letters* **2010,** *10* (11), 4363-4368.
36. Hopkins, P. E.; Baraket, M.; Barnat, E. V.; Beechem, T. E.; Kearney, S. P.; Duda, J. C.; Robinson, J. T.; Walton, S. G., Manipulating Thermal Conductance at Metal–Graphene Contacts via Chemical Functionalization. *Nano Letters* **2012,** *12* (2), 590-595.
37. Guzman, P. A. V.; Sood, A.; Mleczko, M. J.; Wang, B.; Wong, H. S. P.; Nishi, Y.; Asheghi, M.; Goodson, K. E. In *Cross plane thermal conductance of graphene-metal interfaces*, 2014; IEEE: pp 1385-1389.

38. Foley, B. M.; Hernández, S. C.; Duda, J. C.; Robinson, J. T.; Walton, S. G.; Hopkins, P. E., Modifying Surface Energy of Graphene via Plasma-Based Chemical Functionalization to Tune Thermal and Electrical Transport at Metal Interfaces. *Nano Letters* **2015,** *15* (8), 4876-4882.
39. Huang, B.; Koh, Y. K., Improved topological conformity enhances heat conduction across metal contacts on transferred graphene. *Carbon* **2016,** *105*, 268-274.
40. Wei Chen, C.; Ren, F.; Chi, G.-C.; Hung, S.-C.; Huang, Y. P.; Kim, J.; Kravchenko, I. I.; Pearton, S. J., UV ozone treatment for improving contact resistance on graphene. *Journal of Vacuum Science & Technology B, Nanotechnology and Microelectronics: Materials, Processing, Measurement, and Phenomena* **2012,** *30* (6), 060604.
41. Li, W.; Liang, Y.; Yu, D.; Peng, L.; Pernstich, K. P.; Shen, T.; Hight Walker, A. R.; Cheng, G.; Hacker, C. A.; Richter, C. A.; Li, Q.; Gundlach, D. J.; Liang, X., Ultraviolet/ozone treatment to reduce metal-graphene contact resistance. *Applied Physics Letters* **2013,** *102* (18), 183110.
42. Joiner, C. A.; Roy, T.; Hesabi, Z. R.; Chakrabarti, B.; Vogel, E. M., Cleaning graphene with a titanium sacrificial layer. *Applied Physics Letters* **2014,** *104* (22), 223109.
43. McDonnell, S.; Smyth, C.; Hinkle, C. L.; Wallace, R. M., MoS2–Titanium Contact Interface Reactions. *ACS Applied Materials & Interfaces* **2016,** *8* (12), 8289-8294.
44. Lee, J. e. a., Clean transfer of graphene and its effect on contact resistance. *Applied Physics Letters* **2013,** *103* (10), 103104.

3.2 Ultra-High Vacuum Study of Titanium-Graphene Interface Chemistry

Abstract

The chemical interaction between Ti and graphene is of significant interest for engineering low resistance electrical contacts. To study interface chemistry, sequential depositions of Ti are performed on both as-received and UHV-annealed CVD-grown graphene samples. *In-situ* X-ray photoelectron spectroscopy (XPS) reveals no experimental evidence for the reaction of Ti with graphene at room temperature or after heating to 500 °C. The presence of the TiC chemical state is instead attributed to reactions between Ti and background gases in the UHV chamber as well as adventitious carbon on the surface of the graphene sample. We find that surface contamination can be substantially reduced by annealing in UHV. The deposition of Ti on graphene results in n-type doping which manifests in core-level shifts and broadening of the graphene C 1*s* peak. Annealing the sample following the deposition of Ti reverses the n-type doping. Raman spectroscopy results are in agreement with XPS analysis, which together provide insight into the possible mechanisms driving the changes in graphene doping.

3.2.1 Introduction

As discussed, Ti this is thought to form a chemisorbed interface with graphene via hybridization between the π-orbital in graphene and the *d*-orbital of the metal.[1] Reports in the literature indicate that the effects of orbital hybridization between Ti and graphene manifest experimentally in observations of band structure renormalization, carrier scattering, and n-type doping.[2-4] The exact mechanisms behind these phenomena remain ill-specified, however, owing to both a lack of chemical analysis of these interfaces and disagreement surrounding the possibility of graphene reacting with the metal adsorbates.

Recent reports are contradictory in the assessment of a graphene-Ti reaction as part of adsorption. Gong *et al.*[5] and Politou *et al.*[6] both report the presence of TiC in Ti/graphene contacts, attributing it to a reaction at the interface between the two materials. This is supported by other experimental findings in which the addition of transition metal atoms by electron beam deposition lowers the activation energy for vacancy formation in graphene, which could potentially promote reaction with metal adatoms.[7] Conversely, X-ray photoelectron spectroscopy (XPS) work by Hsu *et al.*[8] suggests that graphene does not react with Ti but instead forms a strongly hybridized interface that manifests in the graphene core-level spectrum. Using molecular dynamics simulations, Fonseca *et al.*[9] also conclude that no reaction should occur. Zan *et al.*[10] have found that metals aggregate in hydrocarbon surface contamination rather than directly interacting with the graphene. Here, we seek clarification regarding the chemical nature of Ti/graphene interfaces through a thorough XPS investigation that follows sequential depositions of small quantities of Ti on graphene. Understanding the nature of chemical interactions at the Ti/graphene interface is extremely important for electrical contacts.

In order to understand the intrinsic chemical properties of the interface, it is necessary to perform experiments under ultra-high vacuum with *in-situ* XPS characterization. To understand the effects of surface contamination which have been previously disregarded in the literature [5-6], we examined two separate samples. One was annealed for 12 hours in UHV prior to Ti deposition to remove adventitious carbon, whereas the other underwent Ti depositions in its as-received state. This work concludes that no reaction occurs between graphene and Ti and that interface hybridization effects are observed even in the presence of contamination. TiC formation is attributed instead to reactions with background gases in the chamber and surface contamination.

3.2.2 Materials and Methods

All experiments were performed our UHV system containing both XPS (ScientaOmicron) and an electron beam evaporator (Mantis QUAD-EV-C evaporator)[11] at a base pressure of ~2 x 10^{-10} mbar. XPS measurements were performed using a monochromated Al Kα X-ray source having a photon energy of 1486.7 eV. Data was acquired with a Scienta Omicron R3000 analyzer at a pass energy of 50 eV and a straight slit of 0.8 × 4 mm. XPS spectra were deconvoluted using kolXPD software.[12] Before beginning experiments with Ti on graphene, it was necessary to verify that the Ti source is free of carbon contamination. This allowed us to determine if the Ti evaporation rod (Goodfellow, 99.6+%) and/or gases in the chamber are sources of carbon for the formation of TiC. To achieve this, Au was evaporated in UHV onto a Si substrate to create a completely carbon-free surface. Next, Ti was deposited on the Au surface and XPS was acquired. The spectra of the carbon-free Ti/Au are shown in the following section.

The graphene used in this experiment was obtained from Dr. Ming Huang and Prof. Rodney Ruoff at the Ulsan National Institute of Science and Technology. The graphene was grown on Cu(111) foil at 1050 ºC in an atmosphere of flowing H_2 and CH_4 at rates of 20 and 3 sccm,

respectively, and a pressure of 2 Torr for 30 min. To assess the quality of the material, low energy electron diffraction (LEED), electron microscopy, and electron-backscattered diffraction measurements of our graphene on Cu(111) have been compared with measurements of graphene grown in polycrystalline foils. The results of these measurements are a testament to the high quality, uniformity, and large grain size of our material and have been discussed in a prior publication from the Ruoff group by Bao *et al*.[13] In summary, LEED patterns acquired at random locations of the continuous film had six diffraction spots arranged in a regular hexagon that corresponds to the graphene lattice. The positions of the graphene LEED spots and the underlying Cu surface coincided, indicating that the graphene was grown epitaxially on the Cu(111) foil. The consistent orientation of the LEED patterns acquired at different positions across the whole sample (1×1 cm^2) shows that the graphene film has a single crystalline orientation. In addition to the characterization reported in prior studies, angular resolved photoelectron spectroscopy (ARPES) has been used to verify the presence of a single Dirac cone as shown in Figure 3.2.1. The broadness of the spectrum can be attributed to the roughness of the surface which causes local variations in the analysis-surface angle. This result reconfirms the conclusion drawn from the LEED analysis that the graphene has a single crystal orientation.

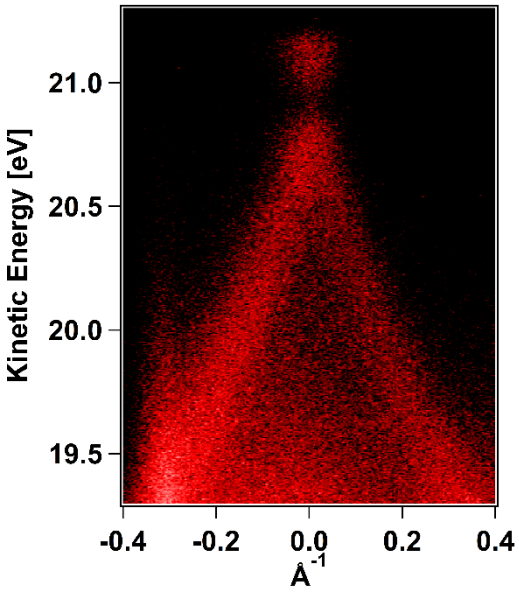

Figure 3.2.1. ARPES image of Gr/Cu(111) acquired with He I photons at an energy of 21.2 eV and a pass energy of 2 eV.

Since polymer residues present from transfer processes are known to have an effect on the resulting interface chemistry[14], this work utilizes graphene on its original Cu growth substrate. To minimize total air exposure time and keep the surface as clean as possible, the samples were vacuum sealed within 30 minutes of synthesis and loaded into UHV within 2 hours of breaking the vacuum seal. The samples were mounted onto Mo plates with Ta foil which were sonicated in acetone and isopropanol prior to mounting and loading in UHV. Following preliminary XPS characterization, the first graphene sample was annealed for 12 hours at a temperature of 550 °C. XPS was acquired again after cooling to ensure adequate removal of physisorbed contaminants. Sequential depositions of thin Ti at a rate of ~ 0.2 Å/min were performed with XPS measurements following each deposition. After the final deposition, the sample was annealed again to 550 °C to determine if heat treatment would promote Ti-graphene reaction. The second sample was not

annealed prior to or following sequential Ti depositions. The process and resulting changes in the material are summarized in Figure 3.2.2.

Raman spectroscopy was performed in ambient using a Renishaw inVia system employing a 405 nm laser as a means of assessing changes in doping and strain. Samples were characterized in their as-received state, after annealing, after Ti deposition and after post-deposition heating. In order to avoid an air break at different stages of the experiment – which would expose the sample to contaminants – Raman was performed on separate samples analogous to those examined with XPS.

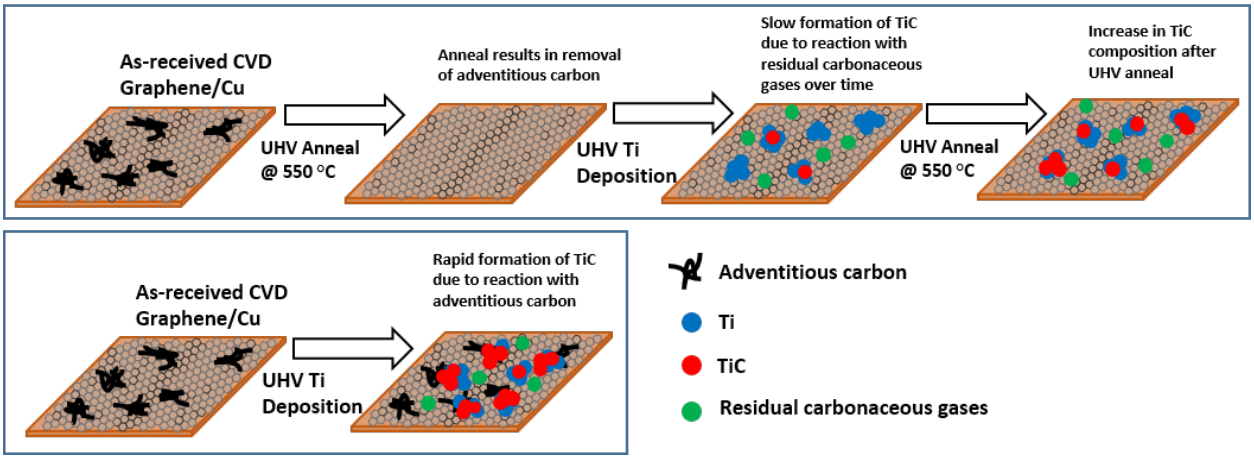

Figure 3.2.2. Schematic illustration of experimental process

3.2.3 Results and Discussion

3.2.3.1 Carbon Contamination in UHV

XPS spectra of the Ti/Au/Si control sample are shown in Figure 3.2.3. Figure 3.2.3(a) shows the Au 4*f* spectrum of the *in-situ* deposited Au starting surface with no carbon contamination. Figure 3.2.3(b) shows the Ti 2*p* spectrum acquired immediately after the deposition of Ti also showing no evidence of carbide. Lastly, Figure 3.2.3(c) displays the C 1*s* spectrum

acquired after 4 hours in UHV with no further Ti depositions. Here we see a new peak at 282 eV which corresponds to the Ti-C chemical state. Since the evaporation material appears to contain no carbon as shown in Figure 3.2.3(a-b), the only possible source of carbon here is the residual gases in the chamber. From the Hertz-Knudsen equation[15], we estimate a flux of about 3.8 x 10^{10} molecules/cm^2 s of hydrocarbon gases in our UHV chamber assuming a partial pressure of 10^{-10} mbar of hydrocarbons. Hsu *et al.*[8] attributed the observed carbide in their work to residual gases as opposed to reaction between graphene and carbon. While the presence of carbide on our Ti/Au/Si sample indicates that carbide forms from gases in the chamber, it does not eliminate the possibility of a reaction between Ti and graphene. The control sample therefore provides a baseline for TiC formation on any Ti surface in our UHV chamber. If other sources of carbon contribute to TiC formation (i.e. graphene or adventitious carbon on the surface of a sample), a faster rate of TiC formation is expected. This will be discussed later.

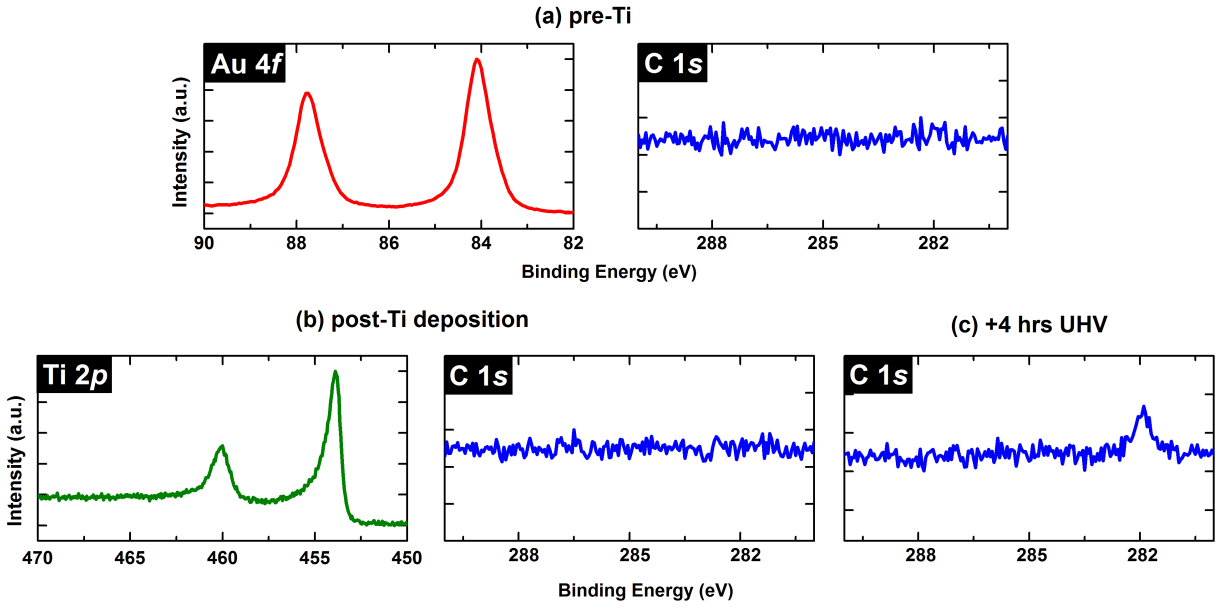

Figure 3.2.3. Control sample comprised of (a) carbon-free UHV-deposited Au and (b) UHV-deposited Ti on Au to show that no carbon contamination is present in the evaporation source. Carbide appears in (c) which was acquired after 4 hours in UHV.

3.2.3.2 Carbon Contamination on As-Received Graphene

To determine the efficacy of a 12-hour heating step for removal of surface contaminants, the C 1*s* and Cu 2*p* spectra of the Gr/Cu sample before and after heating are shown in the black and red curves, respectively, in Figure 3.2.4. The figure demonstrates that annealing the as-received sample substantially reduces the intensity of the C 1*s* signal thereby changing its width and line shape. This is attributed to the desorption of adventitious carbon species such as C-H, C-OH, and C=O groups from the surface of the graphene. The removal of carbon contamination from the surface also leads to an increase in the substrate signal shown in the Cu 2*p* spectrum. Following the anneal, the C 1*s* signal can be fit with a single asymmetric Doniach-Sunjic line shape that is characteristic of metals and metallic graphitic materials.[16-17] Fits of the C 1*s* spectra before and after annealing are shown in Figure 3.2.5. It is clear that only the graphene line shape remains after annealing. The shift of the peak to higher binding energies is consistent with a Fermi level shift, or a change in doping, which has been previously observed to occur at high temperatures due to the removal of surface contaminants.[14, 18]

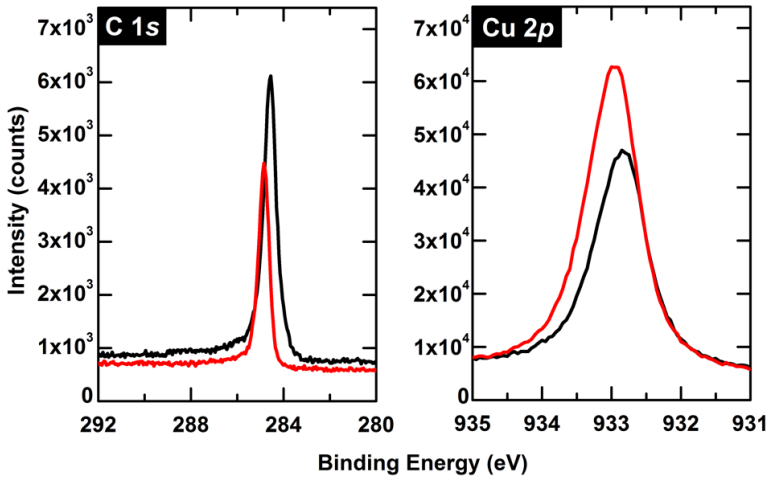

Figure 3.2.4. C 1s and Cu 2p spectra acquired before (black) and after (red) annealing the sample in UHV for 12 hours at 550 °C

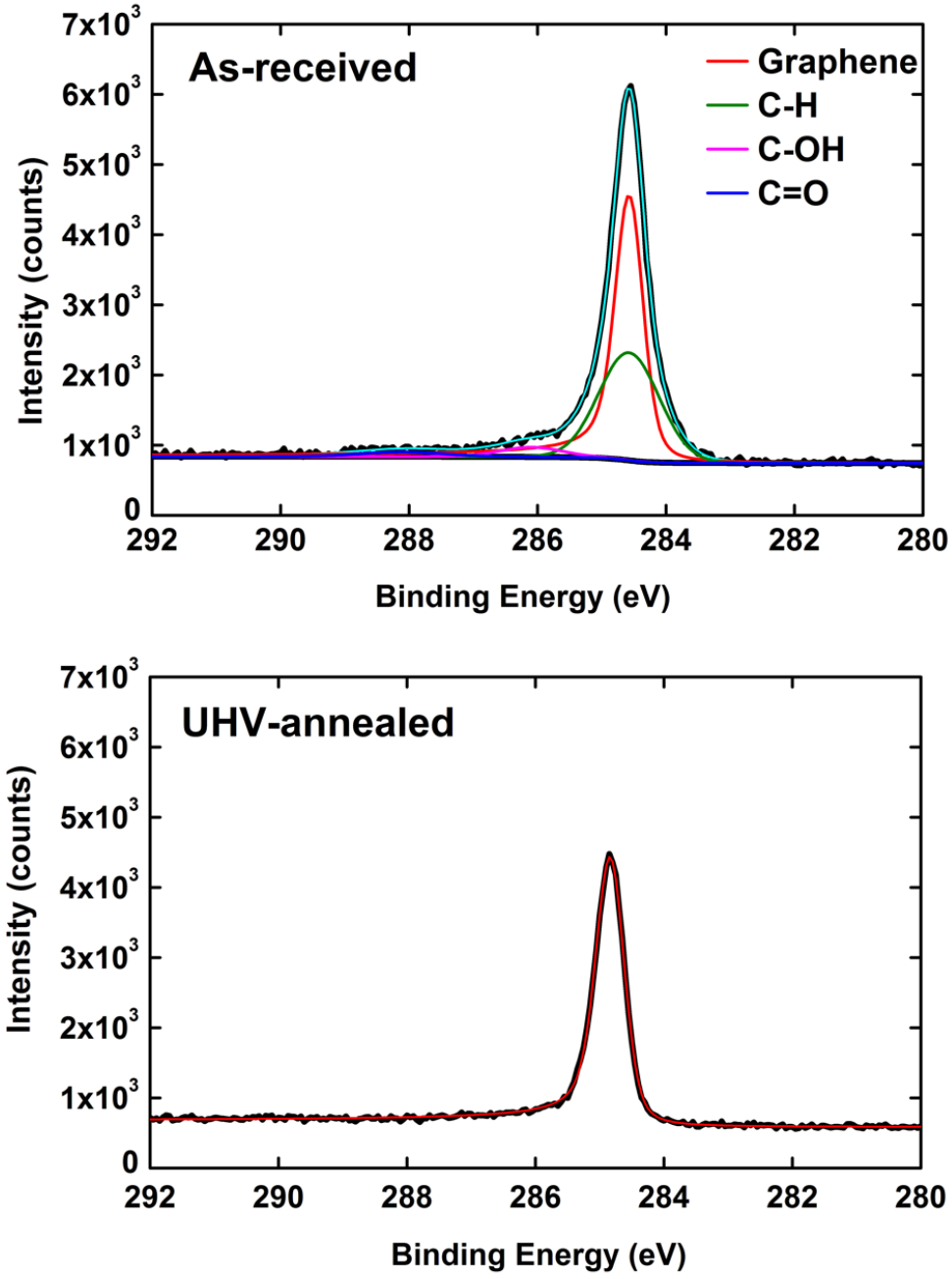

Figure 3.2.5. Comparison of fit results of the C 1*s* spectrum before and after UHV annealing.

3.2.3.3 Titanium Carbide Formation on Graphene

Figure 3.2.6 shows C 1*s* and Ti 2*p* spectra acquired following each Ti deposition on both the annealed (a) and as-received samples (b). Since such small quantities of Ti will form clusters

on graphene [19-20] rather than a continuous film, the quantity of Ti is reported here as % surface coverage assuming that complete surface coverage of graphene occurs at a thickness of 0.6 nm of Ti. This thickness for complete surface coverage of graphene has been verified experimentally by Fallahazad *et al*.[21] The % surface coverage was calculated using core level peak intensities with the method described in Section 2.3.1.5 adapted from Refs. 22-23:

$$I = I_0[1 - X_{Ti}] + X_{Ti} I_0 \mathrm{e}^{\left(\frac{-d}{\lambda_{Ti}\cos\theta}\right)} \qquad \text{Equation 3.1}$$

where I_0 is the intensity at 0% surface coverage, d is the thickness of Ti corresponding to 100% surface coverage of a single monolayer (6 Å[21]), λ_{Ti} is the effective attenuation length (EAL) of a given core level in Ti, and θ is the electron take off angle which is 45°. Attenuation is simply the ratio I/I_0. To calculate the % surface coverage using the experimental values of intensity, the above equation is rearranged yielding:

$$X_{Ti} = \frac{\frac{I}{I_0} - 1}{\mathrm{e}^{\left(\frac{-d}{\lambda_{Ti}\cos\theta}\right)} - 1}. \qquad \text{Equation 3.2}$$

This expression provides an estimate of surface coverage. Systematic errors arise from uncertainties in the EAL and the assumption that the Ti islands are only 0.6 nm in thickness. EAL is taken here to be constant for a given kinetic energy, but is in fact also sensitive to composition and thickness. The X_{Ti} values represented are reported as the average of X_{Ti} calculated using Cu 2p and X_{Ti} calculated with the Cu 3p core level. Using the NIST EAL Database[24], we find the EALs of Cu 2p and Cu 3p in a Ti overlayer to be 13.39 Å and 28.57 Å, respectively. Ideally, calculations with the two core levels should yield identical values, however the systemic errors discussed above lead to the small deviations, particularly at ~ 100% coverage where assumption of Ti islands with only 0.6 nm thickness becomes invalid. As can be seen in Figure 3.2.6, for both the UHV annealed and as-received samples, we observe an increase in the Ti-C signal (~282 eV)

with each subsequent Ti deposition. The feature at ~283 eV, denoted in the literature as C-Ti*, is attributed to a disordered state at TiC grain boundaries or at the interface between carbon and TiC.[25-28]

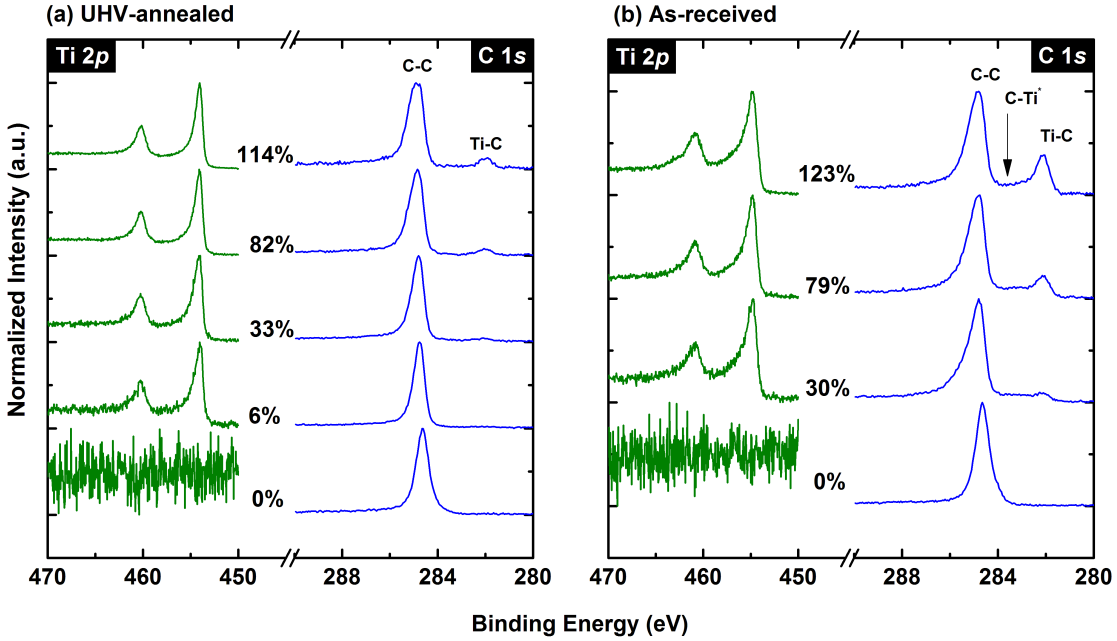

Figure 3.2.6. C1*s* and Ti 2*p* spectra prior Ti deposition and after each Ti deposition for (a) annealed graphene and (b) as received graphene. The percentage value corresponds to % surface coverage of graphene by Ti.

To more carefully examine the effect of surface contamination on the XPS line shape, we address the differences between the spectra corresponding to ~30% surface coverage for each sample. Higher TiC composition is observed for the as-received sample. This is expected given the presence of excess carbon available for reaction at the surface is greater for the as received sample. In order to determine if any graphene has been consumed to form TiC, we have plotted the attenuation of the different core level intensities as a function of Ti coverage and compared the experimental data to theoretical prediction in Figure 3.2.7. In the as-received sample, a graphene/Ti reaction is highly improbable due to the presence of non-graphitic carbon at the interface which

provides additional carbon for reaction with Ti and also acts as a physical barrier for the interaction of Ti with graphene. These other carbon species have been removed from the annealed sample. Therefore, we have implemented the following attenuation analysis on the annealed sample only using Equation 3.1. Given that $EAL_{Cu2p} < EAL_{C1s} < EAL_{Cu3p}$, if the C 1*s* signal corresponding to the graphene peak decreases solely due to attenuation in the clusters, its attenuation curve should fall between that of the two Cu core levels. If any of the graphene were to undergo a chemical reaction to form TiC, the graphene peak would attenuate a faster rate than predicted based on EALs. The fits of the C 1*s* spectra that were used for this analysis are shown in Figure 3.2.8. The sum of the blue and pink peaks is what is used for the attenuation analysis, and these features are well-separated from the carbide peak. Note that since the total integrated intensities of the Cu $2p^{3/2}$ and Cu 3*p* are used, the analysis is not sensitive to spectral deconvolution. These spectra shown in Figure 3.2.9.

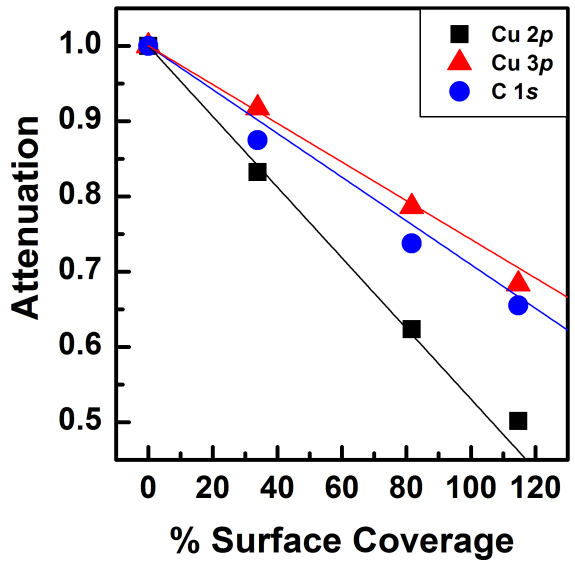

Figure 3.2.7. Attenuation of core-levels as a function of surface coverage.

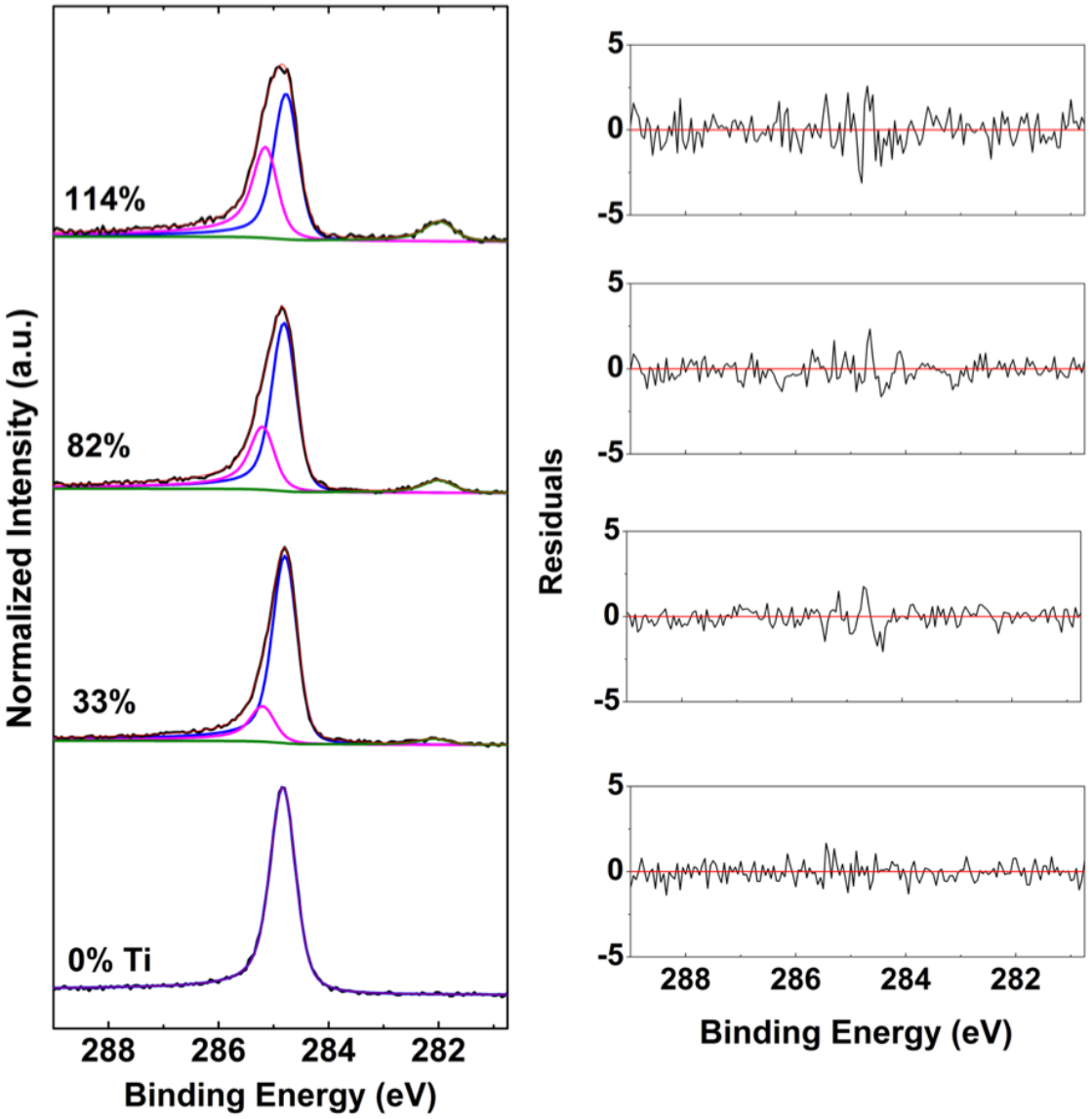

Figure 3.2.8. C 1*s* spectra at different Ti surface coverages, showing the graphene (blue), dopant-induced broadening (magenta) and TiC (green) chemical states and fit residuals on the right.

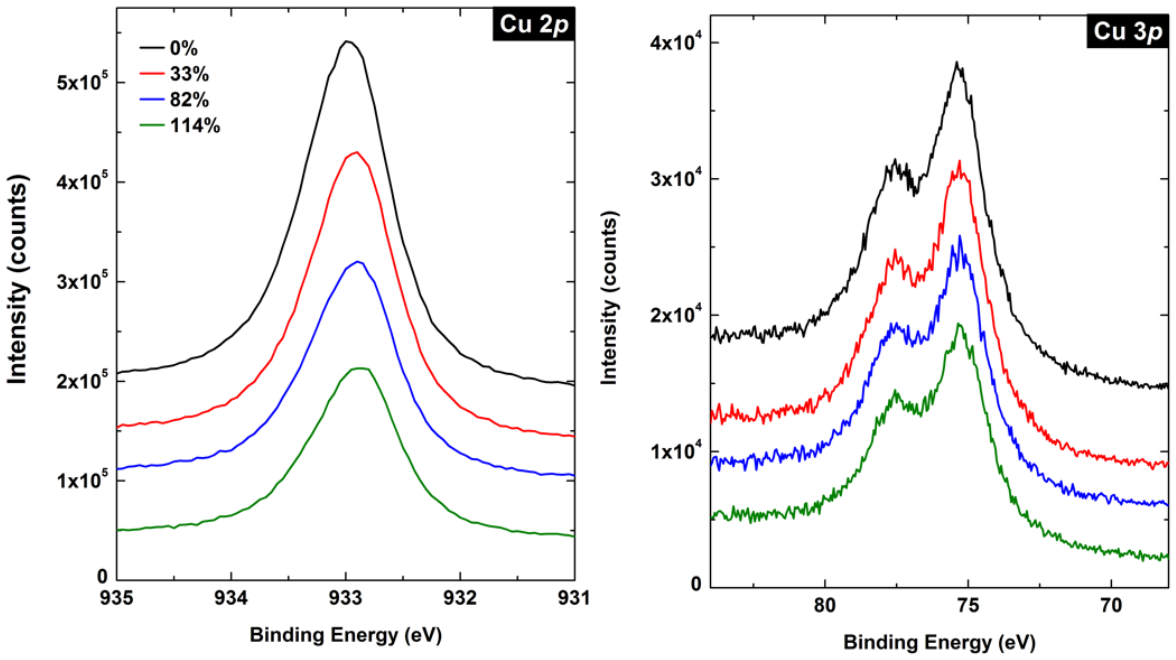

Figure 3.2.9. Spectra of Cu 2*p* and Cu 3*p* (offset along y-axis) acquired for attenuation analysis

The results shown in Figure 3.2.7 therefore provide no evidence that graphene is being consumed by a reaction with Ti as the attenuation of the C 1*s* signal falls firmly between that of the Cu *2p* and Cu *3p* modes, in agreement with the theoretically predicted attenuation curves. This is further supported by the rate of increase in the TiC signal observed for the annealed sample. Quantitatively, the TiC signal in Figure 3.2.6(a) increases by approximately 40 intensity counts per hour (normalized to the number of iterations). We note that each Ti deposition was three to six minutes in length whereas each XPS scan was approximately three hours leaving time for carbon to accumulate on the surface of the sample between each deposition/measurement cycle. This 40 counts/hour rate of increase was also observed for the Ti/Au/Si control sample left in UHV for 4 hours as shown in Figure 3.2.10. The identical rate of increase in TiC for both samples supports the conclusion that graphene is not a source of carbon for TiC formation.

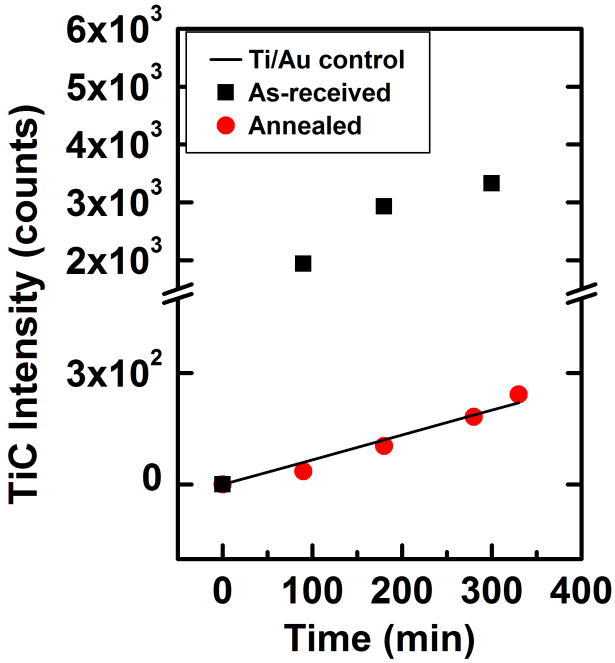

Figure 3.2.10. TiC intensity as a function of time for each sequential Ti deposition showing a steady increase at about ~40 counts per hour for the annealed sample and the Ti/Au control sample. The as-received sample exhibits a significantly higher increase in the carbon signal.

While there is a constant partial pressure of carbon species impinging on the surface of the sample during deposition, we note that no carbide was observed in Figure 3.2.3(b), the spectrum acquired on the control sample within minutes following the deposition of Ti. Thus, we conclude that the majority of carbon accumulates on the surface of the sample during the time between Ti depositions. The amount of carbide that forms during the deposition process at the graphene/Ti interface is below our detection limit. We therefore assume that the graphene is coated in clusters of metallic Ti which form a thin layer of carbide at their surface over an extended period of time.

3.2.3.4 Doping and Hybridization Effects

An important feature to address in Figure 3.2.6 is the spectral broadening that occurs in C 1*s* graphene peak. This has also been observed by Hsu *et al*.[8] In their analysis, it is explained as a splitting of the graphene peak into two contributions where the first contribution retains the original graphene line shape and the second is a broad feature at a higher binding energy that is loosely attributed to the electronic perturbation of the graphene lattice due to surface hybridization with Ti. Our experiment shows a similar result. However, we attribute the broadening of the spectrum more specifically to doping. This phenomenon is predicted by theoretical calculations[16] and supported by experimental results reported in graphene[29] as well as other material systems[30-31]. Based on the doping model, the high binding energy component corresponds to strong plasmon satellites which increases in intensity as a function of doping relative to the intensity of the main peak. It follows that we expect an increase in broadening as a greater fraction of the graphene surface comes into contact with the dopant material, which is what is observed in Figure 3.2.6. Others have also detected an increase in doping as a function of surface coverage via electrical and spectroscopic measurements.[2-4]

The n-type doping of graphene by Ti is extensively reported in the literature and is typically attributed to symmetry matching and spatial overlap of the Ti 3*d* orbital with the C $2p_z$ orbital [3], which forms the π band in graphene. Broadening is observed both in the annealed sample and in the as-received sample, however it is important to note that the two samples exhibit inherently different types of Ti interfaces. Nevertheless, given the well-documented sensitivity of the electronic structure of graphene to its adsorbates, it is not surprising that spectral changes are observed even in the presence of TiC or adventitious carbon at the interface.

3.2.3.5 Effect of Post-Deposition Heat Treatment

Yang *et al.*[32] report TiC formation via microwave sintering of graphene with Ti. This implies that a chemical reaction between Ti and graphene can be driven with adequate energy. The Ti-C phase diagram shows that 550 °C is sufficiently high to drive a reaction between titanium and carbon.[33] Graphene is known to be stable on Cu substrates to temperatures up to 1000 °C [34], however we must consider the affinity for reaction with Ti or the possibility of reaction at defect sites. To examine the thermal stability of the Ti/graphene interface, the Ti/graphene/Cu sample that was annealed prior to Ti deposition was annealed again following the final Ti deposition for 1 hour at 550 °C. The C 1*s* and Ti 2*p* spectra from before and after this heat treatment are shown in Figure 3.2.11. In the comparison of the C 1*s* spectra, we observe narrowing and shifting of the graphene peak as well as an increase in Ti-C intensity. The Ti 2*p* spectra show the transformation from Ti that was mostly metallic (at a binding energy of ~454.1 eV [35]) to a predominant composition of TiC at a binding energy of ~455.0 eV.[36] The TiC signal in the C 1*s* spectrum increased by 150%, over the course of an hour, which is significantly more than expected based on the rate shown in Figure 3.2.10. We report no decrease in the integrated intensity of the graphene peak indicating that no graphene was decomposed for the formation of TiC. The rapid increase in TiC is therefore attributed to diffusion. The high thermal energy in combination with the concentration gradient present in the stacked TiC/Ti structure likely promoted the homogenization of carbon composition in the Ti layer. This resulted in a higher fraction of Ti atoms interacting with carbon, yielding an increase in the intensity of the Ti-C chemical state. This is realistic considering that the nominal diffusion distance in 1 hour at 550 °C is 0.2 μm (one order of magnitude faster than at room temperature) which far exceeds the thickness of Ti deposited. In the C 1*s* spectrum, we observe a shift in the binding energy which indicates a shift of the Fermi level toward the valence band corresponding to a decrease in n-type doping. This is consistent with

findings by McCreery *et al*. which show that a change in the chemical state of metallic Ti adsorbates (via oxidation) leads to a decrease in doping.[4] The apparent restoration of the graphene line shape to its pre-Ti state is similar to the effect observed by Hsu *et al*. following oxidation of the Ti film. Based on the broadening model discussed earlier, the narrowing of the line shape is expected when doping decreases. While our heating experiment resulted in the carbidization of Ti rather than the oxidation of Ti performed by McCreery *et al*. and Hsu *et al*., the changes in the spectrum indicate that a similar effect has occurred, decoupling Ti from graphene. This will be discussed in more detail.

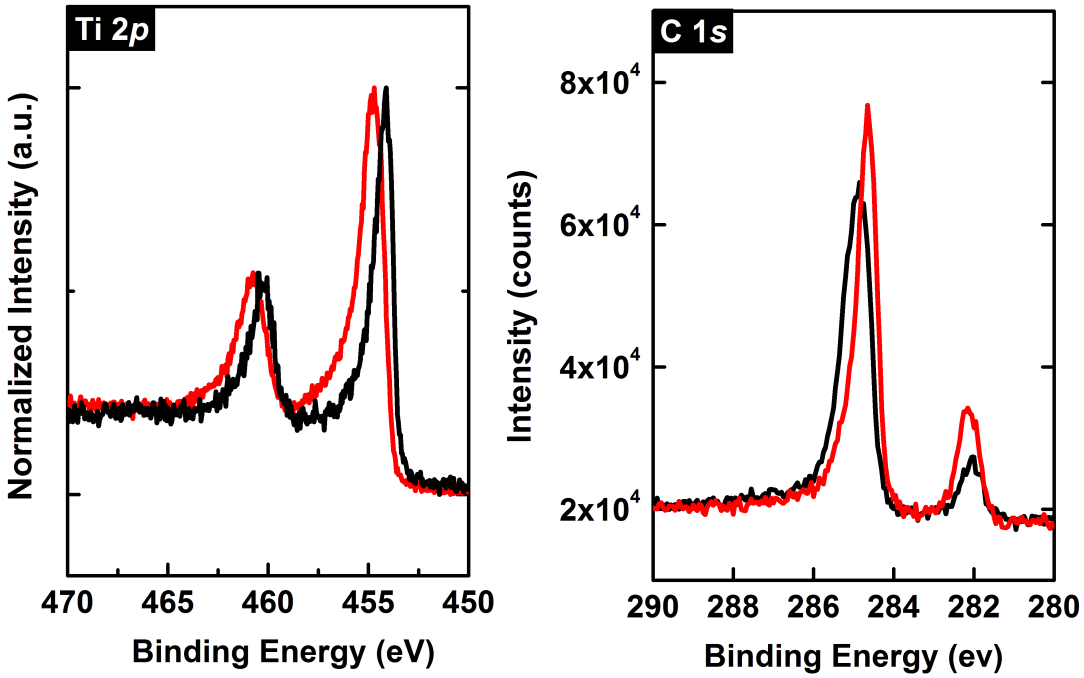

Figure 3.2.11. Ti 2*p* and C 1*s* spectra from before (black) and after annealing (red) the Ti/graphene/Cu sample for 1 hour at 550 °C.

XPS reveals that heating the Ti/graphene/Cu sample leads to an increase in TiC composition and a reduction in the n-type doping that resulted from the initial heating of the sample and the subsequent deposition of Ti. The observed changes in doping are attributed to structural

and chemical changes in the Ti/TiC clusters. Heating nonstoichiometric TiC has been found to induce the redistribution of carbon atoms and structural vacancies, leading to a transformation to ordered phases.[33, 37] As mentioned, we have calculated C/Ti composition of this sample to be approximately 0.2 before heating. After heating, the C/Ti ratio increased to a value of 0.5. This means that following heating, the number of Ti atoms bonded to C atoms increased by a factor greater than 2. The change in C/Ti ratio and the accompanying change in Ti 2*p* chemical state from metal to TiC support the argument that carbon atoms distributed throughout the metal clusters during heating, substantially increasing the total fraction of carbidized Ti atoms. According to the Ti-C phase diagram [33], the equilibrium state at 550 °C in this compositional range is a two-phase composite of nonstoichiometric TiC (Ti_2C) and Ti metal. Based on the diffusion calculations, it is reasonable to conclude that the entire cluster transformed to its equilibrium phase. The electronic interaction at the interface between graphene and the adsorbate was undoubtedly affected by this phase transformation. Since bonding in TiC involves charge transfer to the Ti 3*d* orbital which is essential for hybridization and doping effects in graphene, the increase in the number of Ti-C bonds would explain the observed decoupling effect that is characterized by the resulting Fermi level shifts.

3.2.3.6 Raman Spectroscopy Characterization

Quantitative analysis of Raman data was performed by Thomas Beechem at Sandia National Laboratories. Raman spectroscopy has been previously used to quantify both strain and carrier concentration on multiple forms of including graphene realized by epitaxial[38-39], CVD[40-41], and exfoliated[42-43] methods. To corroborate the conclusions arrived upon with XPS, Raman spectroscopy monitored changes in defects, doping, and strain as a function of the Ti-deposition and heat treatments described above. Qualitatively, the Raman spectra differ most strikingly in the

relative positions and magnitudes of the G- (1580 cm^{-1}) and 2D (2751 cm^{-1})-peaks. In contrast, the so-called defect peak at 1350 cm^{-1} that emerges with disruptions to sp^2 bonding changes to a lesser extent. This is assessed quantitatively in Figure 3.2.12 where the ratio of the I(D)/I(G) ratio at each stage is presented. While small alterations are indubitably observed, their magnitude is small compared to that expected if carbon in the graphene were consumed in a reaction. The reaction of graphene would lead to I(D)/I(G) values exceeding 0.3.[44] This is consistent with the conclusion arrived at with XPS that graphene is not a source of carbon for the formation of TiC.

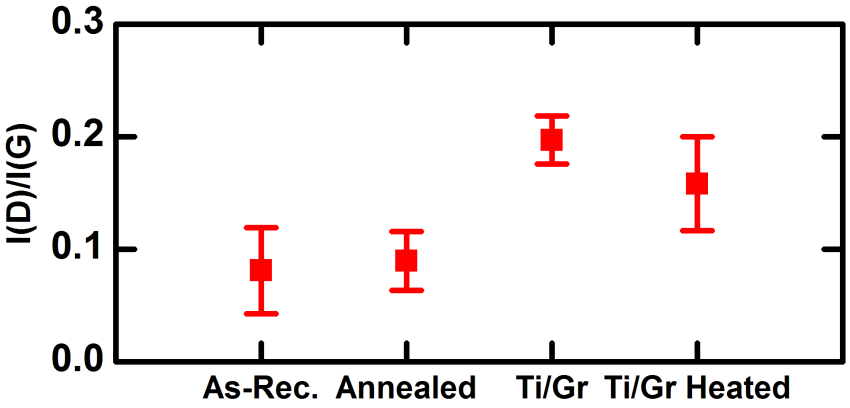

Figure 3.2.12. Ratio of the intensity of the D peak to the intensity of the G peak in the Raman spectra of each sample (average of 10 spots) acquired with a 405 nm laser.

Raman-based quantifications of carrier concentration and strain were performed simultaneously using the methods reported by Schmidt *et al*. [45] While annealing cleans the surface resulting in a net n-type doping as observed with XPS, Figure 3.2.12(a) indicates a small increase in p-type doping for the graphene. This seeming contradiction is entirely expected. Such discrepancies in dopant type have been previously reported when comparing results of measurements performed in UHV to those performed in air.[14] This occurs due to the doping effects of adsorbed H_2O and O_2.[46] Upon deposition of Ti, the hole carrier concentration decreases to almost 0 as a result of n-type doping implicit with the chemisorption of the metal. Evidence of

chemisorption is further observed in the relaxation of tensile stress shown in Figure 3.2.12(b) that occurs owing to "stretching" of the graphene by the Ti, which possesses a 20% larger lattice constant. [47] Upon heating, the effects of n-type doping by Ti are reversed. In total, the results are consistent and corroborate those arrived at with XPS. A summary of the results of XPS and Raman measurements can be found in Table 3.1.

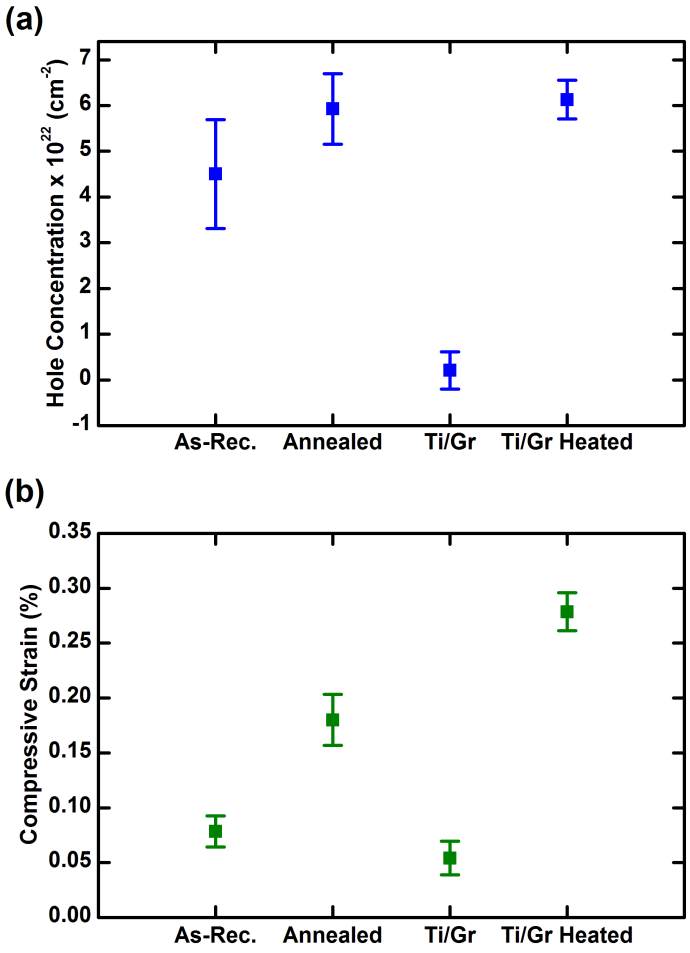

Figure 3.2.13. Summary of (a) hole concentration and (b) compressive strain calculated from fits to Raman spectra acquired with 405 nm laser

Table 3.1. Summary of Results

Process	XPS Result	Raman Result
UHV annealing of as-received graphene at 550 °C	Removal of adventitious carbon Increase in n-type doping*	No damage to graphene lattice Increase in strain Increase in p-type doping*
UHV Ti deposition on UHV	Formation of TiC over time due to reactions with background gases Attenuation of graphene signal solely due to Ti overlayer; no evidence of graphene reaction Increase in n-type doping	No damage to graphene lattice Decrease in strain Increase in n-type doping
UHV annealing after Ti deposition at 550 °C	Increase in TiC composition Increase in p-type doping	No damage to graphene lattice Increase in p-type doping Increase in strain

*discrepancy due to measurement in UHV (XPS) vs. ambient conditions (Raman)

3.2.4 Conclusion and Future Work

This work provides insight into the chemical and electronic interactions of the Ti/graphene interface that is commonly fabricated for electrical contacts to graphene. This work definitely concludes that, despite the observation of TiC bonding, no reactions take place between graphene and adsorbed Ti, either during room temperature deposition, or after a subsequent 550 °C anneal. Graphene can be successfully cleaned of surface contaminants by annealing for 12 hours at 550 °C. On a clean graphene surface, the formation of TiC results from background gases in the chamber. The presence of adventitious carbon on as-received CVD graphene substantially contributes to TiC formation. The n-type doping of graphene by Ti via orbital hybridization manifests in the Raman spectra as well as XPS binding energy shifts and broadening of the graphene C 1s peak. The effects of hybridization can be reversed with heat treatment which promotes diffusion of carbon from the surface into the Ti clusters, resulting in what we believe to

be an ordered non-stoichiometric TiC state. The bonding configuration of Ti in TiC, which changes the electron occupation of the *d* orbital, interferes with the orbital hybridization mechanism that facilitates doping in graphene.

A topic of future study could include Ni/graphene interface behavior. Like Ti, Ni is a commonly used contact to graphene devices.[48-51] As mentioned previously, Ni was used as the substrate material in the early years of CVD graphene growth however the high solubility of C atoms in Ni resulted in poor control over film thickness.[52] While this behavior is well-documented, uncertainty remains regarding the behavior of graphene covered with a Ni contacts. Lahiri *et al*.[53] report that Ni deposited on graphene (grown on a Ni substrate) exhibits a decrease in surface coverage due to diffusion and the formation of Ni carbide at temperatures above 100 ºC. Politou *et al.*[6] have identified Ni-carbide via XPS in Ni-contacted TLM structures, however they also reported Ti carbide in Ti-contacted devices which is now known to be due to reactions with adventitious carbon or background gases. Given that Ni exhibits high reactivity with amorphous carbon[54], it is possible that the observed Ni carbide phases are simply also due to reactions with background gases or adventitious carbon on graphene surfaces. Work demonstrating the ability to transfer graphene using a Ni film is evidence of strong interactions at the interface even under high-vacuum deposition conditions.[55] An experimental procedure of sequential Ni deposition in UHV can be implemented to determine if a Ni-graphene reaction occurs or if electronic interactions at the interface manifest in XPS features.

3.2.5 References

1. Gong, C.; Lee, G.; Shan, B.; Vogel, E. M.; Wallace, R. M.; Cho, K., First-principles study of metal–graphene interfaces. *Journal of Applied Physics* **2010,** *108* (12), 123711.
2. Pi, K.; McCreary, K. M.; Bao, W.; Han, W.; Chiang, Y. F.; Li, Y.; Tsai, S. W.; Lau, C. N.; Kawakami, R. K., Electronic doping and scattering by transition metals on graphene. *Physical Review B* **2009,** *80* (7), 075406.
3. Chen, J.-W.; Huang, H.-C.; Convertino, D.; Coletti, C.; Chang, L.-Y.; Shiu, H.-W.; Cheng, C.-M.; Lin, M.-F.; Heun, S.; Chien, F. S.-S.; Chen, Y.-C.; Chen, C.-H.; Wu, C.-L., Efficient n-type doping in epitaxial graphene through strong lateral orbital hybridization of Ti adsorbate. *Carbon* **2016,** *109*, 300-305.
4. McCreary, K. M.; Pi, K.; Kawakami, R. K., Metallic and insulating adsorbates on graphene. *Applied Physics Letters* **2011,** *98* (19), 192101.
5. Gong, C.; McDonnell, S.; Qin, X.; Azcatl, A.; Dong, H.; Chabal, Y. J.; Cho, K.; Wallace, R. M., Realistic Metal–Graphene Contact Structures. *ACS Nano* **2014,** *8* (1), 642-649.
6. Politou, M.; Asselberghs, I.; Radu, I.; Conard, T.; Richard, O.; Lee, C. S.; Martens, K.; Sayan, S.; Huyghebaert, C.; Tokei, Z.; De Gendt, S.; Heyns, M., Transition metal contacts to graphene. *Applied Physics Letters* **2015,** *107* (15), 153104.
7. Ramasse, Q. M.; Zan, R.; Bangert, U.; Boukhvalov, D. W.; Son, Y.-W.; Novoselov, K. S., Direct Experimental Evidence of Metal-Mediated Etching of Suspended Graphene. *ACS Nano* **2012,** *6* (5), 4063-4071.
8. Hsu, A. L.; Koch, R. J.; Ong, M. T.; Fang, W.; Hofmann, M.; Kim, K. K.; Seyller, T.; Dresselhaus, M. S.; Reed, E. J.; Kong, J.; Palacios, T., Surface-Induced Hybridization between Graphene and Titanium. *ACS Nano* **2014,** *8* (8), 7704-7713.
9. Fonseca, A. F.; Liang, T.; Zhang, D.; Choudhary, K.; Phillpot, S. R.; Sinnott, S. B., Graphene–Titanium Interfaces from Molecular Dynamics Simulations. *ACS Applied Materials & Interfaces* **2017,** *9* (38), 33288-33297.
10. Zan, R.; Bangert, U.; Ramasse, Q.; Novoselov, K. S., Metal−Graphene Interaction Studied via Atomic Resolution Scanning Transmission Electron Microscopy. *Nano Letters* **2011,** *11* (3), 1087-1092.
11. Freedy, K. M.; Litwin, P. M.; McDonnell, S. J., (Invited) In-Vacuo Studies of Transition Metal Dichalcogenide Synthesis and Layered Material Integration. *ECS Transactions* **2017,** *77* (8), 11-25.
12. http://kolxpd.kolibrik.net/.
13. Li, B.-W.; Luo, D.; Zhu, L.; Zhang, X.; Jin, S.; Huang, M.; Ding, F.; Ruoff Rodney, S., Orientation-Dependent Strain Relaxation and Chemical Functionalization of Graphene on a Cu(111) Foil. *Advanced Materials* **2018,** *30* (10), 1706504.
14. Pirkle, A.; Chan, J.; Venugopal, A.; Hinojos, D.; Magnuson, C. W.; McDonnell, S.; Colombo, L.; Vogel, E. M.; Ruoff, R. S.; Wallace, R. M., The effect of chemical residues on the physical and electrical properties of chemical vapor deposited graphene transferred to SiO2. *Applied Physics Letters* **2011,** *99* (12), 122108.
15. Kolasinski, K. W., *Surface science: foundations of catalysis and nanoscience*. John Wiley & Sons: 2012.
16. Sernelius, B. E., Core-level spectra from graphene. *Physical Review B* **2015,** *91* (4), 045402.

17. Susi, T.; Pichler, T.; Ayala, P., X-ray photoelectron spectroscopy of graphitic carbon nanomaterials doped with heteroatoms. *Beilstein Journal of Nanotechnology* **2015,** *6*, 177-192.
18. Marsden, A. J.; Asensio, M.-C.; Avila, J.; Dudin, P.; Barinov, A.; Moras, P.; Sheverdyaeva, P. M.; White, T. W.; Maskery, I.; Costantini, G.; Wilson, N. R.; Bell, G. R., Is graphene on copper doped? *physica status solidi (RRL) – Rapid Research Letters* **2013,** *7* (9), 643-646.
19. Neek-Amal, M.; Reza, A.; Tabar, M. R. R., The formation of atomic nanoclusters on graphene sheets. *Nanotechnology* **2009,** *20* (13), 135602.
20. Mashoff, T.; Convertino, D.; Miseikis, V.; Coletti, C.; Piazza, V.; Tozzini, V.; Beltram, F.; Heun, S., Increasing the active surface of titanium islands on graphene by nitrogen sputtering. *Applied Physics Letters* **2015,** *106* (8), 083901.
21. Fallahazad, B.; Lee, K.; Lian, G.; Kim, S.; Corbet, C. M.; Ferrer, D. A.; Colombo, L.; Tutuc, E., Scaling of Al_2O_3 dielectric for graphene field-effect transistors. *Applied Physics Letters* **2012,** *100* (9), 093112.
22. Himpsel, F. J.; McFeely, F. R.; Taleb-Ibrahimi, A.; Yarmoff, J. A.; Hollinger, G., Microscopic structure of the SiO_2/Si interface. *Physical Review B* **1988,** *38* (9), 6084-6096.
23. McDonnell, S.; Longo, R. C.; Seitz, O.; Ballard, J. B.; Mordi, G.; Dick, D.; Owen, J. H.; Randall, J. N.; Kim, J.; Chabal, Y. J.; Cho, K.; Wallace, R. M., Controlling the atomic layer deposition of titanium dioxide on silicon: dependence on surface termination. *The Journal of Physical Chemistry C* **2013,** *117* (39), 20250-20259.
24. Jablonski, A., NIST Electron Effective-Attenuation-Length Database. **2011**.
25. Magnuson, M.; Lewin, E.; Hultman, L.; Jansson, U., Electronic structure and chemical bonding of nanocrystalline-TiC/amorphous-C nanocomposites. *Physical Review B* **2009,** *80* (23), 235108.
26. Lewin, E.; Wilhelmsson, O.; Jansson, U., Nanocomposite nc-TiC/a-C thin films for electrical contact applications. *Journal of Applied Physics* **2006,** *100* (5), 054303.
27. Zemek, J.; Houdkova, J.; Jiricek, P.; Jelinek, M., Amorphous carbon nanocomposite films doped by titanium: Surface and sub-surface composition and bonding. *Diamond and Related Materials* **2018,** *81*, 61-69.
28. Lewin, E.; Persson, P. O. Å.; Lattemann, M.; Stüber, M.; Gorgoi, M.; Sandell, A.; Ziebert, C.; Schäfers, F.; Braun, W.; Halbritter, J.; Ulrich, S.; Eberhardt, W.; Hultman, L.; Siegbahn, H.; Svensson, S.; Jansson, U., On the origin of a third spectral component of C1s XPS-spectra for nc-TiC/a-C nanocomposite thin films. *Surface and Coatings Technology* **2008,** *202* (15), 3563-3570.
29. Joucken, F.; Tison, Y.; Le Fèvre, P.; Tejeda, A.; Taleb-Ibrahimi, A.; Conrad, E.; Repain, V.; Chacon, C.; Bellec, A.; Girard, Y.; Rousset, S.; Ghijsen, J.; Sporken, R.; Amara, H.; Ducastelle, F.; Lagoute, J., Charge transfer and electronic doping in nitrogen-doped graphene. *Scientific Reports* **2015,** *5*, 14564.
30. Mudd, J. J.; Lee, T.-L.; Muñoz-Sanjosé, V.; Zúñiga-Pérez, J.; Hesp, D.; Kahk, J. M.; Payne, D. J.; Egdell, R. G.; McConville, C. F., Hard x-ray photoelectron spectroscopy as a probe of the intrinsic electronic properties of CdO. *Physical Review B* **2014,** *89* (3), 035203.
31. Egdell, R. G.; Rebane, J.; Walker, T. J.; Law, D. S. L., Competition between initial- and final-state effects in valence- and core-level x-ray photoemission of Sb-doped SnO. *Physical Review B* **1999,** *59* (3), 1792-1799.
32. Yang, W.-Z.; Huang, W.-M.; Wang, Z.-F.; Shang, F.-J.; Huang, W.; Zhang, B.-Y., Thermal and Mechanical Properties of Graphene–Titanium Composites Synthesized by Microwave Sintering. *Acta Metallurgica Sinica (English Letters)* **2016,** *29* (8), 707-713.

33. Lipatnikov, V. N.; Rempel, A. A.; Gusev, A. I., Atomic ordering and hardness of nonstoichiometric titanium carbide. *International Journal of Refractory Metals and Hard Materials* **1997,** *15* (1), 61-64.
34. Mattevi, C.; Kim, H.; Chhowalla, M., A review of chemical vapour deposition of graphene on copper. *Journal of Materials Chemistry* **2011,** *21* (10), 3324-3334.
35. Briggs, D., Handbook of X-ray Photoelectron Spectroscopy. *Surface and Interface Analysis* **1981,** *3* (4), 72-73.
36. Qiang, L.; Zhang, B.; Zhou, Y.; Zhang, J., Improving the internal stress and wear resistance of DLC film by low content Ti doping. *Solid State Sciences* **2013,** *20*, 17-22.
37. Lipatnikov, V. N.; Zueva, L. V.; Gusev, A. I.; Kottar, A., Disorder-order phase transformations and electrical resistivity of nonstoichiometric titanium carbide. *Physics of the Solid State* **1998,** *40* (7), 1211-1218.
38. Beechem, T. E.; Ohta, T.; Diaconescu, B.; Robinson, J. T., Rotational Disorder in Twisted Bilayer Graphene. *ACS Nano* **2014,** *8* (2), 1655–1663.
39. Schmidt, D. A.; Ohta, T.; Beechem, T. E., Strain and Charge Carrier Coupling in Epitaxial Graphene. *Phys. Rev. B* **2011,** *84* (23), 235422.
40. Bronsgeest, M. S.; Bendiab, N.; Mathur, S.; Kimouche, A.; Johnson, H. T.; Coraux, J.; Pochet, P., Strain relaxation in CVD graphene: Wrinkling with shear lag. *Nano letters* **2015,** *15* (8), 5098-5104.
41. Frank, O.; Vejpravova, J.; Holy, V.; Kavan, L.; Kalbac, M., Interaction between graphene and copper substrate: The role of lattice orientation. *Carbon* **2014,** *68*, 440-451.
42. Lee, J. E.; Ahn, G.; Shim, J.; Lee, Y. S.; Ryu, S., Optical Separation of Mechanical Strain from Charge Doping in Graphene. *Nature Communications* **2012,** *3*, 1024.
43. Das, A.; Pisana, S.; Chakraborty, B.; Piscanec, S.; Saha, S.; Waghmare, U.; Novoselov, K.; Krishnamurthy, H.; Geim, A.; Ferrari, A., Monitoring Dopants by Raman scattering in an Electrochemically Top-Gated Graphene Transistor. *Nature Nanotechnology* **2008,** *3* (4), 210-215.
44. Liu, L.; Ryu, S.; Tomasik, M. R.; Stolyarova, E.; Jung, N.; Hybertsen, M. S.; Steigerwald, M. L.; Brus, L. E.; Flynn, G. W., Graphene Oxidation: Thickness-Dependent Etching and Strong Chemical Doping. *Nano Letters* **2008,** *8* (7), 1965-1970.
45. Schmidt, D. A.; Ohta, T.; Beechem, T. E., Strain and charge carrier coupling in epitaxial graphene. *Physical Review B* **2011,** *84* (23), 235422.
46. Melios, C.; Giusca, C. E.; Panchal, V.; Kazakova, O., Water on graphene: review of recent progress. *2D Materials* **2018,** *5* (2), 022001.
47. Khomyakov, P. A.; Giovannetti, G.; Rusu, P. C.; Brocks, G.; van den Brink, J.; Kelly, P. J., First-principles study of the interaction and charge transfer between graphene and metals. *Physical Review B* **2009,** *79* (19), 195425.
48. Giubileo, F.; Di Bartolomeo, A., The role of contact resistance in graphene field-effect devices. *Progress in Surface Science* **2017,** *92* (3), 143-175.
49. Nagashio, K.; Nishimura, T.; Kita, K.; Toriumi, A., Contact resistivity and current flow path at metal/graphene contact. *Applied Physics Letters* **2010,** *97* (14), 143514.
50. Venugopal, A.; Colombo, L.; Vogel, E. M., Contact resistance in few and multilayer graphene devices. *Applied Physics Letters* **2010,** *96* (1), 013512.
51. Gahoi, A.; Wagner, S.; Bablich, A.; Kataria, S.; Passi, V.; Lemme, M. C., Contact resistance study of various metal electrodes with CVD graphene. *Solid-State Electronics* **2016,** *125*, 234-239.

52. Muñoz, R.; Gómez-Aleixandre, C., Review of CVD Synthesis of Graphene. *Chemical Vapor Deposition* **2013,** *19* (10-11-12), 297-322.
53. Lahiri, J.; Batzill, M., Graphene destruction by metal-carbide formation: An approach for patterning of metal-supported graphene. *Applied Physics Letters* **2010,** *97* (2), 023102.
54. Anton, R., On the reaction kinetics of Ni with amorphous carbon. *Carbon* **2008,** *46* (4), 656-662.
55. Kim, J.; Park, H.; Hannon, J. B.; Bedell, S. W.; Fogel, K.; Sadana, D. K.; Dimitrakopoulos, C., Layer-Resolved Graphene Transfer via Engineered Strain Layers. *Science* **2013,** *342* (6160), 833.

3.3 Processing Effects of High Vacuum-Deposited Titanium Contacts to Transferred CVD Graphene

The following section has been adapted from Freedy, K. M.; Giri, A.; Foley, B. M.; Barone, M. R.; Hopkins, P. E.; McDonnell, S., Titanium contacts to graphene: process-induced variability in electronic and thermal transport. *Nanotechnology* **2018,** *29* (14), 145201.

Abstract

Contact Resistance (R_C) is a major limiting factor in the performance of graphene devices. R_C is sensitive to the quality of the interface and the composition of the contact, which are affected by the graphene transfer process and contact deposition conditions. In this work, a linear correlation is observed between the composition of Ti contacts, characterized by X-ray photoelectron spectroscopy, and the Ti/graphene (Gr) contact resistance measured by the transfer length method. Large variability in both oxide composition of the Ti and contact resistance is observed for samples processed by nominally identical procedures. This is attributed to defects introduced inevitably during the transfer process, particularly during the removal of polymer residues. We find that for a single piece of transferred graphene, contact composition is tunable via deposition rate and base pressure, however, variability between separately transferred samples dominates composition irrespective of the deposition conditions. The effect of contact deposition conditions on thermal transport measured by time-domain thermoreflectance is also reported and interfaces with higher oxide composition appear to result in a lower thermal boundary conductance. Possible origins of this thermal boundary conductance change with oxide composition are discussed.

3.3.1 Introduction

The overwhelming majority of reports in the literature on metal/graphene contacts assume ideal interfaces in which R_C is explained by intrinsic interactions between graphene and the metal such as effects of orbital hybridization, electrochemical equalization, and other mechanisms which cause changes in the electronic structure of graphene due to the presence of a metal overlayer.[1] As discussed previously, the effects of processing conditions on the chemistry and properties of the contact are often overlooked. The details of graphene processing procedures and contact deposition conditions such as base pressure and deposition rate are rarely reported in device studies, even in those which focus specifically on characterization of contacts. McDonnel *et al*.[2] have shown that the chemical composition of Ti is extremely sensitive to the deposition environment due to its high reactivity with oxygen species. This warrants a thorough investigation to understand the effect of deposition conditions on interface chemistry and transport properties.

3.3.2 Materials and Methods

The starting material (Graphene Supermarket 4"x4" Gr/Cu) was cut into ~2x2 cm^2 pieces for transfer onto 300 nm SiO_2/Si purchased from University Wafer. A solution of 30 mg/mL PMMA (Sigma Aldrich) dissolved in chlorobenzene was spin-coated at 4000 rpm for 30 seconds onto the Gr/Cu stack. The PMMA/graphene/Cu stack was cured on a hotplate at 60 °C for 10 minutes. The stack was placed in 3:1 deionized (DI) H_2O:HNO_3 for 1 minute followed by DI H_2O for 1 minute to remove graphene from the back of the foil. This was repeated twice. The Cu foil was then dissolved in a solution of 0.5 M ammonium persulfate (APS) for a total of 21 hours. The PMMA/graphene film was then transferred onto a 300 nm SiO_2/Si wafer. Before transfer, the wafer was cleaned with methanol, acetone, and DI water. The Gr/SiO_2 was left to air dry for 30 minutes

and was then heated to 180 °C for 5 minutes. Following this process, PMMA was dissolved in acetone. The samples were then annealed in ultra-high vacuum at 350-410 °C for three hours to remove PMMA residues.[3] Following the anneal, the wafer was diced into smaller pieces to make a sample set for each experiment. This minimizes any variability that might exist between separately transferred samples.

After transfer onto SiO_2, 5 nm of titanium was deposited onto graphene/SiO_2 in a HV electron beam evaporator at pressures of 10^{-7} or 10^{-6} Torr and deposition rates ranging from 0.01 to 0.5 nm/s, indicated by a quartz crystal monitor. Samples for TLM measurements were fixed with a shadow mask prior to metal evaporation. The samples were not exposed to atmosphere following the deposition of Ti. Au was deposited to cap the samples prior to removal from UHV in order to prevent further oxidation of the Ti layer upon air exposure. Au films of 500 nm, 80 nm, and 2 nm were deposited on samples for TLM, thermal measurements, and XPS, respectively. X-ray photoelectron spectroscopy data was collected with a monochromated X-ray source at a pass energy of 50 eV in our Scienta Omicron UHV system described previously in Section 2.3.1.1. The samples were then characterized by the transfer length method (TLM) and time-domain thermoreflectance (TDTR) to determine R_C and thermal boundary conductance, respectively.

An explanation of TLM can be found in Section 2.3.5. We note that TLM data was acquired under ambient conditions within 12 to 14 days of the initial graphene transfer and within one week of contact deposition. Prior to measurement, the samples were stored in a desiccator. On each sample, sixteen TLM structures were measured and the resistances corresponding to each contact separation distance were averaged. Results acquired on the same samples after six months of air exposure show a trend consistent with the original analysis shown in Figure 3.3.5. Other graphene TLM studies utilize a wide range of TLM geometries typically processed by photolithography with

contact spacings less than 100 μm.[4-7] In these studies, typical reactor base pressures and deposition rates were not reported. In our work, potential variations induced by photoresist residue was avoided by using a shadow mask. Several TDTR scans are performed by Ashutosh Giri in Prof. Hopkins Lab at different locations across the samples to ensure repeatability of the measurements, and the data are fit with a model that accounts for thermal diffusion in a two-layer system by fitting for h_K across the Au/SiO_2 interface.

3.3.3 Results and Discussion

3.3.3.1 Deposition Rate and Contact Composition

We have found that oxide composition is largely dependent on the contact deposition conditions. Titanium is highly reactive and will readily oxidize under high-vacuum deposition conditions. As others have suggested[2, 8-9] , the adsorption of oxidizing species onto the substrate surface during deposition will affect the chemistry of the contact which is expected to manifest in the electrical and thermal properties of the interface. Figure 3.3.1 shows oxide composition vs. deposition rate for samples fabricated from three individually transferred pieces of graphene. Each color represents a single piece of graphene transferred to SiO_2 and subsequently split into three (or four) samples to receive metal deposition at three (or four) different deposition rates. Sample-to-sample variability is observed, but there appears to be a trend of decreasing oxide composition with increasing deposition rate. The deposition rate determines the impingement rate of Ti atoms on the surface of the substrate relative to the impingement rate of the oxidizing species from residual gases. It is therefore expected that higher deposition rates result in lower oxide composition, since at higher deposition rates, Ti atoms arrive at the sample surface at faster rates than oxidizing species in the chamber.

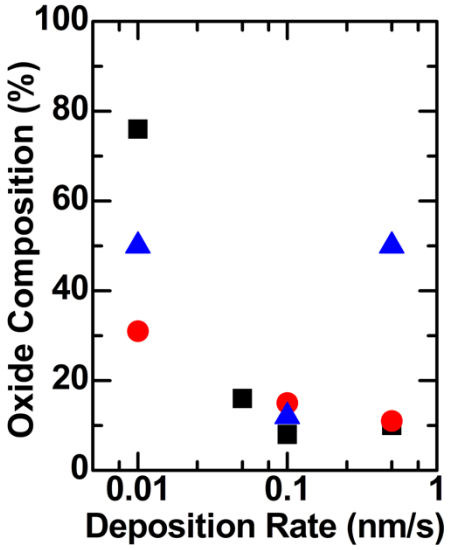

Figure 3.3.1. Plot of Ti oxide composition vs. deposition rate at a pressure of 1x10-7 Torr on graphene/SiO2 samples. Each identical marker shape represents samples cut from the same piece of graphene.

The presence of anomalous data points, namely the blue triangle at 0.5 nm/s, can be explained by the presence of additional oxidizing species from PMMA residues. PMMA is typically removed by dissolution in acetone followed by an anneal in UHV at a temperature high enough to dissociate the various hydrocarbon species.[10] The thermal decomposition of PMMA is inherently a random process, and generated radicals can react with defects in the graphene or form longer polymer chains that cannot be removed.[11] Therefore, samples which undergo the same PMMA removal process can be left with different quantities of PMMA residue, and the quantity of PMMA residue is unlikely to be uniform across a single sample. Lee *et al.* have shown that a PMMA-free transfer process results in lower contact resistance than that which uses PMMA[12], however PMMA is used for photolithography even when PMMA-free transfer processes are employed. As mentioned earlier, PMMA residues are known to dope graphene and alter its electronic properties.[10] Furthermore, transport across the Ti/graphene interface will be inhibited by the presence of contaminants which scatter charge carriers and obstruct hybridization between

the graphene π-orbitals and Ti metal d-orbitals.[1, 13] Orbital hybridization will also be inhibited by the presence of an oxidized contact rather than a metallic one due to the different configuration of the *d* orbitals. It has been shown that PMMA residues react with Ti overlayers to form oxide.[14]

The presence of PMMA residues on the samples used in this experiment is evident in XPS and Raman spectra acquired before and after annealing the transferred graphene. The XPS spectrum in Figure 3.3.2(a) shows the spectra components from PMMA residue, similar to the results reported by Pirkle *et al*.[10] The figure indicates a reduction in in polymeric species following the anneal however it is clear that residue remains. The Raman spectra in Figure 3.3.2(b) show an increase in the D-peak and a broadening of the G-peak following the anneal. This is consistent with results reported by Gong *et al*.[15] and is attributed to the presence of decomposed polymer species.[16]

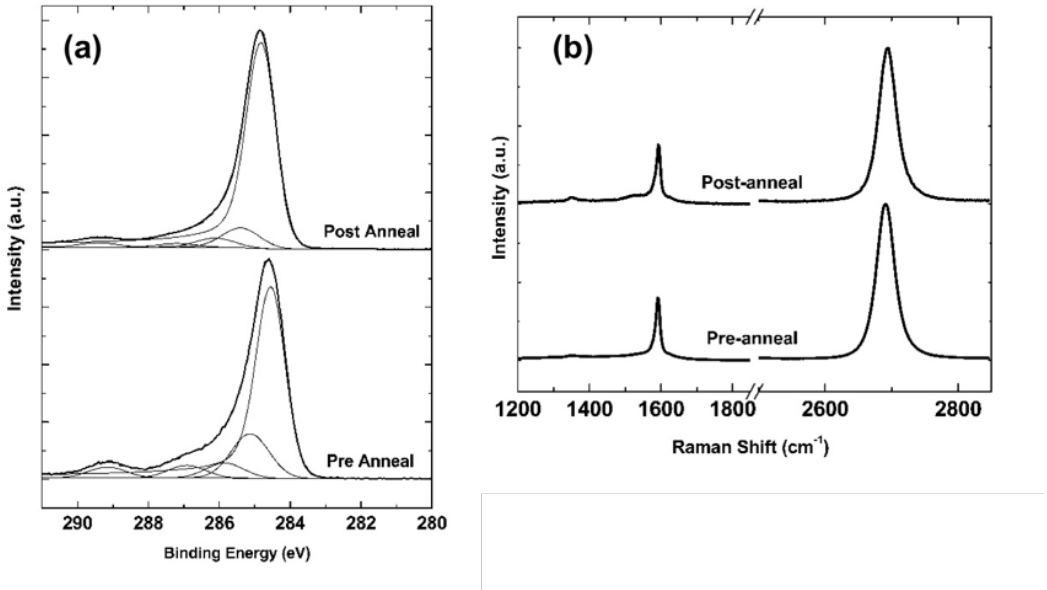

Figure 3.3.2. (a) XPS spectra acquired before and after annealing in UHV where the large peak at 284.8 eV corresponds to graphene and the smaller peaks correspond to different polymer residue species. (b) Raman spectra acquired before and after annealing

Other sources of variability in both the interface and contact chemistry could be related to intrinsic defects in the CVD-grown graphene film or due to other extrinsic effects of transfer process including residual Cu (although no Cu was found within our detection limit), incomplete removal of graphene from the back of the Cu foil, wrinkles and tears in the film, or adsorbates. While measures can be taken to assess the quality and uniformity of the transferred graphene prior to device fabrication, such as characterization with Raman spectroscopy, these defects are inherent to the transfer process and are fundamentally uncontrollable.

3.3.3.2 Effects of Base Pressure on Composition

Base pressure also has a substantial effect which can dominate over deposition rate. The base pressure is a measure of the quantity of residual gases in the chamber. Depositing at higher pressures increases the amount of oxidizing species available for reaction with Ti and low deposition rates increase the impingement rate of Ti relative to that of oxidizing species, resulting in a high coverage of oxidizing species on the surface of the sample which will then react with Ti. This is observed in Figure 3.3.3. To overcome the issue of sample-to-sample variability, each sample represented in Figure 3.3.3 was cut from a single piece graphene/SiO_2 produced in a single transfer. Two out of the three samples were deposited on at the same rate and different base pressures, and two out of three were deposited on at the same base pressure but different rates. In Figure 3.3.3(a), (i) corresponds to a deposition $1x10^{-7}$ Torr and a rate of 0.01 nm/s, (ii) corresponds to a deposition at $1x10^{-7}$ Torr and a rate of 0.1 nm/s and (iii) corresponds to a pressure of $1x10^{-6}$ Torr at a rate of 0.1 nm/s.

The corresponding TLM data for each are shown in Figure 3.3.3(b). Comparison of (i) and (ii) illustrates the effect of deposition rate alone at the same base pressure. As previously discussed, a lower oxide composition results at a faster deposition rate. In (ii) and (iii), we observe the effects

of varying base pressure at the same deposition rate. Depositing at $1x10^{-7}$ Torr yields 25% oxide whereas $1x10^{-6}$ Torr results in 78% oxide. This indicates that base pressure has a substantial effect on oxide composition. These results also show that base pressure has a stronger effect on contact composition than deposition rate, since (i) shows a comparable oxide to (iii). The TLM results corresponding to (i) and (iii) indicate that two samples of similar oxide composition can exhibit markedly different R_C if deposited under different base pressures. It is known that UHV depositions result in cleaner interfaces and improved R_C for unreactive metals like Au.[17] Our comparison of samples processed under lower and higher base pressures show that R_C might be dominated by the composition of the interface rather than the composition of the contact itself. The larger error bars and confidence interval in the TLM data in (iii) are also indicative of greater variability in measured R_C throughout different regions of the sample.

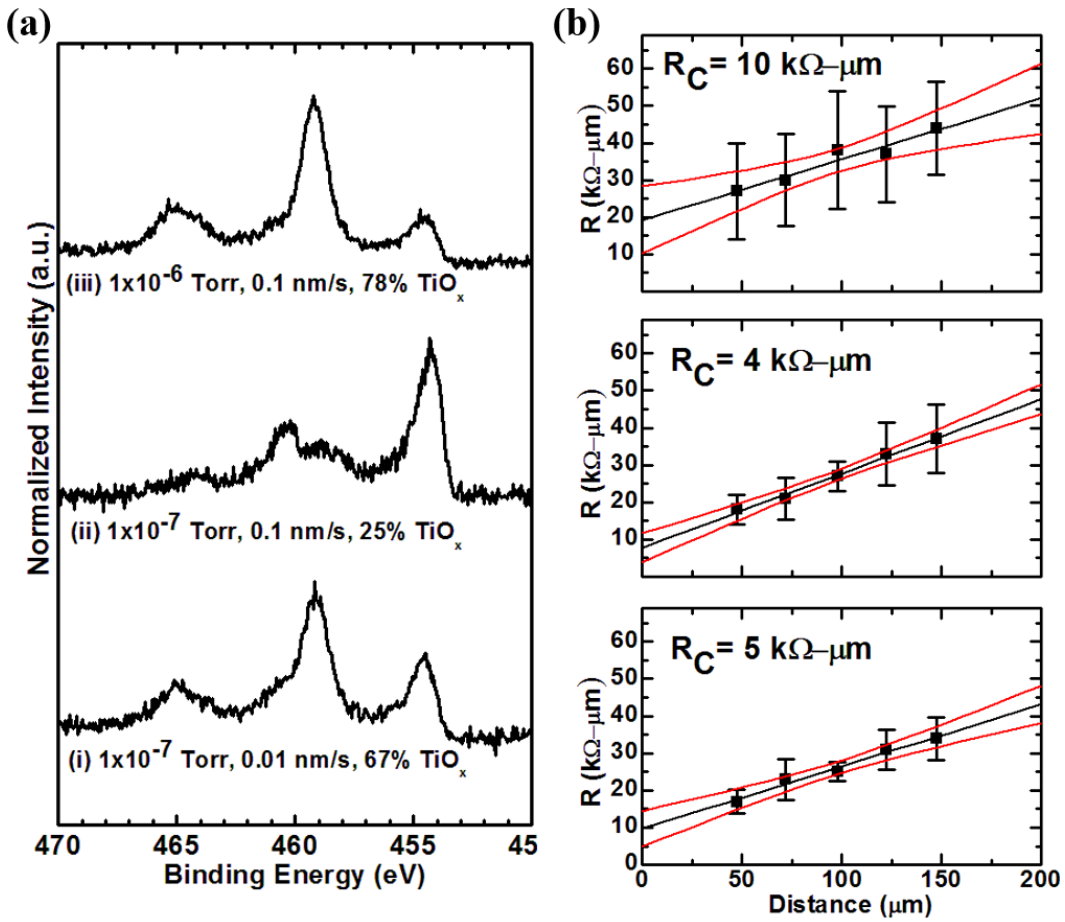

Figure 3.3.3. (a) Ti 2*p* core-level spectra for Ti deposited onto samples cut from a single graphene/SiO_2 sample at different deposition conditions resulting in different oxide compositions. (b) Corresponding TLM results for each sample where black line represents the linear fit and the red lines represent the upper and lower 95% confidence bounds.

3.3.3.3 Effect of Oxide Composition on R_C

We have observed an overall correlation between R_C and the oxide compositions of the contacts shown in Figure 3.3.4. While large sample-to-sample variability is observed, the data has a linear correlation coefficient of 0.7. The extent which there exists a linear correlation between a set of points $(x_1,y_1)\ldots(x_N,y_N)$ is measured by the linear correlation coefficient, r, given by[18]

$$r = \frac{\sigma_{xy}}{\sigma_x \sigma_y} \qquad \text{Equation 3.3}$$

where σ_{xy} is the covariance, and σ_x and σ_y are the standard deviations of *x* and *y*. Eq. 1 can then be written as

$$r = \frac{\sum(x_i - \bar{x})(y_i - \bar{y})}{\sqrt{\sum(x_i - \bar{x})^2 \sum(y_i - \bar{y})^2}} \qquad \text{Equation 3.4}$$

If all points (x_i,y_i) lie exactly on the line $y_i = A + Bx$ then the value of *r* will be ± 1. The quantitative significance of *r* depends on the number of measurements, *N*, which determines the probability that two *uncorrelated* variables will yield a particular value of *r*. This can be applied conversely to determine the probability that a particular value of *r* indicates that two variables are correlated. For the data reported in this work plotted in Figure 3.3.4 of the text, the measurement of oxide composition and R_C on thirteen distinct samples yielded a correlation coefficient of 0.7. By the methods reported in Ref. 18, this represents a 0.8% probability that oxide composition and R_C are uncorrelated. We therefore infer a 99.2% probability that R_C is linearly correlated with oxide composition. This value corresponds to a highly significant probability of linear correlation between oxide composition and R_C. Differences in the cleanliness of the interface observed in Figure 3.3.3 might explain why contacts of similar oxide composition show large variation in R_C as seen in Figure 3.3.4.

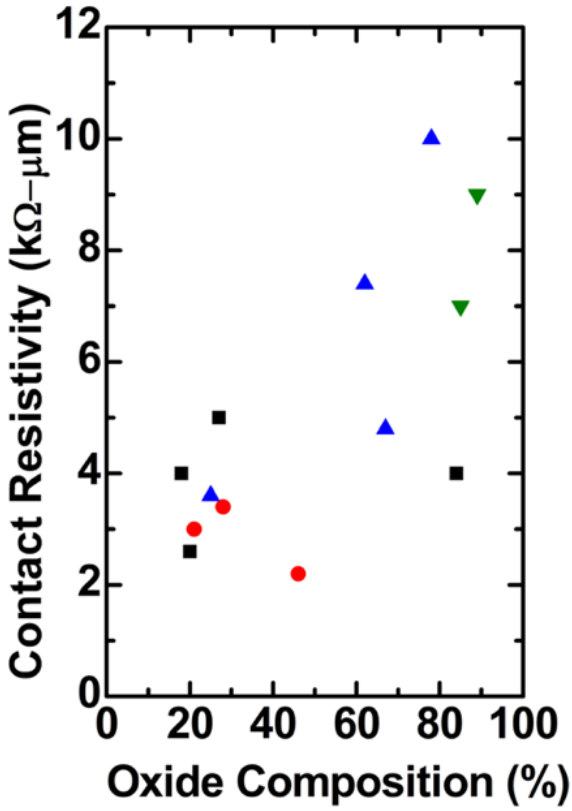

Figure 3.3.4. Plot of width-normalized contact resistivity as a function of oxide composition showing a linear trend with a correlation coefficient of 0.7. Each set of identical markers on the plot corresponds to samples which were cut from the same piece of transferred graphene but processed under different conditions

Despite the inevitable sample-to-sample variability, our results suggest that some degree of control over contact composition is achievable during the deposition process, particularly via deposition rate and base pressure. The overall linear correlation between oxide composition and R_C summarized in Figure 3.3.4 is not surprising given that the electrical resistivity of TiO_2 is orders of magnitude higher than that of metallic Ti.[19] The results presented in Figure 3.3.3 indicate that the cleanliness of the graphene/TiO_x interface, which is affected by the base pressure of the deposition, likely dominates R_C to a greater extent than the oxide composition. While we observe a relationship between deposition rate and oxide composition in Figure 3.3.1, and a correlation between R_C and oxide composition in Figure 3.3.4, it is important to note that deposition rate does

not have a substantial effect on R_C. For example, a difference of 42% in oxide composition can fail to have an appreciate impact on R_C as was shown in Figure 3.3.3. It then follows that oxide composition is not the prevailing factor determining R_C.

3.3.3.4 Effects of Oxide Composition on h_K

The effects of contact processing conditions manifest in thermal transport properties. Figure 3.3.5(a) shows XPS spectra acquired for four samples fabricated with four different deposition rates and (b) shows the corresponding thermal boundary conductance h_K as a function of oxide composition. XPS shows significant oxide composition at the slowest deposition rate of 0.01 nm/s. The oxide composition decreases between 0.01 and 0.1 nm/s. The thermal data indicates that thermal boundary conductance h_K is inversely related to the oxide composition. For the deposition rate of 0.1 nm/s which resulted in the lowest oxide composition, h_K =65±7 MW m^{-2} K^{-1}, whereas for the slowest deposition rate which resulted in the highest oxide composition, h_K =32 ± 3 MW m^{-2} K^{-1}. The values of h_K correspond to Au/SiO_2 interface where the effective interfacial regions between Au and SiO_2 for this analysis is the Ti/graphene layers, as mentioned previously.

The measured value of h_K for the slower deposition rates matches very well with those measured for a similar Au/Ti/graphene/SiO_2 interface deposited at 0.05 nm/s and reported by Koh *et al*.[20] The twofold increase in h_K with the faster deposition rate corresponds to the relative decrease in the oxide composition between the different deposition rates as shown in Figure 3.3.5(a). Thus, a higher oxide composition in the Ti layer at an Au/Ti/graphene/SiO_2 contact leads to a lower h_K (higher resistance) than a lower oxide composition. Stated differently, our results suggest that to minimize the thermal resistance at the Au/Ti/graphene/SiO_2 contact, the Ti should be as metallic as possible. In contrast to thermal transport, electrical transport does not appear to

be as sensitive to the composition of the contact for this particular sample, however the results shown in Figure 3.3.3 indicate that the reactor base pressure does have an impact on R_C.

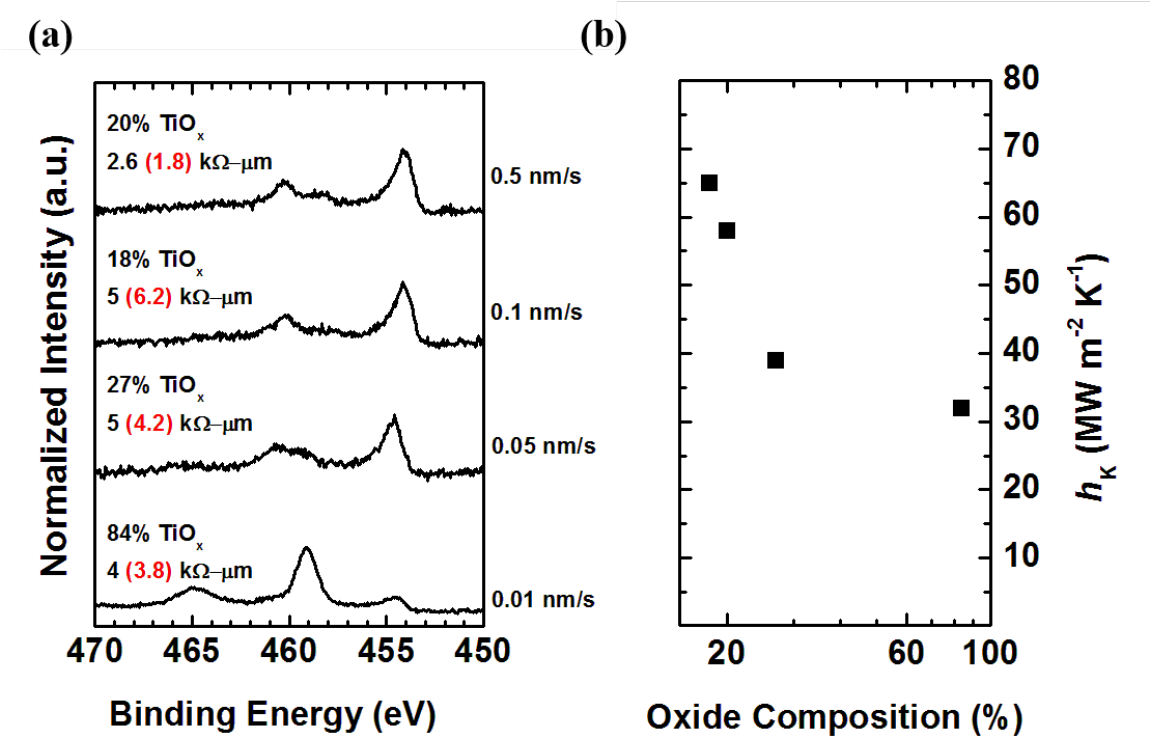

Figure 3.3.5. (a) Ti 2*p* core-level spectra for graphene/SiO_2 deposited at different rates at a base pressure of $1x10^{-7}$ Torr. Values in parenthesis in red were acquired after six months of sample fabrication, indicating that air exposure. (b) Time-domain thermoreflectance data for the same samples as a function of oxide composition.

An in-depth analysis of the thermal transport results was performed by Prof. Hopkins. The value of h_K provides a quantitative metric for the efficacy with which energy is exchanged across interfaces.[21] In practice, these reported values represent the thermal boundary conductance across an Au/SiO_2 contact with contributions from the Ti and graphene layers and contaminant interfaces. These measured Au/SiO_2 thermal boundary conductance values represent a lumped conductance value that accounts for heat flow from the Au, across the Au/Ti interface, through the Ti layer,

across the Ti/Gr interface, and finally across the Gr/SiO_2 interface. Due to the relatively small thicknesses of the Ti and graphene, this Ti/Gr layer is treated as the interfacial layer between the Au and SiO_2, and thus these values for h_K are indicative of the thermal conductance across an Au/SiO2 contact with Ti/Gr in between, consistent with prior TDTR analyses and descriptions on similar systems.[20, 22] The appropriate analysis procedure to measure h_K and the details of the experimental setup are given elsewhere.[23] The specific assumptions in our analysis regarding similar Au/Ti/Gr/SiO_2 systems are outlined in detail in previous work.[22] The possible origins of the change in thermal boundary conductance with change in oxygen content of the Ti layer between the Au and graphene could manifest from various changes in electronic and vibrational scattering and interfacial transport in each layer of the Au/Ti/graphene/SiO_2 boundary region. The major contributors to this change in thermal resistance, $\Delta R = \Delta (1/h_K) \sim 15.9$ m^2 K GW^{-1}, could be the change in h_K at the Au/Ti interface, the change in thermal conductivity of the Ti, and the change in h_K across the Ti/graphene/SiO_2 interface that would occur with a change in oxygen content in the Ti layer. For exemplary purposes we pose the extreme cases in which one would expect the Ti layer to either be fully TiO_2, with a thermal conductivity of ~1.2 W m^{-1} K^{-1}[24] or fully metallic Ti, with a thermal conductivity of ~21.9 W m^{-1} K^{-1}[25] . These cases lead to a change in resistance of this layer as $\Delta R = 5\text{x}10^{-9}/1.2 - 5\text{x}10^{-9}/21.9 \sim 4$ m^2 K GW^{-1}. We note this example calculation considers the extreme case to calculate the maximum hypothetical resistance change of this layer. As is evident, the above calculation for ΔR cannot explain the entire observed change in thermal boundary resistance with different oxygen content in the Ti layer (as previously mentioned, ΔR ~15.9 m^2 K GW^{-1}). We note also that size effects were not considered in this ΔR calculation.[26] Thus, the change in thermal resistance of the Ti layer cannot solely explain the measured changes in thermal boundary conductance.

Another possibility for the observed change in thermal conductance across the Au/Ti/graphene/SiO_2 region is the change in the Ti/graphene/SiO_2 thermal boundary conductance. Our previous work has demonstrated that changes in graphene surface chemistry induced from plasma functionalization (including oxygen functionalization) can lead to appreciable changes in thermal boundary conductance.[22] Thus, one could hypothesize that the change in oxygen stoichiometry in the Ti layer would also lead to changes in how the Ti reacts with residues and thereby lead to changes in the chemistry at the Ti/graphene interface; thus impacting thermal boundary conductance. We note that residual PMMA residue is present on all samples. Therefore it is presumed that all Gr/Ti interfaces will actually be TiO_x/graphene with some variation in the amount of hydrocarbon incorporated.[14] The impact of the variations in hydrocarbon incorporation at the interface on the thermal boundary conductance is unknown and therefore cannot be ruled out as a potential mechanism.

Finally, we consider the change in thermal boundary conductance at the Au/Ti interface as a possible contributor to the measured change in ΔR of the Au/Ti/graphene/SiO_2 interfacial region. At pure metal/metal interfaces, the thermal boundary conductance is driven by the electron density of states at the Fermi energies of the metals[27], and this corresponding thermal boundary conductance can be more than an order of magnitude greater than those at metal/non-metal interfaces.[28] We can assume that the resistance associated with the metallic phase of Ti in contact with the Au will offer negligible resistance as compared to the non-metal oxide phases in the Ti layer. Indeed, typical values for thermal boundary conductances across Au/non-metal interfaces range from ~50 – 100 MW m^{-2} K^{-1},[29-32] limited by the relatively narrow spectral phonon bandwidth in the Au. This corresponds to a ΔR of ~10 – 20 m^2 K GW^{-1}, on the order of our measured change

in thermal boundary conductance with changes in oxygen content in the Ti (ΔR ~15.9 m^2 K GW^{-1}).

We estimate these various electron-electron and phonon-phonon resistances at the Au/Ti layer interface in more quantitative detail through the use of diffuse mismatch models (DMM). As mentioned previously, the electron DMM (eDMM) predicts the thermal boundary conductance between two materials with large electron density of states compared to phonon density of states (e.g., at metal/metal interfaces).[30] Assuming values for the electron density of states at the Fermi energy and calculated Fermi velocities for Au and Ti[33-34], we predict a thermal boundary resistance of $R_{ee,Au/Ti}$ = 0.17 m^2 K GW^{-1} (thermal boundary conductance of 5,970 MW m^{-2} K^{-1} between the electronic systems in Au and Ti, assuming both are pure metals). This eDMM calculation thus predicts the thermal transport across the Au/Ti interface in the case when Ti is fully metallic. When the Ti layer is oxidized, this electron-electron interfacial thermal transport pathway will be reduced, and thus the Au phonon/Ti phonon interfacial thermal transport pathway can become a dominant conductance, since the electronic densities of states of the TiO_x regions of the adhesion layer will be greatly reduced compared to the metallic Ti regions. Thus, we quantify this phonon-phonon thermal boundary resistance using the traditionally implemented phonon DMM (pDMM).[21] We calculate the phonon-phonon thermal boundary resistance of two cases: Au/Ti and Au/TiO_2 (rutile). In our pDMM calculations, we assume sine-type phonon dispersions of the longitudinal and two degenerate transverse acoustic modes in each material with zone edge phonon frequencies taken from Ref. 35 for Au ($\Gamma \rightarrow$X direction), Ref. 36 for Ti ($\Gamma \rightarrow$A direction), and Ref. 37 for rutile ($\Gamma \rightarrow$A direction). From this, we predict phonon-phonon thermal boundary resistances of $R_{pp,Au/Ti}$ = 6.17 m^2 K GW^{-1} ($h_{K,pp,Au/Ti}$ = 162 MW m^{-2} K^{-1}) and $R_{pp,Au/TiO2}$ = 6.76 m^2 K GW^{-1} ($h_{K,pp,Au/TiO2}$ = 148 MW m^{-2} K^{-1}) for the Au/Ti and Au/TiO_2, respectively. Based on these

eDMM and pDMM calculations, the predicted change in thermal boundary resistance associated with the change from a metal/metal Au/Ti interface (electron-electron) to a metal/non-metal Au/Ti (Au/TiO_2) interface (phonon-phonon) as ΔR = 6.0 m^2 K GW^{-1} (6.6 m^2 K GW^{-1}). While this calculation of ΔR is slightly lower than our observed change in thermal boundary resistance across the Au/Ti/graphene/SiO_2 interfaces (ΔR ~15.9 m^2 K GW^{-1}), we caution that the assumptions required for DMM predictions could lead to uncertainties in these predicted values. Regardless, a clear change in Au/Ti thermal boundary conductance will occur when the interfacial transport transitions from an electron to phonon dominated process.

These simple qualitative and quantitative analyses suggest that the changes in thermal boundary conductance across the Au/Ti/graphene/SiO_2 boundary originate from changes in resistance at the Au/Ti interface and possible additional changes in thermal conductivity in the Ti layer. However, much more work needs to be pursued to study this precise interface in more detail and to understand the fundamental electron and phonon scattering mechanisms driving this thermal transport process with respect to changes in oxygen chemistry. This points to the future promise of manipulating metal/metal contacts through metal type and chemistry to impact the thermal resistances of graphene devices.

3.3.4 Conclusion and Future Work

This work sheds light on the inherent variability in graphene devices. By attempting to correlate deposition conditions with the contact composition and contact resistance, we have found that contact resistance is sensitive to the partial pressure during contact deposition, and that the oxide of a Ti contact can strongly impact the thermal boundary conductance. It should be noted that reactor pressure and deposition rate are not parameters that are typically reported when describing device fabrication and yet this work demonstrates that both clearly affect device

properties. The relationship between interface chemistry and contact resistance as well as thermal transport opens doors for interface engineering. The data indicates that conditions which minimize the adsorption of oxidizing species on the substrate, low base pressure and fast deposition rate, result in lower electrical and thermal contact resistance, respectively. Directions for future work are discussed below.

3.3.4.1 Transport Properties of UHV-Deposited Contacts

The results of Chapter 3.2 provide evidence of electronic coupling at the Ti/graphene interface deposited in UHV, and the results of Chapter 3.3 suggest that UHV deposition conditions might be optimal for achieving low R_C and high h_K. Therefore, future work should examine electronic and thermal transport properties of UHV-deposited contacts. For measurements of R_C, it will be necessary to transfer the CVD graphene onto SiO_2. A polymer free transfer process[12, 38] could be used in order to keep the interface as clean as possible. Alternatively, a PMMA-aided process could be performed with UHV metal deposition to in order to study the effect of variations in hydrocarbon incorporation at the interface on transport properties in the absence of other sources of oxide.

3.3.4.2 Deposition Conditions and Contact Morphology

Another topic for future study is the effect of contact deposition conditions on contact morphology, and subsequent effects on transport properties. Our study in Chapter 3.3 accounts for the effect of deposition rate on the chemistry of the interface, however, deposition rate likely also affects morphological properties such grain size and roughness. While comparing the performance of different metal contacts to graphene (all deposited under the same HV conditions at the same deposition rate and thickness), Watanabe *et al*.[39] have found that grain size was a more important factor than metal work function in determining R_C. Metals which yielded low values of R_C

(including Ti) had small grain size and high uniformity, whereas metals which resulted in high R_C exhibited large, non-uniform grains. This work suggests that R_C and h_K are likely also affected by the morphology of contact. Future experiments can utilize transmission electron microscopy and atomic force microscopy to examine the microstructure of the metal/graphene interface and the surface topography of the contact, respectively, for Ti contacts deposited under different deposition conditions.

3.3.5 References

1. Gong, C.; Lee, G.; Shan, B.; Vogel, E. M.; Wallace, R. M.; Cho, K., First-principles study of metal–graphene interfaces. *Journal of Applied Physics* **2010,** *108* (12), 123711.
2. McDonnell, S.; Smyth, C.; Hinkle, C. L.; Wallace, R. M., MoS2–Titanium Contact Interface Reactions. *ACS Applied Materials & Interfaces* **2016,** *8* (12), 8289-8294.
3. Li, X.; Zhu, Y.; Cai, W.; Borysiak, M.; Han, B.; Chen, D.; Piner, R. D.; Colombo, L.; Ruoff, R. S., Transfer of Large-Area Graphene Films for High-Performance Transparent Conductive Electrodes. *Nano Letters* **2009,** *9* (12), 4359-4363.
4. Gahoi, A.; Wagner, S.; Bablich, A.; Kataria, S.; Passi, V.; Lemme, M. C., Contact resistance study of various metal electrodes with CVD graphene. *Solid-State Electronics* **2016,** *125*, 234-239.
5. Xia, F.; Perebeinos, V.; Lin, Y.-m.; Wu, Y.; Avouris, P., The origins and limits of metal-graphene junction resistance. *Nat Nano* **2011,** *6* (3), 179-184.
6. Moon, J. S.; Antcliffe, M.; Seo, H. C.; Curtis, D.; Lin, S.; Schmitz, A.; Milosavljevic, I.; Kiselev, A. A.; Ross, R. S.; Gaskill, D. K.; Campbell, P. M.; Fitch, R. C.; Lee, K. M.; Asbeck, P., Ultra-low resistance ohmic contacts in graphene field effect transistors. *Applied Physics Letters* **2012,** *100* (20), 203512.
7. Venugopal, A.; Colombo, L.; Vogel, E. M., Contact resistance in few and multilayer graphene devices. *Applied Physics Letters* **2010,** *96* (1), 013512.
8. McCreery, R.; Dieringer, J.; Solak, A. O.; Snyder, B.; Nowak, A. M.; McGovern, W. R.; DuVall, S., Molecular Rectification and Conductance Switching in Carbon-Based Molecular Junctions by Structural Rearrangement Accompanying Electron Injection [J. Am. Chem. Soc. 2003, 125, 10748−10758]. . *Journal of the American Chemical Society* **2004,** *126* (19), 6200-6200.
9. McGovern, W. R.; Anariba, F.; McCreery, R. L., Importance of oxides in carbon/molecule/metal molecular junctions with titanium and copper top contacts. *J. Electrochem. Soc.* **2005,** *152* (5), E176-E183.
10. Pirkle, A.; Chan, J.; Venugopal, A.; Hinojos, D.; Magnuson, C. W.; McDonnell, S.; Colombo, L.; Vogel, E. M.; Ruoff, R. S.; Wallace, R. M., The effect of chemical residues on the physical and electrical properties of chemical vapor deposited graphene transferred to SiO2. *Applied Physics Letters* **2011,** *99* (12), 122108.
11. Lin, Y. C.; Lu, C. C.; Yeh, C. H.; Jin, C.; Suenaga, K.; Chiu, P. W., Graphene annealing: how clean can it be? *Nano Lett* **2012,** *12* (1), 414-9.
12. Lee, J. e. a., Clean transfer of graphene and its effect on contact resistance. *Applied Physics Letters* **2013,** *103* (10), 103104.
13. Toriumi, A.; Nagashio, K., Metal Contacts to Graphene. *2D Materials for Nanoelectronics* **2016,** *17*, 53.
14. Joiner, C. A.; Roy, T.; Hesabi, Z. R.; Chakrabarti, B.; Vogel, E. M., Cleaning graphene with a titanium sacrificial layer. *Applied Physics Letters* **2014,** *104* (22), 223109.
15. Gong, C.; Floresca, H. C.; Hinojos, D.; McDonnell, S.; Qin, X.; Hao, Y.; Jandhyala, S.; Mordi, G.; Kim, J.; Colombo, L.; Ruoff, R. S.; Kim, M. J.; Cho, K.; Wallace, R. M.; Chabal, Y. J., Rapid Selective Etching of PMMA Residues from Transferred Graphene by Carbon Dioxide. *The Journal of Physical Chemistry C* **2013,** *117* (44), 23000-23008.
16. Hong, J.; Park, M. K.; Lee, E. J.; Lee, D.; Hwang, D. S.; Ryu, S., Origin of new broad Raman D and G peaks in annealed graphene. *Scientific reports* **2013,** *3*, 2700.

17. English, C. D.; Shine, G.; Dorgan, V. E.; Saraswat, K. C.; Pop, E., Improved Contacts to MoS2 Transistors by Ultra-High Vacuum Metal Deposition. *Nano Letters* **2016,** *16* (6), 3824-3830.
18. Taylor, J. R., *Introduction To Error Analysis: The Study of Uncertainties in Physical Measurements*. University Science Books: 1997.
19. Haynes, W. M., *CRC Handbook of Chemistry and Physics, 92nd Edition*. CRC Press: 2011.
20. Koh, Y. K.; Bae, M.-H.; Cahill, D. G.; Pop, E., Heat Conduction across Monolayer and Few-Layer Graphenes. *Nano Letters* **2010,** *10* (11), 4363-4368.
21. Swartz, E. T.; Pohl, R. O., Thermal boundary resistance. *Reviews of Modern Physics* **1989,** *61* (3), 605-668.
22. Foley, B. M.; Hernández, S. C.; Duda, J. C.; Robinson, J. T.; Walton, S. G.; Hopkins, P. E., Modifying Surface Energy of Graphene via Plasma-Based Chemical Functionalization to Tune Thermal and Electrical Transport at Metal Interfaces. *Nano Letters* **2015,** *15* (8), 4876-4882.
23. Hopkins, P. E.; Serrano, J. R.; Phinney, L. M.; Kearney, S. P.; Grasser, T. W.; Harris, C. T., Criteria for Cross-Plane Dominated Thermal Transport in Multilayer Thin Film Systems During Modulated Laser Heating. *Journal of Heat Transfer* **2010,** *132* (8), 081302-081302.
24. Hopkins, P. E.; Mittal, M.; Phinney, L. M.; Grillet, A. M.; Furst, E. M., Ultra-low thermal conductivity of ellipsoidal TiO2 nanoparticle films. *Applied Physics Letters* **2011,** *99* (13), 133106.
25. Lide, D. R., CRC Handbook for Chemistry and Physics, 89th edition. **2008**.
26. Chen, G., *Nanoscale Energy Transport and Conversion: A Parallel Treatment of Electrons, Molecules, Phonons, and Photons*. Oxford University Press: 2005.
27. Giri, A.; Gaskins, J. T.; Donovan, B. F.; Szwejkowski, C.; Warzoha, R. J.; Rodriguez, M. A.; Ihlefeld, J.; Hopkins, P. E., Mechanisms of nonequilibrium electron-phonon coupling and thermal conductance at interfaces. *Journal of Applied Physics* **2015,** *117* (10), 105105.
28. Hopkins, P. E., Thermal transport across solid interfaces with nanoscale imperfections: effects of roughness, disorder, dislocations, and bonding on thermal boundary conductance. *ISRN Mechanical Engineering* **2013,** *2013*.
29. Duda, J. C.; Yang, C. Y. P.; Foley, B. M.; Cheaito, R.; Medlin, D. L.; Jones, R. E.; Hopkins, P. E., Influence of interfacial properties on thermal transport at gold:silicon contacts. *Applied Physics Letters* **2013,** *102* (8), 081902.
30. Cheaito, R.; Hattar, K.; Gaskins, J. T.; Yadav, A. K.; Duda, J. C.; Beechem, T. E.; Ihlefeld, J. F.; Piekos, E. S.; Baldwin, J. K.; Misra, A., Thermal flux limited electron Kapitza conductance in copper-niobium multilayers. *Applied Physics Letters* **2015,** *106* (9), 093114.
31. Oh, D. W.; Kim, S.; Rogers, J. A.; Cahill, D. G.; Sinha, S., Interfacial Thermal Conductance of Transfer-Printed Metal Films. *Advanced Materials* **2011,** *23* (43), 5028-5033.
32. Donovan, B. F.; Szwejkowski, C. J.; Duda, J. C.; Cheaito, R.; Gaskins, J. T.; Peter Yang, C. Y.; Constantin, C.; Jones, R. E.; Hopkins, P. E., Thermal boundary conductance across metal-gallium nitride interfaces from 80 to 450 K. *Applied Physics Letters* **2014,** *105* (20), 203502.
33. Lin, Z.; Zhigilei, L. V.; Celli, V., Electron-phonon coupling and electron heat capacity of metals under conditions of strong electron-phonon nonequilibrium. *Physical Review B* **2008,** *77* (7), 075133.
34. Jafari, M.; Jahandoost, A.; Vaezzadeh, M.; Zarifi, N., Effect of pressure on the electronic structure of hcp Titanium. *arXiv preprint arXiv:1107.3948* **2011**.
35. Lynn, J.; Smith, H.; Nicklow, R., Lattice dynamics of gold. *Physical Review B* **1973,** *8* (8), 3493.

36. Stassis, C.; Arch, D.; Harmon, B.; Wakabayashi, N., Lattice dynamics of hcp Ti. *Physical Review B* **1979,** *19* (1), 181.
37. Mei, Z.-G.; Wang, Y.; Shang, S.-L.; Liu, Z.-K., First-principles study of lattice dynamics and thermodynamics of TiO2 polymorphs. *Inorganic chemistry* **2011,** *50* (15), 6996-7003.
38. Zhang, G.; Güell, A. G.; Kirkman, P. M.; Lazenby, R. A.; Miller, T. S.; Unwin, P. R., Versatile Polymer-Free Graphene Transfer Method and Applications. *ACS Applied Materials & Interfaces* **2016,** *8* (12), 8008-8016.
39. Watanabe, E.; Conwill, A.; Tsuya, D.; Koide, Y., Low contact resistance metals for graphene based devices. *Diamond and Related Materials* **2012,** *24*, 171-174.

4 TRANSITION METAL DICHALCOGENIDES

4.1 Introduction

4.1.1 Properties, Processing, and Applications

Layered transition metal dichalcogenides (TMDs) are materials with the composition MX_2 where M is a transition metal such as Mo, W, Sn, Hf, or Zr and X is a chalcogen such as S, Se, or Te. Compounds which form layered TMD structures are shown in Figure 3.1.1(a). This part of the dissertation will focus on 2H-MoS_2 with work on 2H-WSe_2 in Chapter 3.3. In a monolayer of a layered TMD, the metal is covalently bonded to the chalcogen atoms on either side of it, yielding a X-M-X sandwich structure.[1-2] Like in graphite, the bonding between layers is characterized as a weak van der Waals interaction. MoS_2 and WSe_2 occur in different polymorphs: hexagonal (2H), rhomboheral (3R), trigonal (1T), and distorted 1T (1T').[3] The semiconducting 2H phase is the most stable and most commonly observed in geological and synthetic MoS_2 and WSe_2, however other phases can be synthesized and stabilized via methods such as metal intercalation, electron beam irradiation, and strain engineering.[3-4] In the 2H polytype, the metal coordination is trigonal prismatic.[1] The in-plane and out-of-plane lattice parameters are, respectively, 3.16 and 12.3 Å for MoS_2 and 3.29 and 12.95 Å for WSe_2.[5-7] The red rhombi in Figure 3.1.1(c) represent the primitive unit cells of both materials.

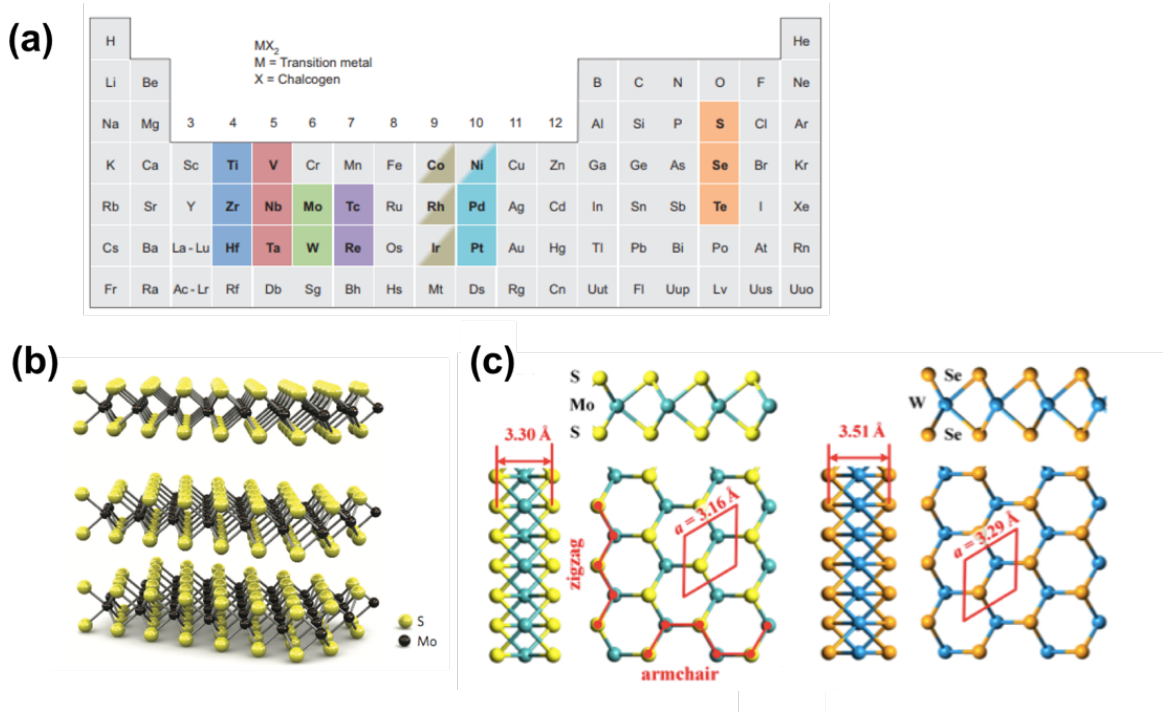

Figure 4.1.1. (a) Periodic table showing the transition metals and chalcogen elements that crystallize in layered structures. The partially highlighted elements are those which form layered structured with only some of the chalcogenides. For example, $NiTe_2$ is layered whereas NiS_2 is not. Adapted from Ref. 1. (b) Structure of 2H-MoS_2, representative of the structure of layered TMDs, adapted from Ref. 8. (c) Three views of the lattice structures of 2H-MoS_2 and WSe_2, adapted from Ref. 7.

For the fabrication of TMD-based devices and for the study of fundamental material properties, geological material is frequently used.[8-13] Geological material can be exfoliated mechanically to produce thin or monolayer flakes via scotch tape or by liquid-phase exfoliation using sonication in solvents or ion intercalation.[14-16] These are the same types of procedures applied to isolate graphene from HOPG. Like with graphene, exfoliation of geological TMD crystals is not suitable for the large-scale development of TMD devices given the low yield and poor control over size and thickness. Exfoliation of flakes of on the order of 10 mm^2 has been demonstrated[17], however

there will always be a fundamental limit due to the crystal size itself. Geological MoS_2 has been found to have a high concentration of impurities and other defects such as S vacancies, Mo-rich metallic clusters and other impurities as well as spatial variation of n- or p-type conductivities.[18-20] Methods of synthesizing TMDs include chemical vapor deposition (CVD)[21-24], molecular beam epitaxy (MBE)[25-31], chemical bath deposition[32-33], chemical vapor transport[34-35]. Synthetic routes to TMDs offer not only potential for large scale processing but also improved control over impurities, stoichiometry, defects, and doping. Geological, CVD, and MBE materials are employed in this work and the procedures are discussed in detail in Chapter 2.2.

The electronic and optical properties of TMDs evolve as a function of the number of layers.[36] Bulk MoS_2, for example, has an indirect band gap of 1.29 eV. The band gap increases with thickness to a direct band gap of approximately 1.90 eV for a monolayer of material.[36-37] A similar indirect-to-direct gap crossover is expected for all MoX_2 and WX_2 compounds in the semiconducting 2H phase spanning a range of band gap energies from 1.1 eV in the bulk to 1.9 eV in the monolayer.[38-41] This phenomenon occurs due to quantum confinement and the change in hybridization between the p_z orbitals on the chalcogen atoms and the *d* orbitals of the metal atoms.[41] Since the band gap of both bulk and monolayer material is close to that of conventional semiconductors such as Si and GaAs (1.1-1.45 eV), TMDs are suitable for use in digital transistors as well as optoelectronics. MoS_2 transistors are predicted to exhibit ON/OFF ratios > 10^{10}.[42] The highest reported value to date is 2.6×10^9.[43] The ability to achieve high ON/OFF ratios with TMDs presents a major advantage over graphene, whose lack of a band gap results in a very poor ON/OFF ratio despite a high ON current.[44]

TMDs are particularly appealing for transistor applications due to the ability to achieve extremely thin channels. The thinness of the material leads to superior gate control over the channel

by reducing short channel effects.[45] Electrostatic control of the channel charge by the gate has been regarded as the biggest challenge in scaling silicon and III-V MOSFETs.[46] One example of a short channel effect is drain-induced barrier lowering (DIBL). This occurs when the threshold voltage of the channel becomes dependent on the bias applied to the drain due to poor electrostatic shielding at short channel lengths. Liu *et al.*[47] demonstrate a factor of 2 difference in DIBL between a 12 nm thick flake and a 5 nm thick flake of MoS_2 at a channel length of 50 nm. Yoon *et al.*[42] calculate that for monolayer MoS_2 with a channel length of 75 nm, DIBL can reach values as low as 10 mV/V while simultaneously realizing the ideal value of ~60 mV/decade for MOSFET subthreshold swing, a measure of the gate voltage required to change the drain current but an order of magnitude.[48] Furthermore, non-classical transistor designs such as tunnel-FETs[48-50]and nonplanar geometries such as FinFETs[51] present an opportunity for further enhancing subthreshold characteristics, making TMDs suitable for low power operation.

Despite the promise of overcoming short channel effects, TMDs present a disadvantage for high speed digital logic applications due to their low carrier mobility, which decreases from the bulk to monolayer scale.[52] The room temperature mobility for bulk MoS_2 is 200-500 $cm^2 V^{-1} s^{-1}$ and the exfoliation of single layers of geological MoS_2 onto a SiO_2 substrate decreases this value to 0.1-10 $cm^2 V^{-1} s^{-1}$.[8, 53]. Bulk WSe_2 has an intrinsic hole mobility of up to 500 $cm^2 V^{-1} s^{-1}$.[54] Due to the weak screening of charge carriers in TMDs, mobility of carriers is highly sensitive to its dielectric environment.[55] The deposition of a high-k dielectric suppresses Coulomb scattering at charged impurities and has been found to result in an improvement in mobility in monolayer MoS_2, yielding values of 150- 200 $cm^2 V^{-1} s^{-1}$ [52, 56-57] Mobility improvements with high k-dielectrics have been demonstrated in graphene[58] and GaAs[59] as well. Synthetic MoS_2 exhibits electron mobility values on the order of ~ 10 $cm^2 V^{-1} s^{-1}$.[60] The theoretical phonon-limited electron mobility of

monolayer MoS_2 at room temperature is 410 $cm^2 V^{-1} s^{-1}$.[52, 61] Similar values are expected for other layered TMDs yet experimental values are typically 5 times lower.[55]

The values of mobility achieved with TMDs are low in comparison to Si (~1000 $cm^2 V^{-1} s^{-1}$) and extremely low in comparison with III-V semiconductors such as GaAs (~7000 $cm^2 V^{-1} s^{-1}$) or InSb (~12000 $cm^2 V^{-1} s^{-1}$).[46] It has been suggested that measured values of mobility are underestimated due to the effects of contact resistance.[10, 62-63] While TMDs are unlikely to compete with III-V devices for high performance applications, their potential in the field of low power electronics is widely recognized.[42, 49-50, 64] Furthermore, due to their band gap energies corresponding to visible light, TMDs are useful for applications in optoelectronics.[65] Tsai *et al.*[66] have reported a type II heterojunction solar cell with monolayer MoS_2/p-Si with an efficiency of 5.23%, showing the ability to integrate TMDs with existing Si technology. More recently, a WSe_2/MoS_2 heterostructure solar with 10% efficiency has been achieved.[67] A number of highly responsive TMD-based photodetectors have also been demonstrated, [68-72] as well as a variety of flexible electronic and optoelectronic devices.[73-75]

Applications in thermoelectric energy conversion have also been suggested.[76-81]. Due to the weak coupling between the 2D layers in TMDs, the materials exhibit low thermal conductivity in the cross-plane direction. Disordered WSe_2 has been found to exhibit the smallest thermal conductivity ever observed in condensed matter, a value of 0.05 W m^{-1} K^{-1} reported by Chiritescu *et al*.[82] Low thermal conductivity in the cross-plane direction allows there to be a large temperature gradient across a layered stack of TMDs sandwiched between two metal contacts, resulting in a large voltage difference via the Seebeck effect, which will be explained in more detail in Chapter 4.4. On the order of 10 nm thickness, electron and phonon transport is ballistic and the power generation mechanism is said to be thermionic rather than thermoelectric.[77, 81, 83] Optimization of

the generated power relies on efficient transport of electrons through the contacts as well as low thermal boundary conductance and good thermal stability at the TMD/metal contact.

In summary, TMDs present a number of unique electronic and optical properties which make them scientifically remarkable while also useful for a range of applications including nanoscale low power electronics, photodetectors, and renewable energy technology including solar and thermoelectric. The focus of the work presented in Part 4 of this dissertation is not specific to a single type of TMD device or application. Instead it is meant to address gaps in the present understanding of the metal/TMD interfaces which exist in all devices that are dependent on the flow of current and heat for optimal operation and reliability. It is widely accepted that contact interface is the dominant performance limiting factor for TMD transistors at short channel lengths[47, 63, 84], and as mentioned previously, high electrical contact resistance is thought to skew measured values of carrier mobility.[10, 62-63] The metal/TMD interface plays a key role in the response speed of phototransistors[71], in the performance of solar cells[73], in the thermoelectric figure of merit[77], and in thermal management.[85] A review of relevant literature on the metal/TMD interface is presented in the following section along with an overview of the experimental work reported in the following chapters.

4.1.2 Metal/TMD Interfaces

4.1.2.1 Electrical Contacts: The Role of Processing and Interface Chemistry

The study of metal/TMD interfaces has been largely motivated by the goal of achieving Ohmic or low resistance contacts for electronic devices. While measurements of electrical contact resistance are not performed in Part 4 of this work, a discussion of electronic properties of metal/TMD contacts provides a context for characterization of metal/TMD interface chemistry. A conventional approach to low resistance contacts stems from the Schottky Mott model, which

predicts that the height of the barrier for electron injection is dependent on the degree of band bending at the metal/semiconductor interface.[19, 86] This is quantified by the absolute value of the difference between the work function of the metal and that of the semiconductor.[87] For an n-type semiconductor, the condition for an Ohmic contact is that the work function of the metal be less than that of the semiconductor. This means that that the charge induced in the semiconductor when the Fermi levels align upon contact is provided by the majority carriers.[88] When the work function of the metal is greater than that of the semiconductor, a Schottky barrier is formed leading to a higher resistance contact. Based on the Schottky Mott model, metal contacts should be chosen based on work function to meet the condition for Ohmic contact. Given the propensity of MoS_2 for n-type doping[89], the ideal candidate contact based on this model would therefore be a low work function metal. WSe_2 is more likely to exhibit p-type doping[90] which would make high work function metals preferable for Ohmic contact. Low work function metals include Ti (4.3 eV)[10, 91], In (4.1 eV)[7], Mo (4.5 eV)[92], Cr (4.5 eV)[91], and Sc (3.5 eV)[10] may seem to be favorable candidates.[7, 55] High work function metals include Ni (5.0 eV)[10], Pt (5.9 - 6.1eV)[10, 93], Au (5.4 - 5.7 eV)[10, 93], Pd (5.6 eV)[7].

It has been experimentally observed that metal/MoS_2 interfaces rarely adhere to the behavior predicted by the Schottky Mott model.[9-10, 84, 91, 93] In other words, contact behavior (Ohmic vs. Schottky or n-type vs. p-type) is found to be not entirely dependent of the work function difference between the semiconductor and the metal. For example, in the first report of a MoS_2 based transistor, Radisavljevic *et al.*[8] report Ohmic behavior for Au contacts to n-type MoS_2. Given the high work function of Au, this result is surprising. Similarly, Das *et al.*[10] show that while the Fermi levels of Ni and Pt are expected to line up close to the valence band of MoS_2 resulting in p-type conduction, FETs produced with these contact metals exhibited n-type characteristics.

Kaushik *et al*.[94] observe the same n-type behavior for devices contacted with Au and Pd. Fontana *et al.*[13] show that Pd can form a p-type contact in agreement with Schottky Mott model, while Au forms an n-type contact in agreement with the results of others.

It is apparent that two types of discrepancies exist in the literature concerning the electronic properties of metal/TMD contacts. The first, as stated previously, is the deviation of experimental results from the Schottky Mott model. The model assumes that the two materials maintain their intrinsic properties upon contact. Given the absence of dangling bonds on the surface of TMDs, they were believed to be chemically inert exhibiting minimal interactions with a metal overlayer.[95] This is in contrast with conventional semiconductors, like Si or III-Vs, which have surface dangling bonds that result in the formation of defect-induced or metal-induced gap states that pin the Fermi level.[96-97] Gong *et al.*[93] suggest that in metal/MoS_2 contacts dipoles formed at the interface modify the metal work function, and that the S-Mo bonding is weakened by the adsorbed metal leading to the formation of states in the band gap of MoS_2. McDonnell *et al.*[19] show that the presence of defects in geological MoS_2, specifically Mo-rich clusters, are a likely explanation for the effective lowering of the Schottky barrier height in MoS_2. These defects provide parallel conduction paths for the electrons and manifest in the measurement of low electron Schottky barrier contacts with high work function metals such as Au. Additionally, a number of low work function metals including Ti, Mn, Ir, Sc, and Cr have been found to react with TMDs.[12, 98-102] Reaction products can also result in the creation of states in the TMD band gap which pin the Fermi level.[12] Ultimately, the deviation from the Schottky Mott model is the result of different chemical and electronic interactions that occur at the metal/TMD interface.

The second discrepancy in contact behavior is that which is found between different reports in the literature studying the same metal/TMD systems. One such example already mentioned is

the n-type conduction observed by Kaushik *et al*. and the p-type conduction reported by Fontana *et al*. for Pd/MoS_2 contacts. Similarly, English *et al*. report that Ti contacts behave worse than Ni contacts whereas Das *et al*. report the opposite. We note that the key finding in the paper by English *et al*. is that Au contacts deposited in UHV (~10^{-9} Torr) exhibit contact resistance that is three times less than that of Au contacts deposited in HV (~10^{-6} Torr). This illustrates that two seemingly identical metal/TMD systems can exhibit different electronic properties due to different processing conditions, highlighting the important role of processing in interface properties that are often discussed in the literature as solely material-dependent. Processing effects also explain deviations between theory and experiment. For example, Chaung *et al.* show that MoO_x contacts to p-type MoS_2 and p-type WSe_2 exhibit Schottky barriers.[103] McDonnell *et al*. note that this deviates from band alignment calculations which predict Ohmic behavior.[104] The disagreement is attributed to the deposition of MoO_x in HV, where the deposition results in a higher concentration of carbon in the film yielding a lower MoO_x work function.

Other investigations published by McDonnell *et al*.[101] and Smyth *et al.*[12, 102, 105] demonstrate that the base pressure during contact deposition, a process parameter that is typically unreported in device papers, has a measurable impact on the chemistry of the interface. In addition to affecting the concentration of carbon in the metal film or at the interface, the base pressure determines which chemical states will be present at the metal/TMD interface. In the case of Ti, for example, the presence of oxygen in HV deposition chambers prevents chemical reactions between Ti and MoS_2 as Ti instead reacts with oxygen species to form TiO_2.[101] In HV deposition of metals on WSe_2, WO_x is found to form at the contact interface with Au, Cr, and Ir, whereas no oxidation of the film is observed in UHV.[12] Cr and Ir react to form Cr-Se and Ir-Se chemical states in both HV and UHV on both MoS_2 and WSe_2 substrates, unlike Ti which reacts with MoS_2 only in UHV.

As mentioned, reactions can contribute to Fermi level pinning, which dominates the behavior of the contact. These findings emphasize that an understanding of the effects of process conditions on interface chemistry is essential for understanding device behavior. Furthermore, achieving control over interface chemistry can be leveraged for property engineering.[105]

4.1.2.2 Control of Interface and Surface Chemistry

The ability to tune interface chemistry via deliberate processing steps is central to the work presented in this part of the dissertation. The processing steps which we address are briefly discussed here. One route to controlling interface chemistry is through post-deposition contact annealing which is explored in Chapter 4.2. Annealing the device after contact deposition is common practice in device processing and notable changes in device transport properties after annealing have been observed. [9, 11, 105-107] English *et al.* report that post-deposition annealing reduces hysteresis and stabilizes electrical measurements for Au contacted FETs.[9] Baugher *et al.* claim that vacuum annealing of devices with Ti/Au contacts eliminated all Schottky behavior.[11] Abraham and Mohney observe decreased contact resistance by rapid thermal annealing of MoS_2 FETs with Ag contacts. [106] The improvement is speculated to be due to the diffusion of Ag into MoS_2, resulting in local doping under the contact. Liu *et al.*[108] show a current improvement of two order of magnitude after vacuum annealing WS_2 FETs with Ti/Au contacts, stating that annealing enhances contact adhesion. In all of the examples mentioned, chemical characterization of the interface is lacking while the observed improvements are almost certainly correlated with change in interface chemistry. Recently, Smyth *et al.*[105] reported substantial improvement after annealing WSe_2 FETs contacted with Pd. They find that annealing Pd/WSe_2 in forming gas at 400 ºC drives the formation of $PdSe_x$ which results in Ohmic band alignment. They also note that annealing in UHV results in a smaller composition of $PdSe_x$ and a higher Schottky barrier in comparison with

annealing in forming gas. It is clear that, like contact deposition annealing, post-deposition annealing conditions also play an important role in determining contact properties. Chemical characterization of as-deposited and annealed metal/TMD interfaces is largely lacking in the literature.

A second method for control of interface chemistry is through an opposite approach. Instead of promoting contact adhesion, diffusion, and chemical reactions via annealing, the metal contact is decoupled from the TMD via an interfacial oxide layer. Improvements in electrical contact resistance, device stability, on-current, and mobility via this method using Ti/TiO_2 contacts have been demonstrated in a number of publications.[109-112] The success of the interfacial oxide approach has been attributed to Fermi level de-pinning by Park *et al.*[109] and Kim *et al.*[111] via electrical measurements of the Schottky barrier height. The presence of an oxide is said to block the penetration of the metal wave function into the semiconductor, preventing metal-induced gap states which pin the Fermi level. Another possible mechanism discussed by Kaushik *et al.*[112] is the lowering of the electron Schottky barrier due to n-type charge-transfer doping from the oxide to MoS_2. We expand this work to consider the impact of an oxide layer on thermal boundary conductance in Chapter 4.3.

Another important aspect of processing that affects the surface and interface chemistry of TMDs is polymer-aided processing. These processes include the initial transfer of a synthetic TMD film from its growth substrate to a target substrate via a carrier film, as well as photolithography which requires a polymer resist. PMMA is very commonly used for both purposes in the fabrication of TMD-based transistors, solar cells, and photodetectors.[66, 106, 113-115] In most cases, PMMA is dissolved in acetone for removal. In graphene-based devices, acetone removal is known to leave substantial PMMA residues resulting in compromised mobility and contact resistance.[116-

[118] As a result, different methods of surface cleaning are typically employed following acetone dissolution, including annealing in UHV or background gases, and exposure to UV-O_3.[116, 119-121] While the removal of residues from graphene has been studied extensively, in MoS_2 this has not been examined. Given that PMMA residues have been shown to react with deposited contact metals[122], inadequate removal of PMMA residues can affect metal/TMD interface properties. The experiments in Chapter 4.5 evaluate the efficacy of PMMA removal procedures on geological and synthetic MoS_2.

4.1.2.3 Thermal Transport at Metal/TMD Contacts

Power dissipation is regarded as a major challenge in scaling devices.[85] Heat transport in the cross-plane direction is critical for devices since it is the direction that contributes the most to thermal resistance.[123] In multilayer material, the weak van der Waals forces result in low thermal conductivity in the cross-plane direction that is nearly 50 times smaller than the in-plane thermal conductivity.[83, 124] Due to their low dimensionality, heat transport in 2D devices is almost entirely limited by their interfaces. At the MoS_2/SiO_2 interface, Raman thermometry and molecular dynamics simulations by Yalon *et al.*[125] and Suryavanshi *et al.*[126] have found the thermal boundary conductance to be 14 ± 4 and 15.5 ± 1.5 MW $m^{-2} K^{-1}$. Using frequency domain thermoreflectance, Goni *et al.*[123] observe that the interfacial thermal conductance is found to be over three times higher for monolayer MoS_2 than multilayer MoS_2. This is explained by the fact that monolayer MoS_2 has been found to conform better to SiO_2 than multilayer material.[127]

The literature currently includes many reports on the intrinsic thermal properties of TMDs and on thermal resistances across interfaces between TMDs and insulating substrates such as SiO_2.[83, 123, 125-126, 128] Very few reports specifically focus on metal/TMD contact interfaces and the majority are based on density function theory, making this topic of research largely uncharted

particularly from an experimental perspective.[129-133] The thermal boundary conductance across metal/TMD interfaces is dominated by phonon transport, with a negligible contribution from electron-phonon coupling.[131] Using DFT, Yan *et al.*[130] found that phonon-phonon coupling and phonon transmission across the metal/TMD interface is strongly dependent on the degree of orbital hybridization between the metal and TMD. Stronger chemical and electronic interactions between the metal and TMD result in a higher thermal boundary conductance. A similar observation with DFT was reported by Mao *et al.*[129] in which thermal boundary conductance was correlated with bonding. They also note that the thermal boundary conductance in metal/TMD interfaces is lower than that of metal/graphene interfaces due to the mass disorder phonon scattering introduced by the heavy metal atoms sandwiched between the lighter chalcogen atoms. Choi *et al.*[134] have experimentally measured h_K at Ti, Al, and Au interfaces with WSe_2, showing that higher degree of bonding at the interface results in an increase in WSe_2-WSe_2 interlayer resistance due to a change in the phonon density of states of the top WSe_2 layer.

Although high thermal boundary conductance is desirable for most device applications for effective heat removal, applications in thermoelectric energy conversion rely on high thermal resistance across the device. Furthermore, the contact must be thermally stable as to not degrade at high temperatures.[135] As discussed previously, WSe_2 is particularly promising for these applications due to its record low thermal conductivity.[78, 82] The dependence of thermal transport on interface chemistry – and the need for control over transport properties to address application-specific requirements – further motivates the understanding of thermal transport properties across different interfaces as well as the development of processes for control of interface chemistry. The topic of thermal transport at metal/TMD interfaces is explored in Chapters 4.3-4.4.

4.1.3 References

1. Chhowalla, M.; Shin, H. S.; Eda, G.; Li, L.-J.; Loh, K. P.; Zhang, H., The chemistry of two-dimensional layered transition metal dichalcogenide nanosheets. *Nat Chem* **2013,** *5* (4), 263-275.
2. Schmidt, H.; Giustiniano, F.; Eda, G., Electronic transport properties of transition metal dichalcogenide field-effect devices: surface and interface effects. *Chemical Society Reviews* **2015,** *44* (21), 7715-7736.
3. Yu, Y.; Nam, G.-H.; He, Q.; Wu, X.-J.; Zhang, K.; Yang, Z.; Chen, J.; Ma, Q.; Zhao, M.; Liu, Z.; Ran, F.-R.; Wang, X.; Li, H.; Huang, X.; Li, B.; Xiong, Q.; Zhang, Q.; Liu, Z.; Gu, L.; Du, Y.; Huang, W.; Zhang, H., High phase-purity 1T′-MoS2- and 1T′-MoSe2-layered crystals. *Nature Chemistry* **2018,** *10* (6), 638-643.
4. Voiry, D.; Mohite, A.; Chhowalla, M., Phase engineering of transition metal dichalcogenides. *Chemical Society Reviews* **2015,** *44* (9), 2702-2712.
5. Molina-Sánchez, A.; Wirtz, L., Phonons in single-layer and few-layer MoS${}_{2}$ and WS${}_{2}$. *Physical Review B* **2011,** *84* (15), 155413.
6. Voß, D.; Krüger, P.; Mazur, A.; Pollmann, J., Atomic and electronic structure of ${\mathrm{WSe}}_{2}$ from ab initio theory: Bulk crystal and thin film systems. *Physical Review B* **1999,** *60* (20), 14311-14317.
7. Kang, J.; Liu, W.; Sarkar, D.; Jena, D.; Banerjee, K., Computational Study of Metal Contacts to Monolayer Transition-Metal Dichalcogenide Semiconductors. *Physical Review X* **2014,** *4* (3), 031005.
8. Radisavljevic, B.; Radenovic, A.; Brivio, J.; Giacometti, V.; Kis, A., Single-layer MoS2 transistors. *Nat Nano* **2011,** *6* (3), 147-150.
9. English, C. D.; Shine, G.; Dorgan, V. E.; Saraswat, K. C.; Pop, E., Improved Contacts to MoS2 Transistors by Ultra-High Vacuum Metal Deposition. *Nano Letters* **2016,** *16* (6), 3824-3830.
10. Das, S.; Chen, H.-Y.; Penumatcha, A. V.; Appenzeller, J., High Performance Multilayer MoS2 Transistors with Scandium Contacts. *Nano Letters* **2013,** *13* (1), 100-105.
11. Baugher, B. W. H.; Churchill, H. O. H.; Yang, Y.; Jarillo-Herrero, P., Intrinsic Electronic Transport Properties of High-Quality Monolayer and Bilayer MoS2. *Nano Letters* **2013,** *13* (9), 4212-4216.
12. Smyth, C. M.; Addou, R.; McDonnell, S.; Hinkle, C. L.; Wallace, R. M., WSe2-contact metal interface chemistry and band alignment under high vacuum and ultra high vacuum deposition conditions. *2D Materials* **2017,** *4* (2), 025084.
13. Fontana, M.; Deppe, T.; Boyd, A. K.; Rinzan, M.; Liu, A. Y.; Paranjape, M.; Barbara, P., Electron-hole transport and photovoltaic effect in gated MoS2 Schottky junctions. *Scientific Reports* **2013,** *3*, 1634.
14. Jawaid, A.; Nepal, D.; Park, K.; Jespersen, M.; Qualley, A.; Mirau, P.; Drummy, L. F.; Vaia, R. A., Mechanism for Liquid Phase Exfoliation of MoS2. *Chemistry of Materials* **2016,** *28* (1), 337-348.
15. Coleman, J. N.; Lotya, M.; O'Neill, A.; Bergin, S. D.; King, P. J.; Khan, U.; Young, K.; Gaucher, A.; De, S.; Smith, R. J.; Shvets, I. V.; Arora, S. K.; Stanton, G.; Kim, H.-Y.; Lee, K.; Kim, G. T.; Duesberg, G. S.; Hallam, T.; Boland, J. J.; Wang, J. J.; Donegan, J. F.; Grunlan, J. C.; Moriarty, G.; Shmeliov, A.; Nicholls, R. J.; Perkins, J. M.; Grieveson, E. M.; Theuwissen, K.;

McComb, D. W.; Nellist, P. D.; Nicolosi, V., Two-Dimensional Nanosheets Produced by Liquid Exfoliation of Layered Materials. *Science* **2011,** *331* (6017), 568.
16. Nicolosi, V.; Chhowalla, M.; Kanatzidis, M. G.; Strano, M. S.; Coleman, J. N., Liquid Exfoliation of Layered Materials. *Science* **2013,** *340* (6139), 1226419.
17. Desai, S. B.; Madhvapathy, S. R.; Amani, M.; Kiriya, D.; Hettick, M.; Tosun, M.; Zhou, Y.; Dubey, M.; Ager, J. W.; Chrzan, D.; Javey, A., Gold-Mediated Exfoliation of Ultralarge Optoelectronically-Perfect Monolayers. *Advanced Materials* **2016,** *28*, 4053-4058.
18. Addou, R.; McDonnell, S.; Barrera, D.; Guo, Z.; Azcatl, A.; Wang, J.; Zhu, H.; Hinkle, C. L.; Quevedo-Lopez, M.; Alshareef, H. N.; Colombo, L.; Hsu, J. W. P.; Wallace, R. M., Impurities and Electronic Property Variations of Natural MoS2 Crystal Surfaces. *ACS Nano* **2015,** *9* (9), 9124-9133.
19. McDonnell, S.; Addou, R.; Buie, C.; Wallace, R. M.; Hinkle, C. L., Defect-dominated doping and contact resistance in MoS2. *ACS nano* **2014,** *8* (3), 2880-2888.
20. Addou, R.; Colombo, L.; Wallace, R. M., Surface Defects on Natural MoS2. *ACS Applied Materials & Interfaces* **2015,** *7* (22), 11921-11929.
21. Cai, Z.; Liu, B.; Zou, X.; Cheng, H.-M., Chemical Vapor Deposition Growth and Applications of Two-Dimensional Materials and Their Heterostructures. *Chemical Reviews* **2018,** *118* (13), 6091-6133.
22. Eichfeld, S. M.; Hossain, L.; Lin, Y.-C.; Piasecki, A. F.; Kupp, B.; Birdwell, A. G.; Burke, R. A.; Lu, N.; Peng, X.; Li, J., Highly Scalable, Atomically Thin WSe2 Grown via Metal–Organic Chemical Vapor Deposition. *ACS nano* **2015,** *9* (2), 2080-2087.
23. Schmidt, H.; Wang, S.; Chu, L.; Toh, M.; Kumar, R.; Zhao, W.; Castro Neto, A. H.; Martin, J.; Adam, S.; Özyilmaz, B.; Eda, G., Transport Properties of Monolayer MoS2 Grown by Chemical Vapor Deposition. *Nano Letters* **2014,** *14* (4), 1909-1913.
24. Zhan, Y.; Liu, Z.; Najmaei, S.; Ajayan, P. M.; Lou, J., Large-Area Vapor-Phase Growth and Characterization of MoS2 Atomic Layers on a SiO2 Substrate. *Small* **2012,** *8* (7), 966-971.
25. Koma, A., Van der Waals epitaxy for highly lattice-mismatched systems. *Journal of Crystal Growth* **1999,** *201–202*, 236-241.
26. Koma, A.; Ueno, K.; Saiki, K., Heteroepitaxial growth by Van der Waals interaction in one-, two- and three-dimensional materials. *Journal of Crystal Growth* **1991,** *111* (1–4), 1029-1032.
27. Saiki, K.; Ueno, K.; Shimada, T.; Koma, A., Application of Van der Waals epitaxy to highly heterogeneous systems. *Journal of Crystal Growth* **1989,** *95* (1), 603-606.
28. Ueno, K.; Shimada, T.; Saiki, K.; Koma, A., Heteroepitaxial growth of layered transition metal dichalcogenides on sulfur-terminated GaAs{111} surfaces. *Applied Physics Letters* **1990,** *56* (4), 327.
29. Aretouli, K. E.; Tsipas, P.; Tsoutsou, D.; Marquez-Velasco, J.; Xenogiannopoulou, E.; Giamini, S. A.; Vassalou, E.; Kelaidis, N.; Dimoulas, A., Two-dimensional semiconductor HfSe2 and MoSe2/HfSe2 van der Waals heterostructures by molecular beam epitaxy. *Applied Physics Letters* **2015,** *106* (14), 143105.
30. Roy, A.; Movva, H. C. P.; Satpati, B.; Kim, K.; Dey, R.; Rai, A.; Pramanik, T.; Guchhait, S.; Tutuc, E.; Banerjee, S. K., Structural and Electrical Properties of MoTe2 and MoSe2 Grown by Molecular Beam Epitaxy. *ACS Applied Materials & Interfaces* **2016,** *8* (11), 7396-7402.
31. Jiao, L.; Liu, H. J.; Chen, J. L.; Yi, Y.; Chen, W. G.; Cai, Y.; Wang, J. N.; Dai, X. Q.; Wang, N.; Ho, W. K.; Xie, M. H., Molecular-beam epitaxy of monolayer MoSe2: growth characteristics and domain boundary formation. *New Journal of Physics* **2015,** *17* (5), 053023.

32. Roy, P.; Srivastava, S. K., Chemical bath deposition of MoS2 thin film using ammonium tetrathiomolybdate as a single source for molybdenum and sulphur. *Thin Solid Films* **2006,** *496* (2), 293-298.
33. Hankare, P. P.; Patil, A. A.; Chate, P. A.; Garadkar, K. M.; Sathe, D. J.; Manikshete, A. H.; Mulla, I. S., Characterization of MoSe2 thin film deposited at room temperature from solution phase. *Journal of Crystal Growth* **2008,** *311* (1), 15-19.
34. Liu, Y.; Ghosh, R.; Wu, D.; Ismach, A.; Ruoff, R.; Lai, K., Mesoscale Imperfections in MoS2 Atomic Layers Grown by a Vapor Transport Technique. *Nano Letters* **2014,** *14* (8), 4682-4686.
35. Ubaldini, A.; Giannini, E., Improved chemical vapor transport growth of transition metal dichalcogenides. *Journal of Crystal Growth* **2014,** *401*, 878-882.
36. Mak, K. F.; Lee, C.; Hone, J.; Shan, J.; Heinz, T. F., Atomically Thin ${\mathrm{MoS}}_{2}$: A New Direct-Gap Semiconductor. *Physical Review Letters* **2010,** *105* (13), 136805.
37. Splendiani, A.; Sun, L.; Zhang, Y.; Li, T.; Kim, J.; Chim, C.-Y.; Galli, G.; Wang, F., Emerging Photoluminescence in Monolayer MoS2. *Nano Letters* **2010,** *10* (4), 1271-1275.
38. Zhao, W.; Ghorannevis, Z.; Chu, L.; Toh, M.; Kloc, C.; Tan, P.-H.; Eda, G., Evolution of Electronic Structure in Atomically Thin Sheets of WS2 and WSe2. *ACS Nano* **2013,** *7* (1), 791-797.
39. Tonndorf, P.; Schmidt, R.; Böttger, P.; Zhang, X.; Börner, J.; Liebig, A.; Albrecht, M.; Kloc, C.; Gordan, O.; Zahn, D. R. T.; Michaelis de Vasconcellos, S.; Bratschitsch, R., Photoluminescence emission and Raman response of monolayer MoS2, MoSe2, and WSe2. *Opt. Express* **2013,** *21* (4), 4908-4916.
40. Sahin, H.; Tongay, S.; Horzum, S.; Fan, W.; Zhou, J.; Li, J.; Wu, J.; Peeters, F. M., Anomalous Raman spectra and thickness-dependent electronic properties of WSe${}_{2}$. *Physical Review B* **2013,** *87* (16), 165409.
41. Wang, Q. H.; Kalantar-Zadeh, K.; Kis, A.; Coleman, J. N.; Strano, M. S., Electronics and optoelectronics of two-dimensional transition metal dichalcogenides. *Nature Nanotechnology* **2012,** *7*, 699.
42. Yoon, Y.; Ganapathi, K.; Salahuddin, S., How Good Can Monolayer MoS2 Transistors Be? *Nano Letters* **2011,** *11* (9), 3768-3773.
43. Wang, X.-F.; Tian, H.; Liu, Y.; Shen, S.; Yan, Z.; Deng, N.; Yang, Y.; Ren, T.-L., Two-Mode MoS2 Filament Transistor with Extremely Low Subthreshold Swing and Record High On/Off Ratio. *ACS Nano* **2019,** *13* (2), 2205-2212.
44. Schwierz, F., Graphene transistors. *Nature Nanotechnology* **2010,** *5*, 487.
45. Fiori, G.; Bonaccorso, F.; Iannaccone, G.; Palacios, T.; Neumaier, D.; Seabaugh, A.; Banerjee, S. K.; Colombo, L., Electronics based on two-dimensional materials. *Nature Nanotechnology* **2014,** *9*, 768.
46. del Alamo, J. A., Nanometre-scale electronics with III–V compound semiconductors. *Nature* **2011,** *479*, 317.
47. Liu, H.; Neal, A. T.; Ye, P. D., Channel Length Scaling of MoS2 MOSFETs. *ACS Nano* **2012,** *6* (10), 8563-8569.
48. Qin, Z.; Wei, Z.; Seabaugh, A., Low-subthreshold-swing tunnel transistors. *IEEE Electron Device Letters* **2006,** *27* (4), 297-300.
49. Das, S.; Prakash, A.; Salazar, R.; Appenzeller, J., Toward Low-Power Electronics: Tunneling Phenomena in Transition Metal Dichalcogenides. *ACS Nano* **2014,** *8* (2), 1681-1689.

50. Sarkar, D.; Xie, X.; Liu, W.; Cao, W.; Kang, J.; Gong, Y.; Kraemer, S.; Ajayan, P. M.; Banerjee, K., A subthermionic tunnel field-effect transistor with an atomically thin channel. *Nature* **2015,** *526*, 91.
51. Chen, M.; Li, K.; Li, L.; Lu, A.; Li, M.; Chang, Y.; Lin, C.; Chen, Y.; Hou, Y.; Chen, C.; Wu, B.; Wu, C.; Yang, I.; Lee, Y.; Shieh, J.; Yeh, W.; Shih, J.; Su, P.; Sachid, A. B.; Wang, T.; Yang, F.; Hu, C. In *TMD FinFET with 4 nm thin body and back gate control for future low power technology*, 2015 IEEE International Electron Devices Meeting (IEDM), 7-9 Dec. 2015; 2015; pp 32.2.1-32.2.4.
52. Yu, Z.; Ong, Z. Y.; Li, S.; Xu, J. B.; Zhang, G.; Zhang, Y. W.; Shi, Y.; Wang, X., Analyzing the Carrier Mobility in Transition-Metal Dichalcogenide MoS2 Field-Effect Transistors. *Advanced Functional Materials* **2017,** *27* (19), 1604093.
53. Fivaz, R.; Mooser, E., Mobility of Charge Carriers in Semiconducting Layer Structures. *Physical Review* **1967,** *163* (3), 743-755.
54. Podzorov, V.; Gershenson, M. E.; Kloc, C.; Zeis, R.; Bucher, E., High-mobility field-effect transistors based on transition metal dichalcogenides. *Applied Physics Letters* **2004,** *84* (17), 3301-3303.
55. Jariwala, D.; Sangwan, V. K.; Lauhon, L. J.; Marks, T. J.; Hersam, M. C., Emerging Device Applications for Semiconducting Two-Dimensional Transition Metal Dichalcogenides. *ACS Nano* **2014,** *8* (2), 1102-1120.
56. Yu, Z.; Ong, Z.-Y.; Pan, Y.; Cui, Y.; Xin, R.; Shi, Y.; Wang, B.; Wu, Y.; Chen, T.; Zhang, Y.-W.; Zhang, G.; Wang, X., Realization of Room-Temperature Phonon-Limited Carrier Transport in Monolayer MoS2 by Dielectric and Carrier Screening. *Advanced Materials* **2016,** *28* (3), 547-552.
57. Joo, M.-K.; Moon, B. H.; Ji, H.; Han, G. H.; Kim, H.; Lee, G.; Lim, S. C.; Suh, D.; Lee, Y. H., Understanding Coulomb Scattering Mechanism in Monolayer MoS2 Channel in the Presence of h-BN Buffer Layer. *ACS Applied Materials & Interfaces* **2017,** *9* (5), 5006-5013.
58. Konar, A.; Fang, T.; Jena, D., Effect of high-$\ensuremath{\kappa}$ gate dielectrics on charge transport in graphene-based field effect transistors. *Physical Review B* **2010,** *82* (11), 115452.
59. Jena, D.; Konar, A., Enhancement of Carrier Mobility in Semiconductor Nanostructures by Dielectric Engineering. *Physical Review Letters* **2007,** *98* (13), 136805.
60. Ye, M.; Zhang, D.; Yap, Y., Recent advances in electronic and optoelectronic devices based on two-dimensional transition metal dichalcogenides. *Electronics* **2017,** *6* (2), 43.
61. Kaasbjerg, K.; Thygesen, K. S.; Jacobsen, K. W., Phonon-limited mobility in n-type single-layer MoS${}_{2}$ from first principles. *Physical Review B* **2012,** *85* (11), 115317.
62. Popov, I.; Seifert, G.; Tománek, D., Designing Electrical Contacts to MoS2 Monolayers: A Computational Study. *Physical Review Letters* **2012,** *108* (15), 156802.
63. Giannazzo, F.; Fisichella, G.; Piazza, A.; Di Franco, S.; Greco, G.; Agnello, S.; Roccaforte, F., Impact of contact resistance on the electrical properties of MoS(2) transistors at practical operating temperatures. *Beilstein Journal of Nanotechnology* **2017,** *8*, 254-263.
64. Jeon, P. J.; Kim, J. S.; Lim, J. Y.; Cho, Y.; Pezeshki, A.; Lee, H. S.; Yu, S.; Min, S.-W.; Im, S., Low Power Consumption Complementary Inverters with n-MoS2 and p-WSe2 Dichalcogenide Nanosheets on Glass for Logic and Light-Emitting Diode Circuits. *ACS Applied Materials & Interfaces* **2015,** *7* (40), 22333-22340.
65. Mak, K. F.; Shan, J., Photonics and optoelectronics of 2D semiconductor transition metal dichalcogenides. *Nat Photon* **2016,** *10* (4), 216-226.

66. Tsai, M.-L.; Su, S.-H.; Chang, J.-K.; Tsai, D.-S.; Chen, C.-H.; Wu, C.-I.; Li, L.-J.; Chen, L.-J.; He, J.-H., Monolayer MoS2 Heterojunction Solar Cells. *ACS Nano* **2014,** *8* (8), 8317-8322.
67. Cho, A.-J.; Song, M.-K.; Kang, D.-W.; Kwon, J.-Y., Two-Dimensional WSe2/MoS2 p–n Heterojunction-Based Transparent Photovoltaic Cell and Its Performance Enhancement by Fluoropolymer Passivation. *ACS Applied Materials & Interfaces* **2018,** *10* (42), 35972-35977.
68. Tsai, D.-S.; Liu, K.-K.; Lien, D.-H.; Tsai, M.-L.; Kang, C.-F.; Lin, C.-A.; Li, L.-J.; He, J.-H., Few-Layer MoS2 with High Broadband Photogain and Fast Optical Switching for Use in Harsh Environments. *ACS Nano* **2013,** *7* (5), 3905-3911.
69. Lopez-Sanchez, O.; Lembke, D.; Kayci, M.; Radenovic, A.; Kis, A., Ultrasensitive photodetectors based on monolayer MoS2. *Nature Nanotechnology* **2013,** *8*, 497.
70. Lee, H. S.; Min, S.-W.; Chang, Y.-G.; Park, M. K.; Nam, T.; Kim, H.; Kim, J. H.; Ryu, S.; Im, S., MoS2 Nanosheet Phototransistors with Thickness-Modulated Optical Energy Gap. *Nano Letters* **2012,** *12* (7), 3695-3700.
71. Zhang, W.; Chiu, M.-H.; Chen, C.-H.; Chen, W.; Li, L.-J.; Wee, A. T. S., Role of Metal Contacts in High-Performance Phototransistors Based on WSe2 Monolayers. *ACS Nano* **2014,** *8* (8), 8653-8661.
72. Choi, W.; Cho, M. Y.; Konar, A.; Lee, J. H.; Cha, G.-B.; Hong, S. C.; Kim, S.; Kim, J.; Jena, D.; Joo, J.; Kim, S., High-Detectivity Multilayer MoS2 Phototransistors with Spectral Response from Ultraviolet to Infrared. *Advanced Materials* **2012,** *24* (43), 5832-5836.
73. Akama, T.; Okita, W.; Nagai, R.; Li, C.; Kaneko, T.; Kato, T., Schottky solar cell using few-layered transition metal dichalcogenides toward large-scale fabrication of semitransparent and flexible power generator. *Scientific Reports* **2017,** *7* (1), 11967.
74. Velusamy, D. B.; Kim, R. H.; Cha, S.; Huh, J.; Khazaeinezhad, R.; Kassani, S. H.; Song, G.; Cho, S. M.; Cho, S. H.; Hwang, I.; Lee, J.; Oh, K.; Choi, H.; Park, C., Flexible transition metal dichalcogenide nanosheets for band-selective photodetection. **2015,** *6*, 8063.
75. Xia, J.; Huang, X.; Liu, L.-Z.; Wang, M.; Wang, L.; Huang, B.; Zhu, D.-D.; Li, J.-J.; Gu, C.-Z.; Meng, X.-M., CVD synthesis of large-area, highly crystalline MoSe2 atomic layers on diverse substrates and application to photodetectors. *Nanoscale* **2014,** *6* (15), 8949-8955.
76. Wang, X.; Zebarjadi, M.; Esfarjani, K., First principles calculations of solid-state thermionic transport in layered van der Waals heterostructures. *Nanoscale* **2016,** *8* (31), 14695-14704.
77. Markov, M.; Zebarjadi, M., Thermoelectric transport in graphene and 2D layered materials. *Nanoscale and Microscale Thermophysical Engineering* **2018**, 1-11.
78. Wang, J.; Xie, F.; Cao, X.-H.; An, S.-C.; Zhou, W.-X.; Tang, L.-M.; Chen, K.-Q., Excellent Thermoelectric Properties in monolayer WSe2 Nanoribbons due to Ultralow Phonon Thermal Conductivity. *Scientific Reports* **2017,** *7*, 41418.
79. Huang, W.; Da, H.; Liang, G., Thermoelectric performance of MX2 (M = Mo,W; X = S,Se) monolayers. *Journal of Applied Physics* **2013,** *113* (10), 104304.
80. Ghosh, K.; Singisetti, U., Thermoelectric transport coefficients in mono-layer MoS2 and WSe2: Role of substrate, interface phonons, plasmon, and dynamic screening. *Journal of Applied Physics* **2015,** *118* (13), 135711.
81. Zhang, G.; Zhang, Y.-W., Thermoelectric properties of two-dimensional transition metal dichalcogenides. *Journal of Materials Chemistry C* **2017,** *5* (31), 7684-7698.
82. Chiritescu, C.; Cahill, D. G.; Nguyen, N.; Johnson, D.; Bodapati, A.; Keblinski, P.; Zschack, P., Ultralow Thermal Conductivity in Disordered, Layered WSe₂ Crystals. *Science* **2007,** *315* (5810), 351.

83. Liu, J.; Choi, G.-M.; Cahill, D. G., Measurement of the anisotropic thermal conductivity of molybdenum disulfide by the time-resolved magneto-optic Kerr effect. *Journal of Applied Physics* **2014,** *116* (23), 233107.
84. Allain, A.; Kang, J.; Banerjee, K.; Kis, A., Electrical contacts to two-dimensional semiconductors. *Nat Mater* **2015,** *14* (12), 1195-1205.
85. Pop, E., Energy dissipation and transport in nanoscale devices. *Nano Research* **2010,** *3* (3), 147-169.
86. Du, Y. Y., Lingming; Liu, Han, Contact research strategy for emerging molybdenum disulfide and other two-dimensional field-effect transistors. *APL Materials* **2014,** *2* (9), 092510.
87. Zhang, Z.; Yates, J. T., Band Bending in Semiconductors: Chemical and Physical Consequences at Surfaces and Interfaces. *Chemical Reviews* **2012,** *112* (10), 5520-5551.
88. Streetman, B. G.; Banerjee, S., *Solid State Electronic Devices*. Pearson Education Limited: 2015.
89. Suh, J.; Park, T.-E.; Lin, D.-Y.; Fu, D.; Park, J.; Jung, H. J.; Chen, Y.; Ko, C.; Jang, C.; Sun, Y.; Sinclair, R.; Chang, J.; Tongay, S.; Wu, J., Doping against the Native Propensity of MoS2: Degenerate Hole Doping by Cation Substitution. *Nano Letters* **2014,** *14* (12), 6976-6982.
90. Wang, Y.; Yang, R. X.; Quhe, R.; Zhong, H.; Cong, L.; Ye, M.; Ni, Z.; Song, Z.; Yang, J.; Shi, J.; Li, J.; Lu, J., Does p-type ohmic contact exist in WSe2–metal interfaces? *Nanoscale* **2016,** *8* (2), 1179-1191.
91. Kim, C.; Moon, I.; Lee, D.; Choi, M. S.; Ahmed, F.; Nam, S.; Cho, Y.; Shin, H.-J.; Park, S.; Yoo, W. J., Fermi Level Pinning at Electrical Metal Contacts of Monolayer Molybdenum Dichalcogenides. *ACS Nano* **2017**.
92. Kang, J.; Liu, W.; Banerjee, K., High-performance MoS2 transistors with low-resistance molybdenum contacts. *Applied Physics Letters* **2014,** *104* (9), 093106.
93. Gong, C.; Colombo, L.; Wallace, R. M.; Cho, K., The Unusual Mechanism of Partial Fermi Level Pinning at Metal–MoS2 Interfaces. *Nano Letters* **2014,** *14* (4), 1714-1720.
94. Kaushik, N.; Nipane, A.; Basheer, F.; Dubey, S.; Grover, S.; Deshmukh, M. M.; Lodha, S., Schottky barrier heights for Au and Pd contacts to MoS2. *Applied Physics Letters* **2014,** *105* (11), 113505.
95. Lince, J. R.; Carré, D. J.; Fleischauer, P. D., Schottky-barrier formation on a covalent semiconductor without Fermi-level pinning: The metal-${\mathrm{MoS}}_{2}$(0001) interface. *Physical Review B* **1987,** *36* (3), 1647-1656.
96. Heine, V., Theory of Surface States. *Physical Review* **1965,** *138* (6A), A1689-A1696.
97. Hasegawa, H.; Sawada, T., On the electrical properties of compound semiconductor interfaces in metal/insulator/ semiconductor structures and the possible origin of interface states. *Thin Solid Films* **1983,** *103* (1), 119-140.
98. Lince, J. R.; Stewart, T. B.; Fleischauer, P. D.; Yarmoff, J. A.; Taleb-Ibrahimi, A., The chemical interaction of Mn with the MoS2(0001) surface studied by high-resolution photoelectron spectroscopy. *Journal of Vacuum Science & Technology A* **1989,** *7* (3), 2469-2474.
99. Durbin, T. D.; Lince, J. R.; Yarmoff, J. A., Chemical interaction of thin Cr films with the MoS2(0001) surface studied by x-ray photoelectron spectroscopy and scanning Auger microscopy. *Journal of Vacuum Science & Technology A* **1992,** *10* (4), 2529-2534.
100. McGovern, I. T.; Dietz, E.; Rotermund, H. H.; Bradshaw, A. M.; Braun, W.; Radlik, W.; McGilp, J. F., Soft X-ray photoemission spectroscopy of metal-molybdenum bisulphide interfaces. *Surface Science* **1985,** *152-153*, 1203-1212.

101. McDonnell, S.; Smyth, C.; Hinkle, C. L.; Wallace, R. M., MoS2–Titanium Contact Interface Reactions. *ACS Applied Materials & Interfaces* **2016,** *8* (12), 8289-8294.
102. Smyth, C. M.; Addou, R.; McDonnell, S.; Hinkle, C. L.; Wallace, R. M., Contact Metal–MoS2 Interfacial Reactions and Potential Implications on MoS2-Based Device Performance. *The Journal of Physical Chemistry C* **2016,** *120* (27), 14719-14729.
103. Chuang, S.; Battaglia, C.; Azcatl, A.; McDonnell, S.; Kang, J. S.; Yin, X.; Tosun, M.; Kapadia, R.; Fang, H.; Wallace, R. M.; Javey, A., MoS2 P-type Transistors and Diodes Enabled by High Work Function MoOx Contacts. *Nano Letters* **2014,** *14* (3), 1337-1342.
104. McDonnell, S.; Azcatl, A.; Addou, R.; Gong, C.; Battaglia, C.; Chuang, S.; Cho, K.; Javey, A.; Wallace, R. M., Hole Contacts on Transition Metal Dichalcogenides: Interface Chemistry and Band Alignments. *ACS Nano* **2014,** *8* (6), 6265-6272.
105. Smyth, C. M.; Walsh, L. A.; Bolshakov, P.; Catalano, M.; Addou, R.; Wang, L.; Kim, J.; Kim, M. J.; Young, C. D.; Hinkle, C. L.; Wallace, R. M., Engineering the Palladium–WSe2 Interface Chemistry for Field Effect Transistors with High-Performance Hole Contacts. *ACS Applied Nano Materials* **2019,** *2* (1), 75-88.
106. Abraham, M.; Mohney, S. E., Annealed Ag contacts to MoS2 field-effect transistors. *Journal of Applied Physics* **2017,** *122* (11), 115306.
107. Han, J.; Lee, J.; Lee, J.; Woo, H.; Kim, J.; Jo, Y.; Cho, S.; Kim, H.; Kim, H.; Pawar, S. M.; Inamdar, A. I.; Jung, W.; Im, H., Electrical properties of N2- and H2 -annealed bulk MoS2/metal junctions. *Journal of the Korean Physical Society* **2015,** *67* (7), 1228-1231.
108. Liu, W.; Kang, J.; Sarkar, D.; Khatami, Y.; Jena, D.; Banerjee, K., Role of Metal Contacts in Designing High-Performance Monolayer n-Type WSe2 Field Effect Transistors. *Nano Letters* **2013,** *13* (5), 1983-1990.
109. Park, W.; Kim, Y.; Sang Kyung, L.; Jung, U.; Jin Ho, Y.; Cho, C.; Yun Ji, K.; Sung Kwan, L.; In Seol, H.; Lee, H.; Byoung Hun, L. In *Contact resistance reduction using Fermi level de-pinning layer for MoS2 FETs*, 2014 IEEE International Electron Devices Meeting, 15-17 Dec. 2014; 2014; pp 5.1.1-5.1.4.
110. Park, W.; Min, J. W.; Shaikh, S. F.; Hussain, M. M., Stable MoS2 Field-Effect Transistors Using TiO2 Interfacial Layer at Metal/MoS2 Contact. *physica status solidi (a)* **2017,** *214* (12).
111. Kim, G.-S.; Kim, S.-H.; Park, J.; Han, K. H.; Kim, J.; Yu, H.-Y., Schottky Barrier Height Engineering for Electrical Contacts of Multilayered MoS2 Transistors with Reduction of Metal-Induced Gap States. *ACS Nano* **2018,** *12* (6), 6292-6300.
112. Kaushik, N.; Karmakar, D.; Nipane, A.; Karande, S.; Lodha, S., Interfacial n-Doping Using an Ultrathin TiO2 Layer for Contact Resistance Reduction in MoS2. *ACS Applied Materials & Interfaces* **2016,** *8* (1), 256-263.
113. Huang, J.; Yang, L.; Liu, D.; Chen, J.; Fu, Q.; Xiong, Y.; Lin, F.; Xiang, B., Large-area synthesis of monolayer WSe2 on a SiO2/Si substrate and its device applications. *Nanoscale* **2015,** *7* (9), 4193-4198.
114. Nguyen, D. A.; Oh, H. M.; Duong, N. T.; Bang, S.; Yoon, S. J.; Jeong, M. S., Highly Enhanced Photoresponsivity of a Monolayer WSe2 Photodetector with Nitrogen-Doped Graphene Quantum Dots. *ACS Applied Materials & Interfaces* **2018,** *10* (12), 10322-10329.
115. Fang, H.; Chuang, S.; Chang, T. C.; Takei, K.; Takahashi, T.; Javey, A., High-Performance Single Layered WSe2 p-FETs with Chemically Doped Contacts. *Nano Letters* **2012,** *12* (7), 3788-3792.
116. Lin, Y. C.; Lu, C. C.; Yeh, C. H.; Jin, C.; Suenaga, K.; Chiu, P. W., Graphene annealing: how clean can it be? *Nano Lett* **2012,** *12* (1), 414-9.

117. Chan, J.; Venugopal, A.; Pirkle, A.; McDonnell, S.; Hinojos, D.; Magnuson, C. W.; Ruoff, R. S.; Colombo, L.; Wallace, R. M.; Vogel, E. M., Reducing Extrinsic Performance-Limiting Factors in Graphene Grown by Chemical Vapor Deposition. *ACS Nano* **2012,** *6* (4), 3224-3229.
118. Pirkle, A.; Chan, J.; Venugopal, A.; Hinojos, D.; Magnuson, C. W.; McDonnell, S.; Colombo, L.; Vogel, E. M.; Ruoff, R. S.; Wallace, R. M., The effect of chemical residues on the physical and electrical properties of chemical vapor deposited graphene transferred to SiO2. *Applied Physics Letters* **2011,** *99* (12), 122108.
119. Gong, C.; Floresca, H. C.; Hinojos, D.; McDonnell, S.; Qin, X.; Hao, Y.; Jandhyala, S.; Mordi, G.; Kim, J.; Colombo, L.; Ruoff, R. S.; Kim, M. J.; Cho, K.; Wallace, R. M.; Chabal, Y. J., Rapid Selective Etching of PMMA Residues from Transferred Graphene by Carbon Dioxide. *The Journal of Physical Chemistry C* **2013,** *117* (44), 23000-23008.
120. Wei Chen, C.; Ren, F.; Chi, G.-C.; Hung, S.-C.; Huang, Y. P.; Kim, J.; Kravchenko, I. I.; Pearton, S. J., UV ozone treatment for improving contact resistance on graphene. *Journal of Vacuum Science & Technology B, Nanotechnology and Microelectronics: Materials, Processing, Measurement, and Phenomena* **2012,** *30* (6), 060604.
121. Li, W.; Liang, Y.; Yu, D.; Peng, L.; Pernstich, K. P.; Shen, T.; Hight Walker, A. R.; Cheng, G.; Hacker, C. A.; Richter, C. A.; Li, Q.; Gundlach, D. J.; Liang, X., Ultraviolet/ozone treatment to reduce metal-graphene contact resistance. *Applied Physics Letters* **2013,** *102* (18), 183110.
122. Joiner, C. A.; Roy, T.; Hesabi, Z. R.; Chakrabarti, B.; Vogel, E. M., Cleaning graphene with a titanium sacrificial layer. *Applied Physics Letters* **2014,** *104* (22), 223109.
123. Goni, M.; Yang, J.; Schmidt, A. J., Enhanced thermal transport across monolayer MoS2. *Nano Research* **2018,** *11* (4), 2173-2180.
124. Muratore, C.; Varshney, V.; Gengler, J. J.; Hu, J.; Bultman, J. E.; Roy, A. K.; Farmer, B. L.; Voevodin, A. A., Thermal anisotropy in nano-crystalline MoS 2 thin films. *Physical Chemistry Chemical Physics* **2014,** *16* (3), 1008-1014.
125. Yalon, E.; McClellan, C. J.; Smithe, K. K. H.; Muñoz Rojo, M.; Xu, R. L.; Suryavanshi, S. V.; Gabourie, A. J.; Neumann, C. M.; Xiong, F.; Farimani, A. B.; Pop, E., Energy Dissipation in Monolayer MoS2 Electronics. *Nano Letters* **2017,** *17* (6), 3429-3433.
126. Suryavanshi, S. V.; Gabourie, A. J.; Farimani, A. B.; Yalon, E.; Pop, E. In *Thermal boundary conductance of the MOS 2-SiO 2 interface*, 2017; IEEE: pp 26-29.
127. Quereda, J.; Castellanos-Gomez, A.; Agraït, N.; Rubio-Bollinger, G., Single-layer MoS2 roughness and sliding friction quenching by interaction with atomically flat substrates. *Applied Physics Letters* **2014,** *105* (5), 053111.
128. Yan, R.; Simpson, J. R.; Bertolazzi, S.; Brivio, J.; Watson, M.; Wu, X.; Kis, A.; Luo, T.; Hight Walker, A. R.; Xing, H. G., Thermal Conductivity of Monolayer Molybdenum Disulfide Obtained from Temperature-Dependent Raman Spectroscopy. *ACS Nano* **2014,** *8* (1), 986-993.
129. Mao, R.; Kong, B. D.; Kim, K. W., Thermal transport properties of metal/MoS2 interfaces from first principles. *Journal of Applied Physics* **2014,** *116* (3), 034302.
130. Yan, Z.; Chen, L.; Yoon, M.; Kumar, S., The Role of Interfacial Electronic Properties on Phonon Transport in Two-Dimensional MoS2 on Metal Substrates. *ACS Applied Materials & Interfaces* **2016,** *8* (48), 33299-33306.
131. Liu, X.; Zhang, G.; Zhang, Y.-W., Thermal conduction across the one-dimensional interface between a MoS2 monolayer and metal electrode. *Nano Research* **2016,** *9* (8), 2372-2383.
132. Brown, D. B.; Li, X.; Xiao, K.; Geohegan, D. B.; Kumar, S. In *Thermal Boundary Conductance Mapping at Metal-MoSe<inf>2</inf>Interface*, 2018 17th IEEE Intersociety

Conference on Thermal and Thermomechanical Phenomena in Electronic Systems (ITherm), 29 May-1 June 2018; 2018; pp 67-72.
133. Parto, K.; Pal, A.; Xie, X.; Cao, W.; Banerjee, K. In *Interfacial Thermal Conductivity of 2D Layered Materials: An Atomistic Approach*, 2018 IEEE International Electron Devices Meeting (IEDM), 1-5 Dec. 2018; 2018; pp 24.1.1-24.1.4.
134. Choi, Y.-G.; Jeong, D.-G.; Ju, H. I.; Roh, C. J.; Kim, G.; Mun, B. S.; Kim, T. Y.; Kim, S.-W.; Lee, J. S., Covalent-bonding-induced strong phonon scattering in the atomically thin WSe2 layer. *arXiv preprint arXiv:1812.02383* **2018**.
135. He, R.; Schierning, G.; Nielsch, K., Thermoelectric Devices: A Review of Devices, Architectures, and Contact Optimization. *Advanced Materials Technologies* **2018,** *3* (4), 1700256.

4.2 Reactivity of MoS_2 with Metal Contacts and Effects of Thermal Annealing

Abstract

The prevalent implementation of thermal annealing in contact processing and the need for contacts to be thermally stable during device operation warrants an investigation of the thermal stability of metal/MoS_2 interfaces, which also requires an investigation of the as-deposited interface chemistry. This work examines Ti, Ni, and Au contacts. Ti has been previously shown to react with MoS_2 at room temperature. Here we perform a detailed analysis of the chemical composition and spatial distribution of reaction products at the Ti/MoS_2 interface with angular resolved XPS, supplemented by transmission electron microscopy with EELS and EDS. In the as-deposited state, Ti diffuses into MoS_2 causing scission of the Mo-S bond and the formation of Ti-S species. Mo metal and Ti-S compounds are found to coexist in the same region with a diffuse interface between disordered Ti-rich and Mo-rich regions. Thermal annealing of the interface to 100 °C shows a small increase in reaction products which increase further upon subsequent annealing to 300 and 600 °C. STEM indicates partial recrystallization of the disordered regions at 400 °C. Ni deposited on MoS_2 is found to exhibit interactions at the interface that manifest in the formation of new chemical states in the Mo 3*d* spectra that resemble sulfur vacancy defects and new chemical states in S 2*p* that likely correspond to Ni-S surface states. A similar result is observed following the deposition of Au. The new states formed at the Ni/MoS_2 interface vanish upon thermal annealing. XPS, AFM, and STEM also provide evidence of agglomeration and diffusion of Ni into MoS_2 upon annealing. Unlike with Ni, the new chemical states at the Au/MoS_2 interfaces remain after annealing. The interaction also manifests in the Au 4*f* spectra.

4.2.1 Introduction

This chapter examines the chemistry of the metal/MoS_2 interface and changes that occur as a result of thermal annealing. This study is motivated by (1) the prevalent implementation of thermal annealing in contact processing and (2) the need for contacts to be thermally stable during device operation. As discussed in the introduction to Part 4, thermal annealing following contact deposition is a common processing step thought to enhance device properties by improving contact adhesion or promoting doping in the semiconductor. These phenomena undoubtedly occur as a result of changes in the chemical composition at the contact/TMD interface that are driven by heating. Reports in the literature generally indicate an improvement in electrical transport as a result of annealing.[1-2] The underlying mechanisms for the observed changes in measured device properties are largely speculated or entirely overlooked.[1, 3-6] Furthermore, the long term stability of devices relies on contacts that retain consistent properties after many cycles of operation. Changes in interface chemistry that occur due to heat dissipated during operating conditions can therefore compromise reliability. This is particularly important for thermoelectric energy conversion devices in which thermal conductivity is low and the device is subject to a large temperature gradient.[7] The acquisition and analysis of XPS data on metal/MoS_2 structures after heating to different temperatures can provide insight to address the aforementioned gaps. The XPS results are supplemented by STEM images of cross-sectioned metal/MoS_2.

Detailed XPS studies examining the reactivity of metal/MoS_2 interfaces at different temperatures were published in the late 1980s and early 1990s when metal/MoS_2 composite coatings were of interest for applications in tribology and heterogeneous catalysis. For example, Durbin *et al.*[8] studied Cr on MoS_2, showing that Cr is reactive with MoS_2 at room temperature forming metallic Mo and Cr-S, and that heating the material following deposition results in an

increase in the reaction products. Lince *et al.*[9-10] report similar behavior for Mn on MoS_2, whereas Fe was found to delaminate from the MoS_2 surface as a result of annealing. These studies illustrate the differences in the behavior of reactive (Cr and Mn) vs. non-reactive (Fe) metals on MoS_2 after thermal annealing, however Mn and Fe are not commonly used as contacts for devices.

For 2D device applications, Ti is thought to be among the best contact metals to MoS_2 due to the low lattice mismatch (1%), high density of delocalized states near the Fermi level, and low and narrow barrier for electron transport.[11] Ti contacts are commonly used and often annealed post deposition at temperatures ranging 200-400 °C.[1, 5-6] McGovern *et al.*[12] and McDonnell *et al.*[13] have demonstrated that a reaction occurs at room temperature when Ti is deposited on MoS_2 in UHV, resulting in the formation of metallic Mo and Ti_xS_y compounds. Wu *et al.*[14] arrived at a similar conclusion with density functional theory and STEM with EELS. The literature currently lacks reports on the effects of annealing on the interface chemistry of Ti/MoS_2. Annealed UHV-deposited Ti contacts to MoS_2 have been found to perform relatively poorly compared to other metals. The focus of this chapter is on developing a thorough understanding of the chemical composition of the as-deposited Ti/MoS_2 interface, and examining changes that occur as a result of annealing. A preliminary investigation of the interface chemistry and thermal stability of Ni and Au contacts to MoS_2 is also presented. A summary of previous work characterizing metal/MoS_2 interfaces is shown in Table 4.1. The table is focused on metals which are analyzed in this chapter (Ti, Ni and Au) and others which are referenced and discussed. XPS studies of the effects of thermal annealing on metal/MoS_2 have been conducted only on Cr, Mn, and Fe which, as mentioned, are not commonly used for electrical contact in devices. XPS for common contacts (Au, Ti, Ni) has only been performed on as-deposited material.

Table 4.1 Summary of literature on experimental chemical and electronic characterization of metal/MoS_2 interfaces. Ti, Ni, and Au are studied in this work. Work in the literature on Cr, Mn, Fe, and Pd is discussed.

	Ref.	Deposition	Annealing	Characterization	Key Result
Ti	12	UHV	None	XPS	Reaction of Ti+MoS_2 →Ti-S + Mo^0 at room temperature
	14	UHV	None	TEM, EELS	Reaction of Ti+MoS_2 →Ti-S + Mo^0 at room temperature
	13	HV and UHV	None	XPS	Reaction occurs in UHV only and not in HV deposition
	1	UHV	300 °C for 2 hr in HV	TLM	High R_C (~7 - 9 kΩ μm)
	15	Unreported*	None	FET I-V Curves	E_F pinned near MoS_2 conduction band (Φ=0.050 eV)
Ni	16, 17	UHV	Heated sequentially in UHV to 927 , time not specified	Auger electron spectroscopy (AES)	- No interactions below 327 °C - Some diffusion of Ni into MoS_2 at 327-527 °C - Agglomeration of Ni film > 527 °C
	1	HV	300 °C for 2 hr in HV	TLM	R_C ~ 4-7 kΩ μm
	15	Unreported*	None	FET I-V Curves	n-type Fermi level pinning (Φ=0.150 eV)
Au	18	UHV	None	XPS	No chemical bonding
	19	HV and UHV	None	XPS	No chemical bonding
	1	HV and UHV	300 °C for 2 hr in HV	TLM FET- IV curves	- R_C for Au ~0.7 - 2 kΩ μm in UHV; ~3.5–5 kΩ μm in HV - Φ = 0.15 eV
	20	Unreported*	Unreported	TLM FET I-V Curves	- R_C ~ 30-45 Ω mm - Φ = 0.12 eV
Cr	8, 21	UHV	Heated sequentially in UHV from 425-850 °C, time not specified	XPS	- Reaction of Cr+MoS_2 →Cr-S + Mo^0 at room temperature - Reaction driven to completion < 425 °C - Increase in S composition at the Cr surface with temp. - Coalescence of Cr > 650 °C
	19	HV and UHV	None	XPS	- Reaction occurs under both HV and UHV conditions - HV deposition conductions also result in CrO_x
Mn	9	HV and UHV	Heated sequentially in UHV from 497-857 °C, time not specified	XPS	- Reaction of Mn+MoS_2 →Mn-S + Mo^0 as deposited - Reaction driven to completion above 497 °C - Increase in S composition at the Mn surface with temp. - Coalescence of Mn > 767 °C
Fe	10	UHV	Heated sequentially in UHV from 327-927 °C, time not specified	XPS	- No evidence of reaction in the bulk - Fe-S surface states and S-vacancy states are observed following initial deposition - Heating eliminates these chemical states
Pd	22	HV	None	XPS	No chemical bonding
	18	UHV	None	XPS	No chemical bonding
	23	UHV	None	XPS	- No chemical bonding - Perturbation of the MoS_2 surface due to Pd overlayer - Pd aligns midgap with MoS_2 (Φ =0.67 eV)
	20	Unreported*	Unreported	TLM FET I-V Curves	- R_C ~ 75-200 kΩ mm - Φ = 0.4 eV

*In cases where deposition conditions are unreported, HV deposition is most likely due to its prevalence in device processing

4.2.2 Materials and Methods

MoS_2 geological crystal samples (SPI[24]) were exfoliated for surface cleaning, mounted onto Mo plates with Ta foil, and then immediately loaded into UHV (base pressure 2 x 10^{-9} mTorr). XPS data was acquired on the pristine samples prior to metal deposition. A thin layer of metal (2-6 nm) was deposited by electron beam evaporation (Mantis Quad EV-C) in our UHV system and XPS data was acquired in-situ after deposition.[25] For the study of thermal treatment, samples were heated in the UHV chamber to 100, 300, and 600 °C for 30 minutes at each temperature. XPS measurements were performed following each heat treatment. All XPS data was collected at a pass energy of 50 eV with a 1486.7 eV Al Kα photon source at 45° takeoff angle. Angular resolved XPS was performed by varying the angle between the sample surface and the analyzer from 30° to 70° in 10° increments. The XPS spectra were analyzed with kolXPD.[26] Samples for STEM analysis were heated to 400 °C. Additional information on the TEM measurement can be found in Section 2.3.4.

4.2.3 Results and Discussion

4.2.3.1 Band Bending and Chemical Composition of As-Deposited Ti/MoS_2

Before investigating the effect of post-deposition annealing, we closely examine the interface chemistry of the Ti/MoS_2 system in its as-deposited state. Normalized XPS spectra of the Mo 3*d* and S 2*p* core levels of the sample before and after deposition are shown in Figure 4.2.1 below. Following the deposition of a thin layer of Ti in UHV, the Mo^0 chemical state is observed in the Mo 3*d* spectrum. New chemical states in the S 2*p* spectrum correspond to Ti-S reaction products. Calculations by both McGovern *et al.* and Lince *et al.* conclude that the reaction to form ideally stoichiometric TiS from Ti + MoS_2 is thermodynamically favorable at 298 K having a Gibbs free energy change of -24.1 kcal/mol.[12, 22] TiS is an extremely rare compound found in

nature for the first time in 2011 in a 2.4 billion year old meteorite.[27-28] As a result, reference XPS spectra are not available. A number of reference spectra are available for TiS_2 and TiS_3.[29-32] TiS_2 has its $2p_{3/2}$ component at 160.8 eV. TiS_3 is characterized by two S *2*p chemical states, one corresponding to the S^{2-} atom at 161.2 eV and one corresponding to the S_2^{2-} disulfide cluster at 162.4 eV. Our S 2*p* spectra do not consistently match with either indicating that a different stoichiometry occurs. In the fit shown in Figure 4.2.1, the Mo-S state intensity yields an RSF normalized S/Mo ratio of ~2, and all widths and spin-orbit splitting values have been fixed based making the fit realistic despite our inability to assign the specific S-Ti states. Calculation of the S/Ti ratio will be revisited in the angular resolved study. The multiple states in the S 2*s* peak of the Mo 3*d* spectrum correspond to those shown in the S 2*p* spectrum. In other words, their relative intensities and positions were fixed to correlate with S 2*p*. A table of fit parameters is shown in Appendix A.

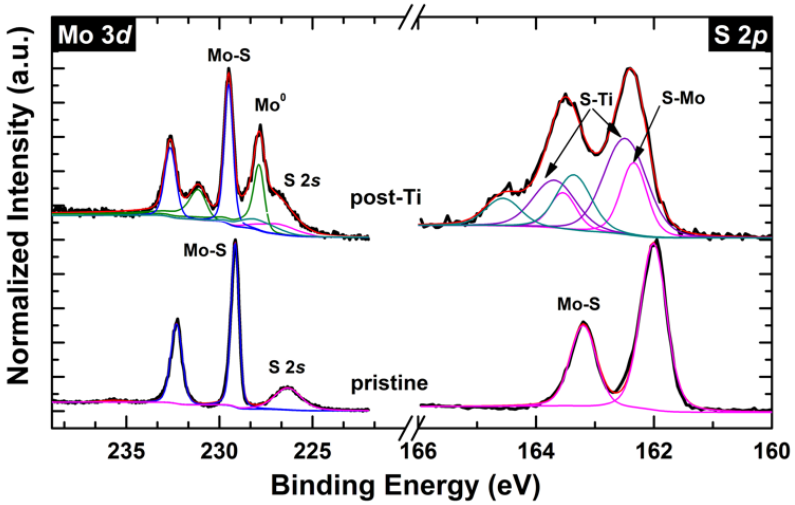

Figure 4.2.1. Mo 3*d* and S 2*p* core levels before and after Ti deposition

Lince *et al.*[22] note that since Mo atoms are unlikely to react with transition metals, any observed core level shifts in the Mo 3*d* spectrum are attributed to band bending. This is in

agreement with work by Domask *et al.*[33] who note that the binary Ti-Mo system shows no intermetallic compounds. In Figure 4.2.1, we observe a Mo 3*d* core-level shift of +0.34 eV (away from E_F) after the deposition of Ti, and an identical shift of +0.34 eV is also observed in the Mo-S peak of the S 2*p* spectrum. The identical shift in both core-levels is expected since Fermi level shifts affect each core level equally. Band-bending, as described by Schottky and Mott, occurs due to the work function difference between the metal and the semiconductor.[34] The work function of geological MoS_2 ranges from 4.5 to 5.4 eV due to variations in local doping.[35] We have measured the work function of UHV-deposited Ti, ϕ_m, to be 4.17 eV. We note that this is lower than the previously reported values of 4.33 eV[36-37] however this is potentially due to differences in film deposition conditions or time between deposition and measurement. The work function is known to be sensitive to carbon concentration[38], and as shown in Chapter 3.2, Ti readily forms carbide even in UHV. Our data was acquired immediately following deposition to minimize the effects of carbide formation on the measured work function.

When the metal-semiconductor contact is formed, charge transfer occurs at the interface until the Fermi levels align. The charge transfer creates an electric field across the interface which shifts the semiconductor valence and conduction band edges, resulting in band bending. The degree of band bending is given as $V_{BB}=\phi_m - \phi_S$. If $\phi_m > \phi_s$, the semiconductor valence and conduction bands bend upward at the interface whereas the bands bend downward at the interface for which $\phi_m < \phi_s$.[34, 39] This is illustrated in Figure 4.4.2. For the case of a n-type semiconductor, $\phi_m < \phi_s$ results in an Ohmic contact whereas for a p-type semiconductor this results in a Schottky contact. The opposite is true when $\phi_m > \phi_s$.

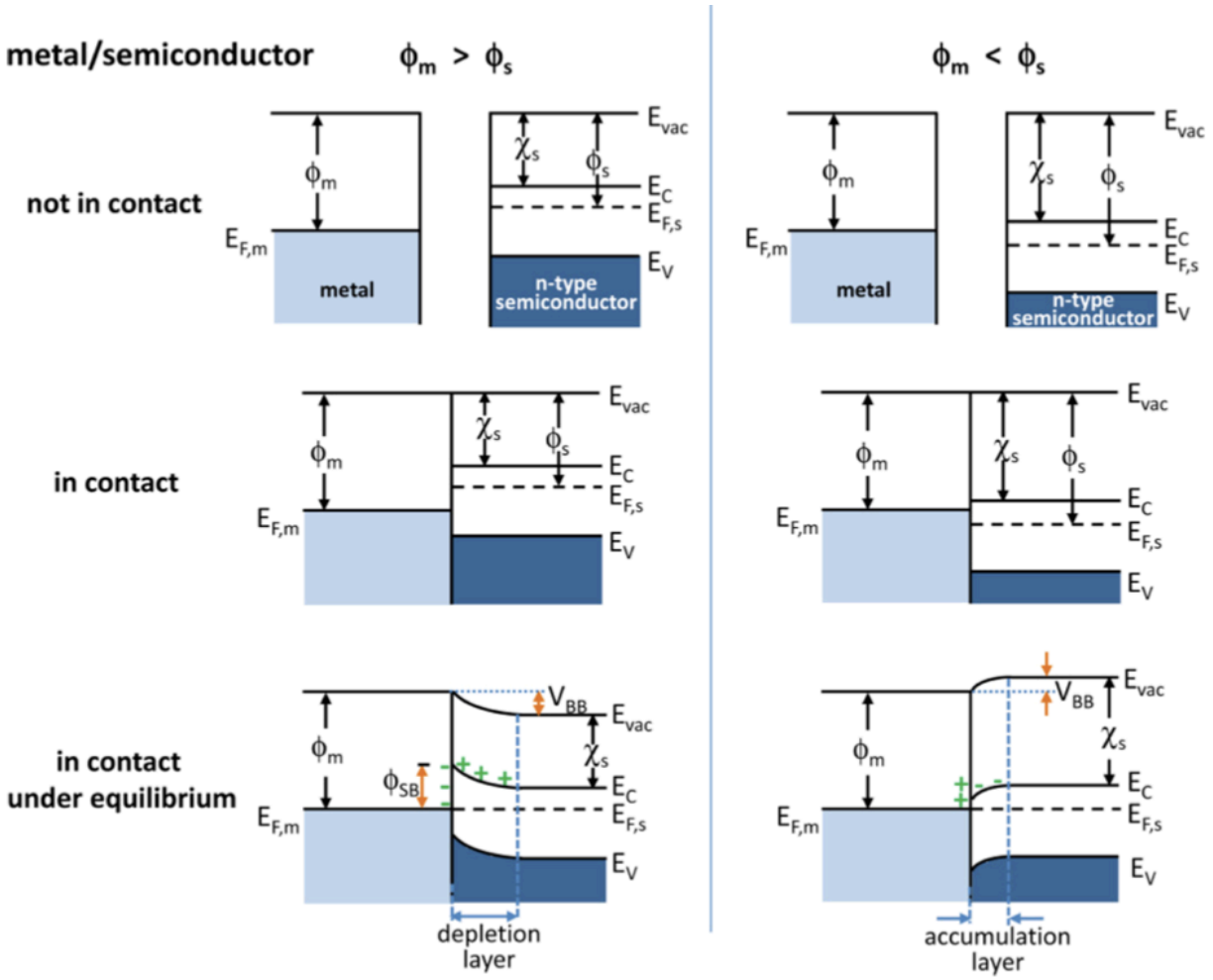

Figure 4.2.2. Band diagrams of metal/n-type semiconductor interface where $\phi_m > \phi_s$ on the left and $\phi_m < \phi_s$ on the right. E_{vac} is the vacuum energy, E_C is the conduction band minimum, E_V is the valence band maximum and χ_s is the electron affinity of the semiconductor. Adapted from Ref. 34.

McDonnell *et al.*[18] report Mo $3d_{5/2}$ binding energies of 229.86 eV for n-type material, and 229.11 eV for p-type material. Based on these values, the material in our experiment is likely p-type, having an initial Mo $3d_{5/2}$ binding energy of 229.16 eV. At the lower limit of the work function of MoS_2, which is 4.5 eV, the value of V_{BB} would be 0.33 eV. At the upper limit of 5.4 eV, V_{BB} = 1.23 eV in a downward direction at the interface. The shift we observe is 0.34 eV toward higher binding energies. It is close to what would be expected for MoS_2 having a work function of

4.5 eV. However, this work function clearly corresponds to n-type material where ours is p-type based on the Mo 3*d* core-level binding energy. Therefore our result deviates from the Schottky Mott model.

McGovern *et al.*[12] observed V_{BB}=0 eV following Ti deposition on air-cleaved MoS_2. They explain that the air-cleaved MoS_2 exhibits Fermi level pinning from carbon contamination making it insensitive to metal overlayers. One potential explanation for the discrepancy between our result and that of McGovern *et al.* is that in our experiment, a different spot on the sample was measured before and after Ti deposition as the sample had to be moved inside the chamber between evaporator to the X-ray source. Variations in doping between different spots on MoS_2 geological crystals have been documented.[18, 35, 40] In order to eliminate the possibility that the apparent core level shift is simply due to spot-to-spot variability on the sample, we examine data from seven separate experiments in which Ti was deposited on different pieces of MoS_2 geological crystal. The Mo $3d_{5/2}$ binding energies of the Mo-S peak before and after Ti deposition are represented in Figure 4.2.3. It is clear from the values of pristine MoS_2 that the material is highly variable, exhibiting both n- and p- type regions. Nevertheless, a shift to higher binding energies is consistently observed. By performing a two-sample t-test for equal group means[41] to test for the statistical significance of the apparent core level shifts at a significance level of 0.05, there is sufficient evidence that a core-level shift does occur due the deposition of Ti (with a 9×10^{-4} probability of error). The appearance of new chemical states at the interface together with the deviation from the Schottky Mott model indicate that the observed Fermi level shift is not simply due to band bending from charge transfer between MoS_2 and Ti. The Fermi level is likely pinned at defect states formed due to chemical reactions.

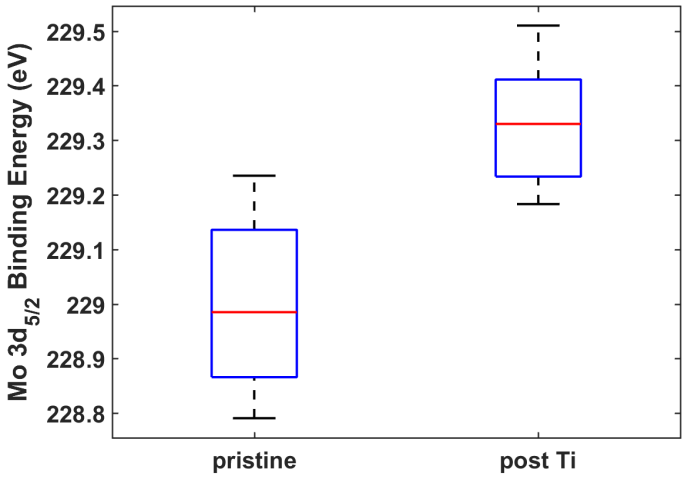

Figure 4.2.3. Representation of Mo $3d_{5/2}$ binding energy (of the Mo-S chemical state) in seven different MoS_2 samples before and after Ti deposition. Dashed lines indicate the maximum and minimum values, the box boundaries represent the 25th and 75th percentiles of the samples, and middle red line represents the median.

The result shown in Figure 4.2.3. indicates that Ti pins E_F within a range of values corresponding to n-type conductance. This is unlike the result observed by Dong *et al.*[23] following the deposition of Pd on MoS_2. In their work, binding energies following the deposition of Pd were reported to be identical on seven different spots on the sample, despite the sample initially exhibiting a high degree of spot-to-spot variability and both n- and p- type conductances in its pristine state. We note that our data was acquired from different samples which may have had varying concentrations of adventitious carbon and oxygen on the surface. Additionally, unlike Pd/MoS_2, the Ti/MoS_2 interface does undergo a reaction. Due to the reactivity of Ti/MoS_2, the Fermi level shift may be more susceptible to inhomogeneity.

4.2.3.2 Angular Resolved XPS Analysis of As-Deposited Titanium on MoS_2

An improved understanding of the vertical distribution of the various chemical species in the Ti/MoS_2 system can be achieved with angular resolved XPS (AR-XPS) measurements as described in the Section 2.3.1.5. In this method, the surface sensitivity of the measurement is varied by adjusting the angle between the sample surface and the analyzer. The spectra acquired at each angle for a MoS_2 substrate with ~3 nm of Ti deposited on MoS_2 are shown in Figure 4.2.4 The most surface sensitive measurement corresponds to the 30° takeoff angle (from the sample surface) whereas the most bulk sensitive corresponds to 70°.

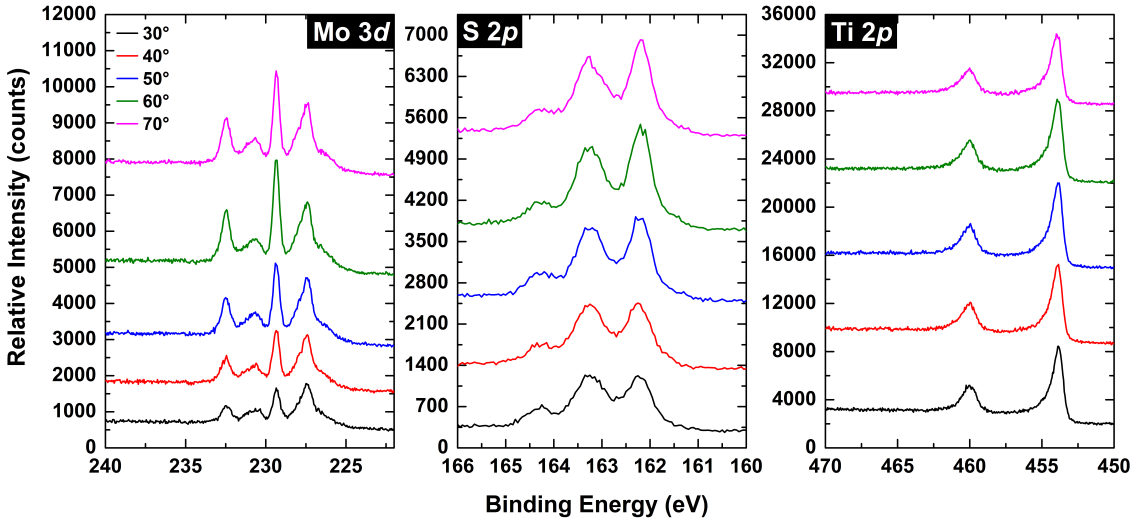

Figure 4.2.4. Angular resolved XPS data of Ti/MoS_2 (as deposited)

Upon examination of the Mo 3*d* spectra, it is clear that the Mo^0 peak intensity (227.3 eV) decreases relative to that of the Mo-S peak (228.4 eV) as the measurement becomes less surface sensitive (more bulk sensitive). This is expected given that Mo^0 forms due to the reaction of MoS_2 with Ti which was deposited on the surface. The Mo^0 layer is therefore expected to be near the surface, most likely at an interlayer between the substrate and Ti. As the measurement becomes more bulk sensitive we also observe an increase in the S 2*p* peak near ~162.2 eV which roughly

corresponds to the position of S bonded to Mo. The Ti 2*p* spectra appear to be predominantly comprised of Ti metal, however the peaks are broader than pure Ti metal due to the superposition of Ti-S chemical states as well as a small quantity of Ti-C. No carbon was present on the surface of the MoS_2 prior to Ti deposition, therefore all carbide formed due to reaction with background gases in the chamber as discussed in Chapter 3.2.[42-43] We note that the rate of carbide formation over time was monitored, and all core level intensities were multiplied by a time-dependent correction factor to compensate for the effects of attenuation in carbide.

An alternative means of visualizing the change in the relative quantities of chemical species is shown in Figure 4.2.5. In this figure the percentages of the signals from different chemical states within the XPS detection volume are plotted as a function of angle. The RSF-normalized intensity from each species was taken as a percentage of the sum of intensities of all chemical states at each angle. This approach treats the total signal as one that originated from an overlayer in which the different species are homogeneously distributed. Given that the percentages change as a function of takeoff angle, which varies the surface sensitivity, it is clear that that the species are not homogeneously distributed and are instead vertically distributed in the sample. The data acquired at 60° appears to deviate from the trend possibly due to spot-to-spot variability as the x-ray spot was refocused between angles. The surface of geological MoS_2 is macroscopically very rough as shown in Figure 4.2.6. Probing a spot that is not flat could result in anomalous data. It is also possible that the edge of the sample was measured. Since only this single data point deviates from the expected trends, it is discounted in the subsequent quantitative analysis. Nevertheless, it is clear that the composition of Ti and S-Ti species decreases as the measurement becomes more bulk sensitive while the signal from Mo-S and Mo increases.

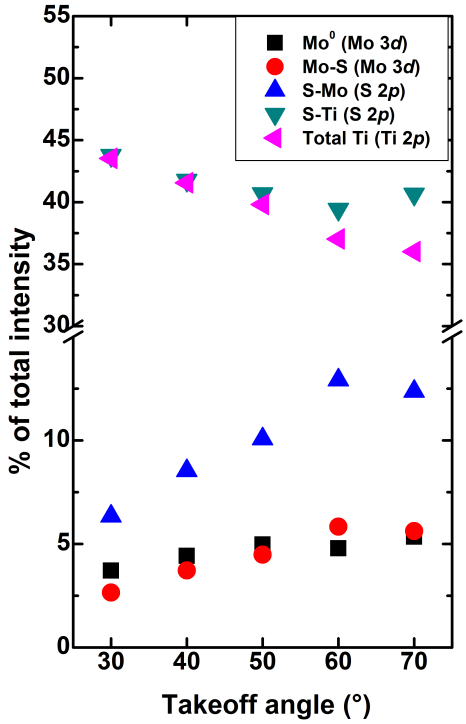

Figure 4.2.5. Percent of total intensity corresponding to different species. Parenthesis indicate the core-level.

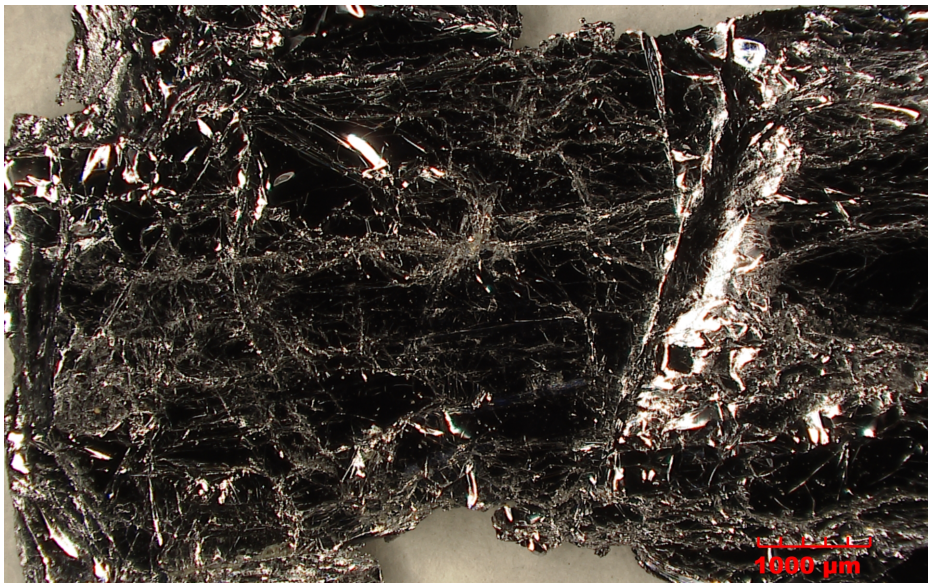

Figure 4.2.6. Optical micrograph of geological MoS_2 showing roughness on the macroscopic scale

Quantitative models reported by Himpsel *et al.*[44] and Vitchev *et al.*[45] described in detail in Section 2.3.1.5 can be applied and compared with the experimental results to determine the approximate distributions and relative thicknesses of the different layers in the system. These models account for the attenuation of a core-level intensity in an overlayer as a function of takeoff angle θ, overlayer thickness d, and the effective attenuation length λ of the core-level signal in the overlayer. The theoretical ratio of core-level intensities from different layers in the material system is computed using the model. The ratio is then compared with the experimental intensity ratio to determine which interface structure is most likely. The models assume that overlayers have uniform coverage. Atomic force microscopy (AFM) characterization of Ti/MoS_2 is shown in Figure 4.2.7. The absence of surface features indicates that Ti does not agglomerate but instead forms a reasonably uniform layer on top of MoS_2.

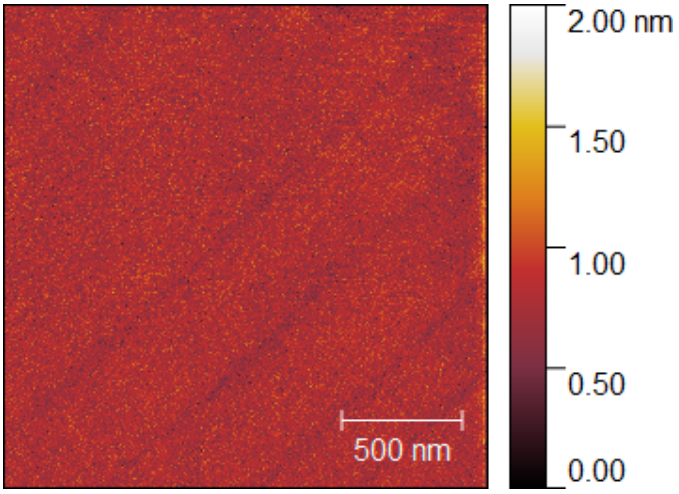

Figure 4.2.7. AFM image of as-deposited Ti/MoS_2. The diagonal streaks are an artefact.

From examination of the raw data and percentages represented in Figure 4.2.5, we consider two possible interface structures. The first is a layered structure of $MoS_2/Mo^0/Ti_xS_y/Ti$. In the second possibility, Mo^0 and Ti_xS_y exist in the same layer, having the structure $MoS_2/Mo^0+Ti_xS_y/Ti$.

These are illustrated schematically in Figure 4.2.8. To test the first possibility, we apply the following equation[45]

$$\frac{I_{Mo^0}}{I_{MoS_2}} = \frac{I_{Mo_\infty}\left(1-\exp\left(-\frac{d_{Mo^0}}{\lambda_{Mo,Mo}sin\theta}\right)\right)\exp\left(-\frac{d_{Ti_xS_y}}{\lambda_{Mo,Ti_xS_y}sin\theta}\right)\exp\left(-\frac{d_{Ti}}{\lambda_{Mo,Ti}sin\theta}\right)}{I_{MoS_2\infty}\exp\left(-\frac{d_{Mo^0}}{\lambda_{Mo,Mo}sin\theta}\right)\exp\left(-\frac{d_{Ti_xS_y}}{\lambda_{Mo,Ti_xS_y}sin\theta}\right)\exp\left(-\frac{d_{Ti}}{\lambda_{Mo,Ti}sin\theta}\right)} \qquad \text{Equation 4.1}$$

to calculate the theoretical intensity ratio assuming a Mo^0 overlayer on MoS_2. The last two exponential terms cancel out since the Mo 3*d* core level intensities from both the MoS_2 and Mo^0 are attenuated equally in the Ti_xS_y/Ti layer due to their nearly identical kinetic energies. We have experimentally measured the ratio of $I_{Mo_\infty}/I_{MoS_2\infty}$ to be 0.4. The value of $\lambda_{Mo,Mo}$ is 15.638 Å and λ_{Mo,Ti_xS_y} is 30.832 Å according to the NIST EAL database.[46]

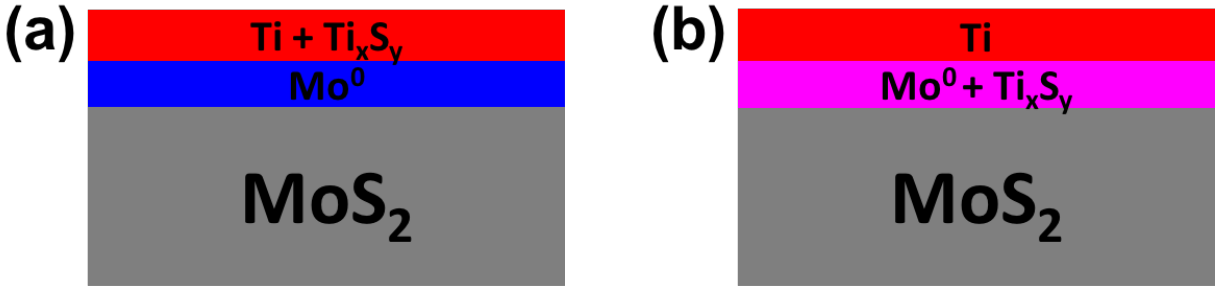

Figure 4.2.8. Schematic illustration of the two layered structures that are considered in this chapter where (a) represents $MoS_2/Mo^0/Ti_xS_y$/Ti and (b) represents MoS_2/Mo^0+Ti_xS_y/Ti

A plot of the theoretical intensity ratios at different thicknesses d_{Mo^0} as a function of takeoff angle is shown in Figure 4.2.9. The bottom curve represents d_{Mo^0}=10 Å and the top curve represents d_{Mo^0}=20 Å. The black circles represent the experimental data. To quantitatively

determine which curve matches best with the data, we define a loss function that is the sum of the absolute values of the deviation[47] between the experimental and theoretical values of $\frac{I_{Mo^0}}{I_{MoS_2}}$ for each curve. The best fit to the data is that at which the loss function is closest to zero. As mentioned previously, the data point acquired at 60° is omitted from all calculations in this chapter. A minimum loss value of 1.15 is found at a thickness of 13 Å of Mo. It is clear that none of the data points, fall close to the same line, even excluding the data at 60°, indicating that the assumption of a Mo^0 layer directly on top of MoS_2 is not correct.

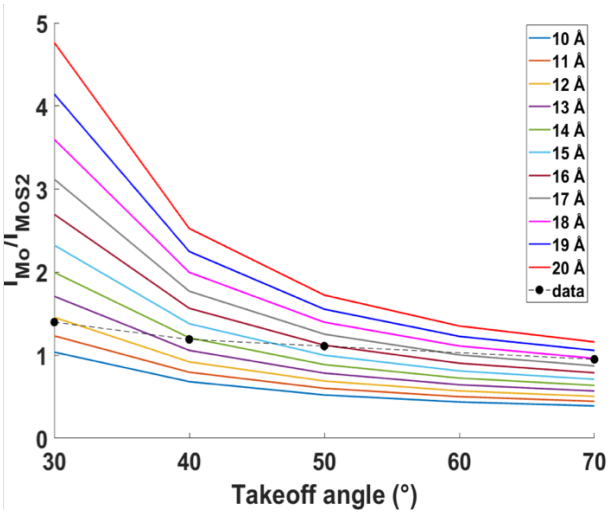

Figure 4.2.9. Theoretical curves of $\frac{I_{Mo^0}}{I_{MoS_2}}$ ratios as a function of angle calculated at Mo^0 layer thicknesses ranging from 10 to 20 Å. Black circles correspond to experimental data.

To test whether a $MoS_2/Mo^0+Ti_xS_y/Ti$ model in Figure 4.2.8(b) results in better agreement with the experimental data, the following equation is implemented[48]

$$\frac{I_{Mo^0}}{I_{MoS_2}} = \frac{I_{Mo\infty}}{I_{MoS_2\infty}} \left[\frac{1-\exp\left(-\frac{-d*a}{\lambda_{Mo,Mo}sin\theta}\right)}{\exp\left(\frac{-d*a}{\lambda_{Mo,Mo}sin\theta}+\frac{-d(a-1)}{\lambda_{Mo,TiS}sin\theta}\right)} \right]. \qquad \text{Equation 4.2}$$

Here we assume a constant overlayer thickness d comprised of a combination of Mo^0 and Ti_xS_y. The relative quantities of Mo^0 and Ti_xS_y are varied with $0 < a < 1$. This approach relies on the optimization of two unknowns, d and a. Figure 4.2.10 shows plots generated using the equation. Each plot corresponds to a fixed value of d that is specified at the top of each plot. The different curves correspond to different values of n, where $d * a$ is the effective thickness of Mo^0 and $d * (a - 1)$ is the effective thickness of Ti_xS_y. Initially, we set a to range from 0.1 to 0.9 in increments of 0.1 with the thickness d ranging from 25 to 30 Å in increments of 1 Å. The minimum deviation of the computed values from the experimental data, a value of 0.12, is observed at a thickness of 28 Å and a composition of 50% Mo^0, 50% Ti_xS_y.

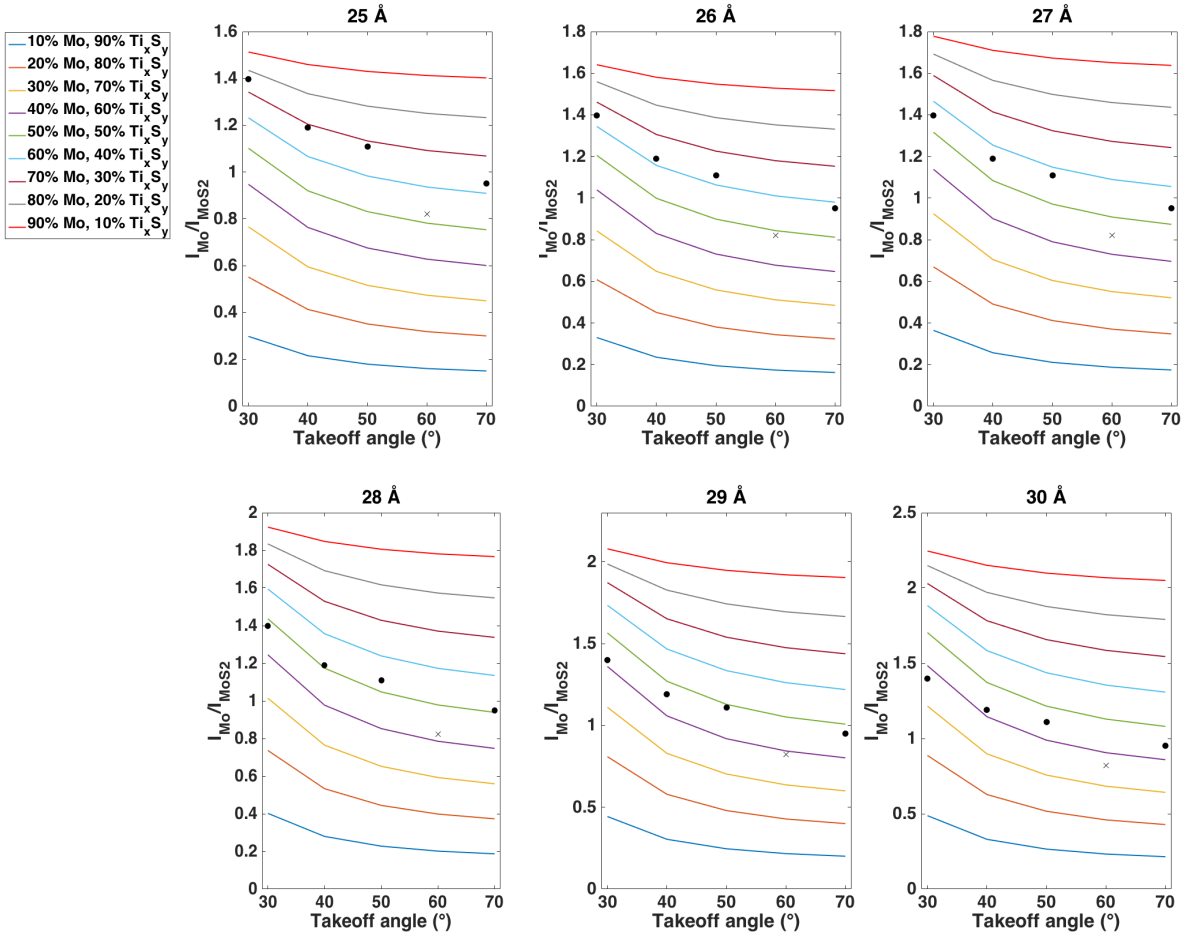

Figure 4.2.10. Theoretical $\frac{I_{Mo^0}}{I_{MoS_2}}$ ratios calculated as a function of angle at fixed overlayer thicknesses with varied compositions of Mo^0 and Ti_xS_y. Each plot represents a different total overlayer thickness. The curves correspond to increasing Mo composition (decreasing Ti_xS_y composition) from top to bottom from 0.1 to 0.9 in increments of 0.1. The data points are represented as black circles. The outlier at 60º is designated with an X and was not used to determine the best fit.

To determine more accurate values of composition and thickness, the second iteration of this analysis was conducted with composition ranging from $0.4 < a < 0.6$ in increments of 0.02. Thickness was varied from 27 to 29 Å. The minimum loss was found to be a value of 0.08 at a thickness of 27 and a composition of 56% Mo, 44% Ti_xS_y. The best fit model and the data are shown below in Figure 4.2.11. It is clear that this model is in better agreement with the

experimental data than the approach implemented in Figure 4.2.9 which assumed a Mo^0 overlayer. The coexistence of both the metal sulfide species and the Mo^0 chemical states at the same depth is consistent with the report by Durbin *et al.* on Cr/MoS_2.[8]

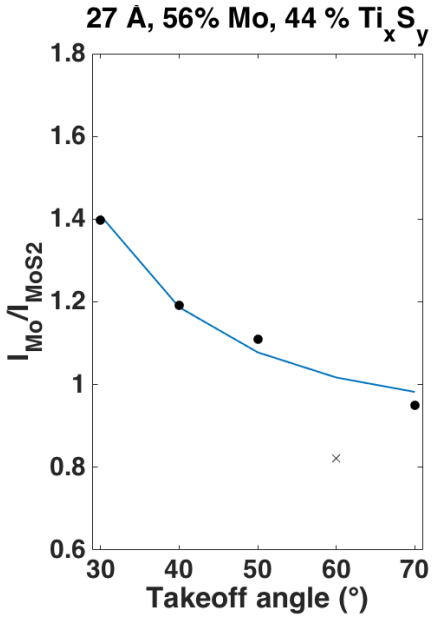

Figure 4.2.11. Best fit result of the second iteration of the model in Equation 1.2 performed with compositional increments of 2%. The curve is computed based on theoretical intensity ratios and the experimental data points are represented as black circles. The outlier at 60º is designated with an X and was not used to determine the best fit.

Next, we determine the thickness of the unreacted Ti layer remaining on the surface using the following equation to calculate the theoretical Ti/Mo intensity ratio:

$$\frac{I_{Ti}}{I_{MoS_2}} = \frac{I_{Ti_\infty}}{I_{MoS_{2\infty}}}\left[\frac{1-\exp\left(\frac{-d_{Ti}}{\lambda_{Ti,Ti}sin\theta}\right)}{\exp\left(\frac{-da}{\lambda_{Mo,Mo}sin\theta}+\frac{-d(a-1)}{\lambda_{Mo,TiS}sin\theta}\right)\exp\left(\frac{-d_{Ti}}{\lambda_{Mo,Ti}sin\theta}\right)}\right]. \qquad \text{Equation 4.3}$$

We note that the Ti 2*p* intensity measured is a superposition of both metallic Ti and Ti_xS_y. Deconvolution of the Ti 2*p* spectrum to resolve Ti from Ti_xS_y cannot be performed with accuracy in the available software given the asymmetric line shape of the peaks and the unknown binding energies and widths of the Ti-S states. As a result, an alternative method is used to determine I_{Ti} based on the results of the previous model. Assuming that Mo^0 comprises 56% of the compound interlayer between the substrate and Ti, we can calculate the total RSF-normalized intensity of the compound interlayer using $I_{compound}=I_{Mo^0}/0.56$. The remaining 44% of the signal from the compound interlayer is from some combination of Ti and S atoms that from the Ti_xS_y states. The relative quantities of Ti and S can be varied with a constant $0 < k < 0.44$ such that

$$I_{compound} = 0.56 * I_{Mo^0} + k * I_{Ti-S} + (0.44 - k) * I_{S-Ti} \qquad \text{Equation 4.4}$$

where I_{Ti-S} is the intensity of Ti atoms bonded to S in the compound layer, I_{S-Ti} is the intensity of S atoms bonded to Ti in the compound layer, and $(0.44 - k)/k$ is the S/Ti ratio. The value of $k * I_{Ti-s}$ is subtracted from the total experimental Ti intensity to determine what the metal overlayer intensity I_{Ti} would be at a given S/Ti ratio in the compound layer. The best fit generated by this model is shown in Figure 4.2.12. The best result is achieved at S/Ti = 0.37, d_{Ti} = 21 Å.

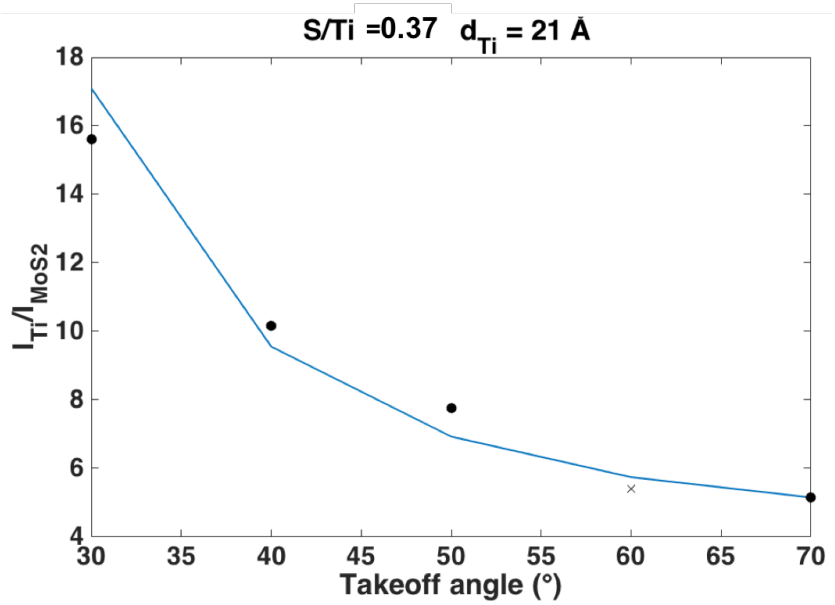

Figure 4.2.12. Best fit of $\frac{I_{Ti}}{I_{MoS_2}}$ as a function of angle with numerical optimization of S/Ti and d_{Ti} as variables

We note that there are a number of sources of error in these calculations such as spot-to-spot variability in XPS measurements due to surface roughness, errors in the fits of the data, and errors in the RSFs, and effective attenuation lengths which vary with angle. Furthermore, our model assumed a layered structure with abrupt interfaces between Ti, the compound layer (Ti_xS_y+M^0), and the substrate. In reality, the interface is likely to be graded where the relative composition of Ti, S, and Mo^0 species is not homogenous within a defined thickness region. Therefore, some deviation from the model would be expected. Electron energy loss spectroscopy (EELS) and transmission electron microscopy (TEM) data from Wu *et al.*[14] indicates that the Ti signal (L_{23} edge) decays as a function of depth in the MoS_2, meaning that there exists a gradient in Ti concentration.

STEM images with EDS data were acquired on our samples at NIST by Dr. Huairuo Zhang and Dr. Albert Davydov. Data acquired on a cross section of as-deposited Ti/MoS_2 is shown in

Figure 4.2.13. The image reveals the presence of a Mo-S rich amorphous layer in contact with MoS_2 and a Ti rich disordered layer on top of the Mo layer. The EDS line scan in (b) provides evidence of Ti diffusion into MoS_2 as well as S diffusion into Ti. This is in agreement with the results of our AR-XPS analysis which concluded that a compound layer of Mo and Ti_xS_y species exists. The data also supports our statement that the assumption of abrupt interfaces is not accurate since the STEM image shows that the interface between the Mo-rich layer and the Ti-rich layer is highly diffuse. While this contributes to some errors in the XPS analysis, nevertheless, the observation of diffuse interfaces does not invalidate our results since the structure is clearly layered. We also note that the disordered layers here appear thicker than the prediction made by XPS. This could likely be related to the fact that a thicker Ti layer was deposited on these samples (6.5 nm) or, less likely, due to damage caused by the ion milling process.

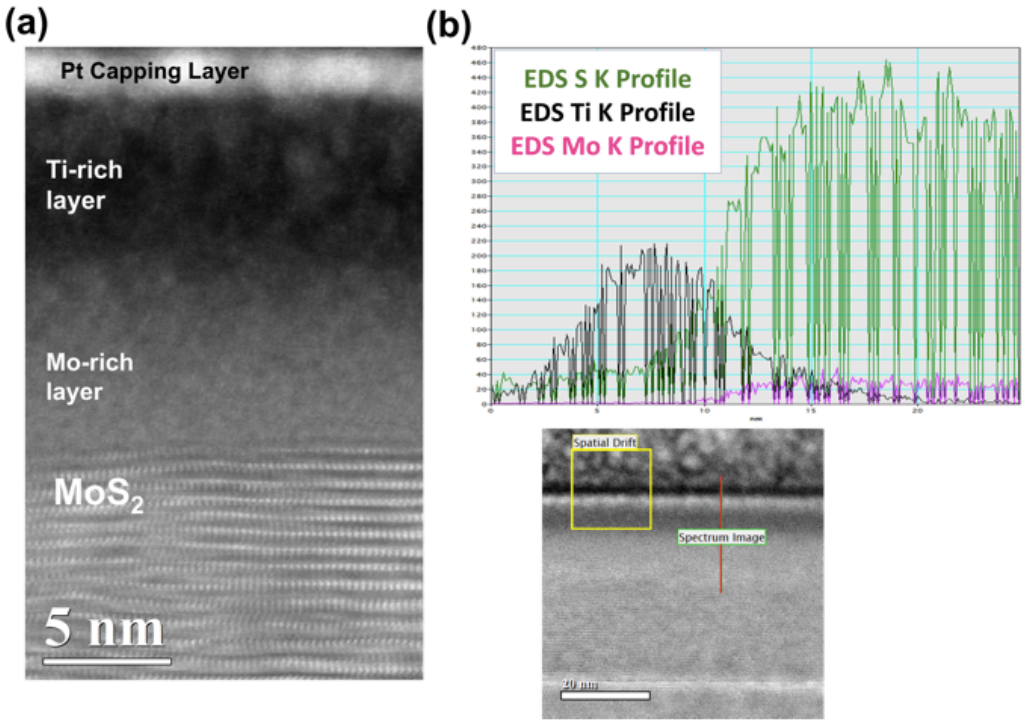

Figure 4.2.13. (a) STEM of as deposited Ti/MoS_2 and (b) Drift-corrected EDS line profile of the S, Ti, and Mo K-edge. The red line on the image below the plot shows the line where the scan was acquired. The yellow square represents the area monitored to correct for spatial drift.

4.2.3.3 Thermal Stability of UHV-Ti/MoS_2

To examine the effects of post-deposition annealing at different temperatures, the as-deposited Ti/MoS_2 samples were heated in the UHV chamber to 100, 300, and 600 °C consecutively. XPS data was acquired after each 30 minute heat treatment as shown in Figure 4.2.14(a). A slight increase in reaction products is observed after 100 °C. While this change is minor in comparison with the other annealing temperatures, it may have important implications for reliability of MoS_2 transistors as 100 °C is within the range of transistor operating temperatures (albeit at the upper extreme).[49] At 300 °C, we observe a clear increase in the Mo^0 intensity relative to that of the Mo-S state, accompanied by an overall broadening of the S 2*p* spectra as more Mo-S bonds are broken. Figure 4.2.14(b) highlights the increase in the total S/MoS_2 ratio, indicative of the increased diffusion of S to the surface. This will be addressed again in the angular resolved study.

The Ti 2*p* spectra exhibit broadening due to the superposition of the different Ti-S states and show a decrease in intensity with increasing temperature. The reason for the apparent increase in the Ti/MoS_2 intensity ratio in 4.2.14(b) is a result of the MoS_2 signal decreasing more significantly than the decrease of the Ti signal. The decrease in Ti intensity can be explained as a result of diffusion into the substrate as well as agglomeration. AFM images shown in Figure 4.2.15 are also indicative of the formation of clusters on the surface. This is similar to the result reported by Durbin *et al.*[21] in the case of Cr/MoS_2, where annealing to 650 °C drives the reaction between Cr and MoS_2 while simultaneously causing coalescence of the Cr-containing portion of the film.

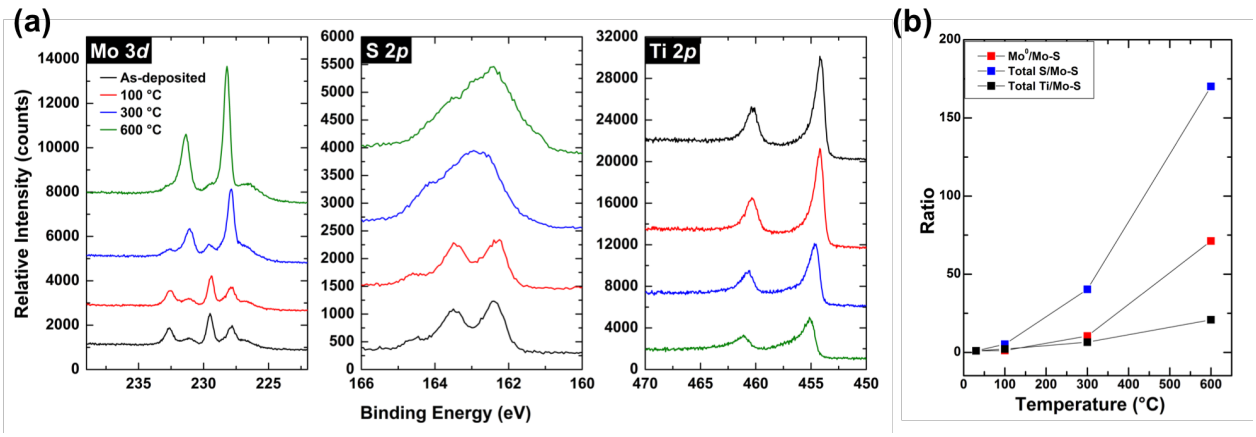

Figure 4.2.14. (a) Mo 3*d*, S 2*p*, and Ti 2*p* spectra acquired on as-deposited Ti/MoS_2 and after 30 minute anneals at three different temperatures. (b) Intensity ratios normalized to the as-deposited sample

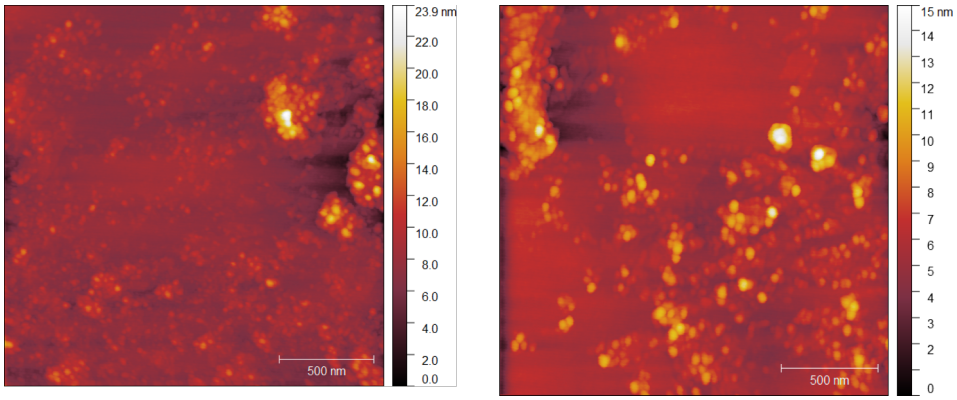

Figure 4.2.15. AFM images of two regions on a Ti/MoS_2 sample heated for 30 min at 600 °C. The scale bar represents 500 nm.

The core-level shift exhibited by the sample increases by another +0.36 eV after the final heating step at 600 °C, amounting to a total shift of +0.70 eV compared to the pristine MoS_2 surface. We note that while the sample was moved between initial XPS characterization and Ti deposition, the sample was maintained in the exact same position after Ti deposition and after each heat treatment. Therefore, the measured core-level shift after heating is not affected by potential spot-to-spot variability. Ti and Mo have been shown to be n-type dopants in MoS_2.[50-51] The extent

of the Fermi level shift is likely correlated with the amount of Ti and Mo incorporated in MoS_2 which clearly increases with temperature.

AR-XPS data was acquired on a separate Ti/MoS_2 sample that underwent a 30 minute anneal at 600 °C in the UHV chamber. The results are shown in Figure 4.2.16, and summary of the relative signal intensities is shown in Figure 4.2.17. We note that the spectra shown here exhibit a higher MoS_2 peak than the 600 ºC spectrum in Figure 4.2.14, however this sample was not heated sequentially to different temperatures prior to the 600 ºC anneal. Due to the evidence of agglomeration provided by the AFM images, the equations previously implemented to analyze the AR-XPS data acquired on the as-deposited sample cannot be applied in this case, as the assumption of layers of uniform thickness becomes invalid. The images also show the nonuniformity in the spatial distribution and size of the clusters resulting in high spot-to-spot variability in XPS. This is likely why the relative composition shown in Figure 4.2.17 fails to follow a clear trend as a function of angle particularly for the Mo chemical states.

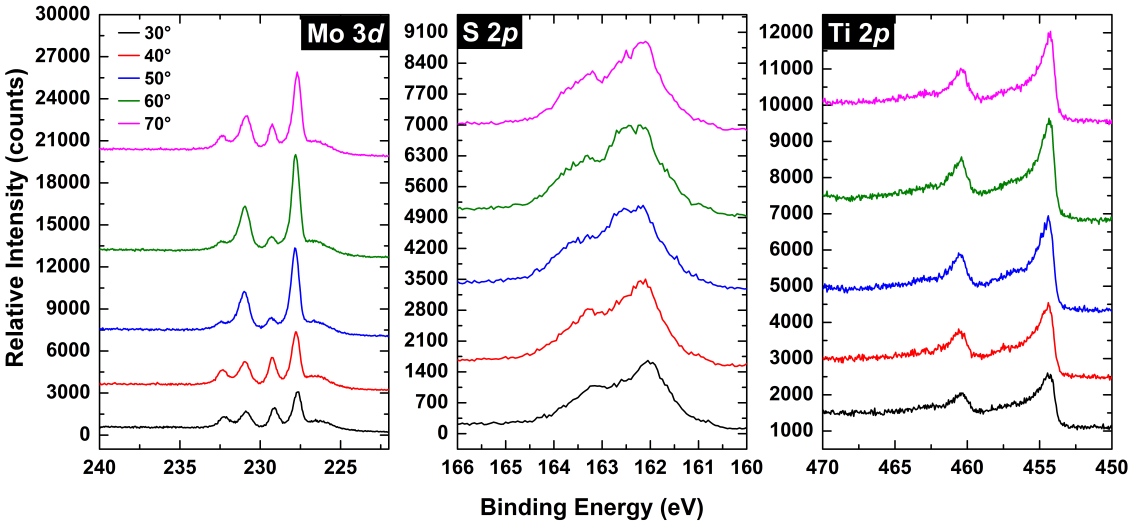

Figure 4.2.16. Angular resolved XPS of Ti/MoS_2 annealed to 600 °C for 30 minutes

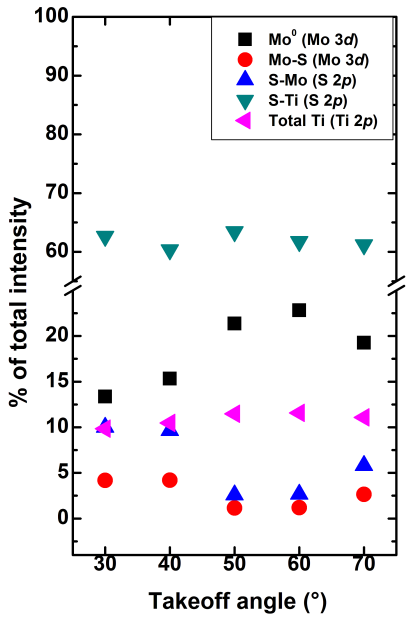

Figure 4.2.17. Percent of total intensity corresponding to different species in the Ti/MoS_2 sample annealed to 600 °C for 30 minutes

Figure 4.2.17 highlights the large amount of S-Ti species at all angles relative to the other chemical states. Given that the Ti signal comprises a much lower composition, this leads us to evaluate whether the assignment of the S-Ti chemical state is correct. In other words, all S in the system has been assumed to be bonded to Mo in the substrate or to Ti in the bulk, while this might not be the case. In their experiment on annealing Cr/MoS_2, Durbin *et al.*[8] observe a similar phenomenon as the S/Cr intensity ratio increases substantially with annealing temperature. They attribute this to the presence of S species adsorbed on the surface of the Cr overlayer. The $2p_{3/2}$ components of these species are found at around ~160.7-161.4 eV and are superimposed with the S-Cr chemical states in the S 2*p* spectrum causing broadening. Close examination of our S 2*p* spectrum in Figure 4.2.16 shows that the valley between the two components of the S 2*p* spectrum becomes better resolved as the measurement becomes less surface sensitive. This is consistent with

the presence of surface adsorbed S species. The sequential heating experiment in Figure 4.2.14 indicates that these chemical states first become prominent at 300 ºC.

STEM images of a sample heated to 400 ºC for 30 min is shown in Figure 4.2.18(a). The material appears to have partially recrystallized in the region above MoS_2. Additionally, a new phase appears to have formed at the interface between this layer and the Ti metal layer. The EELS data shown in (b) indicates that the compositions of S and Ti both decrease in this region. The HAADF intensity, that is dependent on the atomic number, reaches a maximum in this region providing evidence that it is comprised of mostly metallic Mo. The fast Fourier Transform images in (c) provides evidence of lattice ordering in the layer above MoS_2 that was not present prior to annealing. Further quantitative analysis with EELS, EDS, and FFT is needed to determine the composition and crystallographic properties of the layers.

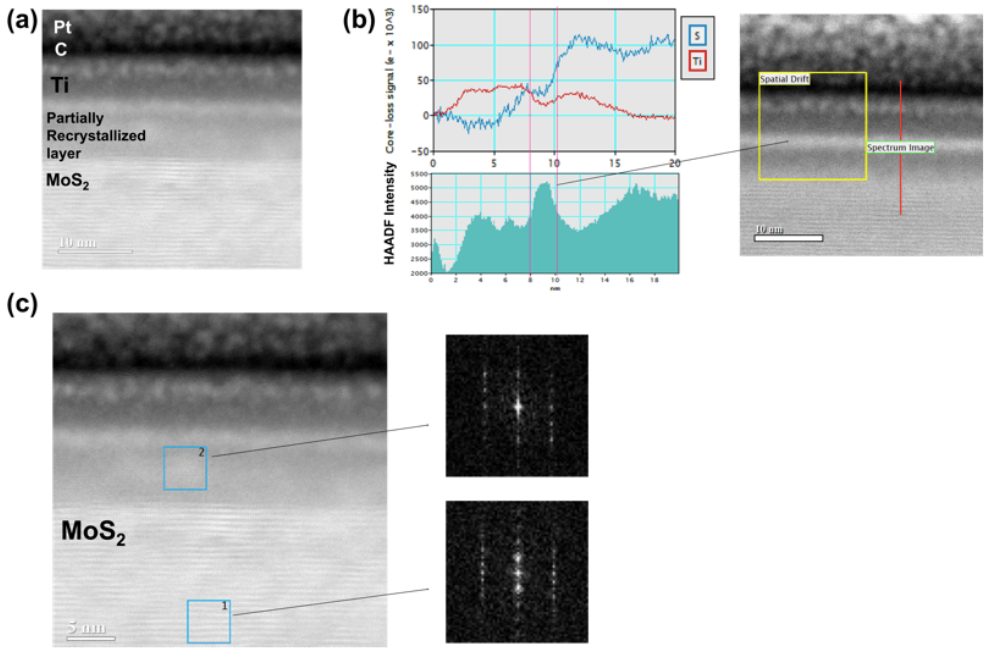

Figure 4.2.18. (a) STEM image of Ti/MoS_2 heated to 400 ºC for 30 minutes showing evidence of partial recrystallization and phase segregation. (b) Drift-corrected EELS and HAADF line scans acquired from the region indicated by the red line with the yellow square representing spatial drift. (c) Fast Fourier Transform of MoS_2 and partially recrystallized region

4.2.3.4 Study of the UHV Ni/MoS_2 Interface

Ni has been used as a contact to MoS_2 transistor in a number of reports and has been shown to exhibit favorable electronic properties.[1, 4, 15, 52-53] The interface chemistry of Ni on MoS_2 has been previously investigated, and ambiguity remains regarding the reactivity of the two materials. In an XPS study, McGovern *et al.*[12] observe that the valley between the spin-orbit split components of the S 2*p* spectra appears to be filled following the deposition of Ni on MoS_2 yet the Mo 3*d* line shape appears unchanged. This finding provides inconclusive evidence of chemical reaction. Using Auger electron spectroscopy, Kamaratos and Papageorgopoulos[16-17] report that no reaction occurs, however they observed diffusion of Ni into MoS_2 at temperatures between 600-800 K and agglomeration of the remaining Ni film above 800 K. English *et al.*[1] report that Ni/MoS_2 contacts degrade following thermal annealing, however since the anneal was performed in high-vacuum (10^{-5} Torr) and the degradation of the contact is attributed to the oxidation of Ni. Giannazzo *et al.*[53] observe significant improvement in device properties after annealing Ni/MoS_2 contacts at 150-220 ºC under a positive bias. Here we examine changes in interface chemistry and surface morphology that occur following annealing at different temperatures in UHV.

Our sequential heating experiment followed the same procedure applied to Ti in the previous section. The data is shown in Figure 4.2.19. An n-type core level shift of 0.14 eV is observed following the deposition of Ni. This is consistent with reports of Ni as an n-type contact despite its high work function.[15] In the as-deposited Ni/MoS_2, we observe the formation of a new feature on the low binding energy side of the Mo 3*d* peaks. The new feature is 0.74 eV to lower binding energy from the Mo-S state. We note that Mo^0 is ~1.2 eV to lower binding energy, indicating that the new state does not correspond to Mo^0 and is therefore not indicative of Mo-S bond scission. The intensity of this new peak is approximately 25% of the total Mo 3*d* intensity

and remains at approximately this value after heating to 100 ºC (< 1% decrease). As the sample is heated to 300 ºC, the new feature decreases in intensity to 7% of the total Mo 3*d* signal, and disappears entirely at 600 ºC. The differences in line shape are more apparent in the normalized spectra shown in Figure 4.2.20.

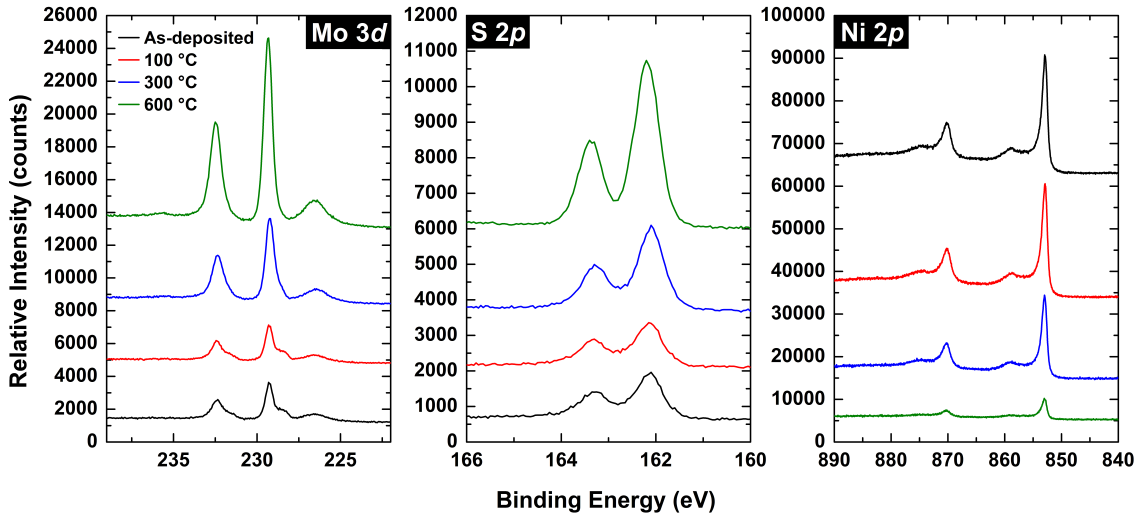

Figure 4.2.19. Mo 3*d*, S 2*p*, and Ni 2*p* spectra acquired on as-deposited Ti/MoS_2 and after 30 minute anneals at three different temperatures

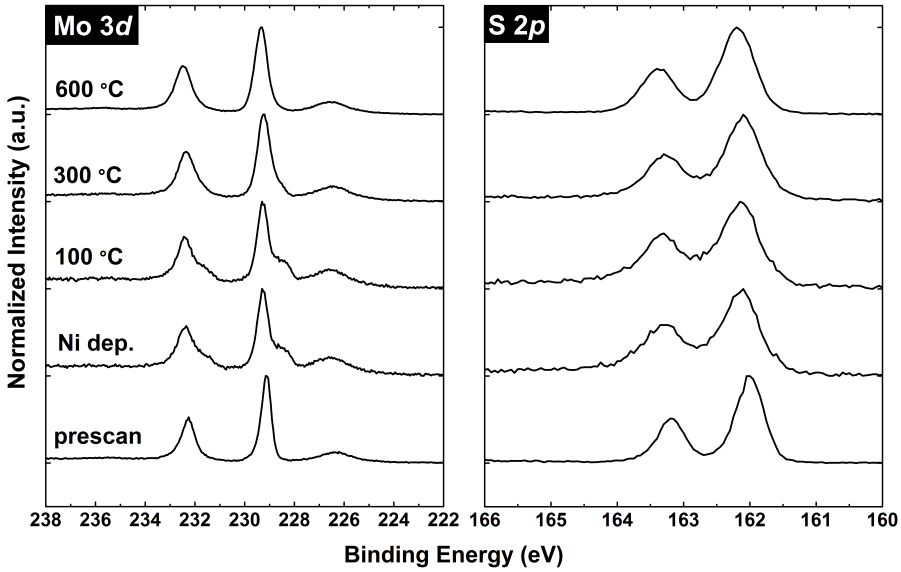

Figure 4.2.20. Normalized Mo 3d and S 2p spectra to highlight changes in line shape

In the S 2*p* peaks, broadening is observed following initial deposition due to the formation of new chemical states. The new chemical state is found at 0.15 eV to higher binding energy from the main S-Mo peak. This causes the filling valley between the $2p_{3/2}$ and $2p_{1/2}$ components. The new chemical state initially comprises 48% of the S 2*p* signal in the as-deposited condition and after heating to 100 °C. After heating at 300 °C it decreases to 33% and then disappears at 600 °C and the line shape of S 2*p* is restored to its pristine condition. The Ni 2*p* spectra show a drastic decrease in intensity with temperature as the Mo 3*d* and S 2*p* signals increase. As discussed previously in regard to Ti, a decrease in the metal overlayer signal can be indicative of diffusion into the substrate and/or the formation of islands which exposes the substrate. AFM images of Ni/MoS_2 before and after heating to 600 °C are shown in Figure 4.2.21 and provide evidence of agglomeration.

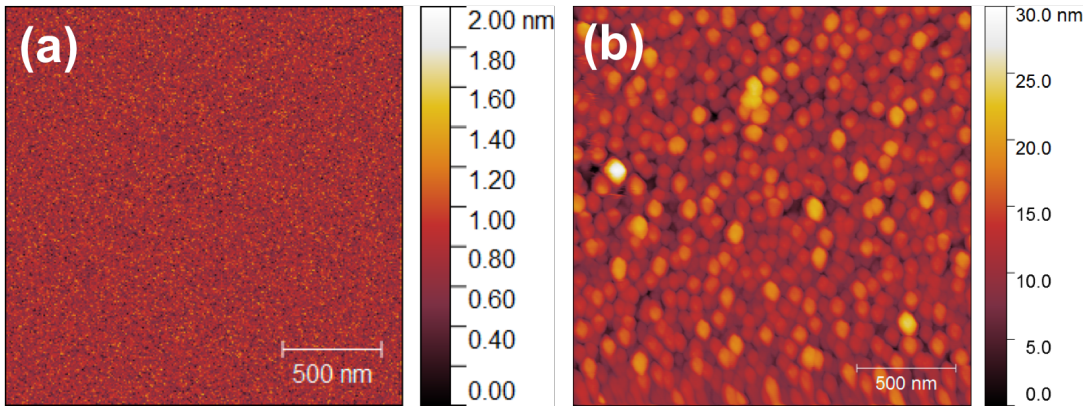

Figure 4.2.21. AFM images of Ni/MoS2 (a) as-deposited and (b) after heating to 600 °C in UHV.

As mentioned, others have reported the diffusion of Ni into MoS_2 occurring concurrently with island formation at high temperatures.[16-17] This is supported by TEM and EDS data acquired at the NIST shown in Figure 4.2.22 below before and after heating to 400 °C. Initially a ~ 1 nm layer of Ni is visible and after heating at 400 °C it appears to have possibly formed islands on the

surface, although the features are also potentially due to ion beam damage. Nevertheless, the layer is clearly no longer present on the sample after annealing. The EELS measurement was not very sensitive to the 1 nm of Ni initially present on the surface as shown in Figure 4.2.23. Therefore the amount of Ni diffused into MoS_2 is below the limit of detection, however the decreased quantity of Ni on the surface visible in the image provides some evidence that Ni diffused into the bulk of MoS_2.

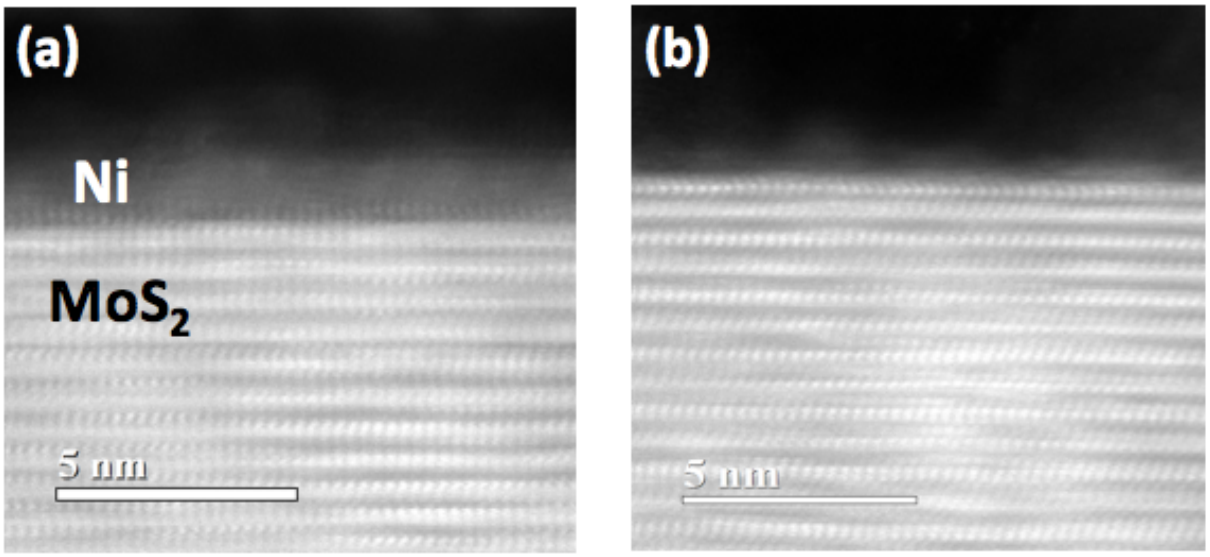

Figure 4.2.22. Cross section TEM image of Ni/MoS2 (a) as-deposited and (b) after heating to 400 °C

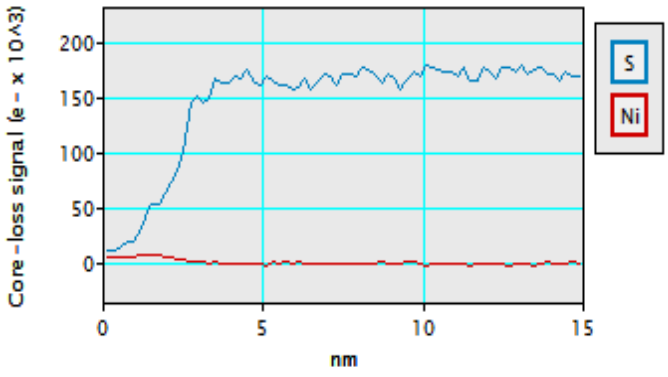

Figure 4.2.23. EELS line scan collected from TEM measurement in the as-deposited Ni/MoS_2 sample showing the low sensitivity to 1 nm of Ni on the surface.

Lince *et al.*[22] calculate a Gibbs free energy change of +2.3 kcal/mol for the reaction of MoS_2 with Ni to form Ni_3S_2 based on bulk equilibrium thermodynamics indicating that the reaction is thermodynamically unfavorable. We observe no Ni-S compounds based on the Ni 2p spectra. The binding energy of the main Ni 2*p* peak in metallic Ni compounds are all within 0.3 eV of Ni^0 making it difficult to identify new chemical states via spectral deconvolution of the 2*p* peaks alone.[54] In Ni compounds, the position of the satellite peak is highly sensitive to the anion in the compound. Nesbitt *et al.*[54] write that Ni^0 has a 2*p*-to- satellite separation of 5.8 eV and Ni bonded to S should have a separation of 6.5 eV. By applying fit parameters from a Ni^0 reference sample, we find that our Ni 2*p* spectra from all annealing temperatures reveals a separation of ~5.9 eV indicating that no detectable composition of bulk Ni-S is formed.

The Gibbs free energy value for the reaction of Ni with MoS_2 (+2.3 kcal/mol) is close to that of the reaction of Fe+MoS_2 to form FeS (+3.0 kcal/mol).[22] The Fe/MoS_2 system has been found to exhibit some degree of surface reactivity and the evolution of the XPS spectra with temperature exhibit similar trends. Lince *et al.*[10] report the formation of a Fe-S surface phase and S-vacancy defects in as-deposited Fe/MoS_2. In their Mo 3*d* spectrum in the as-deposited sample they observe the same chemical state that is found in our experiment that is 0.7 eV away from the main peak. This state is similar to what is observed in MoS_2 with sulfur vacancies.[55-57] If S atoms in MoS_2 are partially bonded with the surface metal layer, the neighboring Mo atom is not fully coordinated. This would arguably have the same effect as the presence of a sulfur vacancy. As their Fe/MoS_2 sample is annealed above 600 K, agglomeration was observed leading to the delamination of Fe from the substrate. This also causes disappearance of the new chemical states in Mo 3*d* and S 2*p*. While Lince *et al.* did not discuss the possibility of the diffusion of Fe into MoS_2, however they observe a similar decrease in the Fe 2*p*/Mo 3*d* ratio.

Dong *et al.*[23] observe a similar phenomenon in the Mo 3*d* and S 2*p* spectra following the deposition of Pd, a high work function metal that is also considered to be unreactive with MoS_2. In their spectra, there is an asymmetry on the low binding energy side of Mo 3*d* and on the high binding energy side of S 2*p*. They attribute this to the perturbation of the MoS_2 surface by the Pd layer due to a redistribution of charges, which presumably results in some degree of hybridization between the metal and the semiconductor that manifests in the core-level spectra. While no study of thermal stability was reported, this finding also supports the idea of the formation of surface states.

Our results presented in this section provide evidence of the formation of Ni-S surface states exhibiting similarity to results previously reported for Fe/MoS_2 and Pd/MoS_2. In its as-deposited state, Ni is found to interact similarly with WSe_2 as shown in Appendix B. Annealing the Ni/MoS_2 contact appears to decouple the interface, restoring the line shapes of the core levels to their pristine form while promoting the agglomeration of the overlayer as shown by AFM and STEM. Despite the disappearance of the new chemical states and delamination of the overlayer from the substrate, the n-type core level shift remains. This is likely due to the diffusion of Ni into MoS_2 layers near the interface.

4.2.3.5 Preliminary Study of the UHV Au/MoS_2 Interface

Au has a well-documented affinity to bond with sulfur-terminated compounds.[58-62] However, due to the stability of Mo-S bonds in MoS_2, Au is typically thought to exhibit a van der Waals gap with MoS_2 exhibiting no chemical reactions at the interface and a lack of orbital overlap.[11, 19, 63-65] The Gibbs free energy of formation of Au_2S has a value of -58.07 kJ/mol whereas MoS_2 has a value of ΔG=-117.99 kJ/mol, making it the more favorable state.[19] Lince *et al.*[22], McDonnell *et al.*[18], Smyth *et al.*[19], and Domask *et al.*[33] explicitly state that no reaction occurs

between the two materials. Despite its presumed large tunnel barrier for electron injection[11, 64], English *et al.*[1] have found that UHV-deposited Au contacts (annealed at 300 °C for two hours) exhibit the lowest electrical contact resistance in comparison with Ti, Ni, and Sc contact metals processed identically. Radisavljevic *et al.*[2] found that annealed Au contacts to MoS_2 show a factor of 10 decrease in contact resistance. This warrants an investigation of the chemical composition of the Au/MoS_2 interface before and after thermal annealing.

A sample of UHV-deposited Au on MoS_2 underwent 600 °C annealing in UHV. In Figure 4.2.24(a), we compare the Au 4*f* spectrum acquired on as-deposited Au/MoS_2 to a reference Au 4*f* spectrum acquired from an infinitely thick Au film deposited on Si in UHV. While the low binding energy sides of both the $4f_{7/2}$ and $4f_{5/2}$ components overlap almost perfectly, we observe an asymmetry on the high binding energy side of each peak. We note that the background of MoS_2 in the Au 4*f* binding energy region is perfectly flat, and this observed asymmetry is therefore not due to a contribution from the background signal of the MoS_2 substrate. Therefore, the asymmetry is believed to be due to a new chemical state superimposed on the high binding energy side of the Au 4*f* peaks.

In the S 2*p* and Mo 3*d* spectra, we compare the as-deposited sample to a reference spectrum of pristine MoS_2. In the S 2*p* spectrum, we observe a filling of the spin-orbit splitting valley between the $2p_{3/2}$ and $2p_{1/2}$ components. The Mo 3*d* spectrum exhibits a slight asymmetry on the low binding energy side. Spectral deconvolution identifies the binding energy of this chemical state to be ~0.6 eV away from the main peak. This is the same as what was observed following the deposition of Ni on MoS_2. In Figure 3.3.17(b), the as-deposited Au/MoS_2 samples shown in (a) are compared with Au/MoS_2 after annealing at 600 °C for 30 min. Upon heating, the degree of asymmetry in Au 4*f* appears to be about the same as its as-deposited state, while the valley in the

S 2*p* spectrum is nearly restored. This is apparent in (c) where the spectra acquired after annealing are compared with the spectra acquired on pristine samples shown in (a). Asymmetry in the Mo 3*d* spectrum appears to increase while the S 2*s* peak increases relative to the noise, indicating the superposition of another chemical state. Unlike with Ni/MoS_2, the asymmetries in all core levels do not vanish after heating indicating a fundamental difference in the interaction mechanism or in the thermal stability of the interaction.

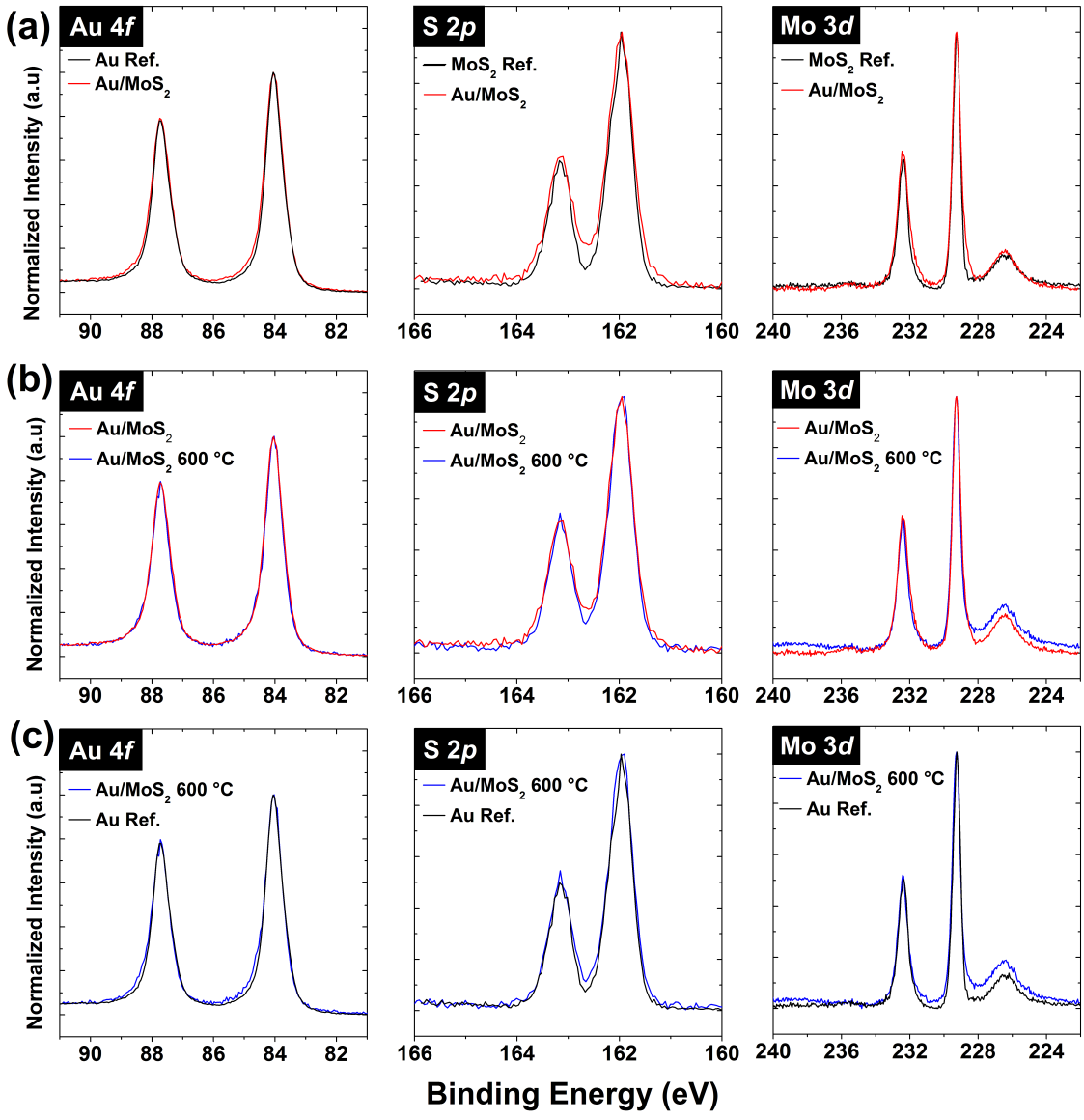

Figure 4.2.24. XPS core level spectra of Au 4*f*, S 2*p*, and Mo 3*d* comparing (a) reference samples to as-deposited Au/MoS_2 and (b) as-deposited Au/MoS_2 to Au/MoS_2 after annealing at 600 °C

The changes in the line shapes of the three spectra lead us to examine two possibilities. The first is the possibility of local doping of the MoS_2 by Au. Gong *et al.*[66] have shown that Au forms islands on MoS_2 with inhomogeneous interfacial spacing between the islands and the substrate. Nonuniformity in surface coverage and spacing between the substrate and metal can lead to variations in doping within the region sampled by XPS which could lead to the superposition of two Mo 3*d* peaks corresponding to n- and p- type regions. However, doping would be expected to cause a Fermi level shift which would affect all core levels equally, which is not what is observed here. The asymmetry in S 2*p* occurs on the high binding energy side of the spectrum whereas the opposite is observed for Mo 3*d*.

Given the known tendency of S to bond with Au and the previously observed behavior of Ni/MoS_2, the second possibility to consider is the formation of Au-S bonds. Au grown epitaxially on MoS_2 has been shown to result in misfit dislocations suggesting that bonding must be stronger than van de Waals forces.[67] DFT calculations by Zhou *et al.* show that the Au-S bond strength in the $Au\text{-}MoS_2$ system is stronger than the van der Waals forces between the MoS_2 layers.[68] This is supported by Desai *et al.*[69] who show that Au deposited on MoS_2 can be used instead of scotch tape to exfoliate flakes. If Au-S bond formation occurs, the asymmetry in the Au 4*f* and S 2*p* is due to Au-S chemical states. The asymmetry in the Mo 3*d* spectrum is similar to what is observed in Ni/MoS_2 in the previous section. We therefore attribute it to Mo atoms that are not fully coordinated by S due to S interactions with the metal overlayer.

To examine the viability of Au-S bonding, the spectra are deconvoluted to determine the positions and amplitudes of the chemical states and to calculate an approximate value of S/Mo ratio. Fits of the Au 4*f* and S 2*p* spectra of the as-deposited and 600 °C annealed samples are shown in Figure 3.3.18. These fits are in agreement of Lustemberg *et al.*[61] who report a binding energy

of 84.7 eV for Au 4*f* and Vericat *et al.*[62] who report a S 2*p* binding energy at ~162.1-162.2 eV for Au-S bonds. Using the RSF-normalized intensity ratios, the S/Au ratio is calculated to be 2.7 in both the as-deposited state and after annealing to 600 °C. We note that the predicted thermodynamically favorable S/Au ratio of 0.5 corresponding Au_2S. Therefore the stoichiometry we calculate is not consistent with a bulk Au-S compound at either temperature. The primary difference observed between the as-deposited and 600 °C spectra is narrowing of the Gaussian widths of the Au-S states after annealing in both the S 2*p* and Au 4*f* core levels. This narrowing could be attributed to an increase in bond ordering with temperature.

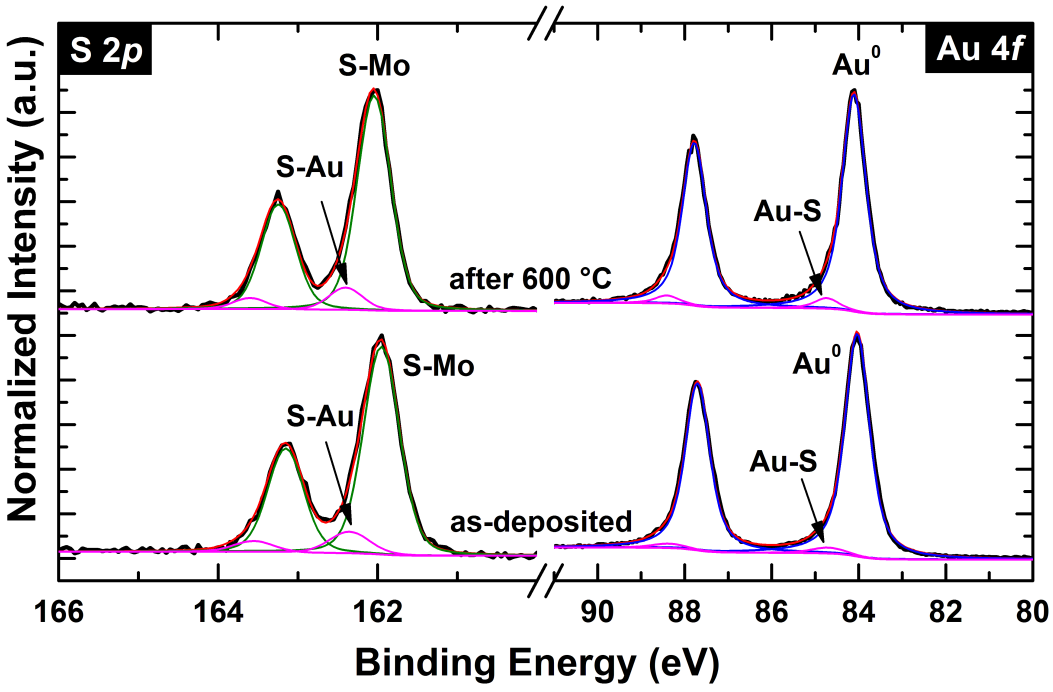

Figure 4.2.25. Spectral deconvolution of S 2*p* and Au 4f chemical states in the as-deposited sample and after annealing to 600 °C.

Popov *et al.*[11] comment that in multilayer MoS_2, Au can chemically bond to non-saturated S atoms at the edge, making an edge-contact geometry a potential route to better transport for multilayer devices. The bulk geological sample has step edges making this a possible explanation

for the observed formation of Au-S bonds. Since no Mo-S bonds need not be broken for this reaction to occur, Mo^0 is not observed. We note if the mechanism of bonding is by edge-contact formation, our observed formation of Au-S bonds does not explain the superior performance of Au/MoS_2 contacts in the work by English *et al*.[1] This is because their work examined top contacts to a monolayer of MoS_2 in which there are no step edges. Previous XPS work by Smyth *et al.*[19] in which Au was deposited on MoS_2 in UHV concluded that no chemical bonding occurs. If the Au-S bonding occurs only at step edges or defects, this was likely undetected in their experiment since a much smaller XPS spot size (~300 μm) was used in their system. Another possible explanation to reconcile our findings and those of Smyth *et al*. and English *et al*. is that bonding occurs on the basal plane but to a lesser extent. This would also explain why Smyth *et al*. did not detect it by XPS but why Au/MoS_2 contact is improved upon annealing in monolayer flakes. Further study is necessary to achieve a conclusive understanding of the nature of Au-MoS_2 interactions. A study of the evolution of surface morphology could also shed light on the observed changes in the XPS spectra. Nevertheless, this work highlights the possibility of Au-S interactions at room temperature with improved ordering upon annealing.

4.2.4 Conclusion and Future Work

This chapter provides a detailed analysis of the Ti/MoS_2 interface chemistry. While the reactive nature of this interface has been previously documented[12-14], the chemical composition of the interface and the spatial distribution of the chemical species had never been explored in detail. Furthermore, no chemical analysis of the effects of annealing has been reported. It been previously reported that annealing has detrimental effects on electrical contact resistance. We see that in the as-deposited state the interface is a disordered mixture of different chemical states with compositional grading from Mo-rich to Ti-rich at the top. Our results show drastic changes in

interface chemistry upon annealing, resulting in the crystallization of a new compound and segregation of compositionally different layers. This is unlike Au, which appears to maintain the same interface chemistry before and after annealing. Here we find that drastic changes in interface chemistry occur when annealing Ti/MoS_2 contacts. The disorder of the MoS_2 lattice is a likely explanation for the poor contact resistance measured in annealed UHV Ti contacts by English *et al*.[1] Understanding interface chemistry is an essential step in improving post-deposition processing procedures for achieving lower resistance contacts. Additional analysis of the STEM results is necessary for understanding the exact crystallographic and chemical changes that occur as a result of annealing.

While work in this chapter was focused on the effects of annealing from the perspective of device processing, the observed changes in the Ti/MoS_2 XPS spectra after annealing at 100 ºC suggest that heat generated during device operation is sufficient to elicit changes in interface chemistry with potential detriment to device properties. This implies that highly reactive contacts such as UHV-Ti are not optimal for long term device stability, however this would require further study. We also report that chemical interactions occur at the MoS_2 interface with Ni and Au contacts. The interaction at the Ni/MoS_2 interface vanishes upon annealing while the Au/MoS2 interface is thermally stable at 600 ºC. Suggestions for other future experiments based on our findings are summarized below.

4.2.4.1 Evolution of the Work Function at Ti/MoS_2 Contacts

As discussed in Section 4.2.3.1, core level shifts following the deposition of Ti on MoS_2 deviate from the band bending predicted by the Schottky Mott model. We calculate band bending by taking the difference between the MoS_2 and Ti work functions, however the contribution of the chemical states at the interface is overlooked. A more rigorous understanding of the band

alignment at the interface can be achieved by taking work function measurements and core level XPS on a pristine MoS_2 surface and after sequential Ti depositions until an infinitely thick film is deposited. This can be achieved in-situ using ultra-violet photoelectron spectroscopy. A similar study has been previously conducted by Zhou *et al.*[70] no changes in interface chemistry were reported.

4.2.4.2 Interaction Mechanism of Minimally Reactive Metals

Both Ni and Au are reported to be nonreactive with MoS_2, yet our results suggest otherwise. As noted previously, geological samples have large bunched step edges (apparent in Figure 4.2.6) with a high density of dangling bonds, providing a preferential site for bonding with metal adlayers. To determine whether the metal/MoS_2 interactions which we observed are confined to large defects, XPS can be performed in a system with variable spot size such as the PHI VersaProbe III in the NanoMaterials Characterization Facility. As the spot size is decreased, presumably the probability of probing an area with large defects will be decreased. The relative intensities of the new chemical states which are indicative of metal/MoS_2 interactions can be monitored as a function of spot size to determine if a correlation exists between the spot size and the detection of additional chemical states that suggest metal/MoS_2 bonding. If no correlation is found, this provides strong evidence for metal-MoS_2 interactions along the basal plane or along atomic step edges. Another option is to use the XPS mapping capability of the PHI system. This will also present the possibility of directly correlating spectral features with sample morphology.

4.2.4.3 Device-Relevant Properties and Processes

The focus of this chapter was on chemical characterization of UHV-deposited and annealed metal/MoS_2 interfaces, however the motivation for this work stems from device applications. The overarching goal of these interface chemistry studies is to aid the optimization of post-contact

annealing procedures for enhanced transport properties by providing insight into the changes that occur at the interface on the atomic scale. To establish a clear process-structure-properties relationship, interface chemistry analysis by XPS (ideally supplemented by TEM and EDS as discussed) should be performed in parallel with characterization of electrical and thermal transport properties, similar to the study executed on Ti/graphene in Chapter 3.2 where XPS, TLM, and TDTR were performed on identically processed samples. This will allow for a correlation of chemical composition and band alignment with device properties, enabling us to understand which processes result in optimal properties and to identify the underlying physical mechanism. Smyth *et al.*[71] have performed a similar type of study on the Pd/WSe_2 interface. They showed that while a reaction is not observed at room temperature, annealing promotes a reaction to form $PdSe_x$ which changes the character of the contact from Ohmic to Schottky.

The effects of thermal annealing certainly depend not only on the type of metal and annealing temperature, but also on contact deposition conditions as well as the annealing conditions. The vast majority of devices are processed with contact deposition in high vacuum which results in drastically different interface chemistry.[13, 19] Furthermore, post-contact annealing is typically performed in high vacuum, forming gas, or an inert ambient.[1-2, 4] The study by Smyth *et al.*[71] showed that annealing in forming gas was far more effective in promoting a reaction between Pd and WSe_2. Therefore, future work should examine the effects process variables other than temperature including a combination of different contact deposition conditions and annealing ambients by performing XPS in parallel with device characterization as suggested previously. The findings of such a study would be more widely applicable than one solely conducted in UHV due to the prevalence of non-UHV processing conditions. This could be implemented by depositing

contacts in the UVA Microfabrication Laboratory (cleanroom) and annealing them in the reaction chamber of the PHI VersaProbe III in the NMCF in UHV and other inert gases.

4.2.5 References

1. English, C. D.; Shine, G.; Dorgan, V. E.; Saraswat, K. C.; Pop, E., Improved Contacts to MoS2 Transistors by Ultra-High Vacuum Metal Deposition. *Nano Letters* **2016,** *16* (6), 3824-3830.
2. Radisavljevic, B.; Radenovic, A.; Brivio, J.; Giacometti, V.; Kis, A., Single-layer MoS2 transistors. *Nat Nano* **2011,** *6* (3), 147-150.
3. Abraham, M.; Mohney, S. E., Annealed Ag contacts to MoS2 field-effect transistors. *Journal of Applied Physics* **2017,** *122* (11), 115306.
4. Han, J.; Lee, J.; Lee, J.; Woo, H.; Kim, J.; Jo, Y.; Cho, S.; Kim, H.; Kim, H.; Pawar, S. M.; Inamdar, A. I.; Jung, W.; Im, H., Electrical properties of N2- and H2 -annealed bulk MoS2/metal junctions. *Journal of the Korean Physical Society* **2015,** *67* (7), 1228-1231.
5. Qiu, H.; Pan, L.; Yao, Z.; Li, J.; Shi, Y.; Wang, X., Electrical characterization of back-gated bi-layer MoS2 field-effect transistors and the effect of ambient on their performances. *Applied Physics Letters* **2012,** *100* (12), 123104.
6. Li, H.-M.; Lee, D.-Y.; Choi, M. S.; Qu, D.; Liu, X.; Ra, C.-H.; Yoo, W. J., Metal-Semiconductor Barrier Modulation for High Photoresponse in Transition Metal Dichalcogenide Field Effect Transistors. *Scientific Reports* **2014,** *4*, 4041.
7. Markov, M.; Zebarjadi, M., Thermoelectric transport in graphene and 2D layered materials. *Nanoscale and Microscale Thermophysical Engineering* **2018**, 1-11.
8. Durbin, T. D.; Lince, J. R.; Didziulis, S. V.; Shuh, D. K.; Yarmoff, J. A., Soft X-ray photoelectron spectroscopy study of the interaction of Cr with MoS2(0001). *Surface Science* **1994,** *302* (3), 314-328.
9. Lince, J. R.; Stewart, T. B.; Fleischauer, P. D.; Yarmoff, J. A.; Taleb‐Ibrahimi, A., The chemical interaction of Mn with the MoS2(0001) surface studied by high‐resolution photoelectron spectroscopy. *Journal of Vacuum Science & Technology A* **1989,** *7* (3), 2469-2474.
10. Lince, J. R.; Stewart, T. B.; Hills, M. M.; Fleischauer, P. D.; Yarmoff, J. A.; Taleb-Ibrahimi, A., Photoelectron spectroscopic study of the interaction of thin Fe films with the MoS2(0001) surface. *Surface Science* **1989,** *223* (1), 65-81.
11. Popov, I.; Seifert, G.; Tománek, D., Designing Electrical Contacts to MoS2 Monolayers: A Computational Study. *Physical Review Letters* **2012,** *108* (15), 156802.
12. McGovern, I. T.; Dietz, E.; Rotermund, H. H.; Bradshaw, A. M.; Braun, W.; Radlik, W.; McGilp, J. F., Soft X-ray photoemission spectroscopy of metal-molybdenum bisulphide interfaces. *Surface Science* **1985,** *152-153*, 1203-1212.
13. McDonnell, S.; Smyth, C.; Hinkle, C. L.; Wallace, R. M., MoS2–Titanium Contact Interface Reactions. *ACS Applied Materials & Interfaces* **2016,** *8* (12), 8289-8294.
14. Wu, R. J.; Udyavara, S.; Ma, R.; Wang, Y.; Chhowalla, M.; Koester, S. J.; Neurock, M.; Mkhoyan, K. A., An Inside Look at the Ti-MoS2 Contact in Ultra-thin Field Effect Transistor with Atomic Resolution. *arXiv preprint arXiv:1807.01377* **2018**.
15. Das, S.; Chen, H.-Y.; Penumatcha, A. V.; Appenzeller, J., High Performance Multilayer MoS2 Transistors with Scandium Contacts. *Nano Letters* **2013,** *13* (1), 100-105.
16. Kamaratos, M.; Papageorgopoulos, C., A study of the behavior of Fe and Ni on MoS2. *Solid State Communications* **1984,** *49* (7), 715-718.
17. Papageorgopoulos, C.; Kamaratos, M., Adsorption studies of Ni on MoS2 and O2 on Ni-covered MoS2. *Surface Science* **1985,** *164* (2), 353-366.

18. McDonnell, S.; Addou, R.; Buie, C.; Wallace, R. M.; Hinkle, C. L., Defect-dominated doping and contact resistance in MoS2. *ACS nano* **2014,** *8* (3), 2880-2888.
19. Smyth, C. M.; Addou, R.; McDonnell, S.; Hinkle, C. L.; Wallace, R. M., Contact Metal–MoS2 Interfacial Reactions and Potential Implications on MoS2-Based Device Performance. *The Journal of Physical Chemistry C* **2016,** *120* (27), 14719-14729.
20. Kaushik, N.; Nipane, A.; Basheer, F.; Dubey, S.; Grover, S.; Deshmukh, M. M.; Lodha, S., Schottky barrier heights for Au and Pd contacts to MoS2. *Applied Physics Letters* **2014,** *105* (11), 113505.
21. Durbin, T. D.; Lince, J. R.; Yarmoff, J. A., Chemical interaction of thin Cr films with the MoS2(0001) surface studied by x‐ray photoelectron spectroscopy and scanning Auger microscopy. *Journal of Vacuum Science & Technology A* **1992,** *10* (4), 2529-2534.
22. Lince, J. R.; Carré, D. J.; Fleischauer, P. D., Schottky-barrier formation on a covalent semiconductor without Fermi-level pinning: The metal-${\mathrm{MoS}}_{2}$(0001) interface. *Phys. Rev. B* **1987,** *36* (3), 1647-1656.
23. Dong, H.; Gong, C.; Addou, R.; McDonnell, S.; Azcatl, A.; Qin, X.; Wang, W.; Wang, W.; Hinkle, C. L.; Wallace, R. M., Schottky Barrier Height of Pd/MoS2 Contact by Large Area Photoemission Spectroscopy. *ACS Applied Materials & Interfaces* **2017,** *9* (44), 38977-38983.
24. Carlsson, J.-O.; Martin, P. M., Chapter 7 - Chemical Vapor Deposition. In *Handbook of Deposition Technologies for Films and Coatings (Third Edition)*, Martin, P. M., Ed. William Andrew Publishing: Boston, 2010; pp 314-363.
25. Freedy, K. M.; Litwin, P. M.; McDonnell, S. J., (Invited) In-Vacuo Studies of Transition Metal Dichalcogenide Synthesis and Layered Material Integration. *ECS Transactions* **2017,** *77* (8), 11-25.
26. http://kolxpd.kolibrik.net/.
27. Nakamura-Messenger, K.; Keller, L.; Messenger, S.; Rubin, A.; Choi, B.-G.; Petaev, M.; Clemett, S.; Zhang, S.; Rahman, Z.; Oikawa, K., The Formation of Wassonite: A New Titanium Monosulfide Mineral in the Yamato 691 Enstatite Chondrite. In *Workshop on Formation of the First Solids in the Solar System*, Kauai, HI; United States, 2011.
28. Nakamura-Messenger, K.; Clemett, S. J.; Rubin, A. E.; Choi, B.-G.; Zhang, S.; Rahman, Z.; Oikawa, K.; Keller, L. P., Wassonite: A new titanium monosulfide mineral in the Yamato 691 enstatite chondrite. *American Mineralogist* **2012,** *97* (5-6), 807-815.
29. Endo, K.; Ihara, H.; Watanabe, K.; Gonda, S.-I., XPS study of one-dimensional compounds: TiS3. *Journal of Solid State Chemistry* **1982,** *44* (2), 268-272.
30. Hawkins, C. G.; Whittaker-Brooks, L., Controlling Sulfur Vacancies in TiS2–x Cathode Insertion Hosts via the Conversion of TiS3 Nanobelts for Energy-Storage Applications. *ACS Applied Nano Materials* **2018,** *1* (2), 851-859.
31. Gonbeau, D.; Guimon, C.; Pfister-Guillouzo, G.; Levasseur, A.; Meunier, G.; Dormoy, R., XPS study of thin films of titanium oxysulfides. *Surface Science* **1991,** *254* (1–3), 81-89.
32. Fleet, M. E.; Harmer, S. L.; Liu, X.; Nesbitt, H. W., Polarized X-ray absorption spectroscopy and XPS of TiS3: S K- and Ti L-edge XANES and S and Ti 2p XPS. *Surface Science* **2005,** *584* (2), 133-145.
33. Domask, A. C.; Gurunathan, R. L.; Mohney, S. E., Transition Metal–MoS2 Reactions: Review and Thermodynamic Predictions. *Journal of Electronic Materials* **2015,** *44* (11), 4065-4079.
34. Zhang, Z.; Yates, J. T., Band Bending in Semiconductors: Chemical and Physical Consequences at Surfaces and Interfaces. *Chemical Reviews* **2012,** *112* (10), 5520-5551.

35. Addou, R.; McDonnell, S.; Barrera, D.; Guo, Z.; Azcatl, A.; Wang, J.; Zhu, H.; Hinkle, C. L.; Quevedo-Lopez, M.; Alshareef, H. N.; Colombo, L.; Hsu, J. W. P.; Wallace, R. M., Impurities and Electronic Property Variations of Natural MoS2 Crystal Surfaces. *ACS Nano* **2015,** *9* (9), 9124-9133.
36. Michaelson, H. B., The work function of the elements and its periodicity. *Journal of Applied Physics* **1977,** *48* (11), 4729-4733.
37. Eastman, D. E., Photoelectric work functions of transition, rare-earth, and noble metals. *Physical Review B* **1970,** *2* (1), 1.
38. McDonnell, S.; Azcatl, A.; Addou, R.; Gong, C.; Battaglia, C.; Chuang, S.; Cho, K.; Javey, A.; Wallace, R. M., Hole Contacts on Transition Metal Dichalcogenides: Interface Chemistry and Band Alignments. *ACS Nano* **2014,** *8* (6), 6265-6272.
39. Rhoderick, E. H., Metal-semiconductor contacts. *IEE Proceedings I - Solid-State and Electron Devices* **1982,** *129* (1), 1.
40. Addou, R.; Colombo, L.; Wallace, R. M., Surface Defects on Natural MoS2. *ACS Applied Materials & Interfaces* **2015,** *7* (22), 11921-11929.
41. Cressie, N. A. C.; Whitford, H. J., How to Use the Two Sample t-Test. *Biometrical Journal* **1986,** *28* (2), 131-148.
42. Freedy, K. M.; Beechem, T. E.; Litwin, P. M.; Sales, M. G.; Huang, M.; Ruoff, R. S.; McDonnell, S. J., Unraveling Chemical Interactions between Titanium and Graphene for Electrical Contact Applications. *ACS Applied Nano Materials* **2018,** *1* (9), 4828-4835.
43. Hsu, A. L.; Koch, R. J.; Ong, M. T.; Fang, W.; Hofmann, M.; Kim, K. K.; Seyller, T.; Dresselhaus, M. S.; Reed, E. J.; Kong, J.; Palacios, T., Surface-Induced Hybridization between Graphene and Titanium. *ACS Nano* **2014,** *8* (8), 7704-7713.
44. Himpsel, F. J.; McFeely, F. R.; Taleb-Ibrahimi, A.; Yarmoff, J. A.; Hollinger, G., Microscopic structure of the SiO_2/Si interface. *Physical Review B* **1988,** *38* (9), 6084-6096.
45. Vitchev, R. G.; Pireaux, J. J.; Conard, T.; Bender, H.; Wolstenholme, J.; Defranoux, C., X-ray photoelectron spectroscopy characterisation of high-k dielectric Al2O3 and HfO2 layers deposited on SiO2/Si surface. *Applied Surface Science* **2004,** *235* (1), 21-25.
46. Jablonski, A., NIST Electron Effective-Attenuation-Length Database. **2011**.
47. Least Absolute Deviation Regression. In *The Concise Encyclopedia of Statistics*, Springer New York: New York, NY, 2008; pp 299-302.
48. McDonnell, S. Spectroscopic characterisation of high dielectric constant materials on semiconducting surfaces. Dublin City University, 2009.
49. Giannazzo, F.; Fisichella, G.; Piazza, A.; Di Franco, S.; Greco, G.; Agnello, S.; Roccaforte, F., Impact of contact resistance on the electrical properties of MoS(2) transistors at practical operating temperatures. *Beilstein Journal of Nanotechnology* **2017,** *8*, 254-263.
50. Tsai, Y.; Li, Y., Impact of Doping Concentration on Electronic Properties of Transition Metal-Doped Monolayer Molybdenum Disulfide. *IEEE Transactions on Electron Devices* **2018,** *65* (2), 733-738.
51. Feng, L.-p.; Su, J.; Liu, Z.-t., Effect of vacancies in monolayer MoS 2 on electronic properties of Mo–MoS 2 contacts. *RSC Advances* **2015,** *5* (26), 20538-20544.
52. Liu, H.; Neal, A. T.; Ye, P. D., Channel Length Scaling of MoS2 MOSFETs. *ACS Nano* **2012,** *6* (10), 8563-8569.
53. Giannazzo, F.; Fisichella, G.; Piazza, A.; Di Franco, S.; Greco, G.; Agnello, S.; Roccaforte, F., Effect of temperature–bias annealing on the hysteresis and subthreshold behavior of multilayer MoS2 transistors. *physica status solidi (RRL)–Rapid Research Letters* **2016,** *10* (11), 797-801.

54. Nesbitt, H. W.; Legrand, D.; Bancroft, G. M., Interpretation of Ni2p XPS spectra of Ni conductors and Ni insulators. *Physics and Chemistry of Minerals* **2000,** *27* (5), 357-366.
55. Donarelli, M.; Bisti, F.; Perrozzi, F.; Ottaviano, L., Tunable sulfur desorption in exfoliated MoS2 by means of thermal annealing in ultra-high vacuum. *Chemical Physics Letters* **2013,** *588*, 198-202.
56. Lince, J. R.; Carre, D. J.; Fleischauer, P. D., Effects of argon-ion bombardment on the basal plane surface of molybdenum disulfide. *Langmuir* **1986,** *2* (6), 805-808.
57. McIntyre, N. S.; Spevack, P. A.; Beamson, G.; Briggs, D., Effects of argon ion bombardment on basal plane and polycrystalline MoS2. *Surface Science* **1990,** *237* (1), L390-L397.
58. Häkkinen, H., The gold–sulfur interface at the nanoscale. *Nature Chemistry* **2012,** *4*, 443.
59. Pensa, E.; Cortés, E.; Corthey, G.; Carro, P.; Vericat, C.; Fonticelli, M. H.; Benítez, G.; Rubert, A. A.; Salvarezza, R. C., The Chemistry of the Sulfur–Gold Interface: In Search of a Unified Model. *Accounts of Chemical Research* **2012,** *45* (8), 1183-1192.
60. Grönbeck, H.; Curioni, A.; Andreoni, W., Thiols and Disulfides on the Au(111) Surface: The Headgroup−Gold Interaction. *Journal of the American Chemical Society* **2000,** *122* (16), 3839-3842.
61. Lustemberg, P. G.; Vericat, C.; Benitez, G. A.; Vela, M. E.; Tognalli, N.; Fainstein, A.; Martiarena, M. L.; Salvarezza, R. C., Spontaneously Formed Sulfur Adlayers on Gold in Electrolyte Solutions: Adsorbed Sulfur or Gold Sulfide? *The Journal of Physical Chemistry C* **2008,** *112* (30), 11394-11402.
62. Vericat, C.; Vela, M. E.; Andreasen, G.; Salvarezza, R. C.; Vázquez, L.; Martín-Gago, J. A., Sulfur−Substrate Interactions in Spontaneously Formed Sulfur Adlayers on Au(111). *Langmuir* **2001,** *17* (16), 4919-4924.
63. Allain, A.; Kang, J.; Banerjee, K.; Kis, A., Electrical contacts to two-dimensional semiconductors. *Nat Mater* **2015,** *14* (12), 1195-1205.
64. Kang, J.; Liu, W.; Sarkar, D.; Jena, D.; Banerjee, K., Computational Study of Metal Contacts to Monolayer Transition-Metal Dichalcogenide Semiconductors. *Physical Review X* **2014,** *4* (3), 031005.
65. Yan, Z.; Chen, L.; Yoon, M.; Kumar, S., The Role of Interfacial Electronic Properties on Phonon Transport in Two-Dimensional MoS2 on Metal Substrates. *ACS Applied Materials & Interfaces* **2016,** *8* (48), 33299-33306.
66. Gong, C.; Huang, C.; Miller, J.; Cheng, L.; Hao, Y.; Cobden, D.; Kim, J.; Ruoff, R. S.; Wallace, R. M.; Cho, K.; Xu, X.; Chabal, Y. J., Metal Contacts on Physical Vapor Deposited Monolayer MoS2. *ACS Nano* **2013,** *7* (12), 11350-11357.
67. Stowell, M. J., Moiré patterns and coherent double-positioning boundaries in {111} epitaxial gold films AU - Jacobs, M. H. *The Philosophical Magazine: A Journal of Theoretical Experimental and Applied Physics* **1965,** *11* (111), 591-603.
68. Zhou, Y.; Kiriya, D.; Haller, E. E.; Ager III, J. W.; Javey, A.; Chrzan, D. C., Compliant substrate epitaxy: Au on MoS 2. *Physical Review B* **2016,** *93* (5), 054106.
69. Desai, S. B.; Madhvapathy, S. R.; Amani, M.; Kiriya, D.; Hettick, M.; Tosun, M.; Zhou, Y.; Dubey, M.; Ager, J. W.; Chrzan, D.; Javey, A., Gold-Mediated Exfoliation of Ultralarge Optoelectronically-Perfect Monolayers. *Advanced Materials* **2016,** *28*, 4053-4058.
70. Zhou, P.; Song, X.; Yan, X.; Liu, C.; Chen, L.; Sun, Q.; Zhang, D. W., Controlling the work function of molybdenum disulfide byin situmetal deposition. *Nanotechnology* **2016,** *27* (34), 344002.

71. Smyth, C. M.; Walsh, L. A.; Bolshakov, P.; Catalano, M.; Addou, R.; Wang, L.; Kim, J.; Kim, M. J.; Young, C. D.; Hinkle, C. L.; Wallace, R. M., Engineering the Palladium–WSe2 Interface Chemistry for Field Effect Transistors with High-Performance Hole Contacts. *ACS Applied Nano Materials* **2019,** *2* (1), 75-88.

4.3 Interface Chemistry and Thermal Transport at Ti/MoS_2 Contacts with Interfacial Oxide

Abstract

The deposition of a thin oxide layer at metal/semiconductor interfaces has been previously reported as a means of reducing contact resistance in 2D electronics. Using X-ray photoelectron spectroscopy with *in-situ* Ti deposition, we fabricate Au/Ti/TiO_x/MoS_2 samples as well as Au/Ti/MoS_2 and Au/TiO_x/MoS_2 for comparison. Elemental titanium reacts strongly with MoS_2 whereas no interface reactions are observed in the two types of samples containing TiO_x/MoS_2 interfaces. Using time domain thermoreflectance for the measurement of thermal boundary conductance, we find that samples contacted with Ti and a thin TiO_x layer at the interface (≤1.5 nm) exhibit the same behavior as samples contacted solely with pure Ti. The Au/TiO_x/MoS_2 samples exhibit ~20% lower thermal boundary conductance, despite having the same MoS_2 interface chemistry as the samples with thin oxide at the interface between Ti and MoS_2. We identify the mechanism for this phenomenon, attributing it to the difference in thermal boundary conductance at the top Au contact. This work demonstrates that the use of thin interfacial oxide layers to reduce electrical contact resistance does not compromise heat flow in 2D electronic devices. The results also suggest that the Ti layer thickness must be considered for optimal thermal transport.

4.3.1 Introduction

As discussed in the Chapter 4.1, an approach to the reduction of electrical contact resistance at the metal/TMD interface is the deposition of thin oxide interlayers at the interface between the semiconductor and the metal.[1-7] Park *et al*.[1-2] have shown a reduction in electrical contact resistance and an improvement in device stability in MoS_2 field effect transistors with 2 nm TiO_2 films deposited by atomic layer deposition (ALD) at the interface between the MoS_2 and the Ti contact. The observed improvements were attributed to Fermi level de-pinning and interface dipole effects. Kim *et al*.[3], who observed a decrease in Fermi level pinning with 1 nm interfacial TiO_2, suggested that the presence of an interfacial oxide reduces the density of metal induced gap states by blocking the penetration of the electron wave function from the metal. Similarly, Kaushik *et al*.[4] concluded from density functional theory that the Schottky barrier height is reduced due to charge-transfer doping from the TiO_2 layer to MoS_2. They have experimentally shown a twenty four-fold reduction in contact resistance and tenfold improvement in on-current and field effect mobility with the incorporation of an interfacial oxide layer.

While the use of an interfacial oxide has been found to be highly beneficial to electronic properties in the aforementioned studies, thermal characterization of this interface is relatively lacking. An understanding of thermal transport is crucial as thermal resistances at the contact interface can inhibit heat removal from 2D electronic devices, compromising their performance and reliability.[8] The MoS_2/SiO_2 substrate interface present in most 2D devices is typically low, ~14 MW m^{-2} K^{-1}.[9] Therefore caution must be taken when introducing additional interfaces to the device that could potentially increase the total resistance of the system. Our previous work has shown that transport across contact interfaces is highly sensitive to the oxide composition of Ti for graphene as well as 3D substrates.[10-11] McDonnell *et al.*[12] have demonstrated that Ti/MoS_2 and

TiO_2/MoS_2 interfaces exhibit vastly different chemical compositions and suggested potential detrimental effects on thermal transport due to the higher thermal resistance of TiO_2 compared to metallic Ti. They noted that work by Duda *et al.*[13] concludes that the removal of native oxide along with the deposition of a Ti adhesion layer has been found to be critical to lowering thermal resistances at metal-semiconductor interfaces.

Similarly, Hopkins *et al.*[14] have shown a substantial decrease in thermal boundary conductance due to the presence of native oxides at metal-semiconductor interfaces. Density functional theory calculations conclude that phonon-phonon coupling and phonon transmission across the metal/MoS_2 interface is strongly dependent on the degree of orbital hybridization at the contact, and that stronger chemical and electronic interactions at the contact result in higher thermal boundary conductance.[15-16] This would imply that the inclusion of oxide instead of metal at the MoS_2 interface could potentially result in diminished thermal transport, warranting an investigation of the thermal boundary conductance across Ti contacts to MoS_2 with interfacial oxides, and this thermal boundary conductance's potential dependence on interface chemistry.

4.3.2 Materials and Methods

Prior to loading to UHV, bulk MoS_2 geological crystals (purchased from SPI) were exfoliated with scotch tape to clean the surface by removing the top layer. Preliminary XPS was collected in our ScientaOmicron UHV system described in Chapter 2.3, All XPS data were acquired at a pass energy of 50 eV, using an Al Kα source with a photon energy of 1486.7 eV. The Mantis QUAD-EVC 4 pocket evaporator was used to deposit Ti onto the sample *in-situ*. Titanium was evaporated at a rate of approximately 1 Å/min. For oxide deposition, a pressure of 5×10^{-6} mbar of ultra-high purity O_2 was maintained in the chamber during deposition. XPS was acquired after each Ti and TiO_x deposition. The thicknesses of the deposited layers were calculated using

the attenuation of the Mo 3*d* core level intensity via methods described in Section 2.3.1.5. The samples were then capped with 1-2 nm Au in-situ to prevent oxidation in air upon removal from UHV. An additional ~70 nm of Au was deposited in *ex-situ* in the UVML cleanroom e-beam evaporator for TDTR measurements as described in Section 2.3.6. TDTR measurement and analysis was conducted by David Hans Olson in Prof. Hopkins' lab.

4.3.3 Results and Discussion

4.3.3.1 Thermal Boundary Conductance and MoS_2 Interface Chemistry

Thermal boundary conductance, h_K, is plotted as a function of TiO_x thickness in Figure 4.3.1 In the limit of zero TiO_x thickness, corresponding to samples with pure Ti metal overlayers (Au/Ti/MoS_2), the average h_K value was approximately 21.5 ± 5.6 MW m^2 K^{-1}. This value is roughly equivalent to the h_K value of the Au/MoS_2 reference sample (20.8 ± 1.1 MW m^2 K^{-1}.). The results are also consistent with previously measured values of metal/MoS_2 interfaces.[17-18] We note that the three Au/Ti/MoS_2 samples had Ti thicknesses ranging from 2.9 to 5.2 nm and Ti metal thickness had no effect on h_K for these samples, suggesting that the intrinsic resistance of the Ti does not contribute to the overall resistance of the system. Similarly, the figure shows that TiO_x/MoS_2 samples with TiO_x thicknesses from 1.7 to 4.6 nm all exhibit roughly the same value of 16.0 ± 2.8 MW m^2 K^{-1}. The lack of thickness dependence of the Ti/MoS_2 and TiO_x/MoS_2 samples indicates that thermal transport is dominated by interfacial resistances and not by the intrinsic thermal resistance of metal or oxide layers.

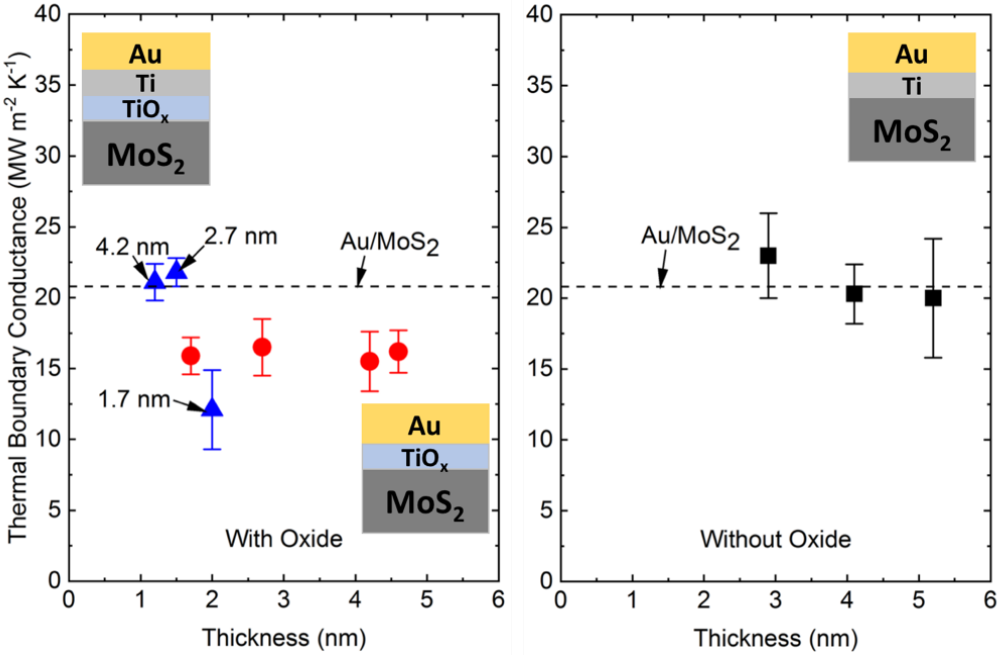

Figure 4.3.1. Thermal boundary conductance as a function interfacial layer thickness for the MoS_2 substrates with Au/Ti (black squares), Au/TiO_x (red circles), and Au/Ti/TiO_x (blue triangles) in addition to a reference sample of Au/MoS_2 (dashed line). The arrows indicate the Ti metal thickness for each Ti/TiO_x samples where data is plotted as a function of TiO_x thickness.

Figure 4.3.2(a) shows the core-level XPS spectra before and after the deposition of 4.1 nm Ti metal in UHV. Spectra of all samples used in this work are shown in Appendix C. Before the deposition of Ti metal (black curve), MoS_2 is characterized by Mo $3d_{5/2}$ state at ~228.9 eV with a spin orbit splitting value of 3.1 eV, and the S $2p_{3/2}$ state at ~161.8 eV with a spin orbit splitting of 1.2 eV. Following the deposition of Ti, the spectra exhibit new chemical states including Mo metal (Mo^0) at 227.5 eV in the Mo 3*d* spectrum and Ti-S states in the S 2*p* spectrum. This result is discussed in detail in Chapter 4.2.

Figure 4.3.2(b) shows XPS spectra corresponding to a sample with 4.6 nm of TiO_x. The spectra indicate that the Mo-S bonds are preserved and no chemical reaction occurs between Ti and the substrate. As previously reported by McDonnell *et al.*[12], the presence of a partial pressure

of oxygen during the deposition of Ti on MoS_2 inhibits the reaction between them as Ti reacts with oxygen impinging on the surface of the substrate during deposition. The Mo 3*d* and S 2*p* core levels exhibit a 0.64 eV shift to higher binding energy, corresponding to a change in the position of the Fermi level. This indicates that the presence of an oxide overlayer causes n-type doping in the sample. This result is similar to that of Kaushik *et al.*[4] who reported a 0.5 eV core-level shift for a 2 nm of ALD TiO_2 on MoS_2. We note that the oxide which forms under the deposition conditions in our UHV chamber is comprised of two chemical states. The TiO_2 state has its $2p_{3/2}$ component at 459.2 eV with a spin-orbit splitting of 5.7 eV and comprises ~80% of the oxide layer deposited. The second chemical state, which appears at 457.65 eV with a spin-orbit splitting of 5.5 eV corresponds to Ti_2O_3.[19-20] Spectral deconvolution of the oxide is shown in Figure 4.3.3.

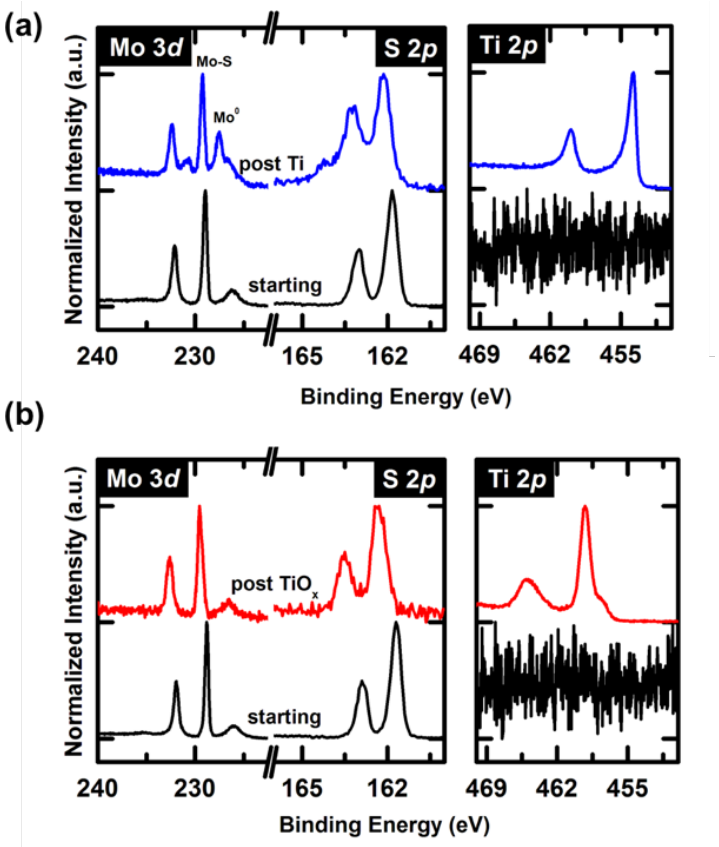

Figure 4.3.2. Core level XPS spectra before and after the deposition of (a) 4.1 nm Ti on MoS_2 and (b) 4.6 nm TiO_x on MoS_2

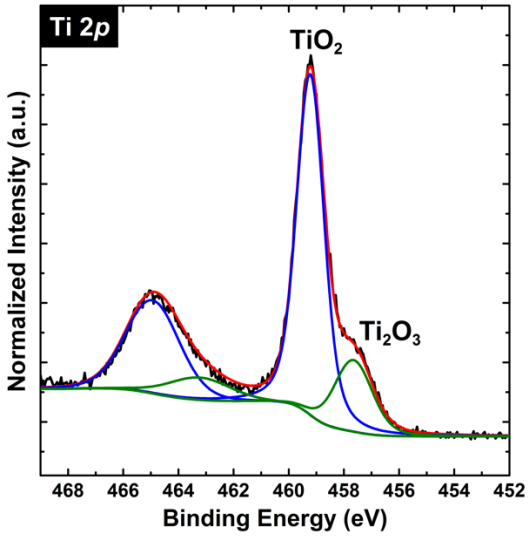

Figure 4.3.3. Representative spectral deconvolution of the Ti 2*p* core level for TiOx deposited in an oxygen partial pressure of 5 ×10-6 mbar at a deposition rate of 1 Å/min.

Unlike the pure metal and oxide samples, h_K of the Au/Ti/TiO_x/MoS_2 samples exhibits a decrease with increasing oxide thickness as shown in Figure 4.3.1. The two samples with TiO_x thicknesses ≤ 1.5 nm have h_K values comparable to that of the Au/Ti/MoS_2 and Au/MoS_2 samples, whereas the Au/Ti(1.7 nm)/TiO_x(2.0 nm)/MoS_2 is comparable to the Au/TiO_x/MoS_2 samples with no metal overlayer, within uncertainty. The reduction in h_K for this sample could be due to two possible reasons. The first is the increase in the oxide thickness compared to the heterostructures with TiO_x thickness ≤ 1.5 nm. However, given that no oxide thickness dependence for h_K of the Au/TiO_x/MoS_2 samples is observed, the increased oxide thickness is unlikely to be the dominant factor here. The second explanation is that the thickness of the Ti in the heterostructure (1.7 nm) is quite thin. From previous works, it has been shown that a reduction in the interfacial conductance is observed as the thickness of an interfacial adhesion layer becomes very thin (e.g., Cu and Cr).[21] This reduction in our experiment is explained using similar predictions of accumulated thermal boundary conductance, whereby phonons in Ti with wavelengths less than the total Ti thickness

participate in transport across the interface. In this way, the reduction in the population of Ti phonons due to a decrease in total Ti thickness ultimately results in a reduced h_K at the interface. We believe this to be the case when the thickness of the Ti becomes very thin in the heterostructures, making our results consistent with those of Jeong *et al.*[21]

The XPS spectra of a Ti(2.7 nm)/TiO_x(1.5 nm)/MoS_2 sample are shown in Figure 4.3.4. The TiO_x/MoS_2 interface (red curve) is chemically identical to that shown in Figure 4.3.2(b), exhibiting a n-type Fermi level shift and no other chemical changes following the deposition of Ti metal (blue curve). The only observable changes are broadening of the peaks and an increase in noise, which occur due to scattering and attenuation in the TiO_x and Ti overlayers [22]. The lack of interface reactions with the presence of interfacial oxide is one possible explanation for the Fermi level de-pinning effect reported by others.[1-3] Fermi level pinning has been attributed to interfacial reaction products which create new electronic states within the semiconductor band gap.[23] By blocking interface reactions via direct contact with an unreactive oxide layer, MoS_2 retains its intrinsic band structure with no new states which could pin the Fermi level.

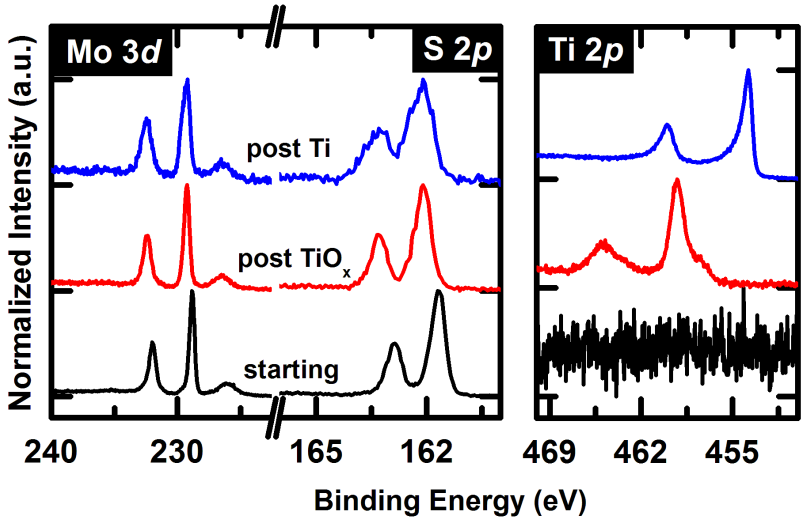

Figure 4.3.4. XPS spectra of the Ti/TiO_x/MoS_2 samples

It is clear from comparison of Figure 4.3.2(b) and Figure 4.3.4 that the chemistry at the interface with MoS_2 does not explain the differences in behavior of h_K, as the TiO_x/MoS_2 interface in both the pure oxide and metal/oxide samples are chemically identical. Therefore, the behavior of h_K is likely dominated by one of the other interfaces present in the device. For the metal/oxide heterostructure sample these interfaces include the Au/Ti and Ti/TiO_x, whereas the oxide sample has the Au/TiO_x. The resistance from the Au/Ti interface is not a contributing factor, since thermal transport across metal/metal interfaces is governed by electrons near the Fermi energy, yielding thermal boundary conductance values that are far higher than those across metal/non-metal interfaces (i.e., negligible thermal resistances at these metal/metal interfaces).[24-27] The negligible contribution of this interface is evident in Figure 4.3.1, which shows that $Au/Ti/MoS_2$ exhibits the same h_K as the Au/MoS_2 reference sample. Our measured value is consistent with previous measurements of thermal boundary conductance at Au/graphene and Au/Ti/graphene interfaces.[28]

4.3.3.2 Analysis of Thermal Boundary Conductances

To determine the extent of the contribution of the thermal conductances across the Au/TiO_x, Au/Ti, and Ti/TiO_x interfaces to the overall measured h_K, we fabricated several reference samples. We first deposited 80 nm Au on single crystal sapphire (Al_2O_3) with a 5 nm Al adhesion layer in a cleanroom evaporator at high vacuum (HV). Al_2O_3 was selected as our substrate to maximize sensitivity to potentially large conductances. The conductance at the $Au/Al/Al_2O_3$ interface was found to be 49 ± 5.0 MW m^{-2} K^{-1}. Following this measurement, the surface of the Au was cleaned via UV-O_3 exposure as to remove adventitious carbon. The sample was loaded back to UHV. Since the process was found to leave residual oxygen on the Au surface, the sample was capped with ~ 2 nm Au in UHV to create a pristine surface before depositing subsequent Ti layers. Three separate samples with Ti (2.3 nm), TiO_x (2 nm), and a Ti (2.2 nm)/TiO_x (4.4 nm)

were created and capped with ~1-2 nm Au in UHV. To account for the contribution of residual oxygen at the interface between the HV and UHV Au, we fabricate a reference sample that is a UV-O_3 treated HV Au sample that is then capped with Au in UHV. This sample is measured to determine the contribution of the oxygenated Au interface to the total interfacial conductance in structures containing Ti and TiO_x.

Following the UHV deposition processes, the samples were transferred back to the HV electron-beam evaporator, and capped with ~ 67 nm of Au following an O_2 plasma cleaning procedure. This is the same capping process that was applied to the MoS_2 samples. TDTR was performed on the samples, fitting for the conductance across the newly deposited interfacial structure as the underlying Au/Al/Al_2O_3 interfacial conductance was measured prior to the deposition of the structures. The conductance across the Au/Au interface containing residual oxygen from the UV-O_3 process is measured to be 376 ± 31 MW m^{-2} K^{-1}, and is accounted for in subsequent derivations of Au/Ti and Au/TiO_x conductances. We model each of the thermal conductances measured as series resistors models, accounting for the interfaces present in the system, and disregarding the intrinsic resistances of the layers due to the constant thermal boundary conductances observed in our samples as a function of thickness. A summary of all measured and calculated h_K and R_K values is shown in Table 4.2. The analysis implemented to derive the Au/Ti and Au/TiO_x conductances is presented below.

Table 4.2. Measured and derived values of Ti/TiO_x structures on MoS_2 and sandwiched between Au. The

Interface	h_K (MW m^{-2} K^{-1})	R_k (m^2 K GW^{-1})
Au/O/Au	376 ± 31	2.66 ± 0.22
Au/Ti (2.3 nm)/Au/O/Au	260 ± 20	3.85 ± 0.29
Au/TiO_x (2 nm)/Au/O/Au	44.5 ± 3.2	22.5 ± 1.6
Au/Ti (2.2 nm)/TiO_x (4.4 nm)/Au/O/Au	65.2 ± 4.5	15.3 ± 1.0
Au/O*	752 ± 61	1.33 ± 0.11
Au/Ti*	1680 ± 190	0.59 ± 0.07
Au/TiO_x*	101 ± 11	9.91 ± 1.07
Ti/TiO_x*	459 ± 87	2.18 ± 0.41
Au/MoS_2	20.8 ± 1.1	48.1 ± 2.54
$Au/Ti/MoS_2$	21.1 ± 5.7	47.4 ± 12.8
$Au/TiO_x/MoS_2$	16.0 ± 2.8	62.5 ± 10.9
$Au/Ti/TiO_x/MoS_2$†	21.5 ± 1.6	46.5 ± 3.46
TiO_x/MoS_2*	19.1 ± 3.8	52.4 ± 10.4

* denotes values that are derived from measurements.
† the average of the heterostructures with TiO_x thicknesses of 1.5 and 2.0 nm, omitting that with 1.7 nm Ti.

The Au/Ti (2.3 nm)/Au/O/Au interfacial region can be modeled as such:

$$\frac{1}{h_{K,Au/Ti/Au/O/Au}} = \frac{2}{h_{K,Au/Ti}} + \frac{1}{h_{K,Au/O/Au}}. \qquad \text{Equation 4.5}$$

In this equation, $h_{K,Au/Ti/Au/O/Au}$ represents the total, measured conductance, $h_{K,Au/Ti}$ represents the conductance at the Au/Ti interface, and $h_{K,Au/O/Au}$ accounts for the resistance of the Au/Au oxygenated layer. Because we have previously measured $h_{K,Au/O/Au}$, we can calculate $h_{K,Au/Ti}$ to be 1680 ± 190 MW m^{-2} K^{-1}. We estimate this to be the lower bound for the conductance at the Au/Ti interface. This could be a result of the limitations of TDTR to measure ultrahigh boundary conductances, quasi-ballistic influences as a result of the thinness of the Ti layer, and extrinsic or chemical effects that prevent the Au/Ti interface from being an otherwise perfect interface which will be addressed later. Regardless, the conductance of metal-metal interfaces is quite high—the

electron diffuse-mismatch model predicts a conductance of 5970 MW m^{-2} K^{-1} at the Au/Ti interface.[24] Thus, the contribution of the Au/Ti interface in the total interfacial resistance is negligible compared to others resistances present in these systems.

In a similar manner, the conductance at the Au/TiO_x (2.0 nm)/Au/O/Au region can be defined as

$$\frac{1}{h_{K,Au/TiOx\,(2.0\,nm)/Au/O/Au}} = \frac{2}{h_{K,Au/TiOx}} + \frac{1}{h_{K,Au/O/Au}}, \qquad \text{Equation 4.6}$$

where $h_{K,Au/TiOx}$ is the conductance across the Au/TiO_x interface. The Au/TiO_x (2 nm)/Au conductance is measured to be 44.5 ± 3.2 MW m^{-2} K^{-1}, resulting in an interfacial conductance at the Au/TiO_x interface to be 101 ± 11 MW m^{-2} K^{-1}. Finally, the Ti (2.2 nm)/TiO_x (4.4 nm) heterostructure can be modeled using the following equation:

$$\frac{1}{h_{K,Au/Ti\,(2.2\,nm)/TiOx\,(4.4\,nm)/Au/O/Au}} = \frac{1}{h_{K,Au/Ti}} + \frac{1}{h_{K,Ti/TiOx}} + \frac{1}{h_{K,Au/TiOx}} + \frac{1}{h_{K,Au/O/Au}}. \qquad \text{Equation 4.7}$$

In this equation, $h_{K,Ti/TiOx}$ is the conductance at the Ti/TiO_x interface. If one assumes that the Ti/TiO_x interfacial resistance is negligible (i.e., 1/ $h_{K,Ti/TiOx}$ -> 0), then the calculated conductance taking into account just $h_{K,Au/Ti}$, $h_{K,Au/TiOx}$, and $h_{K,Au/O/Au}$ results in a net conductance across the heterostructure of 76.0 ± 13.0 MW m^{-2} K^{-1}. This is in good agreement with the measured value of the heterostructure (65.2 ± 4.5 MW m^{-2} K^{-1}), and suggests that the interfacial conductance at the Ti/TiO_x interface is relatively high at 459 ± 87 MW m^{-2} K^{-1}. This value is large compared to that across the Au/TiO_x,. Our results imply that the Au/TiO_x interface presents a non-negligible thermal

resistance due to the relative weak atomic interactions between Au and TiO_x; in fact, in this case of this $Au/TiO_x/Au/Al/Al_2O_3$ multilayer film system, the Au/TiO_x offers the limiting thermal resistance to heat flow.

This same type of analysis is used to determine the thermal conductance at the TiO_x/MoS_2 interface from the values determined above. The thermal conductance across the $Au/TiO_x/MoS_2$ interface can be modeled with a series resistance approach:

$$\frac{1}{h_{K,meas}} = \frac{1}{h_{K,Au/TiO_x}} + \frac{1}{h_{K,TiO_x/MoS_2}} \qquad \text{Equation 4.8}$$

where $h_{K,meas}$ is the measured conductance across the $Au/TiO_x/MoS_2$ interface (averaged over all TiO_x thicknesses), $1/h_{K,Au/TiOx}$ is the resistance of the Au/TiO_x interface, and $1/h_{K,TiOx/MoS2}$ is the resistance of the TiO_x/MoS_2 interface. Again, we neglect the contribution from the intrinsic resistance of the TiO_x layer based on the h_K observed for the range of TiO_x thicknesses that are presented in Figure 4.3.1. Taking $h_{K,meas}$ to be 16.0 ± 2.8 MW m^{-2} K^{-1}, and $h_{K,Au/TiOx}$ from our measurements on this control interface discussed above, we calculate $h_{K,TiOx/MoS2}$ to be 19.1 ± 3.8 MW m^{-2} K^{-1}. The larger comparable conductance at the TiO_x/MoS_2 interface as compared to $h_{K,meas}$ suggests that the Au/TiO_x interfacial conductance is again playing a non-negligible role in the reduction of heat transport across these interfaces, albeit, the TiO_x/MoS_2 represents the dominant thermal resistance in this system. This reduction can be circumvented by implementing a Ti/TiO_x heterostructure at the interface, provided that the Ti layer is thicker than ~ 2 nm as discussed previously, whereby we see an increased boundary conductance as compared to just a TiO_x adhesion layer. This also suggests that the Ti/TiO_x conductance is negligible compared to that of the Au/TiO_x and TiO_x/MoS_2 interface, allowing for a compromise of transport properties from both an electrical and thermal perspective.

4.3.3.3 Au/Ti Interface Chemistry

XPS characterization of the Au/Ti and Au/TiO_x interfaces shows that chemical bonding occurs at Au/Ti interfaces while no chemical interactions are observed in Au/TiO_x interfaces. The formation of intermetallic compounds in Au/Ti interfaces deposited in UHV at room temperature has been previously reported by others.[29-31] Figure 4.3.5 shows XPS acquired on Ti and TiO_x samples deposited in our UHV system before and after the deposition of ~2-3 Å of Au. In the Ti 2*p* spectrum of the Ti metal sample shown in (a), the spectrum exhibits a core level shift of 0.15 eV as well as broadening due to the presence of Au-Ti bonding at the interface following the deposition of Au. The TiO_x spectra shown in (b) acquired before and after Au deposition overlap perfectly showing no change in binding energy or line shape. In the Au 4*f* spectrum in (c), Au deposited on Ti exhibits a prominent asymmetry and 0.33 eV shift to higher binding energy which is characteristic of intermetallic formation[32], while Au deposited on TiO_x retains the spectral features of elemental Au indicating no interaction occurs. The observed bonding at the Au/Ti interface is a potential explanation for the lower measured h_K of the Au/Ti interface in comparison with the value calculated based on the electron diffuse-mismatch model, which does not account for the formation of an intermetallic compound at the interface.[24] It has been shown by others that the thermal boundary conductance can become dominated by the thermal conductance of an interfacial compound layer.[24] Furthermore, intermetallic compounds have been found to exhibit low values of thermal conductivity in comparison with their pure metal constituents.[33] Nevertheless, the electron mediated thermal transport at metallic Au/Ti interface results in a h_K value that is far higher than that corresponding to Au/TiO_x.

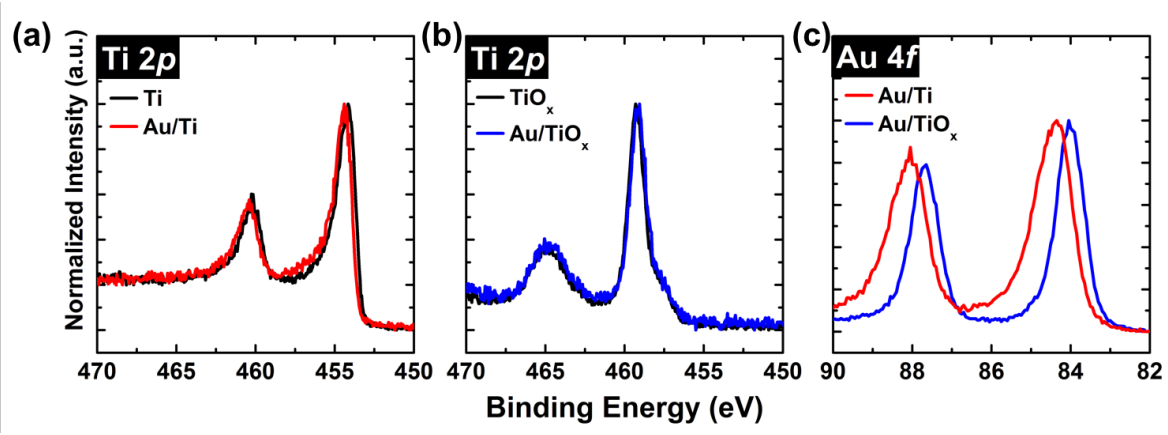

Figure 4.3.5. Ti 2*p* spectra acquired on (a) Ti and (b) TiO_x films before and after the deposition of Au, with Au 4*f* spectra corresponding to these samples shown in (c).

4.3.4 Conclusion and Future Work

In summary, we find that Au/TiO_x/MoS_2 exhibit ~20% lower thermal boundary conductance than Au/Ti/MoS_2. Samples with a thin TiO_x layer (~ 1-1.5 nm) at the interface between Ti and MoS_2 exhibit the same thermal boundary conductance as those with pure Ti metal. The difference in h_K between the TiO_x/MoS_2 and Ti/TiO_x/MoS_2 samples is observed despite the chemically identically TiO_x/MoS_2 interfaces present in both samples. The differences in h_K arise due to the different interfaces with the top Au contact. Whereas Au/Ti has negligible resistance, that of Au/TiO_x is substantial making this interface the dominant resistor in the system. Our results suggest that thin interfacial oxide layers which can be used to enhance electronic properties have no negative impact on thermal transport in 2D electronic devices. The thickness of the Ti layer in the Ti/TiO_x structure must be considered when implementing this type of contact.

4.3.4.1 Limits of Ti Layer Thickness

Future work should focus on developing an understanding of the role of the contact layer thickness. It is clear that h_K of $Au/TiO_x/MoS_2$ and $Au/Ti/MoS_2$ interfaces is independent of the layer thickness. For the heterostructure-contacted sample with 2.0 nm TiO_x and 1.7 nm Ti, h_K is lower than the values measured for the samples with thinner TiO_x (1-1.5 nm) and thicker Ti layers ($\geq$ 2.7 nm). Given the TiO_x thickness independence of the $Au/TiO_x/MoS_2$ samples, we speculate that this is likely due to the thinness of the Ti layer which limits the phonon wavelengths involved in transport at the interface. In order to examine the Ti thicknesses dependence of h_K, different samples should be created where the Ti thicknesses is varied from 0.5 –3 nm in increments of 0.5 nm, and the TiO_x thickness is held constant (at 1-1.5) nm in each sample. This will help identify trends in the behavior which can provide insight into the mechanism.

4.3.4.2 Other metal/oxide/MoS_2 Interfaces

The results presented in this chapter also warrant a study of thermal transport at other metal/oxide/MoS_2 interfaces since the top metal/oxide resistance is found to dominate the resistance of the device. High work function MoO_x has been demonstrated to be an effective p-type contact to MoS_2 which typically exhibits n-type conduction.[34] In this work by Chaung *et al.* the MoO_x layer is capped with Pd yielding a $Pd/MoO_x/MoS_2$ structure. Our results would suggest that a Mo/MoO_x interface might be beneficial, analogous to the Ti/TiO_x structure created in this work.

4.3.5 References

1. Park, W.; Kim, Y.; Sang Kyung, L.; Jung, U.; Jin Ho, Y.; Cho, C.; Yun Ji, K.; Sung Kwan, L.; In Seol, H.; Lee, H.; Byoung Hun, L. In *Contact resistance reduction using Fermi level de-pinning layer for MoS2 FETs*, 2014 IEEE International Electron Devices Meeting, 15-17 Dec. 2014; 2014; pp 5.1.1-5.1.4.
2. Park, W.; Min, J. W.; Shaikh, S. F.; Hussain, M. M., Stable MoS2 Field-Effect Transistors Using TiO2 Interfacial Layer at Metal/MoS2 Contact. *physica status solidi (a)* **2017,** *214* (12).
3. Kim, G.-S.; Kim, S.-H.; Park, J.; Han, K. H.; Kim, J.; Yu, H.-Y., Schottky Barrier Height Engineering for Electrical Contacts of Multilayered MoS2 Transistors with Reduction of Metal-Induced Gap States. *ACS Nano* **2018,** *12* (6), 6292-6300.
4. Kaushik, N.; Karmakar, D.; Nipane, A.; Karande, S.; Lodha, S., Interfacial n-Doping Using an Ultrathin TiO2 Layer for Contact Resistance Reduction in MoS2. *ACS Applied Materials & Interfaces* **2016,** *8* (1), 256-263.
5. Agrawal, A.; Lin, J.; Barth, M.; White, R.; Zheng, B.; Chopra, S.; Gupta, S.; Wang, K.; Gelatos, J.; Mohney, S. E.; Datta, S., Fermi level depinning and contact resistivity reduction using a reduced titania interlayer in n-silicon metal-insulator-semiconductor ohmic contacts. *Applied Physics Letters* **2014,** *104* (11), 112101.
6. Chen, J.-R.; Odenthal, P. M.; Swartz, A. G.; Floyd, G. C.; Wen, H.; Luo, K. Y.; Kawakami, R. K., Control of Schottky Barriers in Single Layer MoS2 Transistors with Ferromagnetic Contacts. *Nano Letters* **2013,** *13* (7), 3106-3110.
7. Dankert, A.; Langouche, L.; Kamalakar, M. V.; Dash, S. P., High-Performance Molybdenum Disulfide Field-Effect Transistors with Spin Tunnel Contacts. *ACS Nano* **2014,** *8* (1), 476-482.
8. Pop, E., Energy dissipation and transport in nanoscale devices. *Nano Research* **2010,** *3* (3), 147-169.
9. Yalon, E.; McClellan, C. J.; Smithe, K. K. H.; Muñoz Rojo, M.; Xu, R. L.; Suryavanshi, S. V.; Gabourie, A. J.; Neumann, C. M.; Xiong, F.; Farimani, A. B.; Pop, E., Energy Dissipation in Monolayer MoS2 Electronics. *Nano Letters* **2017,** *17* (6), 3429-3433.
10. Freedy, K. M.; Giri, A.; Foley, B. M.; Barone, M. R.; Hopkins, P. E.; McDonnell, S., Titanium contacts to graphene: process-induced variability in electronic and thermal transport. *Nanotechnology* **2018,** *29* (14), 145201.
11. Olson, D. H.; Freedy, K. M.; McDonnell, S. J.; Hopkins, P. E., The influence of titanium adhesion layer oxygen stoichiometry on thermal boundary conductance at gold contacts. *Applied Physics Letters* **2018,** *112* (17), 171602.
12. McDonnell, S.; Smyth, C.; Hinkle, C. L.; Wallace, R. M., MoS2–Titanium Contact Interface Reactions. *ACS Applied Materials & Interfaces* **2016,** *8* (12), 8289-8294.
13. Duda, J. C.; Yang, C. Y. P.; Foley, B. M.; Cheaito, R.; Medlin, D. L.; Jones, R. E.; Hopkins, P. E., Influence of interfacial properties on thermal transport at gold:silicon contacts. *Applied Physics Letters* **2013,** *102* (8), 081902.
14. Hopkins, P. E.; Phinney, L. M.; Serrano, J. R.; Beechem, T. E., Effects of surface roughness and oxide layer on the thermal boundary conductance at aluminum/silicon interfaces. *Physical Review B* **2010,** *82* (8), 085307.
15. Yan, Z.; Chen, L.; Yoon, M.; Kumar, S., The Role of Interfacial Electronic Properties on Phonon Transport in Two-Dimensional MoS2 on Metal Substrates. *ACS Applied Materials & Interfaces* **2016,** *8* (48), 33299-33306.

16. Mao, R.; Kong, B. D.; Kim, K. W., Thermal transport properties of metal/MoS2 interfaces from first principles. *Journal of Applied Physics* **2014,** *116* (3), 034302.
17. Liu, J.; Choi, G.-M.; Cahill, D. G., Measurement of the anisotropic thermal conductivity of molybdenum disulfide by the time-resolved magneto-optic Kerr effect. *Journal of Applied Physics* **2014,** *116* (23), 233107.
18. Goni, M.; Yang, J.; Schmidt, A. J., Enhanced thermal transport across monolayer MoS2. *Nano Research* **2018,** *11* (4), 2173-2180.
19. Xiong, L.-B.; Li, J.-L.; Yang, B.; Yu, Y., Ti 3+ in the Surface of Titanium Dioxide: Generation, Properties and Photocatalytic Application. *Journal of Nanomaterials* **2012,** *2012*, 13.
20. Jackman, M. J.; Thomas, A. G.; Muryn, C., Photoelectron Spectroscopy Study of Stoichiometric and Reduced Anatase TiO2(101) Surfaces: The Effect of Subsurface Defects on Water Adsorption at Near-Ambient Pressures. *The Journal of Physical Chemistry C* **2015,** *119* (24), 13682-13690.
21. Jeong, M.; Freedman, J. P.; Liang, H. J.; Chow, C.-M.; Sokalski, V. M.; Bain, J. A.; Malen, J. A., Enhancement of Thermal Conductance at Metal-Dielectric Interfaces Using Subnanometer Metal Adhesion Layers. *Physical Review Applied* **2016,** *5* (1), 014009.
22. Rafati, A.; Ter Veen, R.; Castner, D. G., Low energy ion scattering: Determining overlayer thickness for functionalized gold nanoparticles. *Surface and interface analysis : SIA* **2013,** *45* (11-12), 10.1002/sia.5315.
23. Smyth, C. M.; Addou, R.; McDonnell, S.; Hinkle, C. L.; Wallace, R. M., WSe2-contact metal interface chemistry and band alignment under high vacuum and ultra high vacuum deposition conditions. *2D Materials* **2017,** *4* (2), 025084.
24. Gundrum, B. C.; Cahill, D. G.; Averback, R. S., Thermal conductance of metal-metal interfaces. *Physical Review B* **2005,** *72* (24), 245426.
25. Giri, A.; Gaskins, J. T.; Donovan, B. F.; Szwejkowski, C.; Warzoha, R. J.; Rodriguez, M. A.; Ihlefeld, J.; Hopkins, P. E., Mechanisms of nonequilibrium electron-phonon coupling and thermal conductance at interfaces. *Journal of Applied Physics* **2015,** *117* (10), 105105.
26. Cheaito, R.; Hattar, K.; Gaskins, J. T.; Yadav, A. K.; Duda, J. C.; Beechem, T. E.; Ihlefeld, J. F.; Piekos, E. S.; Baldwin, J. K.; Misra, A., Thermal flux limited electron Kapitza conductance in copper-niobium multilayers. *Applied Physics Letters* **2015,** *106* (9), 093114.
27. Wilson, R. B.; Cahill, D. G., Experimental Validation of the Interfacial Form of the Wiedemann-Franz Law. *Physical Review Letters* **2012,** *108* (25), 255901.
28. Foley, B. M.; Hernández, S. C.; Duda, J. C.; Robinson, J. T.; Walton, S. G.; Hopkins, P. E., Modifying Surface Energy of Graphene via Plasma-Based Chemical Functionalization to Tune Thermal and Electrical Transport at Metal Interfaces. *Nano Letters* **2015,** *15* (8), 4876-4882.
29. Tisone, T. C.; Drobek, J., Diffusion in Thin Film Ti–Au, Ti–Pd, and Ti–Pt Couples. *Journal of Vacuum Science and Technology* **1972,** *9* (1), 271-275.
30. Tsud, N.; Šutara, F.; Matolínová, I.; Veltruská, K.; Dudr, V.; Cháb, V.; Prince, K. C.; Matolín, V., Structure and electronic properties of gold adsorbed on Ti(0001). *Applied Surface Science* **2006,** *252* (15), 5428-5431.
31. Tsud, N.; Šutara, F.; Matolínová, I.; Veltruská, K.; Dudr, V.; Prince, K. C.; Matolín, V., Interaction of oxygen with Au/Ti (0001) surface alloys studied by photoelectron spectroscopy. *Journal of Physics: Condensed Matter* **2010,** *22* (26), 265002.
32. Bzowski, A.; Sham, T. K., Electronic structure of Au–Ti intermetallics. *Journal of Vacuum Science & Technology A* **1993,** *11* (4), 2153-2157.

33. Terada, Y.; Ohkubo, K.; Mohri, T.; Suzuki, T., Thermal Conductivity of Intermetallic Compounds with Metallic Bonding. *MATERIALS TRANSACTIONS* **2002,** *43* (12), 3167-3176.
34. Chuang, S.; Battaglia, C.; Azcatl, A.; McDonnell, S.; Kang, J. S.; Yin, X.; Tosun, M.; Kapadia, R.; Fang, H.; Wallace, R. M.; Javey, A., MoS2 P-type Transistors and Diodes Enabled by High Work Function MoOx Contacts. *Nano Letters* **2014,** *14* (3), 1337-1342.

4.4 Interface Chemistry and Thermal Transport at Titanium and Oxide Contacts to WSe_2

Abstract

WSe_2 has demonstrated potential for applications in thermoelectric energy conversion. Optimization of such devices requires control over interfacial thermal and electrical transport properties. Repeatable growth of ~ 1 nm WSe_2 films by MBE is demonstrated. Ti, TiO_x, and Ti/TiO_x contacts to the MBE-grown WSe_2 are characterized by XPS and transport measurements. The deposition of Ti is found to result in W-Se bond scission yielding metallic W and Ti-Se chemical states. The interfacial thermal conductance h_K is found to be equivalent to that of $Au/Ti/MoS_2$ and Au/MoS_2 reported in the previous chapter with a value of 22.2 ± 2.5 MW m^{-2} K^{-1}. When the WSe_2 film thickness is increased to 2 nm, the thermal boundary conductance decreases to 6.77 ± 0.63 MW m^{-2} K^{-1} due to the low intrinsic thermal conductivity of WSe_2. The deposition of Ti on WSe_2 in the presence of a partial pressure of O_2, which yields a TiO_x overlayer, results in the formation of substoichiometric WSe_x ($x<2$) as well as WO_x. This is unlike MoS_2 in which the deposition of TiO_x inhibits interface reactions and no oxidation is observed.

4.4.1 Introduction

In this chapter, Ti, TiO_x, and Ti/TiO_x contacts to MBE-grown WSe_2 are characterized by XPS and transport measurements. While interface chemistry of Au, Cr, Ir, Ag, Cu, and Pd contacts to WSe_2 has been previously examined[1-5], no reports on the Ti/WSe_2 interface exist to date. A number of studies have reported Ti contacts for WSe_2 devices.[6-9] Ti is predicted to exhibit strong orbital overlap and covalent bonding with WSe_2 resulting in an Ohmic contact[10], however Liu *et al.*[7] report that the Ti contacts to WSe_2 exhibit contact resistance that is four orders of magnitude higher than In contacts and three orders of magnitude higher than Ag contacts. Experimental results by Fang *et al*.[8] show that Ti/WSe_2 contacts result in low-current ambipolar characteristics and that Pd contacts behave far more favorably. Kim *et al*.[6] have demonstrated that ion beam irradiation of WSe_2 prior to contact deposition, which causes Se vacancies, results in a drastic increase in p-type field effect mobility and on/off ratio. They speculate the observed improvement to be due to the formation of Ohmic contacts as a result of defect-mediated Fermi level pinning near the valence band. A fundamental study of interface chemistry is necessary to gain insight into the discrepancies between theory and experiment and to better understand the effect of processing. In the previous chapter on geological MoS_2, we have demonstrated the ability to inhibit interface reactions in a deposition pressure that is typical of cleanroom evaporators used in device fabrication. We have also demonstrated the ability to circumvent the thermal resistance of the Au/TiO_x interface by depositing a layered $Au/Ti/TiO_x$ structure. The effect of these processes on MBE-deposited WSe_2 are examined here.

WSe_2 has attracted significant attention for its ultra-low thermal conductivity in both in-plane and cross-plane directions. First principle calculations yield a value of 3.935 W m^{-1} K^{-1} for monolayer WSe_2 (in-plane), which is an order of magnitude lower than calculated values for

MoS_2.[11] In the cross-plane direction, the thermal conductivity has been reported to be as low as 0.05 W m^{-1} K^{-1}.[12] The low thermal conductivity makes the material a promising candidate for thermoelectric energy conversion such as 2D solid-state thermionic devices as proposed by Wang *et al.*[13] Thermionic emission can also be used for integrated cooling of high power electronic devices through refrigeration and active cooling.[14-17] Both thermionic power generation and refrigeration are optimized when high electrical conductivity is combined with low thermal conductivity to enable a large temperature gradient. Efficient passive cooling is achieved when both electrical and thermal conductivity are high. The interfacial band alignment is also what determines the Seebeck coefficient in these devices.[13, 16, 18] It is clear that regardless of the application, engineering of these devices requires a high degree of control over the thermal and electrical resistances at the interface, which dominate the device properties at the nanoscale. This further motivates the work presented in this chapter.

4.4.2 Materials and Methods

WSe_2 films were grown on HOPG substrates by MBE using the procedure described in Section 2.2.3. Following MBE growth, XPS was acquired. The samples were then removed from UHV for taping of a shadow mask. The shadow masks used here are the same which were used in Chapter 3.3 with pads measuring 200 μm × 500 μm. The time of air exposure for taping the shadow mask was approximately 10 minutes for all samples, and XPS was acquired again following air exposure. The Mantis QUAD-EVC 4 pocket evaporator was used to deposit Ti onto the sample *in-situ*. The titanium was evaporated at a rate of approximately 1 Å/min. For oxide deposition, a pressure of 5×10^{-6} mbar of ultra-high purity O_2 was maintained in the chamber during deposition. XPS was acquired after each Ti deposition. The thicknesses of the deposited layers were calculated using the attenuation of the Mo 3*d* core level intensity via methods described in Supporting

Information. The samples were then capped with 1-2 nm Au in-situ to prevent oxidation in air upon removal from UHV. An additional *ex-situ* Au deposition of 80 nm of Au was performed in the UVML cleanroom evaporator. A small region of the sample was masked off for TDTR measurement by taping a piece of thin Mo foil after the initial 80 nm Au deposition. Another 120 nm of Au were deposited for probe station measurements of cross-plane electrical resistance and Seebeck coefficient. TDTR (performed by David Hans Olson in Prof. Hopkins lab), and electrical resistance and Seebeck coefficient measurements (performed by Tianhui Zhu in Prof. Zebarjadi's lab) are described in Sections 2.3.6-2.3.8.

4.4.3 Results and Discussion

4.4.3.1 XPS Characterization of MBE WSe_2

XPS spectra of as-grown WSe_2 samples are shown in Figure 4.4.1. The W $4f_{7/2}$ peak appears at ~32.4 eV with a spin orbit splitting of 2.14 eV. The small feature at ~37.8 eV is the W 5*p* peak. Four of the five spectra appear nearly identical demonstrating reasonably good control over stoichiometry and thickness in our MBE growth process. During growth, the RHEED patterns were monitored to achieve an approximate thickness of a WSe_2 bilayer. In other words, assuming the RHEED pattern of the substrate disappears after complete surface coverage at a minimum of one monolayer, the duration of the growth was set to be double the time it takes for the RHEED pattern to disappear. This is merely an approximation given that the material grows in islands resulting of variable thickness as evident in AFM images of films grown using this procedure shown in Figure 4.4.2. The contrast at the edge of the flakes in the AFM image is due to oxidation (formation of WO_x) following prolonged air exposure (~ 1 week) and has been previously observed by Park *et al*. in STM/STS studies of MBE-grown WSe_2.[19] Selective oxidation at flake edges occurs due to the presence of dangling bonds.

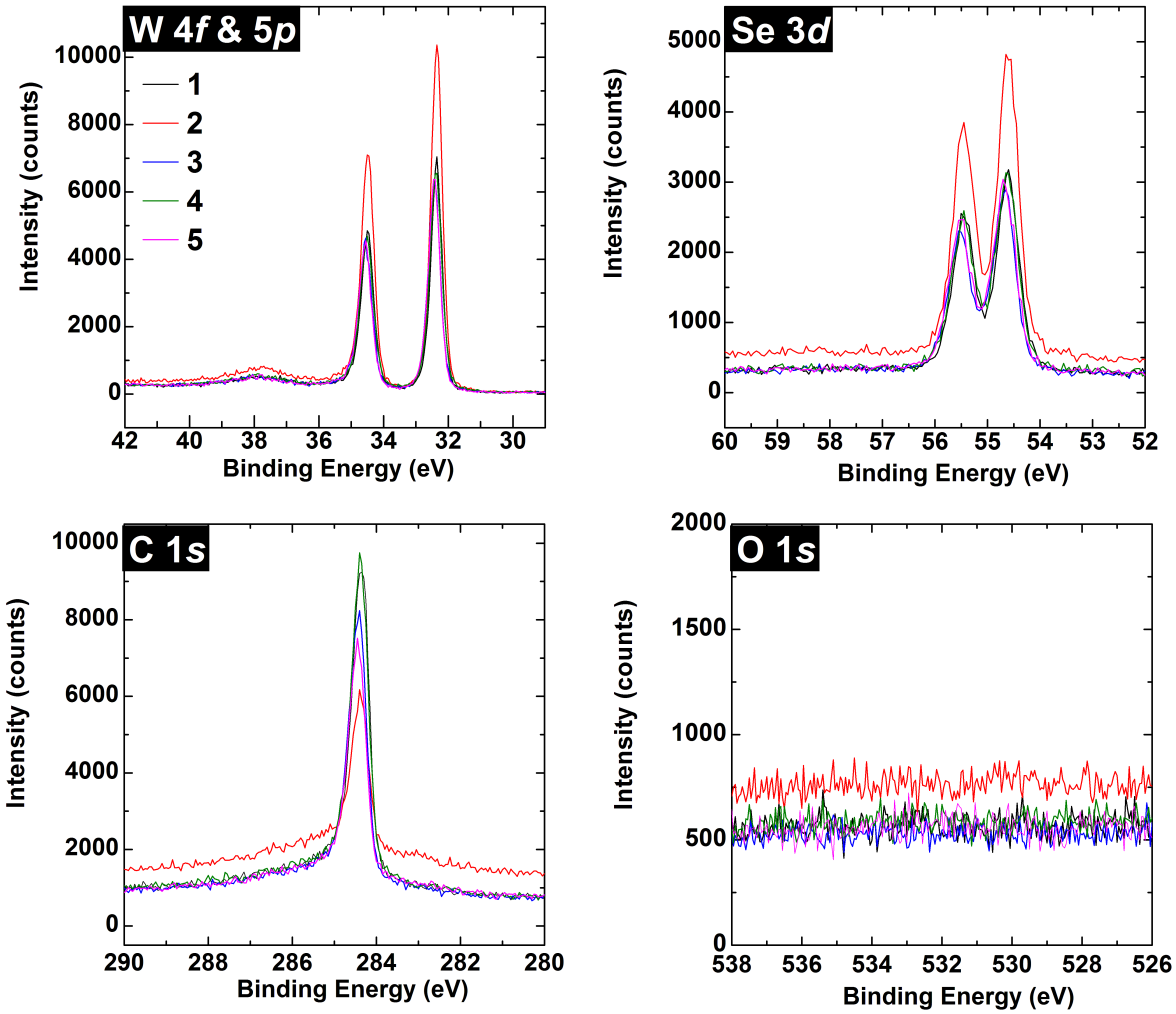

Figure 4.4.1. XPS spectra of WSe_2 films deposited under identical conditions by MBE

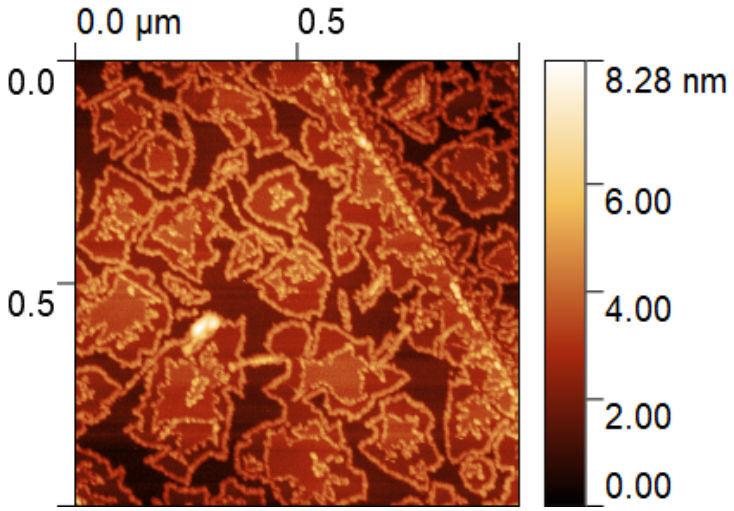

Figure 4.4.2. AFM image of "bilayer" WSe_2 showing flakes exhibiting regions of monolayer, bilayer and trilayer coverage on top of a fully coalesced layer. The sample was exposed to air for ~ 1 week. No metal overlayer was deposited on this sample.

The effective thickness of each as-grown WSe_2 film is calculated using the attenuation of the C 1*s* signal in the WSe_2. We note that the C 1*s* peak overlaps with the $L_3M_{23}M_{45}(^3P)$ Se Auger feature.[20] In order to account for this, the Auger is subtracted from the C 1*s* region using data from a reference sample grown on a different substrate, Al_2O_3, in which no other spectral feature overlaps with the Auger. We take the ratio of the Se 3*d* intensity of our film to that of the reference sample. The Auger feature in the reference film is multiplied by the ratio and subtracted from the C 1*s* spectra corresponding to our samples. This is demonstrated in Figure 4.4.3. The C 1*s* peak is fit with a Doniach-Sunjic convoluted with Gaussian in kolXPD and the attenuation equation in Section 2.3.1.5 is used to calculate the WSe_2 film thickness with an effective attenuation length of 17.949 Å for the C 1*s* core level electrons.[21] Due to the nonuniform morphology of the sample apparent in the AFM image, the calculated value is referred to as an "effective" thickness since the thickness calculation assumes that the overlayer has uniform thickness.

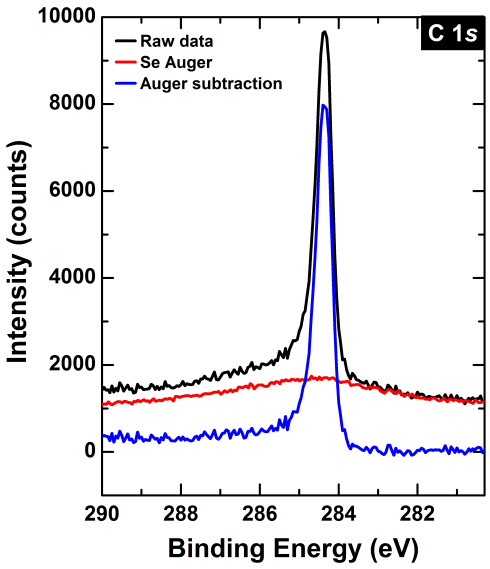

Figure 4.4.3. Subtraction of Se Auger from C 1*s*

Four of the five samples have an effective thickness close to 1 nm while one is double. The anomalous thickness observed in one of the samples is likely due to instabilities the W flux. The values of binding energy, spin orbit splitting, Gaussian FWHM, Se/W ratio, and effective thickness of the five films are reported in Table 4.3. Binding energy, FWHM, and spin-orbit splitting values are accurate within 0.05 eV. The Se/W ratio value was calculated by taking the RSF-normalized ratio of the Se 3*d* to W 4*f* intensities. The value is likely inaccurate due to errors in RSF mentioned previously in Section 2.3.14 however it provides a measure of the variability of between samples.

The samples were briefly removed from UHV following initial XPS measurements in order to tape a shadow mask for contact deposition. The spectra following ~10 min of air exposure are shown in Figure 4.4.4. The chemical state corresponding to WO_x is reported to exhibit a peak near 35.09 – 35.25 eV in the W *4f* spectrum and at 530.55 - 530.79 eV in the O 1*s* spectrum.[3] The amount of WO_x present is below our detection limit for all samples except for Sample 1 in which the O 1*s* peak was higher than the others. A small amount of physisorbed oxygen and carbon

species are present on the surface. No significant core level shifts are observed after air exposure indicating negligible doping by surface adsorbates.

Table 4.3. Comparison of five WSe_2 films grown by MBE with identical processes

Sample number	W $4f_{7/2}$ BE (eV)	Spin orbit splitting (eV)	FWHM (eV)	Se $3d_{5/2}$ BE (eV)	Spin orbit splitting (eV)	FWHM (eV)	Effective Thickness (Å)	S/W Ratio	Se $3d_{5/2}$ BE - W $4f_{7/2}$ BE (eV)
1	32.36	2.14	0.32	54.61	0.85	0.39	9.9	2.35	22.25
2	32.35	2.14	0.32	54.60	0.85	0.36	19.9	2.30	22.25
3	32.43	2.14	0.35	54.68	0.85	0.42	13.5	2.38	22.25
4	32.38	2.14	0.35	54.63	0.84	0.40	9.7	2.37	22.25
5	32.43	2.14	0.34	54.68	0.85	0.40	11.7	2.30	22.25

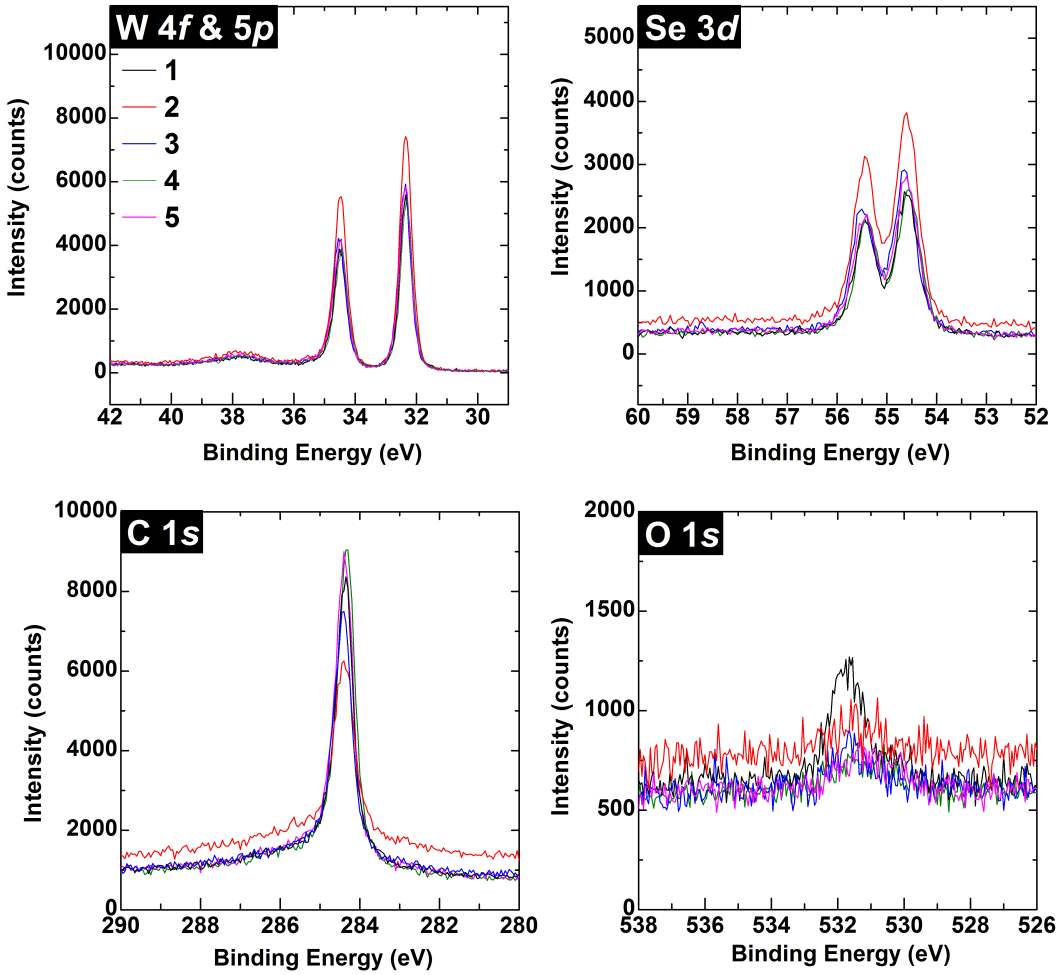

Figure 4.4.4. XPS spectra acquired following 10 min. air exposure

4.4.3.2 XPS Characterization of Contact Interface Chemistry

XPS acquired following the deposition of ~2 nm of pure Ti metal is shown in Figure 4.4.5. The thickness of the metal contact was calculated from the attenuation of the Se 3*d* core level. In the W 4*f* spectrum in (a), it is clear that metallic W appears as a result of W-Se bond scission. The Ti 3*p* peak, shown in red, overlaps with the W 4*f* spectral region with an asymmetric peak centered 32.93 eV. This Ti 3*p* line shape was determined from a reference Ti sample and its intensity was determined based on the ratio of the Ti 2p peak intensities in our sample and the reference sample. In Figure 4.4.5(b), the Ti 3*p* contribution is subtracted from the W 4*f* spectrum and fits of the W^0 and WSe_2 chemical states are shown in blue and green, respectively. The Se 3*d* and Ti 2*p* spectra exhibit broadening due to the presence of new chemical states attributed to the Ti + Se reaction products. TiSe has been found to have an enthalpy of formation ($\Delta H^{\circ}_{f,298\,K}$) of –222 ± 42 kJ/mol which is significantly lower than that of WSe_2 which is reported to be -185.5 ± 5.5 kJ/mol.[22] Values of $\Delta H^{\circ}_{f,298\,K}$ ranging from -352 ± 7.0 to -345 ± 2 kJ/mol have been calculated for Se/Ti stoichiometries ranging from 2 to 1.80.[23] The binding energy of $TiSe_2$ is reported to be at 456 eV in the Ti 2*p* spectrum and 54.3 eV in the Se 3d spectrum.[24] Spectral deconvolution of the Se 3*d* and Ti 2*p* regions is challenging, particularly given the asymmetric line shape of Ti 2*p* and the high level of noise in our Se 3*d* spectrum. Nevertheless, it is apparent in the Se 3*d* spectrum that at least one new chemical state is present in addition to W-Se. The core level shift that occurs in the W 4*f* peak of WSe_2 following the deposition of Ti is within the error margins of 0.05 eV indicating no significant band bending.

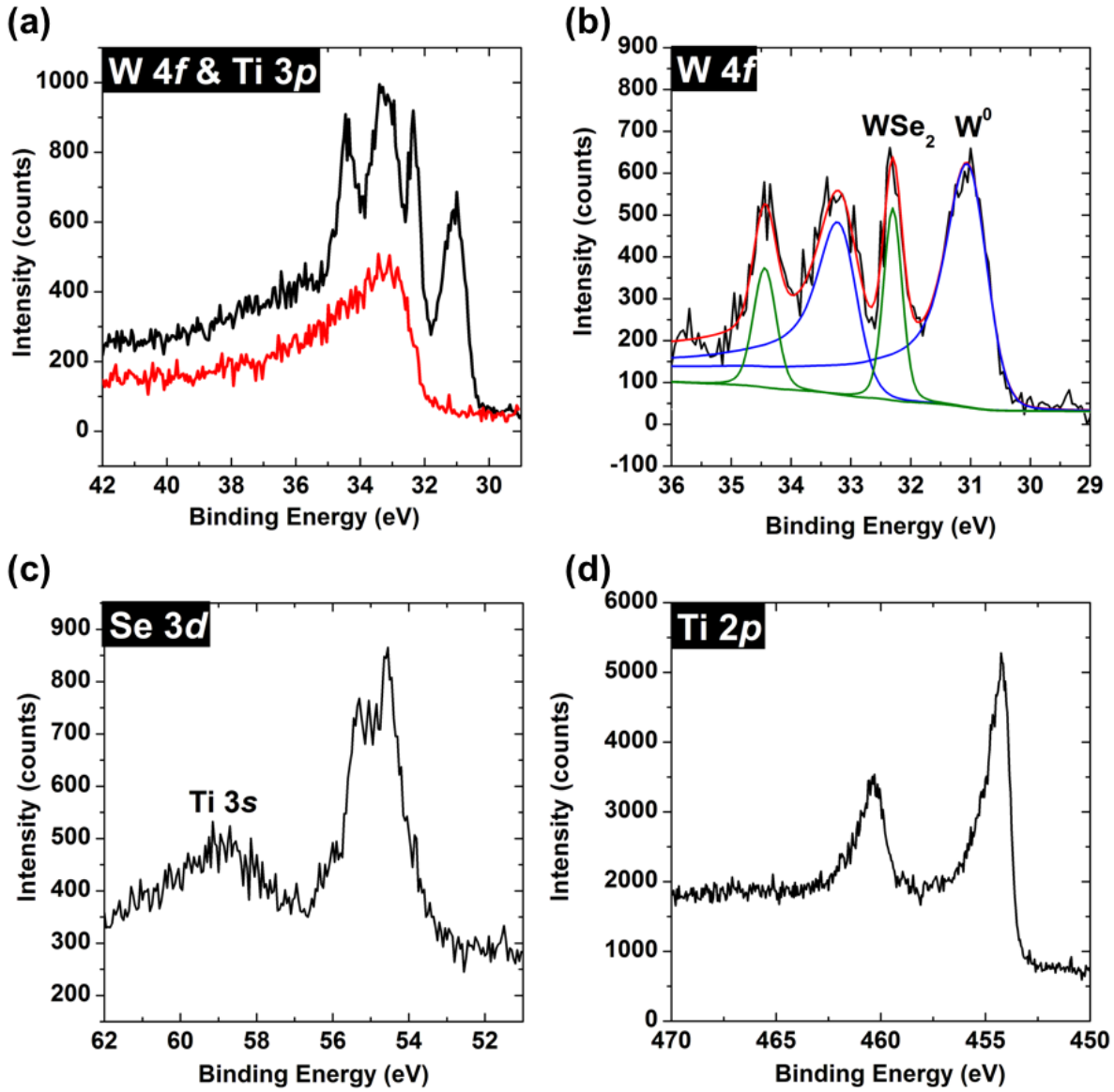

Figure 4.4.5. XPS spectra acquired following the deposition of Ti on WSe2 where (a) shows the overlap of W 4*f* with Ti 3*p* and in (b) the Ti 3*p* contribution to the W 4*f* signal is subtracted. (c) and (d) show Se 3*d* and Ti 2*p*.

Next, the interface chemistry resulting from the deposition of 2.5 nm TiO_x is examined. The deposition of TiO_x is performed with a partial pressure of oxygen in the chamber as in the previous chapter. The W 4*f* spectrum in Figure 4.4.6 shows a shoulder at lower binding energy as indicated by the arrows. This could possibly correspond to chemical states such as WSe_x ($x < 2$)

at 31.83 eV or WO_xSe_y at 32.38 eV.[3] However, given that the Ti 3*p* peak is ~3 eV to higher binding energy than the W 4*f* peaks, we consider the possibility that the background of the Ti 3*p* peak contributes to the line shape of the W 4*f* peaks and is the source of the observed shoulder at lower binding energies. To do this, a Ti 3*p* spectrum was acquired on a reference TiO_x sample.

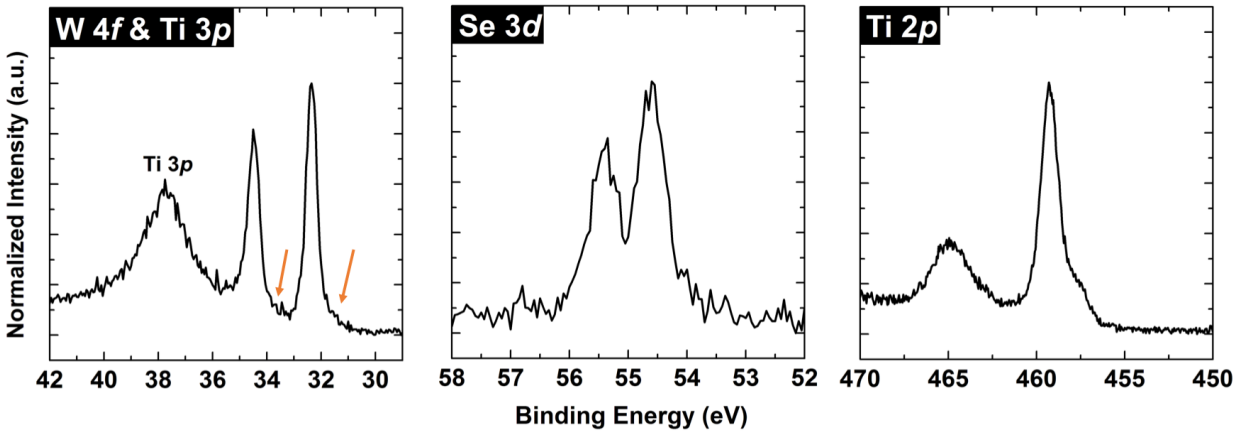

Figure 4.4.6. XPS spectra acquired after the deposition of TiO_x. Arrows point to the asymmetry in the spectra.

Figure 4.4.7(a) shows the raw data in black and the Ti 3*p* spectrum from the reference sample in red. Like in the Ti metal sample, the Ti 2*p* spectra were used to determine the intensity of the Ti 3*p* peak in our sample. The blue curve is the result of the subtraction of the red curve (Ti 3*p*) from the black spectrum (experimental raw data). In (b), the subtracted data is compared with the W 4*f* spectrum acquired prior to Ti deposition (post-air exposure). The low binding energy shoulder is still present in comparison with a pristine film, indicating that another chemical state exists, however it is likely close to the limit of detection and not prominent due to the high level of noise. Fits to the raw data shown in Figure 4.4.6(a) are shown below in Figure 4.4.8(a). In the fit we see a low binding energy chemical state which occurs at 31.64 eV. This is close to reported values of WSe_x (31.83 eV) indicating that a reaction occurred between WSe_2 and Ti resulting in

the formation of a small amount of $TiSe_x$. We also observe the formation of WO_x at 35.09 eV. In total, the W 4*f* signal reflects a composition of 90% WSe_2, 4% WSe_x and 6% WO_x. In other words, only 10% of the WSe_2 reacted during TiO_x deposition. The formation of WSe_x and WO_x under a deposition pressure of 5×10^{-6} mbar has been previously reported by Smyth *et al.* with the deposition of Ir on geological WSe_2 crystals.[3] They also identified the WO_x chemical state after the deposition of Au in the absence of any interface reactions with WSe_2. This indicates that the formation of WO_x occurs independently of W-Se bond scission in HV deposition conditions, likely at step edges as discussed previously. In the case of the deposition of a reactive metal, the metal is possibly catalyzing the oxidation reaction by breaking W-Se bonds, leaving W sites uncoordinated.

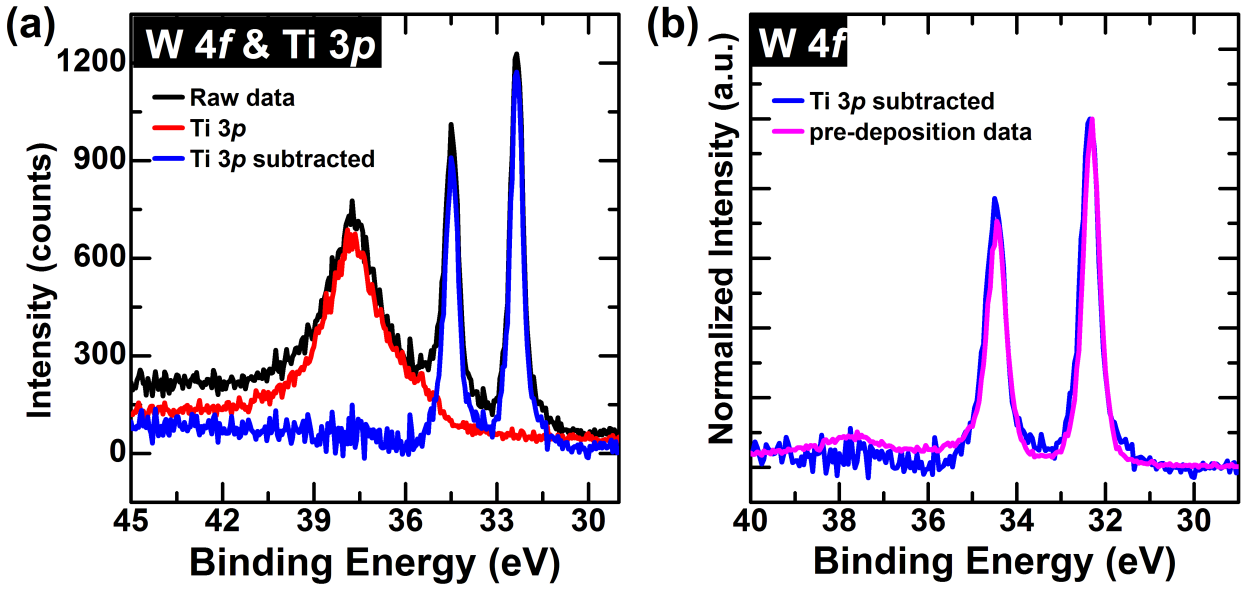

Figure 4.4.7. (a) Subtraction of the Ti 3p contribution to W 4*f* spectrum and (b) comparison of the subtracted data a spectrum acquired before Ti deposition. The presence of a shoulder at the low binding energy of the W 4f peaks suggests that an interface reaction occurred.

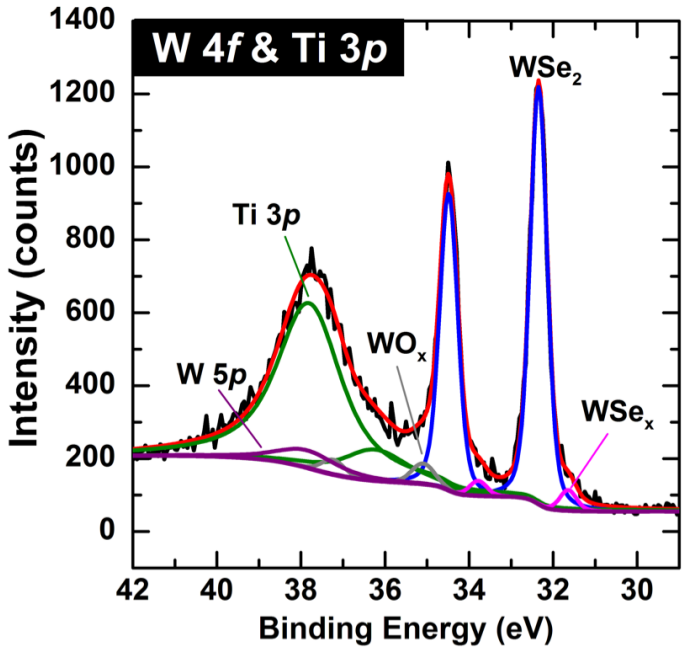

Figure 4.4.8. Fits to W 4*f* and Ti 3*p* of WSe2 with a TiO_x overlayer

The third type of interface created was a Ti/TiO_x heterostructure similar to that reported in the previous chapter. Here, 1.5 nm of TiO_x were deposited on WSe_2. XPS acquired after this deposition is shown in Figure 4.4.9 in black. The TiO_x composition is comparable to that of Sample 4 (83% TiO_2) resulting in identical interface chemistry where the W 4*f* spectrum shows a composition of 90% WSe_2, 4% WSe_x and 6% WO_x. This suggests that repeatable interface composition is achievable under identical deposition conditions. The subsequent deposition of 2.4 nm of Ti metal, corresponding to the red spectra, does not result in the formation of additional WSe_x or W^0 as the TiO_x layer acts as a barrier preventing additional reactions with the top Ti layer.

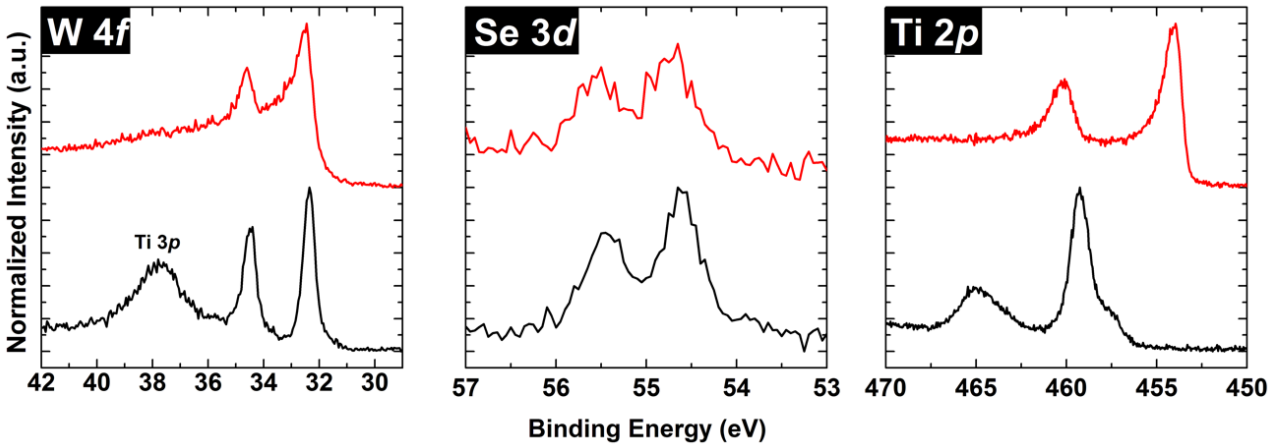

Figure 4.4.9. XPS acquired on WSe_2 after the deposition of 1.8 nm TiO_x in (a) the deposition of 1.7 nm Ti in (b)

4.4.3.3 Thermal Boundary Conductance of Contacts to WSe_2

TDTR was performed to determine the thermal boundary conductance across the interfaces. The results are shown in Table 4.4 and compared with those reported on MoS_2 substrates in the previous chapter. A plot of the data is shown in Figure 4.4.10. Deposition of Au/Ti contacts on the ~ 1 nm WSe_2/HOPG sample and on geological MoS_2 results in comparable values of h_K of 22.2 ± 2.5 and 21.1 ± 5.7 MW m^{-2} K^{-1}, respectively. For the second Ti-contacted sample, which corresponds to ~ 2 nm WSe_2, a much lower value of 6.77 ± 0.63 MW m^{-2} K^{-1} is measured. If we assume the resistances across the Ti/WSe_2 and WSe_2/HOPG to be the same in both samples, then the difference in h_K is attributed to the difference in the thickness of the WSe_2 layer. Given the extremely low intrinsic cross-plane conductivity of WSe_2[11-12, 25] (up to two orders or magnitude lower than that of TiO_x), a film containing more WSe_2 layers is expected to cause the total interfacial conductance to decrease.

Table 4.4. Measured h_K for different contacts to MBE WSe_2/HOPG compared with bulk geological MoS_2 reported in Chapter 4.3.

Contacts	Total Interfacial Conductance MBE WSe_2/HOPG samples (MW m^{-2} K^{-1})	Total Interfacial Conductance Bulk geological MoS_2 (MW m^{-2} K^{-1})
Au/Ti	22.2 ± 2.5 (1 nm WSe_2) 6.77 ± 0.63 (2 nm WSe_2)	21.1 ± 5.7
Au/TiO_x	9.57 ± 0.72 10.5 ± 0.92	16.0 ± 2.8
Au/Ti/TiO_x	12.9 ± 1.3	12.1 ± 2.8 (for Ti = 1.7 nm) 21.5 ± 1.6 (for Ti ≥ 2.7 nm)

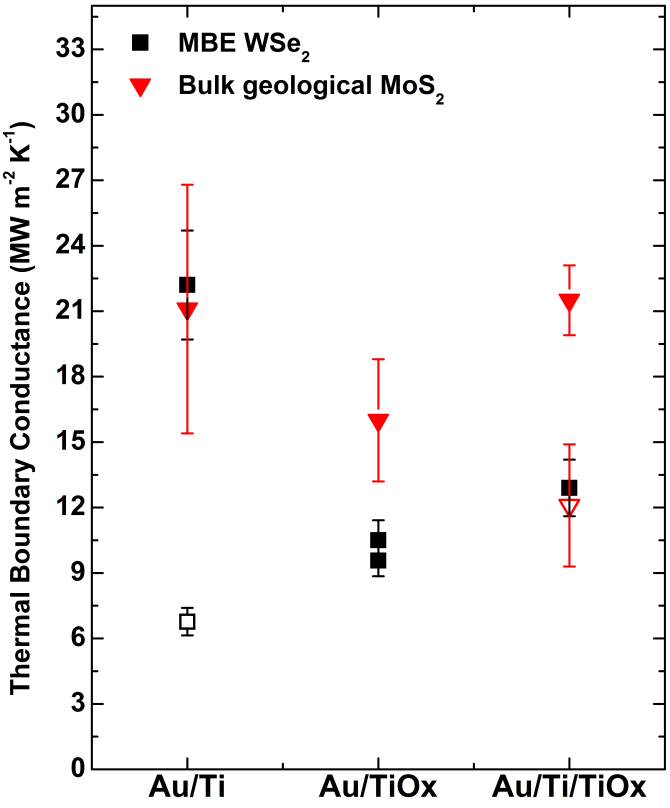

Figure 4.4.10. Plot of h_K values tabulated in Table 4.4. Shaded markers correspond to samples of comparable WSe_2 and Ti layer thicknesses. Open markers represent samples where a thickness difference in the WSe_2 film (black square corresponding to 2 nm WSe_2) or Ti layer (red triangle corresponding to 1.7 nm Ti) likely dominates h_K.

With the assumption that the Ti/WSe_2 and WSe_2/HOPG contributions to the total resistance are the same in both sample, we calculate the difference in the resistance between the two samples determine the effective difference in resistance between 2 nm and 1 nm of WSe_2. The result of the subtraction is 9.74 ± 0.15 MW m^{-2} K^{-1}. Assuming a sample that is 1 nm thick, this equates to an effective thermal conductivity of ~0.01 W m^{-1} K^{-1}. This value is close to the reported cross-plane thermal conductivity of 0.05 W m^{-1} K^{-1} for disordered WSe_2. Since our WSe_2 is highly polycrystalline as shown in Figure 4.4.2, it is not surprising that this calculated effective thermal conductivity is on the same order of magnitude as the reported value. We note that the values are not directly comparable given that the reported value was directly measured by TDTR on a 62 nm-thick WSe_2 film.[12] Nevertheless, our analysis highlights the dominating contribution of the intrinsic cross-plane resistance of WSe_2 to the measured value of h_K. Choi *et al.*[26] have proposed that a high degree of bonding at the interface results in an increase in WSe_2/WSe_2 interlayer resistance due to a change in the phonon density of states (pDOS) of the top WSe_2 layer that is bonded to the metal. Bonding at the metal/WSe_2 interface is speculated to shift the pDOS toward that of the metal. This reduces the pDOS mismatch at the metal/WSe_2 interface, but increases the pDOS mismatch at the WSe_2/WSe_2 interface. This mechanism could also possibly explain the very low calculated effective thermal conductivity in our thicker Ti/WSe_2 sample. The effective thermal resistance in the work by Choi *et al*. is measured to be 4×10^{-8} m^2 K W^{-1} which equals 0.025 W m^{-1} K^{-1} at 1 nm thickness. This is very close to our calculated value.

Table 4.4 and Figure 4.4.10 show that Au/TiO_x contacts resulted in a lower h_K for the MBE WSe_2 films than for bulk geological MoS_2. This could be related to the differences in interface chemistry examined previously. Whereas TiO_x/MoS_2 interfaces exhibit no chemical reactions, the TiO_x/WSe_2 interface is comprised of additional chemical states including WSe_x and WO_x that

contribute to phonon scattering. Two samples were measured and exhibit the same h_K values within error. The Au/Ti/TiO_x contact to WSe_2 results in a slightly higher h_K than the Au/TiO_x contact. This is expected given the results presented in the previous chapter.

4.4.3.4 Preliminary Thermoelectric Property Measurement

Seebeck coefficient and cross-plane electrical resistance measurements were performed using methods described in Sections 2.3.7-2.3.8. The thermal boundary conductance combined with the Seebeck coefficient and cross-plane electrical conductance determine the efficacy of thermoelectric energy conversion which is given by the figure of merit $ZT = \frac{S^2\sigma}{\kappa}T$ where S is the Seebeck coefficient, σ is the electrical conductivity and κ is the thermal conductivity.[27] The quantity $S^2\sigma$ is known as the power factor. We have performed preliminary measurements of electrical resistance and Seebeck coefficient. Data was acquired on different days following sample fabrication to determine the stability of the samples. The average electrical resistance and Seebeck coefficients measured on 3-4 different pads each measured 3-4 times is tabulated here for WSe_2 with Ti and TiO_x contacts (samples 2 and 4 in Table 4.3). The Ti sample exhibits a small increase in resistance between the first two days likely due to oxidation of the contact from the side. The resistance in the TiO_x sample remains within error at all three time points. The Seebeck coefficient remains roughly within error as a function of time for both samples. A decrease in resistance is expected to result in an increase in the Seebeck coefficient but this is not observed here. This indicates that the measured value of the Seebeck coefficient is likely not dominated by the contact interface. Further study is necessary to better understand the behavior observed here.

Table 4.5. Cross-plane electrical resistance and Seebeck coefficient

	Ti/ 2 nm WSe_2/HOPG (sample 2)			TiO_x/1 nm WSe_2/HOPG (sample 4)		
	Day 1	Day 2	Day 8	Day 1	Day 2	Day 10
Resistance (mΩ)	31.43 ± 1.3	39.82±2.76	41.22±4.6	53.42±2.01	52.34±7.67	62.63±10.14
Seebeck (uV/K)	65.16±8.39	52.7 ± 6.99	48.72±9.2	63.88±5.77	65.25±6.06	45.15±7.60

4.4.4 Conclusion and Future Work

The work in this chapter has demonstrated our ability to grow WSe_2 by MBE with reasonably good repeatability. The films exhibit minimal or no oxidation upon 10 minutes of air exposure. The deposition of Ti metal on WSe_2 causes W-Se bond scission resulting in the formation of W^0. This is similar to what is observed for MoS_2 and a similar value of h_K is reported. Unlike with MoS_2, the deposition of Ti in a partial pressure of O_2 does not completely prevent interface reactions as the formation WSe_x and WO_x is observed. This could potentially be attributed to the lower enthalpy formation of MoS_2 (-271.8 ± 4.9 kJ/mol) compared to that of WSe_2 (-185.5 ± 5.5 kJ/mol) which is indicative of higher thermodynamic stability.[28]. The Ti-contacted samples exhibit a higher thermal boundary conductance and lower cross-plane electrical resistivity than those contacted with TiO_x. Further study is needed to understand the behavior of the Seebeck coefficient. Additional topics for further study are discussed below.

4.4.4.1 Property Engineering with Control of Interface Bonding

Our result measured on the 2 nm WSe_2 contacted with metallic Ti showed that it is possible to achieve extremely low thermal boundary conductance with low electrical resistivity. The work previously discussed by Choi *et al*.[26] demonstrates that the degree of bonding at the metal/WSe_2 interface is inversely related to the cross-plane thermal conductivity between the WSe_2 layers in bilayer material. This phenomenon can be exploited to optimize electrical and thermal transport at

the contact without compromising the thermal gradient in the material for thermoelectric applications. Lastly, the work mentioned previously by Kim *et al*.[6] suggests that WSe_x (the result of ion irradiation of WSe_2) has advantageous properties for electrical transport. The ability to control the quantity of WSe_x with O_2 pressure offers an alternative and possibly preferable route to interface engineering as ion irradiation has been found to be detrimental to thermal properties.[12] In combination with engineering interface chemistry with O_2 partial pressure during deposition, this opens many doors for tuning transport properties.

4.4.4.2 Doping with WO_x

Our results show that the deposition of Ti and TiO_x overlayers on WSe_2 causes negligible band bending meaning that the semiconductor is not doped by the overlayer or reaction products via charge transfer. Charge-transfer doping with MoO_x overlayers has been previously demonstrated on MoS_2, WSe_2, as well as graphene.[29-31] Yamamoto *et al*[32] have shown that exposure of geological WSe_2 to UV-O_3 at 100 ºC causes oxidation of the top layers that results in heavy hole doping. In other words, instead of depositing MoO_x, the "native oxide" WO_x can serve the same purpose. The rapid controllable oxidation in UV-O_3 is preferable to prolonged air exposure which also results in the adsorption of adventitious carbon that suppresses charge injection at the WSe_2/WO_x interface, however Rack *et al*. demonstrate that physisorbed species in air suppress n-type conduction while increasing p-type conduction.[33] Future work can implement this method to oxidize the MBE-grown WSe_2 at the surface and examine the resulting changes in interface chemistry, band bending, and thermal/electrical properties. Deliberate doping of the material can help overcome the challenge of ambipolar conduction.[30, 34-35]

4.4.5 References

1. Jaegermann, W.; Pettenkofer, C.; Parkinson, B. A., Cu and Ag deposition on layered p-type WSe2: Approaching the Schottky limit. *Physical Review B* **1990,** *42* (12), 7487-7496.
2. Jaegermann, W.; Pettenkofer, C.; Parkinson, B. A., Ag on p-WSe2(0001) surfaces: approaching the Schottky limit? *Vacuum* **1990,** *41* (4), 800-803.
3. Smyth, C. M.; Addou, R.; McDonnell, S.; Hinkle, C. L.; Wallace, R. M., WSe2-contact metal interface chemistry and band alignment under high vacuum and ultra high vacuum deposition conditions. *2D Materials* **2017,** *4* (2), 025084.
4. Smyth, C. M.; Walsh, L. A.; Bolshakov, P.; Catalano, M.; Addou, R.; Wang, L.; Kim, J.; Kim, M. J.; Young, C. D.; Hinkle, C. L.; Wallace, R. M., Engineering the Palladium–WSe2 Interface Chemistry for Field Effect Transistors with High-Performance Hole Contacts. *ACS Applied Nano Materials* **2019,** *2* (1), 75-88.
5. Klein, A.; Pettenkofer, C.; Jaegermann, W.; Lux-Steiner, M.; Bucher, E., A photoemission study of barrier and transport properties of the interfaces of Au and Cu with WSe2(0001) surfaces. *Surface Science* **1994,** *321* (1), 19-31.
6. Kim, D. D. H. K., T.; Shin, S.; Kim, S.; Lee CW.; Lee J.; Cheong, H.; Seo, D. H.; Se, S., The enhanced low resistance contacts and boosted mobility in two-dimensional p-type WSe2 transistors through Ar+ ion-beam generated surface defects. *AIP Advances* **2016,** *6* (10), 105307.
7. Liu, W.; Kang, J.; Sarkar, D.; Khatami, Y.; Jena, D.; Banerjee, K., Role of Metal Contacts in Designing High-Performance Monolayer n-Type WSe2 Field Effect Transistors. *Nano Letters* **2013,** *13* (5), 1983-1990.
8. Fang, H.; Chuang, S.; Chang, T. C.; Takei, K.; Takahashi, T.; Javey, A., High-Performance Single Layered WSe2 p-FETs with Chemically Doped Contacts. *Nano Letters* **2012,** *12* (7), 3788-3792.
9. Zhang, W.; Chiu, M.-H.; Chen, C.-H.; Chen, W.; Li, L.-J.; Wee, A. T. S., Role of Metal Contacts in High-Performance Phototransistors Based on WSe2 Monolayers. *ACS Nano* **2014,** *8* (8), 8653-8661.
10. Kang, J.; Liu, W.; Sarkar, D.; Jena, D.; Banerjee, K., Computational Study of Metal Contacts to Monolayer Transition-Metal Dichalcogenide Semiconductors. *Physical Review X* **2014,** *4* (3), 031005.
11. Zhou, W.-X.; Chen, K.-Q., First-Principles Determination of Ultralow Thermal Conductivity of monolayer WSe2. *Scientific Reports* **2015,** *5*, 15070.
12. Chiritescu, C.; Cahill, D. G.; Nguyen, N.; Johnson, D.; Bodapati, A.; Keblinski, P.; Zschack, P., Ultralow Thermal Conductivity in Disordered, Layered WSe₂ Crystals. *Science* **2007,** *315* (5810), 351.
13. Wang, X.; Zebarjadi, M.; Esfarjani, K., First principles calculations of solid-state thermionic transport in layered van der Waals heterostructures. *Nanoscale* **2016,** *8* (31), 14695-14704.
14. Shakouri, A.; Bowers, J. E., Heterostructure integrated thermionic coolers. *Applied Physics Letters* **1997,** *71* (9), 1234-1236.
15. Mahan, G. D., Thermionic refrigeration. *Journal of Applied Physics* **1994,** *76* (7), 4362-4366.
16. Markov, M.; Zebarjadi, M., Thermoelectric transport in graphene and 2D layered materials. *Nanoscale and Microscale Thermophysical Engineering* **2018**, 1-11.

17. Zebarjadi, M., Electronic cooling using thermoelectric devices. *Applied Physics Letters* **2015,** *106* (20), 203506.
18. Poudel, N.; Liang, S.-J.; Choi, D.; Hou, B.; Shen, L.; Shi, H.; Ang, L. K.; Shi, L.; Cronin, S., Cross-plane Thermoelectric and Thermionic Transport across Au/h-BN/Graphene Heterostructures. *Scientific Reports* **2017,** *7* (1), 14148.
19. Park, J. H.; Vishwanath, S.; Liu, X.; Zhou, H.; Eichfeld, S. M.; Fullerton-Shirey, S. K.; Robinson, J. A.; Feenstra, R. M.; Furdyna, J.; Jena, D.; Xing, H. G.; Kummel, A. C., Scanning Tunneling Microscopy and Spectroscopy of Air Exposure Effects on Molecular Beam Epitaxy Grown WSe2 Monolayers and Bilayers. *ACS Nano* **2016,** *10* (4), 4258-4267.
20. Briggs, D., Handbook of X-ray Photoelectron Spectroscopy. *Surface and Interface Analysis* **1981,** *3* (4), 72-73.
21. Jablonski, A., NIST Electron Effective-Attenuation-Length Database. **2011**.
22. Olin, Å.; Agency, O. N. E., *Chemical Thermodynamics of Selenium*. Elsevier: 2005.
23. Zelenina, L. N.; Chusova, T. P.; Titov, A. N., Thermodynamic properties of titanium selenides with variable composition TiSe2-TiSe1.80. *Russian Chemical Bulletin* **2011,** *60* (3), 581.
24. Sun, L.; Chen, C.; Zhang, Q.; Sohrt, C.; Zhao, T.; Xu, G.; Wang, J.; Wang, D.; Rossnagel, K.; Gu, L.; Tao, C.; Jiao, L., Suppression of the Charge Density Wave State in Two-Dimensional 1T-TiSe2 by Atmospheric Oxidation. *Angewandte Chemie* **2017,** *129* (31), 9109-9113.
25. Norouzzadeh, P.; Singh, D. J., Cross-plane thermal conductivity of tungsten diselenide. *physica status solidi c* **2017,** *14* (3-4), 1700078.
26. Choi, Y.-G.; Jeong, D.-G.; Ju, H. I.; Roh, C. J.; Kim, G.; Mun, B. S.; Kim, T. Y.; Kim, S.-W.; Lee, J. S., Covalent-bonding-induced strong phonon scattering in the atomically thin WSe2 layer. *arXiv preprint arXiv:1812.02383* **2018**.
27. Zhang, G.; Zhang, Y.-W., Thermoelectric properties of two-dimensional transition metal dichalcogenides. *Journal of Materials Chemistry C* **2017,** *5* (31), 7684-7698.
28. O'Hare, P. A. G.; Lewis, B. M.; parkinson, B. A., Standard molar enthalpy of formation by fluorine-combustion calorimetry of tungsten diselenide (WSe2). Thermodynamics of the high-temperature vaporization of WSe2. Revised value of the standard molar enthalpy of formation of molybdenite (MoS2). *The Journal of Chemical Thermodynamics* **1988,** *20* (6), 681-691.
29. McDonnell, S.; Azcatl, A.; Addou, R.; Gong, C.; Battaglia, C.; Chuang, S.; Cho, K.; Javey, A.; Wallace, R. M., Hole Contacts on Transition Metal Dichalcogenides: Interface Chemistry and Band Alignments. *ACS Nano* **2014,** *8* (6), 6265-6272.
30. Zhou, C.; Zhao, Y.; Raju, S.; Wang, Y.; Lin, Z.; Chan, M.; Chai, Y., Carrier Type Control of WSe2 Field-Effect Transistors by Thickness Modulation and MoO3 Layer Doping. *Advanced Functional Materials* **2016,** *26* (23), 4223-4230.
31. Meyer, J.; Kidambi, P. R.; Bayer, B. C.; Weijtens, C.; Kuhn, A.; Centeno, A.; Pesquera, A.; Zurutuza, A.; Robertson, J.; Hofmann, S., Metal Oxide Induced Charge Transfer Doping and Band Alignment of Graphene Electrodes for Efficient Organic Light Emitting Diodes. *Scientific Reports* **2014,** *4*, 5380.
32. Yamamoto, M.; Nakaharai, S.; Ueno, K.; Tsukagoshi, K., Self-Limiting Oxides on WSe2 as Controlled Surface Acceptors and Low-Resistance Hole Contacts. *Nano Letters* **2016,** *16* (4), 2720-2727.
33. Hoffman, A. N.; Stanford, M. G.; Zhang, C.; Ivanov, I. N.; Oyedele, A. D.; Sales, M. G.; McDonnell, S. J.; Koehler, M. R.; Mandrus, D. G.; Liang, L.; Sumpter, B. G.; Xiao, K.; Rack, P. D., Atmospheric and Long-term Aging Effects on the Electrical Properties of Variable Thickness WSe2 Transistors. *ACS Applied Materials & Interfaces* **2018,** *10* (42), 36540-36548.

34. Oh, H. M.; Park, C.; Bang, S.; Yun, S. J.; Duong, N. T.; Jeong, M. S., Suppressing Ambipolar Characteristics of WSe2 Field Effect Transistors Using Graphene Oxide. *Advanced Electronic Materials* **2019,** *5* (2), 1800608.
35. Wang, Z.; Li, Q.; Chen, Y.; Cui, B.; Li, Y.; Besenbacher, F.; Dong, M., The ambipolar transport behavior of WSe2 transistors and its analogue circuits. *NPG Asia Materials* **2018,** *10* (8), 703-712.

4.5 Removal of Polymer Residues from MoS_2

The following chapter has been adapted from Freedy, K. M.; Sales, M. G.; Litwin, P. M.; Krylyuk, S.; Mohapatra, P.; Ismach, A.; Davydov, A. V.; McDonnell, S. J., MoS_2 cleaning by acetone and UV-ozone: Geological and synthetic material. *Applied Surface Science* **2019,** *478*, 183-188.

Abstract

The effects of poly(methyl methacrylate) (PMMA) removal procedures on the surface chemistry of both geological and synthetic MoS_2 are investigated. X-ray photoelectron spectroscopy (XPS) is employed following acetone dissolution, thermal annealing, and ultraviolet-ozone (UV-O_3) treatment of PMMA-coated MoS_2 samples. Specifically, we focus on the efficacy of polymer residue removal procedures and oxidation resistance of the different samples. Acetone dissolution followed by ultra-high vacuum (UHV) annealing was highly effective in removing carbon residues from one type of geological sample however not for a synthetic sample produced by sulfurization. Similarly, different types of samples require varying lengths of UV-O_3 exposure time for proper removal of residues, and some exhibit oxidation as a result. UV-O_3 exposure followed by a UHV anneal resulted in successful removal of carbon residues from MoS_2 produced by sulfurization while a substantial carbon signal remained on a chemical vapor deposited MoS_2 sample subjected to the same process. Differences in the effects of removal procedures are attributed to differences in surface morphology and material quality. For device fabrication applications, this work highlights the importance of developing PMMA removal processes specific to the MoS_2 used with full consideration for the processing required to obtain the MoS_2.

4.5.1 Introduction

Poly(methyl methacrylate) (PMMA) is commonly used for the transfer and photolithographic processing of graphene and TMD devices.[1-9] Studies on PMMA processing of graphene reveal that dissolution of PMMA in acetone leaves polymer residues on the surface of the sample.[10-12] The presence of polymer residues has been found to significantly affect important device properties such as doping, mobility, and contact resistance.[13-17] Contamination from polymer residues can also result in non-conformal growth of gate dielectric layers.[18] To decompose the residues following PMMA dissolution in acetone, graphene samples are typically annealed in vacuum or a controlled gas environment. Exposure to ultraviolet-ozone (UV-O_3) has also been suggested to aid in the removal of PMMA residues, manifesting in reduced contact resistance in graphene devices.[15, 17] While the removal of residues from graphene has been studied extensively, the effects of PMMA residues and means of their removal from MoS_2 are not reported to date. In most TMD device studies, PMMA is dissolved in acetone with no subsequent removal procedures[2-3, 8, 19-20] despite the fact that previous work on graphene would suggest that acetone treatment alone is not sufficient for removal of polymer residues. This work uses X-ray photoelectron spectroscopy (XPS) to characterize MoS_2 following different PMMA removal procedures, including acetone dissolution, UV-O_3 treatment, thermal annealing in ultra-high vacuum (UHV), and a combination of the three processes.

UV-O_3 treatment of MoS_2 has been previously implemented for a variety of applications in film growth and device processing on MoS_2 materials of different types. For example, Azcatl *et al* use UV-O_3 to functionalize the surface of mechanically exfoliated geological MoS_2 for improved atomic layer deposition of gate dielectrics[21-22] and Van Le *et al.* demonstrate improved performance of photovoltaics with UV-O_3 treatment of MoS_2 nanosheets derived from sonication

of MoS_2 powder.[23] Evidence suggests that different types of MoS_2 material can exhibit differences in surface chemistry upon UV-O_3 exposure. For example, Azcatl *et al.*[21] show that geological MoS_2 exposed to UV-O_3 for 15 min does not form Mo oxide nor exhibit MoS_2 bond scission, whereas Yang *et al.*[24] and Van Le *et al.*[23] observe oxidation of MoS_2 monolayer nanosheets after 3 min and 15 min of UV-O_3 treatment, respectively. Park *et al.*[25] demonstrate that the formation of oxide is dependent on UV-O_3 power settings. Power settings are scarcely reported meaning that results from independent studies in the literature cannot be compared in an attempt to discern differences between different types of MoS_2. Understanding potential differences requires a side-by-side comparison of samples processed with identical parameters. This was performed by Kurabayashi *et al.*[26], who report that geological MoS_2 has a higher oxidation resistance to UV-O_3 than chemical vapor deposited (CVD) material. Nevertheless, the effect of UV-O_3 treatment on polymer removal from geological and synthetic MoS_2 are not yet reported. This chapter examines UV-O_3 for polymer removal from synthesized films and bulk geological MoS_2 crystals, both of which are frequently used for device fabrication.

4.5.2 Materials and Methods

Two types of synthetic material were examined in this study. The first synthetic MoS2, referred to as Synthetic A throughout this chapter, was supplied to us by Dr. Sergiy Krylyuk and Dr. Albert V. Davydov at the National Institute of Standards and Technology. These samples were produced by sulfurization of metallic Mo via a method similar to that of Tarasov et al.[27] Mo films 4 nm thick were e-beam deposited onto SiO_2/Si substrates that were cleaned with acetone, isopropanol and de-ionized water. The substrates were loaded into a home-built horizontal CVD reactor and sulfurized at 750 °C and 1.6 kPa for 20 min using 30 sccm (standard cm^3/min) flow of H_2S diluted with 1000 sccm Ar carrier gas. This method produced ~10 nm thick polycrystalline

MoS2 films with an average grain size of ~20 nm. The second type of synthetic sample, referred to as Synthetic B, was provided by Dr. Pranab Mohapatra and Dr. Ariel Ismach at Tel Aviv University. The sample was synthesized using a micro-cavity based CVD technique at atmospheric pressure while flowing ultrahigh pure Ar gas. MoO_3 and sulfur powders were evaporated at 750 °C onto a sapphire substrate sonicated in acetone and isopropanol.[28] The MoS_2 films were transferred to a SiO_2/Si substrate following reported procedures using a polystyrene film.[29] Geological MoS_2 samples from two different vendors (SPI[30] and Ward Science[31]) were investigated in addition to the synthetic samples. Bulk geological crystals were mechanically exfoliated for surface cleaning immediately prior to PMMA spin coating.

Both types of synthetic and geological MoS_2 samples were spin coated with a 30 mg/mL solution of PMMA (Mw ≈ 996,000 by GPC) in chlorobenzene at 3000 rpm for 1 min and then 1000 rpm for 1 min with an acceleration rate of 1000 rpm/sec.[13] After spin coating, the samples were left on a hot plate for 10 min at 60 °C to cure the PMMA. The samples were then soaked in acetone for 2 h and subsequently treated under different conditions before XPS characterization. UV-O_3 treatment was performed in air using a UV grid lamp connected to a 3 kV, 0.03 A power supply (BHK, Inc.). XPS data was acquired using two different systems. Experiments 1 and 2 described in Table 4.6 were performed in the McDonnell lab's ScientaOmicron R3000 analyzer at a pass energy of 50 eV with a monochromated Al kα X-ray source in a ScientaOmicron UHV system. Experiment 3 described in Table 4.6 was performed in a PHI VersaProbe III UHV system at UVA's NMCF. Data was acquired with a monochromated Al kα X-ray source at a pass energy of 26 eV and a spot size of 100 μm. In all experiments, annealing was performed in the same UHV chamber as the XPS, meaning that the samples were not exposed to air after the final annealing step. AFM images for Experiment 1 were acquired using Prof. Floro's NT-MDT Spectrum

Instruments AFM and those in Experiment 3 were acquired at James Madison University using the Bruker Dimension Icon.

Table 4.6. Polymer Residue Removal Experiment Overview

	Process	Samples
Experiment 1	PMMA spin-coating 2 h removal in acetone 30 min UHV anneal at 550 °C	Synthetic A (Sulfurized MoS_2) Geological A (SPI)
Experiment 2	PMMA spin-coating 2 h removal in acetone Sequential UV-O_3 exposures 30 min UHV anneal at 550 °C	Synthetic A (Sulfurized Mo) Geological A (SPI)
Experiment 3	PMMA spin-coating 2 h removal in acetone 2 min UV-O_3 exposures 30 min UHV anneal at 550 °C	Synthetic A (Sulfurized Mo) Synthetic B (CVD) Geological A (SPI) Geological B (Ward's)

4.5.3 Results and Discussion

Figure 4.5.1(a) shows the C 1*s* spectra for both samples after PMMA dissolution in acetone and after annealing in UHV at 550 °C for 30 min (Experiment 1). The carbon on the starting material is adventitious carbon with a primary component at about 284 eV corresponding to C-C bonds and higher binding energy components corresponding to C-O-C and C-OH bonds. [32] After spin coating, curing, and dissolving PMMA in acetone, the total carbon signal increased by approximately a factor of 2 in the Synthetic A sample and by a factor of 5 in the Geological A sample. These numbers indicate a substantial quantity of PMMA residues when compared with adventitious carbon. It is not surprising that less adventitious carbon was present on the starting surface of the geological sample since it was exfoliated immediately prior to the experiment. There is also less PMMA residue left on the geological sample.

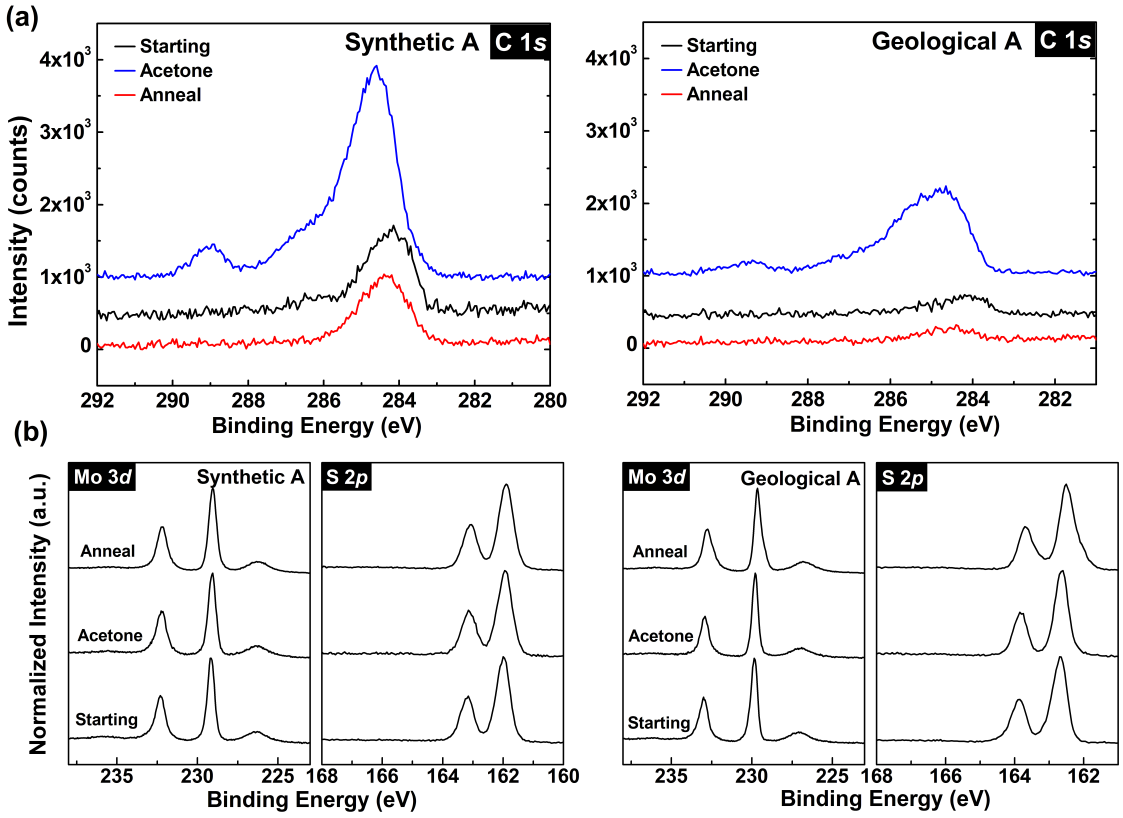

Figure 4.5.1. (a) C 1*s*, (b) Mo 3*d* and S 2*p* spectra acquired on starting material, after acetone dissolution, and after UHV annealing.

The difference in the efficacy of the removal process might be explained by the fact that the two samples exhibit drastically different surface morphologies as shown in the atomic force microscopy (AFM) images in Figure 3.4.2. The root-mean-square (RMS) surface roughness of the Synthetic A sample was found to be 1.7 nm (Figure 4.5.2(a)) whereas the Geological A sample has a surface roughness of 73 pm (Figure 4.5.2(b)) in agreement with literature values [33], indicating that it is atomically flat. Higher surface roughness in the synthetic sample also provides more surface area for PMMA residues to physisorb. We also note the emergence of a state at ~290 eV corresponding to C=O bonds [34-35] which disappears after annealing. Following annealing, 30 % of the acetone-dissolved PMMA carbon signal remains on the Synthetic A sample whereas only 9 %

remains on the Geological A sample. It is clear that annealing after solvent dissolution of PMMA is not sufficient for achieving a clean MoS_2 surface. As Figure 4.5.1(b) indicates, no significant changes in the Mo 3*d* and S 2*p* regions are observed in the Synthetic A sample. We note that after annealing there is an asymmetry on the low binding energy side of the Mo and S regions of the geological sample. This is likely due to the variations in local doping typical of geological samples.[36]

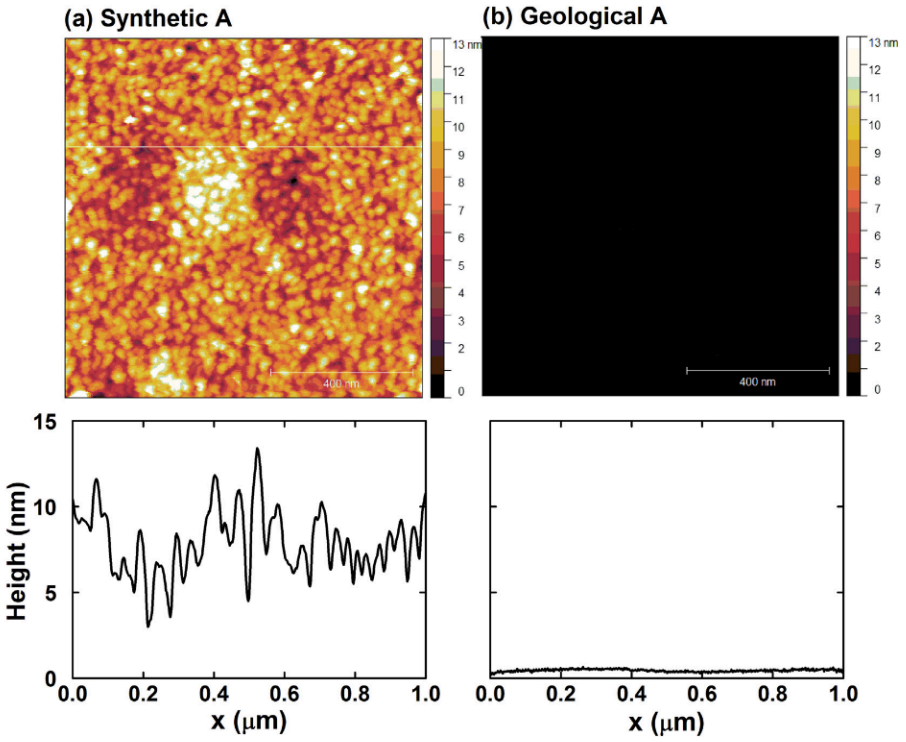

Figure 4.5.2. AFM images of (a) sulfurized MoS_2 and (b) geological material showing a drastic difference in surface roughness.

To determine if UV-O_3 treatment prior to UHV annealing can enhance the removal of carbon, a second set of samples were sequentially exposed to UV-O_3 for varying lengths of time after an initial PMMA dissolution with acetone (Experiment 2). These samples were measured with XPS after each treatment. The carbon spectra for synthetic and geological samples after UV-

O_3 treatment are shown in Figure 4.5.3(a). Air exposure between treatments led to a slight increase in the carbon signal of the geological sample between the 0.5 min and 1 min treatments, however the general trend for both samples is a steady reduction in the carbon signal with increasing UV-O_3 exposure time. All carbon is removed from the surface of the synthetic sample after a total of 10 min and from the geological sample after 5 min.

Spectral changes are observed in the Mo 3*d* and S 2*p* regions, shown in Figure 3.4.3(b), indicating modifications in the surface chemistry of the material as a result of UV-O_3 and post-treatment annealing. In the Synthetic A sample, we detect the increase of the Mo-O state after 2 min of exposure. The state increases in intensity relative to the Mo-S state as UV-O_3 exposure time is increased. After 10 min of exposure, 50 % of the Mo signal corresponds to Mo-O. In contrast, no Mo-O is observed in the Geological A sample at any time meaning that Mo-S bonds are preserved. The RSF-normalized S/Mo ratio of the Mo-S state stays constant at a value of approximately 2 for all exposure times for both samples. In the S 2*p* spectrum, we begin to see a new doublet after 5 min in the Synthetic A sample and after 2 min in the Geological A sample at a binding energy of ~164.8 eV. This state was also reported by Azcatl *et al*[21] in a geological MoS_2 sample without any evidence of Mo-S bond scission, and is therefore thought to correspond to S-O bonds from oxygen adsorbed to rehybridized sulfur atoms on the surface of the material. The appearance of this state in our geological sample, which also does not exhibit Mo-S bond scission, is consistent with this assignment. In the Synthetic A sample, we begin to observe the S^{6+} oxidation state at ~168 eV[37] after 5 min, indicating the presence of SO_x. The formation of sulfur oxide in the film is not surprising given the formation of MoO_x, which is indicative of Mo-S bond scission. Synthetic MoS_2 is known to have inferior crystalline quality (i. e., higher density of defects) compared to geological materials.[38] This explains its susceptibility to damage by UV-O_3 in

comparison to the geological sample. After UV-O_3, the samples were annealed in UHV at 550 °C resulting in some removal of oxide states. In both samples, the surface-bonded oxygen was thermally desorbed, and no change in S/Mo stoichiometry was observed. While the MoS_2 chemistry is comparable to its initial condition, the effects of UV-O_3 damage on the electronic properties of the material are not examined here.

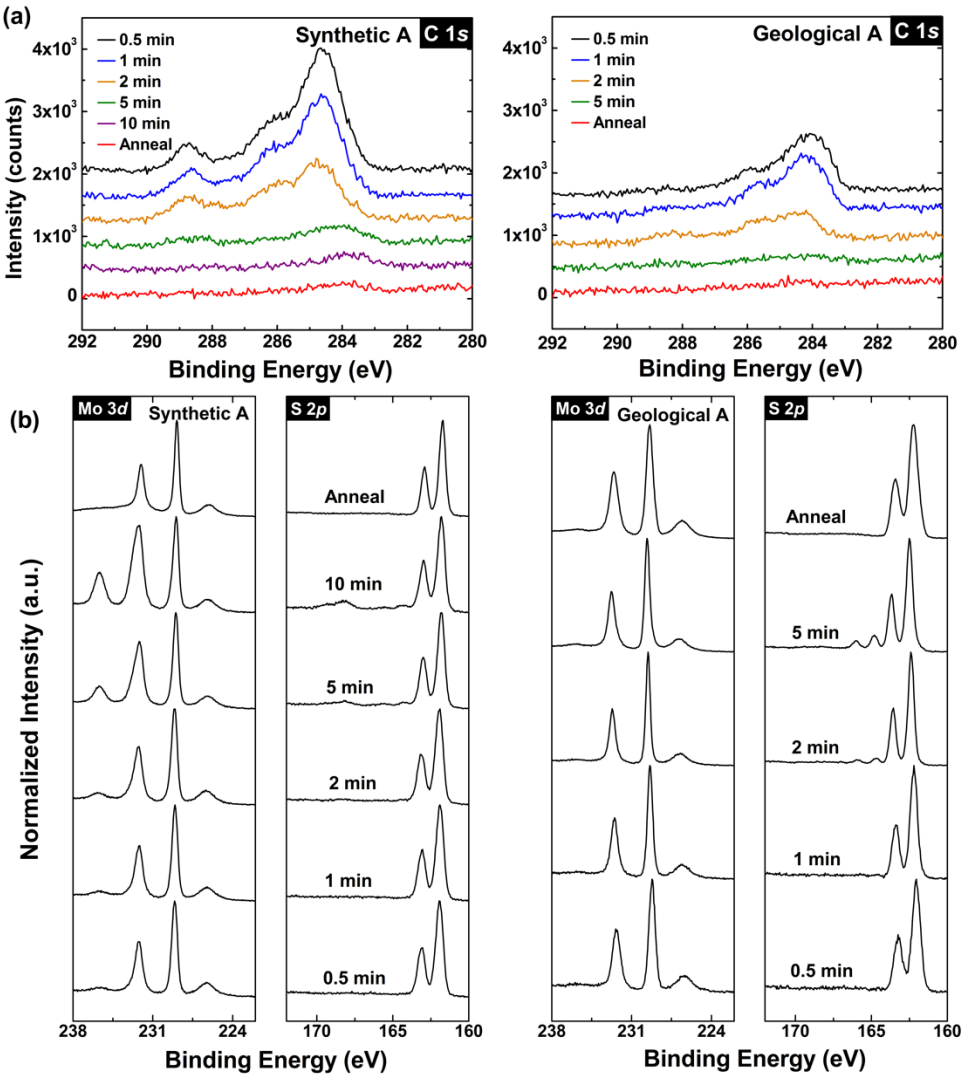

Figure 4.5.3. (a) C 1*s*, (b) Mo 3*d* and S 2*p* spectra acquired after varying lengths of of UV-O_3 exposure time.

We note that Mo oxide in Synthetic A was present not only during sequential UV-O_3 exposure, but also in the starting sulfurized material and after the final annealing step. The presence of a small quantity of oxide is not easily discerned from the Mo 3*d* spectra alone due to the overlap of the Mo-O $3d_{5/2}$ peak with the Mo-S $3d_{3/2}$ peak. We therefore use the O 1*s* spectra to detect changes in oxidation. The spectra are shown below in Figure 4.5.4 and are comprised of three components: the Mo-O peak at ~530.5 eV (corresponding to MoO_3), the Si-O peak from the substrate at ~532 eV, and a broad feature corresponding to physisorbed oxygen species at ~533 eV. In the starting material, the dominant feature is that of the substrate. With PMMA dissolution in acetone and initial UV-O_3 exposure we observe an increase in physisorbed oxygen species. After 5 min of UV-O_3 exposure, the Mo-O signal increases substantially relative to that of the substrate. The substrate is visible since the sulfurized MoS_2 film does not fully cover the substrate. This is consistent with changes observed in the Mo 3*d* spectra shown in Figure 4.5.3. While annealing results in a reduction in Mo-O, comparison of the initial and final spectra reveals that there remains a higher fraction of Mo oxide at the end of this process than was present in the starting material. The atom% values denoted in the figure represents the composition of oxygen bonded to Mo considering the total composition of S, Mo, and O (only from Mo-O bonds). Figure 4.5.3 indicates that a SO_x state exists in the S 2*p* spectra corresponding to 5 and 10 min UV-O_3 exposure. This was omitted from the analysis of the O 1s spectra, however the peak widths and positions of the other O 1*s* chemical states were fixed to be the same in each spectrum, meaning that the relative change in the magnitude of the Mo-O peak provides a semi-quantitative measure of the oxidation of the sample as a function of UV-O_3 exposure time. The minor decrease in at% O that is observed between the initial and acetone treated samples is attributed to attenuation due

to the polymer residue overlayer. With increasing UV-O_3 exposure time, as polymer residues are removed and Mo becomes oxidized, the at% O increases until the reduction of MoO_3 by annealing.

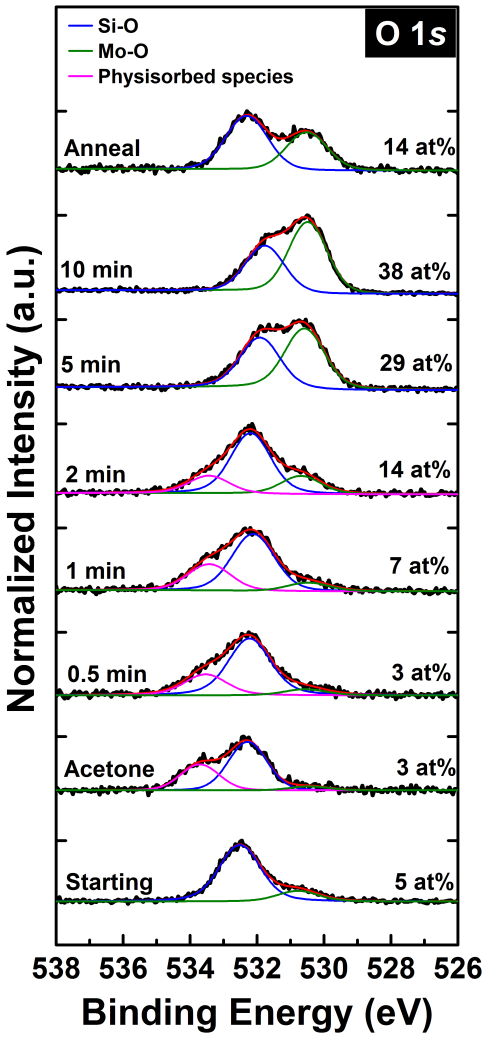

Figure 4.5.4. Normalized O 1*s* spectra acquired at various stages of the experiment, revealing changes in Mo oxide composition.

The material used in Experiments 1 and 2 is not a comprehensive sampling of the wide variety geological and synthetic MoS_2 that are available. We highlight this by expanding our study to include geological and synthetic MoS_2 (Geological B and Synthetic B) from separate sources

processed in parallel with Geological A and Synthetic A. The two Synthetic samples were produced by different processes, sulfurization and CVD. The CVD sample underwent a polystyrene-mediated transfer process following deposition from the growth substrate onto SiO_2. As a result of the different fabrication techniques, these two samples inherently exhibit different properties. Furthermore, Synthetic A is a vertically aligned sample while Synthetic B and the geological samples are planar.[39] The two geological samples are obtained from different vendors. The purpose of Experiment 3 is to examine the effect of the same PMMA removal process on the four different materials. AFM images of Synthetic B and Geological B are shown in Figure 4.5.5.

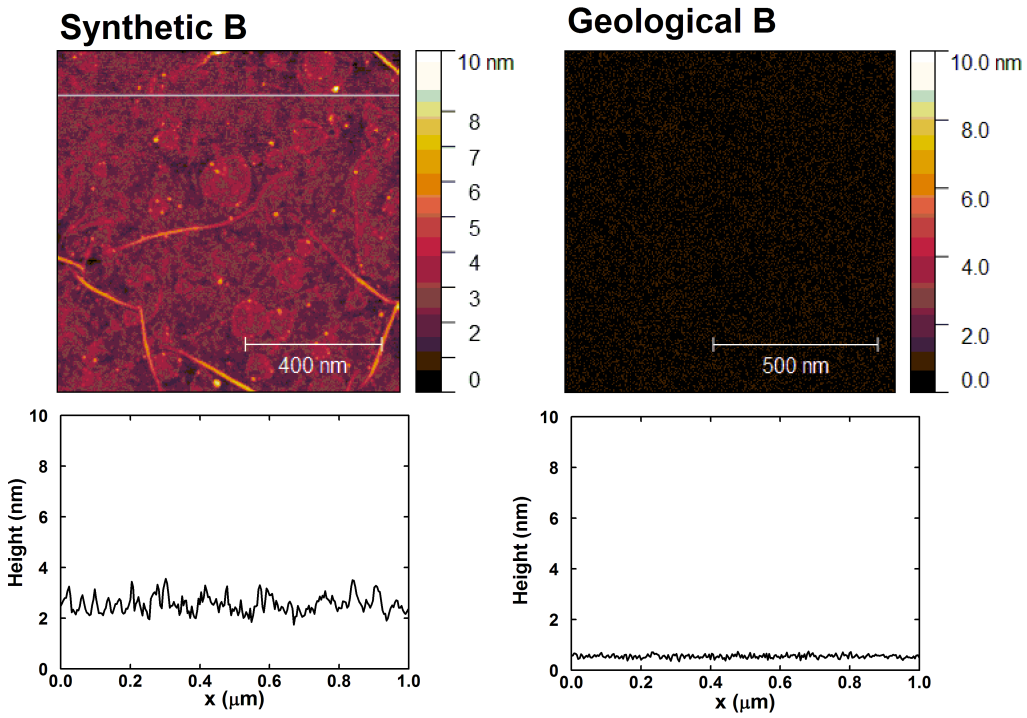

Figure 4.5.5. Atomic force microscopy images of Synthetic B and Geological B

All four samples were spin-coated with PMMA, soaked in acetone, exposed to UV-O_3 for 2 minutes, and annealed in UHV at 550 °C for 30 min. XPS data, as shown in Figure 4.5.6, was acquired following acetone dissolution, UV-O_3 exposure, and the final annealing step. In the C 1*s*

spectra, it is apparent that carbon removal was more effective in Synthetic B than Synthetic A, and more effective in Geological A than Geological B. Furthermore we note that Synthetic B shows no signs of Mo-O features that are the evidence of Mo-S bond scission in synthetic A. We note that Synthetic B exhibits a significantly lower RMS surface roughness value (~450 pm) than Synthetic A (1.7 nm). Similarly, Geological A exhibits a lower RMS surface roughness (73 pm) than Geological B (120 pm). For a given family of materials (synthetic vs. geological), surface roughness likely plays a role in the efficacy of PMMA removal treatments. While Geological B had a lower RMS surface roughness than Synthetic B, carbon removal was more effective for the synthetic sample. The reason for this is not clear, but it could potentially be due macroscopic defects in the geological sample, such as bunched step edges or other defects, resulting in high sticking coefficient regions that could be missed by AFM but fall within the analysis area of XPS.

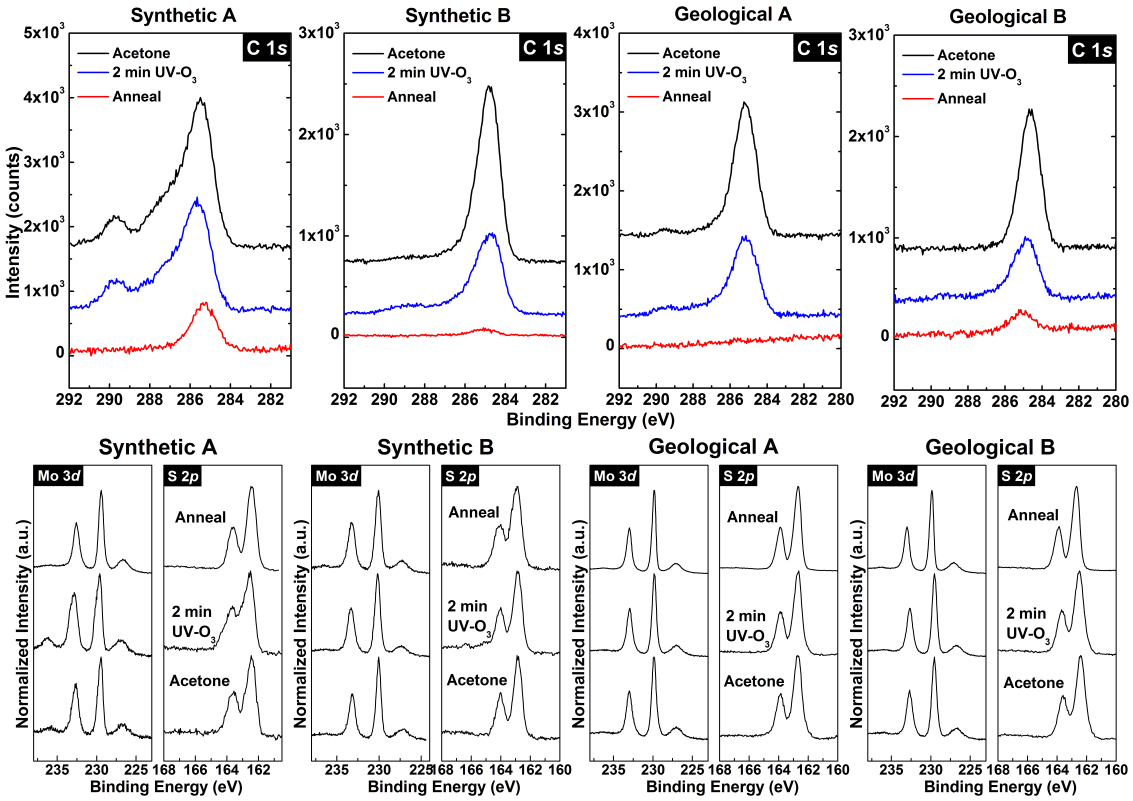

Figure 4.5.6. C 1*s*, Mo 3*d* and S 2*p* spectra acquired after acetone dissolution, after 2 min of UV-O_3 exposure, and after UHV annealing.

4.5.4 Conclusion and Future Work

The experiments presented here show that optimal process parameters for PMMA removal vary depending on the type of MoS_2 material due to differences in surface morphology and material quality. We note that this study examined geological material from two particular vendors and synthetic material fabricated using two specific methods, and our results may not be generalizable for all geological and synthetic samples. This work highlights that not all MoS_2 is created equal, and that optimum PMMA removal process conditions cannot be generalized but are instead dependent on the source of MoS_2. For device fabrication applications, this work demonstrates the importance of developing PMMA removal processes specific to the MoS_2 used. Suggestions for future work related to this topic are discussed below.

4.5.4.1 Study of Residue Removal Procedures as a Function of Morphology

Our results suggest that both the efficacy of PMMA residue removal and the oxidation resistance of the sample is related to its surface morphology. To better understand this correlation, MoS_2 synthesis procedures can be varied systematically to achieve samples with a range of different grain sizes[38, 40] produced by the two different synthetic methods. The study can also be expanded to include MBE-grown samples. After producing samples via different methods with a range of grain sizes and characterizing their morphology with AFM, PMMA removal processes can be implemented on the different samples followed by XPS characterization. Raman spectroscopy can also be used to compare the structrual quality of films grown under different conditions.[38] The carbon and Mo oxide XPS peak intensities can be plotted as a function of grain size and as a function of E^1_{2g}/A_{1g} ratio in Raman which is indicative of structrual quality. This analysis should be performed separately for sulfurized, CVD samples, and MBE samples due to their inherently different grain alignment due to different growth kinetics.

4.5.4.2 Effect on Contact Properties

The study reported in this chapter was focused on the surface chemistry of MoS_2 following polymer removal procedures. Future work can utilize XPS to examine interface chemistry following metal depositions on MoS_2 which underwent different PMMA residue removal procedures. The XPS study should be performed in parallel with thermal and/or electrical transport measurements. The incomplete removal of polymer residues and/or oxidation of MoS_2 from UV-O_3 exposure could potentially hinder the chemical and electronic interactions which occur at the interface with metals and a contribute to electron and phonon scattering. While the removal of polymer residues is desriable, oxidation of the material by UV-O_3 is likely harmful to transport. This is particularly important for synthetic samples which are susceptible to oxidation, making it important to develop processes which adequately remove residues without damaging the material.

4.5.5 References

1. Radisavljevic, B.; Radenovic, A.; Brivio, J.; Giacometti, V.; Kis, A., Single-layer MoS2 transistors. *Nat Nano* **2011,** *6* (3), 147-150.
2. Fang, H.; Chuang, S.; Chang, T. C.; Takei, K.; Takahashi, T.; Javey, A., High-Performance Single Layered WSe2 p-FETs with Chemically Doped Contacts. *Nano Letters* **2012,** *12* (7), 3788-3792.
3. Tsai, M.-L.; Su, S.-H.; Chang, J.-K.; Tsai, D.-S.; Chen, C.-H.; Wu, C.-I.; Li, L.-J.; Chen, L.-J.; He, J.-H., Monolayer MoS2 Heterojunction Solar Cells. *ACS Nano* **2014,** *8* (8), 8317-8322.
4. Huang, J.; Yang, L.; Liu, D.; Chen, J.; Fu, Q.; Xiong, Y.; Lin, F.; Xiang, B., Large-area synthesis of monolayer WSe2 on a SiO2/Si substrate and its device applications. *Nanoscale* **2015,** *7* (9), 4193-4198.
5. Abraham, M.; Mohney, S. E., Annealed Ag contacts to MoS2 field-effect transistors. *Journal of Applied Physics* **2017,** *122* (11), 115306.
6. Nguyen, D. A.; Oh, H. M.; Duong, N. T.; Bang, S.; Yoon, S. J.; Jeong, M. S., Highly Enhanced Photoresponsivity of a Monolayer WSe2 Photodetector with Nitrogen-Doped Graphene Quantum Dots. *ACS Applied Materials & Interfaces* **2018,** *10* (12), 10322-10329.
7. Li, X.; Zhu, Y.; Cai, W.; Borysiak, M.; Han, B.; Chen, D.; Piner, R. D.; Colombo, L.; Ruoff, R. S., Transfer of Large-Area Graphene Films for High-Performance Transparent Conductive Electrodes. *Nano Letters* **2009,** *9* (12), 4359-4363.
8. Bai, H.; Ma, J.; Wang, F.; Yuan, Y.; Li, W.; Mi, W.; Han, Y.; Li, Y.; Tang, D.; Zhao, W.; Li, B.; Zhang, K., A controllable synthesis of uniform MoS2 monolayers on annealed molybdenum foils. *Materials Letters* **2017,** *204*, 35-38.
9. Baugher, B. W. H.; Churchill, H. O. H.; Yang, Y.; Jarillo-Herrero, P., Intrinsic Electronic Transport Properties of High-Quality Monolayer and Bilayer MoS2. *Nano Letters* **2013,** *13* (9), 4212-4216.
10. Li, R.; Li, Z.; Pambou, E.; Gutfreund, P.; Waigh, T. A.; Webster, J. R. P.; Lu, J. R., Determination of PMMA Residues on a Chemical-Vapor-Deposited Monolayer of Graphene by Neutron Reflection and Atomic Force Microscopy. *Langmuir* **2018,** *34* (5), 1827-1833.
11. Lin, Y. C.; Lu, C. C.; Yeh, C. H.; Jin, C.; Suenaga, K.; Chiu, P. W., Graphene annealing: how clean can it be? *Nano Lett* **2012,** *12* (1), 414-9.
12. Macintyre, D. S.; Ignatova, O.; Thoms, S.; Thayne, I. G., Resist residues and transistor gate fabrication. *Journal of Vacuum Science & Technology B: Microelectronics and Nanometer Structures Processing, Measurement, and Phenomena* **2009,** *27* (6), 2597-2601.
13. Pirkle, A.; Chan, J.; Venugopal, A.; Hinojos, D.; Magnuson, C. W.; McDonnell, S.; Colombo, L.; Vogel, E. M.; Ruoff, R. S.; Wallace, R. M., The effect of chemical residues on the physical and electrical properties of chemical vapor deposited graphene transferred to SiO2. *Applied Physics Letters* **2011,** *99* (12), 122108.
14. Chan, J.; Venugopal, A.; Pirkle, A.; McDonnell, S.; Hinojos, D.; Magnuson, C. W.; Ruoff, R. S.; Colombo, L.; Wallace, R. M.; Vogel, E. M., Reducing Extrinsic Performance-Limiting Factors in Graphene Grown by Chemical Vapor Deposition. *ACS Nano* **2012,** *6* (4), 3224-3229.
15. Wei Chen, C.; Ren, F.; Chi, G.-C.; Hung, S.-C.; Huang, Y. P.; Kim, J.; Kravchenko, I. I.; Pearton, S. J., UV ozone treatment for improving contact resistance on graphene. *Journal of Vacuum Science & Technology B, Nanotechnology and Microelectronics: Materials, Processing, Measurement, and Phenomena* **2012,** *30* (6), 060604.

16. Lee, J. e. a., Clean transfer of graphene and its effect on contact resistance. *Applied Physics Letters* **2013,** *103* (10), 103104.
17. Li, W.; Liang, Y.; Yu, D.; Peng, L.; Pernstich, K. P.; Shen, T.; Hight Walker, A. R.; Cheng, G.; Hacker, C. A.; Richter, C. A.; Li, Q.; Gundlach, D. J.; Liang, X., Ultraviolet/ozone treatment to reduce metal-graphene contact resistance. *Applied Physics Letters* **2013,** *102* (18), 183110.
18. McDonnell, S.; Brennan, B.; Azcatl, A.; Lu, N.; Dong, H.; Buie, C.; Kim, J.; Hinkle, C. L.; Kim, M. J.; Wallace, R. M., HfO2 on MoS2 by atomic layer deposition: Adsorption mechanisms and thickness scalability. *ACS nano* **2013,** *7* (11), 10354-10361.
19. Kim, H.-U.; Kim, M.; Jin, Y.; Hyeon, Y.; Kim, K. S.; An, B.-S.; Yang, C.-W.; Kanade, V.; Moon, J.-Y.; Yeom, G. Y.; Whang, D.; Lee, J.-H.; Kim, T., Low-temperature wafer-scale growth of MoS2-graphene heterostructures. *Applied Surface Science* **2019,** *470*, 129-134.
20. Oh, H. M.; Han, G. H.; Kim, H.; Jeong, M. S., Influence of residual promoter to photoluminescence of CVD grown MoS2. *Current Applied Physics* **2016,** *16* (9), 1223-1228.
21. Azcatl, A.; McDonnell, S.; K. C, S.; Peng, X.; Dong, H.; Qin, X.; Addou, R.; Mordi, G. I.; Lu, N.; Kim, J.; Kim, M. J.; Cho, K.; Wallace, R. M., MoS2 functionalization for ultra-thin atomic layer deposited dielectrics. *Applied Physics Letters* **2014,** *104* (11), 111601.
22. Azcatl, A.; Santosh, K.; Peng, X.; Lu, N.; McDonnell, S.; Qin, X.; De Dios, F.; Addou, R.; Kim, J.; Kim, M. J., HfO2 on UV–O3 exposed transition metal dichalcogenides: interfacial reactions study. *2D Materials* **2015,** *2* (1), 014004.
23. Van Le, Q.; Nguyen, T. P.; Jang, H. W.; Kim, S. Y., The use of UV/ozone-treated MoS 2 nanosheets for extended air stability in organic photovoltaic cells. *Physical Chemistry Chemical Physics* **2014,** *16* (26), 13123-13128.
24. Yang, X.; Fu, W.; Liu, W.; Hong, J.; Cai, Y.; Jin, C.; Xu, M.; Wang, H.; Yang, D.; Chen, H., Engineering crystalline structures of two-dimensional MoS2 sheets for high-performance organic solar cells. *Journal of Materials Chemistry A* **2014,** *2* (21), 7727-7733.
25. Park, S.; Kim, S. Y.; Choi, Y.; Kim, M.; Shin, H.; Kim, J.; Choi, W., Interface Properties of Atomic-Layer-Deposited Al2O3 Thin Films on Ultraviolet/Ozone-Treated Multilayer MoS2 Crystals. *ACS Applied Materials & Interfaces* **2016,** *8* (18), 11189-11193.
26. Kurabayashi, S.; Nagashio, K., Tolerance to UV-O3 Exposure of CVD and Mechanically Exfoliated MoS2 & Fabrication of Top-Gated CVD MoS2 FETs. In *2015 International Conference on Solid State Devices and Materials*, 2015.
27. Tarasov, A.; Campbell, P. M.; Tsai, M. Y.; Hesabi, Z. R.; Feirer, J.; Graham, S.; Ready, W. J.; Vogel, E. M., Highly Uniform Trilayer Molybdenum Disulfide for Wafer-Scale Device Fabrication. *Advanced Functional Materials* **2014,** *24* (40), 6389-6400.
28. Liu, Y.; Ghosh, R.; Wu, D.; Ismach, A.; Ruoff, R.; Lai, K., Mesoscale Imperfections in MoS2 Atomic Layers Grown by a Vapor Transport Technique. *Nano Letters* **2014,** *14* (8), 4682-4686.
29. Gurarslan, A.; Yu, Y.; Su, L.; Yu, Y.; Suarez, F.; Yao, S.; Zhu, Y.; Ozturk, M.; Zhang, Y.; Cao, L., Surface-energy-assisted perfect transfer of centimeter-scale monolayer and few-layer MoS2 films onto arbitrary substrates. *ACS nano* **2014,** *8* (11), 11522-11528.
30. SPI, https://www.2spi.com/.
31. Ward's, https://www.wardsci.com/store/

.
32. Barr, T. L.; Seal, S., Nature of the use of adventitious carbon as a binding energy standard. *Journal of Vacuum Science & Technology A* **1995,** *13* (3), 1239-1246.

33. Quereda, J.; Castellanos-Gomez, A.; Agraït, N.; Rubio-Bollinger, G., Single-layer MoS2 roughness and sliding friction quenching by interaction with atomically flat substrates. *Applied Physics Letters* **2014,** *105* (5), 053111.
34. Beamson, G.; Bunn, A.; Briggs, D., High-resolution monochromated XPS of poly(methyl methacrylate) thin films on a conducting substrate. *Surface and Interface Analysis* **1991,** *17* (2), 105-115.
35. Briggs, D.; Beamson, G., Primary and secondary oxygen-induced C1s binding energy shifts in x-ray photoelectron spectroscopy of polymers. *Analytical Chemistry* **1992,** *64* (15), 1729-1736.
36. McDonnell, S.; Addou, R.; Buie, C.; Wallace, R. M.; Hinkle, C. L., Defect-dominated doping and contact resistance in MoS2. *ACS nano* **2014,** *8* (3), 2880-2888.
37. Brown, N. M. D.; Cui, N.; McKinley, A., An XPS study of the surface modification of natural MoS2 following treatment in an RF-oxygen plasma. *Applied Surface Science* **1998,** *134* (1), 11-21.
38. Laskar, M. R.; Ma, L.; Kannappan, S.; Sung Park, P.; Krishnamoorthy, S.; Nath, D. N.; Lu, W.; Wu, Y.; Rajan, S., Large area single crystal (0001) oriented MoS2. *Applied Physics Letters* **2013,** *102* (25), 252108.
39. Jung, Y.; Shen, J.; Liu, Y.; Woods, J. M.; Sun, Y.; Cha, J. J., Metal Seed Layer Thickness-Induced Transition From Vertical to Horizontal Growth of MoS2 and WS2. *Nano Letters* **2014,** *14* (12), 6842-6849.
40. Zhang, J.; Yu, H.; Chen, W.; Tian, X.; Liu, D.; Cheng, M.; Xie, G.; Yang, W.; Yang, R.; Bai, X.; Shi, D.; Zhang, G., Scalable Growth of High-Quality Polycrystalline MoS2 Monolayers on SiO2 with Tunable Grain Sizes. *ACS Nano* **2014,** *8* (6), 6024-6030.

5 IMPLICATIONS OF METAL/2D INTERFACE STUDIES

The work presented in this dissertation provides insight into interface chemistry and a number of different device-relevant aspects of processing and properties which have been largely overlooked in the literature to date. The broader implications of each chapter are summarized here. In Chapter 3.2 we see a pronounced difference in surface chemistry between a CVD graphene sample in its as-received state and one which has been subject to surface cleaning via UHV annealing. This results in a drastic difference in the composition of the contact, highlighting the impact of pre-deposition surface cleaning on the chemical composition of the contact interface. The result also shows that carbon contamination is present in UHV and leads to an increase in TiC composition over time even on a clean graphene surface. This is important to note for any future UHV experiments involving Ti and other metals which form carbides. Most importantly, the publication which resulted from Chapter 3.2 is the first in the literature to provide conclusive evidence that Ti does not react with graphene. This implies that previously proposed models of spontaneous formation of end-contacts are not accurate, and that deliberate processing must be implemented to achieve end-contacts.

Through systematic variations of depositions conditions of Ti contacts to graphene in HV, the work in Chapter 3.3 draws attention to the importance of reporting contact deposition conditions in all device and contact studies. The results clearly show that base pressure and deposition rate are directly linked with electrical and thermal transport properties in graphene devices. A difference of one order of magnitude in deposition base pressure can translate to a factor of 2 difference in electrical contact resistance. Similarly, a factor of 2 difference in thermal boundary conductance can result from a difference in one order of magnitude in deposition rate. It

was previously stated in the introduction that a wide range of contact resistance values is reported for Ti/graphene contacts, 23-7500 Ω μm, and a similarly wide range is reported for other contact metals. Our work directly demonstrates that differences in processing conditions can explain discrepancies in contact resistance values reported in the literature. Additionally, the results suggest that electrical and thermal transport properties are improved when metal deposition is performed at lower base pressures and faster deposition rates which limit the incorporation of oxygen in the contact.

In Chapter 4.2, we examine the reactivity of metal/MoS_2 interfaces in the as-deposited condition and following heating to temperatures from 100º to 600 ºC. Annealing devices following metal contact deposition is very commonly implemented to improve device properties however no studies to date have examined the effects on interface chemistry of Ti, Au, and Ni. In the case of Ti which exhibits a high degree of reactivity, drastic changes in the chemistry and structure of the interface are observed upon annealing. Metals which have are typically considered to be non-reactive, Au and Ni, are found to interact with the substrate in their as-deposited condition. At the interface with Ni, annealing appears to decouple the electronic interactions whereas this is not the case for Au. Unlike Ti, Au has been previously reported to exhibit improved contact resistance upon annealing. The results of this work strongly suggest that the reactivity metals should be taken into account when applying annealing processes. Furthermore, we find that chemical changes can occur under device operating conditions. This indicates that highly reactive metals are likely not optimal for long term device stability.

A very large volume of work has focused on engineering contacts to improve electrical transport to TMDs, but thermal transport at metal/TMD interfaces has been relatively neglected despite the widespread knowledge that heat dissipation presents a major obstacle. In Chapter 4.3

we characterized thermal transport in structures with a TiO_x interlayer at the Ti/MoS_2 contact. This contact engineering method has been previously shown by others to improve electrical contact resistance. While previous work has suggested that an oxide layer at the interface would be detrimental to thermal transport, the heterostructured Ti/TiO_x contacts to MoS_2 were found to exhibit favorable thermal transport comparable to that of metal/MoS_2 interfaces (provided the Ti layer is sufficiently thick). An analysis of the different interfaces contributing to the total resistance revealed that it is the Au/TiO_x interface that dominates thermal resistance. In addition to demonstrating that Au/Ti/TiO_x contacts can be used without compromising heat dissipation, the work suggests that metal/oxide interfaces should be avoided. This is important given the demonstrated efficacy of high work function oxide contacts in achieving p-type conduction in MoS_2.

In Chapter 4.4, Ti, TiO_x, and Ti/TiO_x contacts to MBE-grown WSe_2 are characterized. No previous reports on Ti/WSe_2 interface chemistry exist. Beyond transistor and photodetector applications, WSe_2 has attracted interest for applications in thermoelectric energy conversion yet the overwhelming majority of work in this field is theoretical. Our repeatable MBE growth of WSe_2 and the ability to perform *in-situ* metal deposition and characterization, combined with e*x-situ* electrical and thermal measurements, opens doors for future experimental investigation of thermoelectric properties in 2D thermionic devices based on WSe_2. A sample with ultra-low thermal boundary conductance was fabricated. We have also demonstrated control over interface chemistry with the deposition of TiO_x.

The final chapter focuses on polymer aided processes, which are extremely common in device fabrication for both photolithography and transfer of the TMD film between different substrates. Residues have detrimental effects on device properties, and the vast majority of device

studies apply the same processes for polymer residue removal with no characterization to determine process efficacy and no consideration of the type of material. In Chapter 4.5, polymer residue removal processes are applied to different types of geological and synthetic material. MoS_2 flakes exfoliated from geological material exhibit very different morphology than synthetic material. Furthermore, different synthetic routes to MoS_2 also yield material with different properties. The key finding of this study is that the efficacy of a given polymer residue removal process is dependent on the type of material and its surface morphology. In other words, residue removal processes cannot be generalized.

The goal of most research in the field of 2D electronics is to improve the properties of 2D devices and drive the development of new technology. The performance of devices will ultimately be dictated by the properties of the material from which they are made and the resulting effects of the processes which they undergo. This concept is central to the field of materials science. In the case of 2D electronics, the intrinsic material properties become less relevant as the interface dominates the total device area. As Nobel Prize winner Herbert Kroemer once said, "the interface is the device." This work sheds light on the range of complex chemical, electronic, and thermal phenomena that occur at metal/2D interfaces, highlighting the important role of interface chemistry in the design of 2D devices and development of fabrication processes.

Appendix A. Fit Procedure and Error in XPS Spectra of Ti/MoS_2

Fit Parameters

The Mo 3*d* spectra were fit with the parameters shown in the table below. The metallic Mo fit parameters were fixed based on a Mo metal reference shown in Figure A1 that was fit with a Doniach Sunjic line shape convoluted with Gaussian. All other chemical states were fit with a symmetric Voigt function line shape. The Mo-S and S-Mo fit parameters were based on the pristine material prior to deposition. The S 2*s* chemical states were constrained to match the relative intensity ratios and relative positions of the states in the S 2*p* core level. Values which were not constrained (excluding amplitudes) are indicated by the symbol *. Example fits and their residuals are shown in Figure A2.

Core level	Chemical state	BE (eV)	Lorentzian width (eV)	Gaussian width (eV)	Asymmetry	Amplitude (counts)
Mo 3*d*	Mo^0 $3d_{5/2}$	227.43–227.47*	0.15	0.61–0.67*	0.14	Sample dependent
	Mo^0 $3d_{3/2}$	BE($3d_{5/2}$) + 3.13	0.15	0.92–0.96*	0.21	amp($3d_{3/2}$)*0.68
	Mo-S $3d_{5/2}$	229.34–229.35*	0.15	0.40	n/a	Sample dependent
	Mo-S $3d_{5/2}$	BE($3d_{5/2}$) + 3.13	0.15	0.60	n/a	amp($3d_{5/2}$)*0.68
S 2*s*	S-Mo 2*s*	226.68–226.73	0.6	2	n/a	Sample dependent
	S-Ti (1) 2*s*	BE(S-Mo $2p_{3/2}$) + 0.14	0.6	2	n/a	Fixed based on S 2*p*
	S-Ti (2) 2*s*	BE(S-Mo $2p_{3/2}$) + 1.0	0.6	2	n/a	Fixed based on S 2*p*
	S-Ti (3) 2*s*	BE(S-Mo $2p_{3/2}$) - 0.63	0.6	2	n/a	Fixed based on S 2*p*
S 2*p*	S-Mo $2p_{3/2}$	162.157–162.173*	0.15	0.44	n/a	Sample dependent

	S-Mo $2p_{1/2}$	BE($2p_{3/2}$) + 1.2	0.15	0.44	n/a	amp($2p_{3/2}$)*0.5
	S-Ti (1) $2p_{3/2}$	BE(S-Mo $2p_{3/2}$) + 0.14	0.15	0.77	n/a	Sample dependent
	S-Ti (1) $2p_{1/2}$	BE($2p_{3/2}$) + 1.2	0.15	0.77	n/a	amp($2p_{3/2}$)*0.5
	S-Ti (2) $2p_{3/2}$	BE(S-Mo $2p_{3/2}$) + 1.0	0.15	0.50	n/a	Sample dependent
	S-Ti (2) $2p_{1/2}$	BE($2p_{3/2}$) + 1.2	0.15	0.50	n/a	amp($2p_{3/2}$)*0.5
	S-Ti (3) $2p_{3/2}$	BE(S-Mo $2p_{3/2}$) - 0.63	0.15	0.60	n/a	Sample dependent
	S-Ti (3) $2p_{1/2}$	BE($2p_{3/2}$) + 1.2	0.15	0.60	n/a	amp($2p_{3/2}$)*0.5

* corresponds to values which were not constrained to a specific number. The range of numbers provided represents the range exhibited by the data set of the angular resolved XPS spectra when all other parameters were constrained as specified in the table. The range is within or close to our uncertainty of 0.05 eV.

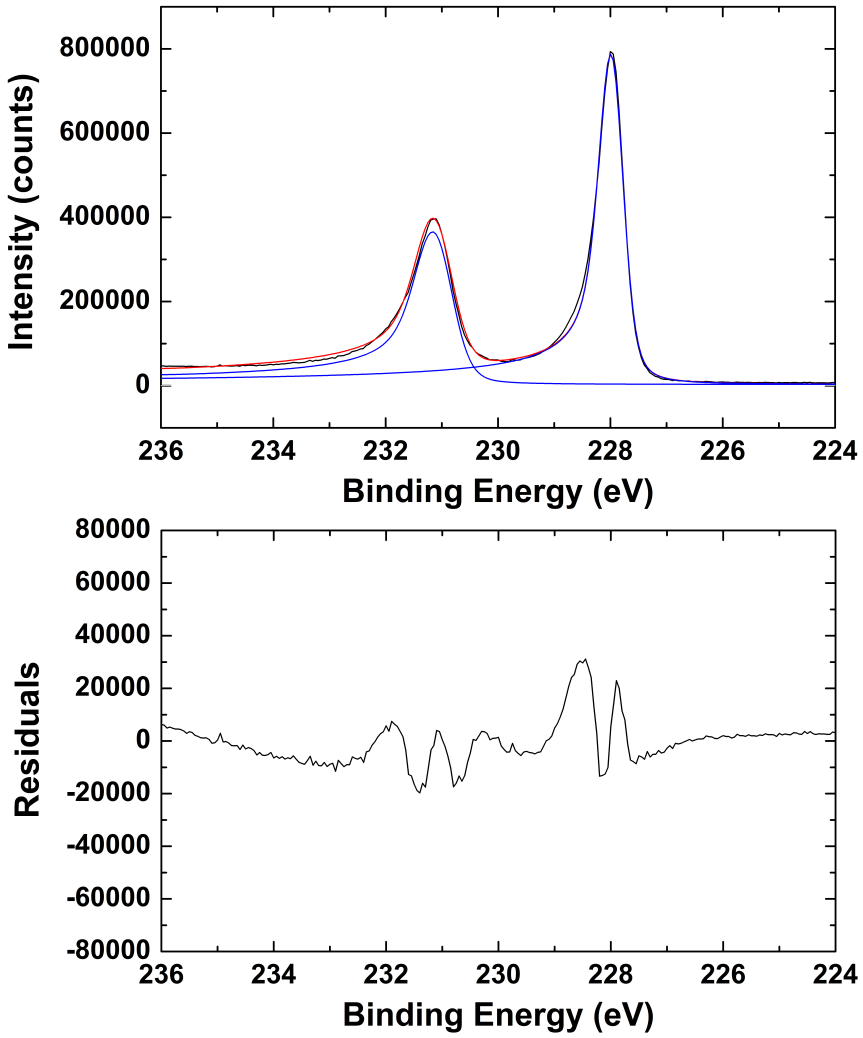

Figure A1. Fit to Mo metal references sample with residuals shown below.

Sources of Error in Fits

A number of factors contribute to error in the fits of these samples. One source error is the Mo metal reference spectrum that is used to fit the Mo^0 chemical states in the Mo 3*d* core level spectra. It is clear from Figure A1 that the fit to the reference sample deviates from the data, however this is the best achievable fit with kolXPD. Furthermore, we make the assumption that the Mo^0 chemical state which forms has the same line shape as the bulk reference sample which

was measured. While the asymmetry and Lorentzian width were fixed in the experimental spectra to match those of the reference sample, the difference in crystalline properties between the reference sample and the experimental material is accounted for by allowing the Gaussian widths to vary in the experimental spectra. The reference sample has Gaussian widths of 0.40 and 0.65 eV for the $3d_{5/2}$ and $3d_{1/2}$ components, respectively, while the experimental samples exhibit Gaussian widths of ~0.6 eV and ~0.9 eV respectively.

A second potential source of error is that the Gaussian widths of the Mo-S and S-Mo states in Mo 3*d* and S 2*p* were assumed to be the same values before and after the deposition of Ti. Due to the chemical reaction that occurs at the interface, it is likely that the crystalline disorder introduced results in broadening of the Gaussian components of the peaks. However, from the TEM images in Section 4.4.3.2 we note that the disordered region is a mixture of the Mo and S-Ti chemical states where the underlying MoS_2 substrate retains its crystallographic ordering and only the topmost layer appears perturbed. It is therefore reasonable to assume that the bulk of the Mo-S and S-Mo signals should retrain the spectral features of pristine material. The Gaussian widths of the S-Ti states were not constrained in early iterations of these fits, however they were fixed in later iterations for consistency between spectra, as shown in the table.

A third source of error originates from the assumption that the relative intensities (or intensity ratios) of the different S 2*p* chemical states are equal in the S 2*s* chemical states. These two core levels occur at different kinetic energies, and the various chemical states are distributed at different spatial depths in the material (i.e. S-Mo is from the substrate whereas S-Ti is near the surface). This means that the chemical states will exhibit different degrees of attenuation in the overlayer. The S 2*p* core level occurs at a kinetic energy of ~1324 eV while the S 2*s* core level has a kinetic energy of ~1260 eV. For the purpose of this discussion, if we assume a pure Ti overlayer

on MoS_2 (with no reaction products), this corresponds to an attenuation length of 27.18 Å for S 2*p* and 25.78 Å for S 2*s*. Using the exponential expression for attenuation we find that the S 2*p* to S 2*s* intensity ratio of a signal attenuated in a Ti overlayer with an arbitrarily chosen thickness value of 30 Å is 0.92. The difference in attenuation is not accounted for in our fits as we set this ratio to have a value of 1. Given the overlap of the S 2*s* peaks with the Mo^0 peak, error in the S 2*s* amplitudes propagates to error in the Mo^0 area. A 10% increase in the total S 2*s* area is found to result in a 5% decrease in the Mo^0 area while the Mo-S area is changed by < 1%. This then results in a 5% difference in the Mo^0/MoS_2 that is used in the semiquantitative attenuation model. Additionally, we note that errors in the effective attenuation length can also contribute systematically to errors in the model.

Lastly, error in the area calculated from fits in general is believed to be approximately 5-10%. This is demonstrated in Figure A2 where we show the fit and residuals of the experimental spectrum before and after the area of the Mo^0 peaks in the Mo 3*d* spectrum was fixed to be 5% and 10% greater than its initial value. We can see that the fit still appears reasonable based on visual inspection as well as the plot of the residuals. In Figure A3 we see a comparison of the residuals indicating that the 5-10% change in the area manifests in negligible deviation from the original fit. While a number of assumptions and extrinsic factors contribute to error in the analysis, the fits are used here for semiquantitative analysis and a small error in the calculated peak areas does not affect the conclusions of the work.

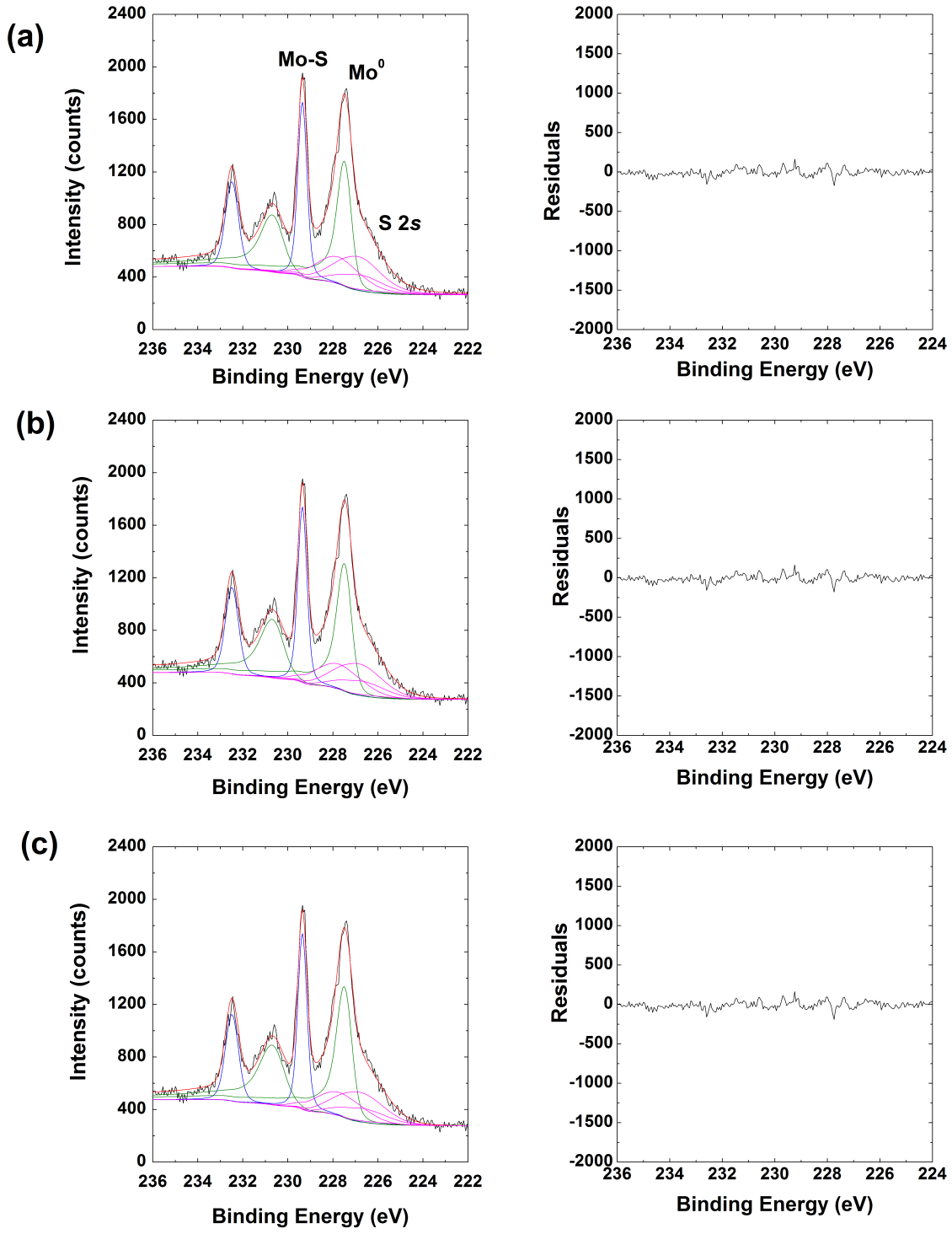

Figure A2. Example fit and residuals of Mo 3*d* from as-deposited Ti/MoS2 acquired at 40 from the surface to detector. Best fit in (a) and after 5% area is added to Mo metal in (b) and 10% added in (c). All fits appear equally good.

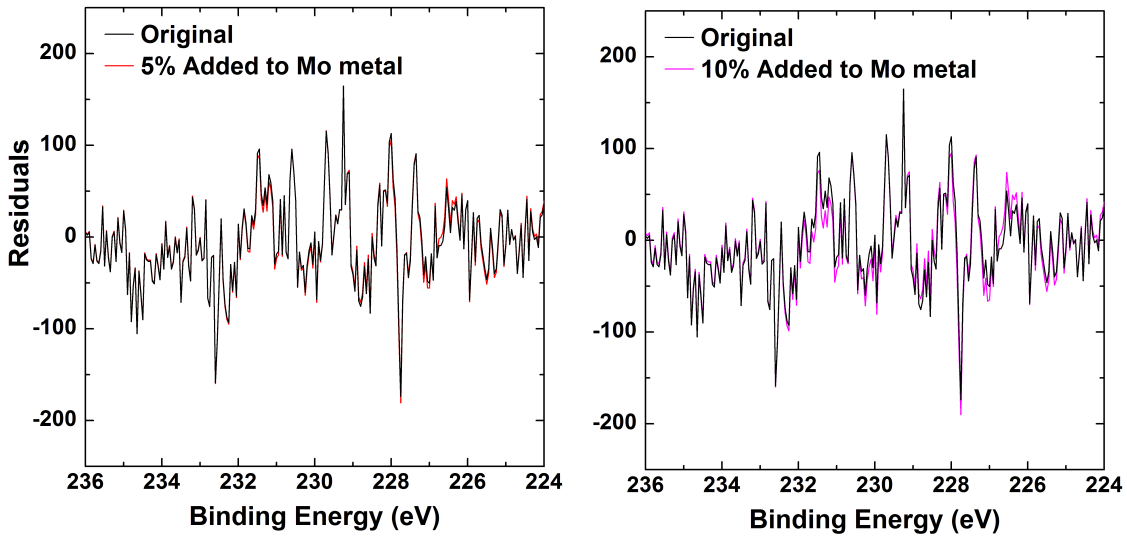

Figure A2. Comparison of the residuals shown in the previous figure. A larger deviation from the original residuals is observed when the Mo area is increased by 10%.

Appendix B. Nickel on MBE-grown WSe_2

XPS spectra acquired on MBE-grown WSe_2 on HOPG before and after the deposition of 9.5 Å of Ni in UHV are presented here. We observe a result similar to that which occurs following the deposition of Ni on MoS_2 (described in Chapter 4.2), namely the appearance of a new chemical state that is ~0.67 eV to lower binding energy relative to the main peak of the transition metal in the TMD. Additionally, the sample exhibits a p-type shift of 0.19 eV.

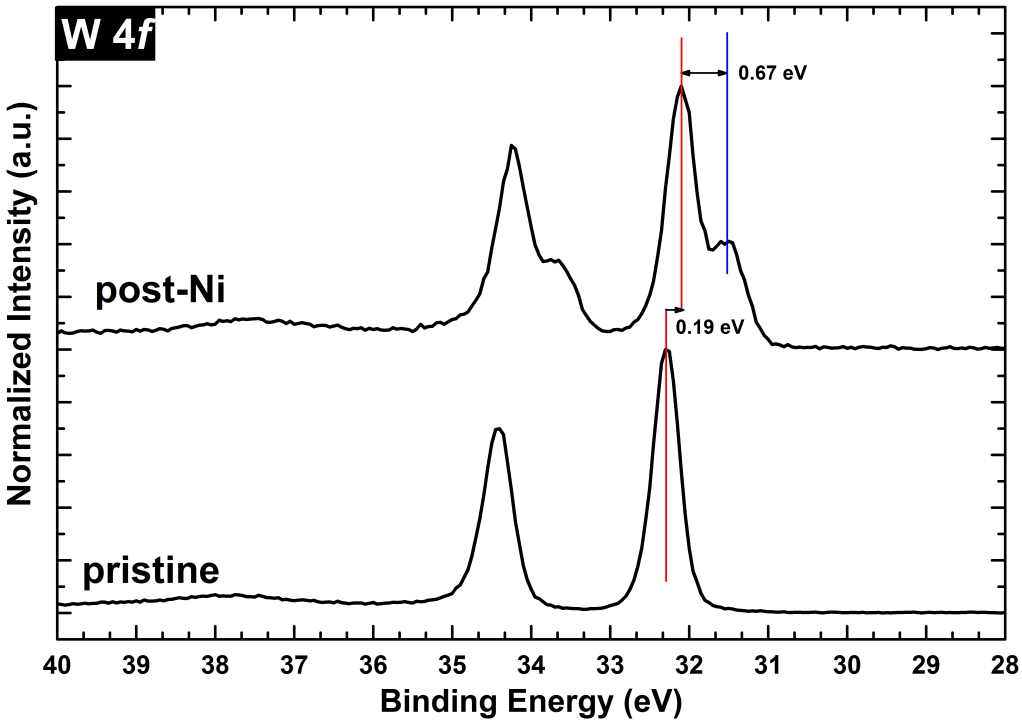

Figure B1. Mo 3*d* spectra acquired before and after Ni deposition on WSe_2/HOPG

The S 2*p* spectra are shown in Figure B2. A core level shift equal to that observed in the Mo 3*d* spectra occurs due to band bending from charge transfer at the interface. A p-type shift is expected given the high work function of Ni (5.0 eV)[1] relative to the work function of WSe_2.[2-3] The inset shows the pristine and post-Ni spectra are energy-aligned and superimposed to better illustrate the change in line shape that occurs following Ni deposition. The broadening observed

in the spectrum is due to the appearance of new chemical states, possibly corresponding to Ni-S interactions at the surface as was reported for Ni/MoS_2 in Chapter 4.2.

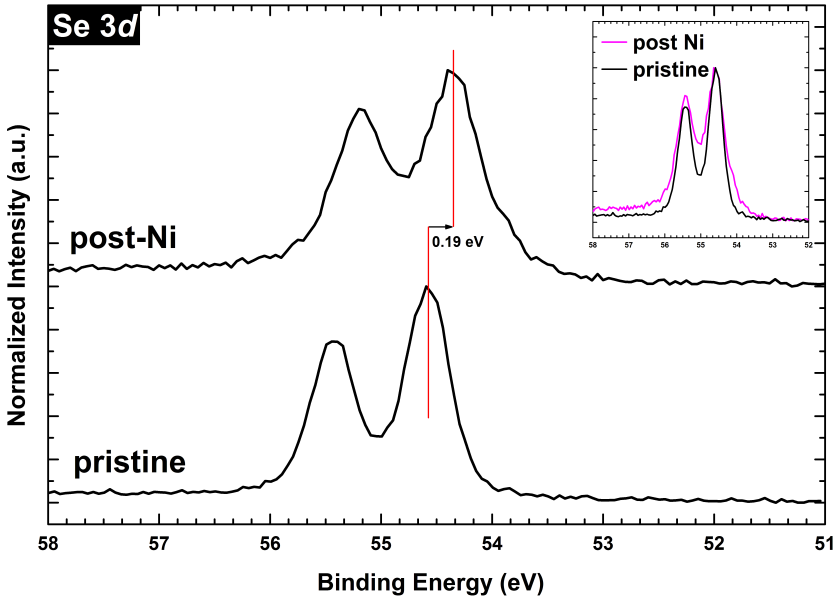

Figure B2. S 2*p* spectra acquired before and after Ni deposition on WSe_2/HOPG

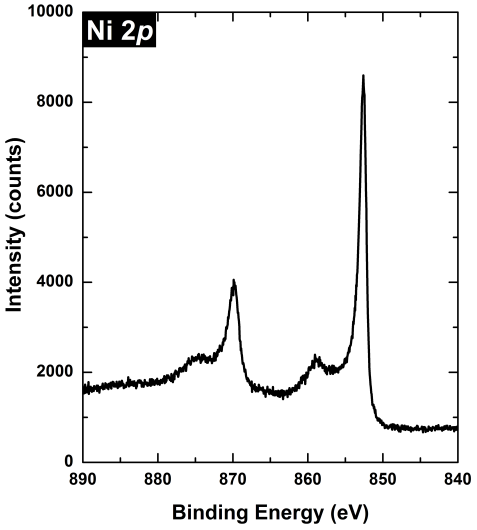

Figure B3. Ni 2*p* spectrum acquired following the deposition of 1 nm Ni on WSe_2/HOPG

References

1. Das, S.; Chen, H.-Y.; Penumatcha, A. V.; Appenzeller, J., High Performance Multilayer MoS2 Transistors with Scandium Contacts. *Nano Letters* **2013,** *13* (1), 100-105.
2. Britnell, L.; Ribeiro, R. M.; Eckmann, A.; Jalil, R.; Belle, B. D.; Mishchenko, A.; Kim, Y. J.; Gorbachev, R. V.; Georgiou, T.; Morozov, S. V.; Grigorenko, A. N.; Geim, A. K.; Casiraghi, C.; Neto, A. H. C.; Novoselov, K. S., Strong Light-Matter Interactions in Heterostructures of Atomically Thin Films. *Science* **2013,** *340* (6138), 1311.
3. McDonnell, S.; Azcatl, A.; Addou, R.; Gong, C.; Battaglia, C.; Chuang, S.; Cho, K.; Javey, A.; Wallace, R. M., Hole Contacts on Transition Metal Dichalcogenides: Interface Chemistry and Band Alignments. *ACS Nano* **2014,** *8* (6), 6265-6272.

Appendix C. XPS of Ti/MoS_2, TiO_x/MoS_2, and Ti/TiO_x/MoS_2 Samples in Chapter 4.3.

Spectra of all samples measured in this work are shown here in Figures B1-3. With thicker overlayers, the Mo 3*d* and S 2*p* signals are increasingly diminished in intensity due to attenuation. In Figure C1, it is apparent that the ratio of the Mo^0 to MoS_2 peak intensities increases with Ti thickness. This difference in the relative quantities of the chemical states, a result of differences in Ti thickness, has no measurable effect on h_K. In Figure B2, which shows spectra corresponding to the Ti/TiO_x interfaces, all samples exhibit identical interface chemistry since no chemical reaction takes place. The same is true for the Ti/TiO_x/MoS_2 samples in Figure C3.

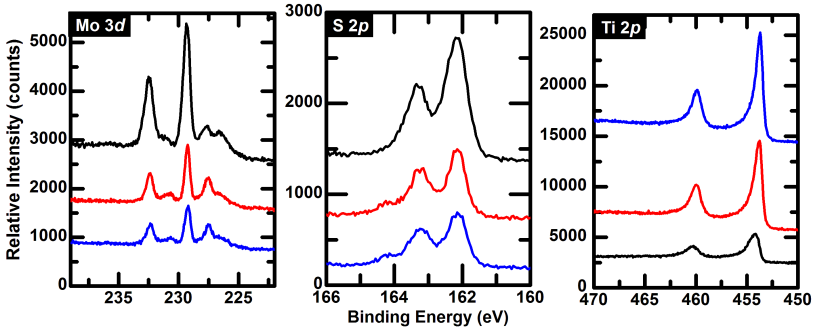

Figure C1. XPS spectra of the Mo 3*d*, S 2*p*, and Ti 2*p* core-levels for all Ti/MoS_2 samples with Ti thicknesses of 2.9 nm (black), 4.1 nm (red), and 5.2 nm (blue).

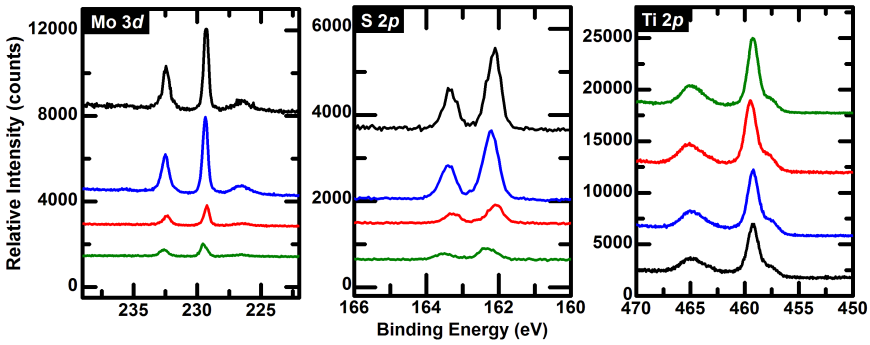

Figure C2. XPS spectra of Mo 3*d*, S 2*p*, and Ti 2*p* core levels for TiO_x/MoS_2 with TiOx thickness of 1.7 nm (black), 2.7 nm (blue), 4.2 nm (red), and 4.6 nm (green)

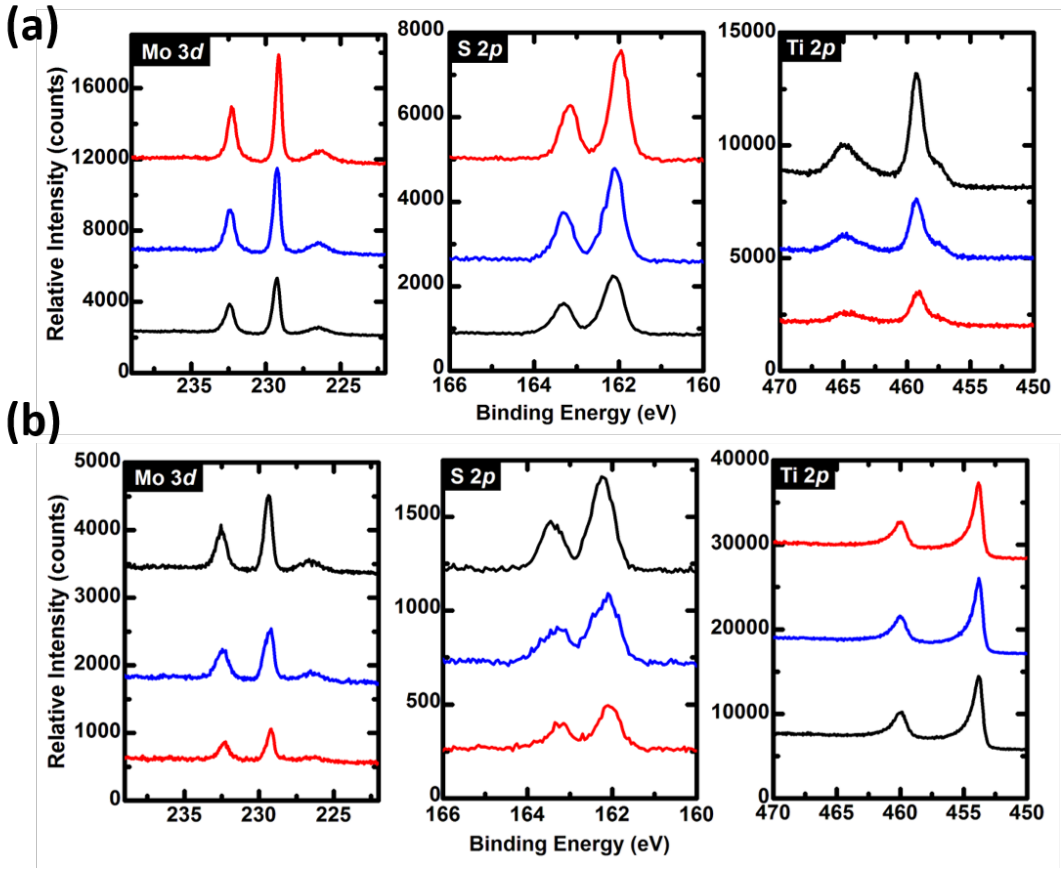

Figure C3. XPS spectra of Mo 3*d*, S 2*p*, and Ti 2*p* core levels for Ti/TiO_x/MoS2 samples after the deposition of TiO_x in (a) and then Ti in (b). The red curve corresponds to 1.2 nm TiO_x + 4.2 nm Ti, the blue curve corresponds to 1.5 nm TiO_x + 2.7 nm Ti, and the black curve corresponds to 2.0 nm +1.7 nm Ti

Appendix D. Suggested Future Work for Metal/2D Interface Chemistry

Previous discussions of future work have addressed the possibility of expanding metal/2D interface studies by simultaneously varying different processing conditions including pre-deposition processes such as polymer residue removal, deposition pressures (UHV vs. HV), and post-deposition annealing temperatures and ambients. Additionally, interface engineering can be implemented to control thermal and electrical transport across interfaces to meet device specific requirements. These suggested experiments broaden the scope of the study and further bridge the gap between interface chemistry, device fabrication processes, and transport properties. However, these studies do not directly address the fundamental materials science questions that have been brought about by the results presented in the dissertation.

One of these questions is regarding the length scale and nature of interaction at the Au/MoS_2 interface. This question is of particular importance because the overwhelming majority of reports in the literature, including those which utilize XPS[1-2], state that the Au/MoS_2 interface is nonreactive. Furthermore, computational studies model the interface as one that exhibits a van der Waals gap.[3-4] The results reported in Section 4.2.3.5 indicate that the interface exhibits some degree of reactivity that is reflected in the Au 4*f*, S 2*p*, and Mo 3*d* spectra, and that the interaction is stable after annealing to 600 ºC. The discrepancy between our results and those previously reported in the literature provides significant motivation for further investigation of this topic. As discussed previously, the discrepancy between our results and previous XPS studies could be potentially explained by the differences in the XPS spot size. The spot size in our system is ~4×1 mm. Within this macroscopically large area on the sample, geological MoS_2 exhibits bunched step

edges where the S atoms at the edge are uncoordinated, providing a site for the formation of Au-S bonds. Here we discuss routes to determine if an interaction is detectable in the basal plane.

In the PHI VersaProbe XPS system that is available at UVA's Nanomaterials Characterization Facility, the spot size can be set to minimum size of 9 μm. Within this length scale, the probability of measuring bunched step edges is far lower. The majority of the area probed is likely to be atomically flat MoS_2. Furthermore, in the VersaProbe, it is possible to perform a mapping measurement where XPS spectra are acquired serially within a defined rectangular array that corresponds to a specific location on the sample. From these spectra, an image can be generated in which each pixel represents the intensity of a specific peak. Prior to the XPS experiment, the sample should be characterized with the Hirox optical microscope and atomic force microscopy to determine an approximate density of surface features such as step edges. The XPS peaks of interest for analysis would be those that are indicative of the Au/MoS_2 interaction. These include the Au-S chemical state in Au 4*f*, the S-Au chemical state in S 2*p*, or the Mo defect state in Mo 3*d*. The creation of intensity maps from the raw data would require the core level spectra to be deconvolved in kolXPD (or Casa XPS for more efficient batch-processing) to determine the intensity of the states of interest. Using a data visualization tool such as MATLAB, it is possible to generate plots of the intensity of each chemical state as a function of spatial position. By comparing these plots to optical and AFM images, it is possible to determine if the Au/MoS_2 interaction occurs only at defects.

Failure to observe evidence of Au/MoS_2 interaction in atomically flat regions is not indicative of the absence of an interaction. It simply means that the chemical states that result from the Au/MoS_2 interaction are below the limit of detection with XPS. The demonstrated ability to exfoliate MoS_2 using a Au film[5] provides strong evidence for interaction in the basal plane.

Another route to studying this phenomenon is cross section scanning transmission electron microscopy (STEM) with electron energy loss spectroscopy (EELS). In EELS, the high energy electron beam from the STEM measurement ($\geq$ 100 keV) causes ionization of the different core levels.[6] The amount of energy lost by the beam as a result of ionization of atoms in the sample is related to the ionization energy of the particular core level giving rise to a peak known as the ionization edge. Like XPS, the signal from EELS – specifically the energy loss near edge structure (ELNES)[6] – is also sensitive to changes in the electronic environment of the emitted electron that occur due to orbital hybridization and electronic interactions. ELNES refers to the small intensity fluctuations that occur above the edge onset. These occur as a result of the excitation of the atom from the ground state configuration to an excited state in which the ejected electron occupies a previously unoccupied energy level. The ELNES is therefore related to the density of states. Unlike XPS, EELS can be performed at much smaller spot sizes as low as 0.2 nm making ELNES extremely useful for examining bonding over small length scales. EELS scans across the Au/MoS_2 interface can be acquired to determine how the ELNES changes between the interface and the bulk. In order to resolve the bulk components of the structure from the interface components, a difference spectrum can be taken.[7] Additionally, experimental ELNES spectra can be compared with those simulated using methods based on density functional theory.[8]

References

1. McDonnell, S.; Addou, R.; Buie, C.; Wallace, R. M.; Hinkle, C. L., Defect-dominated doping and contact resistance in MoS2. *ACS nano* **2014,** *8* (3), 2880-2888.
2. Smyth, C. M.; Addou, R.; McDonnell, S.; Hinkle, C. L.; Wallace, R. M., Contact Metal–MoS2 Interfacial Reactions and Potential Implications on MoS2-Based Device Performance. *The Journal of Physical Chemistry C* **2016,** *120* (27), 14719-14729.
3. Kang, J.; Liu, W.; Sarkar, D.; Jena, D.; Banerjee, K., Computational Study of Metal Contacts to Monolayer Transition-Metal Dichalcogenide Semiconductors. *Physical Review X* **2014,** *4* (3), 031005.
4. Popov, I.; Seifert, G.; Tománek, D., Designing Electrical Contacts to MoS2 Monolayers: A Computational Study. *Physical Review Letters* **2012,** *108* (15), 156802.
5. Desai, S. B.; Madhvapathy, S. R.; Amani, M.; Kiriya, D.; Hettick, M.; Tosun, M.; Zhou, Y.; Dubey, M.; Ager, J. W.; Chrzan, D.; Javey, A., Gold-Mediated Exfoliation of Ultralarge Optoelectronically-Perfect Monolayers. *Advanced Materials* **2016,** *28*, 4053-4058.
6. Keast, V. J.; Scott, A. J.; Brydson, R.; Williams, D. B.; Bruley, J., Electron energy-loss near-edge structure – a tool for the investigation of electronic structure on the nanometre scale. *Journal of Microscopy* **2001,** *203* (2), 135-175.
7. Fu, Q.; Wagner, T., Interaction of nanostructured metal overlayers with oxide surfaces. *Surface Science Reports* **2007,** *62* (11), 431-498.
8. Tait, E. W.; Ratcliff, L. E.; Payne, M. C.; Haynes, P. D.; Hine, N. D. M., Simulation of electron energy loss spectra of nanomaterials with linear-scaling density functional theory. *Journal of Physics: Condensed Matter* **2016,** *28* (19), 195202.